Fakultät für Chemie

Lehrstuhl für Pharmazeutische Radiochemie

Structural modifications of PSMA ligands to optimize their pharmacokinetics

Alexander Schmidt

Vollständiger Abdruck der von der Fakultät für Chemie der Technischen Universität München zur Erlangung des akademischen Grades eines

Doktors der Naturwissenschaften (Dr.rer.nat.)

genehmigten Dissertation.

Vorsitzender: Prof. Dr. Dr. h. c. Horst Kessler

Prüfer der Dissertation:

1. Prof. Dr. Hans-Jürgen Wester
2. Priv.-Doz. Dr. Matthias Eiber

Die Dissertation wurde am 17.08.2017 bei der Technischen Universität München eingereicht und durch die Fakultät für Chemie am 2.11.2017 angenommen.

-- Meiner Familie –

- mic drop -

hand

Table of Contents

Abstract

Prostate cancer (PCa) remains one of the most common malignancies in men. Androgen deprivation therapy (ADT) is initially highly effective but biochemical recurrence is often inevitable after several months or years, thus further treatment options are needed. The prostate specific membrane antigen (PSMA) was recognized as promising molecular target in the past and enabled the development of specific radiolabeled tracer for PCa imaging and endoradiotherapy. Primary goal of this work was the development and identification of structural modifications to optimize the pharmacokinetic profile of ligands based on PSMA I&T.

Four essential structural regions were modified and investigated. The combination of solution and solid phase peptide synthesis afforded rapid tracer development. Human prostate cancer (LNCaP) cells were used to determine IC_{50} values in a competitive binding assay using ([^{125}I]I-BA)KuE as radioligand. Internalization and externalization kinetics of ^{68}Ga- and ^{177}Lu-labeled inhibitors enabled evaluation of cell uptake and retention. Lipophilicity of the radiolabeled ligands was determined applying the shake flask method. Binding towards human serum albumin (HSA) was measured employing a modified RP-HPLC method. The metabolic stability as well as the pharmacokinetic profile were evaluated in PET and biodistribution studies using LNCaP tumor-bearing CB-17 SCID mice. Subcellular murine S9 liver and kidney fractions were used to establish an *ex vivo* metabolite assay and quantitative autoradiographic studies allowed the evaluation of affinity towards murine PSMA (mPSMA).

The extension of the peptide spacer with 4-amino-L-phenylalanine in combination with an optimized stereochemical spacer configuration resulted in an affinity (IC_{50}) of 1.1 ± 0.1 nM for [^{nat}Lu]**PSMA-31**, being sevenfold higher compared to the lead compound [^{nat}Lu]**PSMA I&T**. Carbohydration reduced unspecific binding of [^{68}Ga]**PSMA-20** in PET and biodistribution studies. The observed fast disposition *in vivo* and reduction of renal accumulation rendered carbohydration as valuable tool for the design of imaging agents. Enhancement of plasma protein binding (> 97%) through linker modification with 4-iodo-D-phenylalanine allowed extended target delivery with increasing tumor uptake of [^{177}Lu]**PSMA-41** from 8.5 ± 1.1% ID/g at 1 h p.i. to 14.01 ± 1.3% ID/g at 24 h p.i..

The transition from the binding scaffold EuK to EuE in combination with 2,4-dinitrobenzoic acid residues elevated internalization to the highest value of 359.5 ± 22.6% for [^{177}Lu]**PSMA-61**, demonstrating an almost fivefold increase compared to [^{177}Lu]**PSMA I&T**. The final optimization led to the design of the trimesic acid substituted PSMA ligand **PSMA-66**. Lower nanomolar affinity (3.8 ± 0.8 nM vs. 7.9 ± 2.4 nM), drastically improved internalization (297.8 ± 2.0% vs. 75.5 ± 1.6%), elevated *in vitro* tumor cell retention (90.1 ± 3.5% vs. 62.8 ± 0.4%,

60 min incubation) together with lower unspecific binding *in vivo*, reduced renal accumulation (117.5 ± 6.9% ID/g vs. 128.9 ± 16.7% ID/g) and a more than twofold increase in tumor uptake (10.0 ± 0.4% vs. 4.7 ± 1.0% ID/g), demonstrated the superiority of [^{177}Lu]**PSMA-66** in direct comparison to [^{177}Lu]**PSMA I&T**. The increased affinity and internalization together with the strong intracellular retention should lead in human applications to extensive lesion uptake and decelerated clearance from the tumor tissue, thus enhancing the endoradiotherapeutic outcome. Despite the still high renal uptake, **PSMA-66** is a remarkably potent tracer with advanced tumor-targeting and pharmacokinetic properties. First-in-human application will help to elucidate if the preclinical optimization will lead to clinical advantages regarding imaging and endoradiotherapy of recurrent PCa.

Finally, the utilization of subcellular S9-fractions in the established *ex vivo* metabolite assay allowed the reduction of necessary laboratory animals for metabolic stability in a fast and efficient assessment. The results confirmed the beneficial influence of L- to D-amino acid transition and demonstrated the superiority of the conducted S9-assay in comparison to blood plasma incubation. In order to validate the results of the S9-assay, further preclinical investigations are necessary. However, the S9-assay will help to eliminate unfavorable modifications during tracer development and provides a rapid and comprehensive metabolic stability screen.

Zusammenfassung

Das Prostatakarzinom (PCa) ist eine der häufigsten bösartigen Tumorerkrankungen bei Männern. Obgleich die initiale Hormontherapie hoch effektiv ist, zeigt sich in nahezu allen Fällen nach einigen Monaten bzw. Jahren ein biochemisches Rezidiv, welches weitere Behandlungsoptionen notwendig macht. Das Prostata-spezifische Membranantigen (PSMA) wurde in der Vergangenheit als vielversprechende molekulare Zielstruktur des PCa entdeckt und ermöglichte die Entwicklung von spezifischen radiomarkierten Substanzen für die Bildgebung und Endoradiotherapie des PCa. Das primäre Ziel dieser Arbeit war die Entwicklung und Identifizierung struktureller Modifikationen welche das pharmakokinetische Profil von PSMA I&T-basierter Liganden optimieren können.

Die Kombination aus Flüssig- und Festphasen-Peptidsynthese ermöglichte eine einfache und effiziente Ligandensynthese. Die Auswirkungen der durchgeführten strukturellen Modifikationen wurden detailliert untersucht. Hierzu wurden LNCaP-Zellen in kompetitiven Bindungsassays verwendet und IC_{50}-Werte unter Verwendung von ([^{125}I]I-BA)KuE als Radioligand ermittelt. Sowohl Internalisierung als auch Externalisierungsexperimente an LNCaP-Zellen erlaubten die Evaluierung von Zellaufnahme und zellulärer Retention der ^{68}Ga- und ^{177}Lu-markierten Inhibitoren. Die Lipophilie der PSMA Inhibitoren wurde anhand der Schüttelmethode evaluiert. Mit Hilfe einer modifizierten RP-HPLC-Methode wurde der Einfluss der strukturellen Variationen und der Stereochemie auf die Plasmaprotein-Bindung bestimmt. Die metabolische Stabilität sowie das pharmakokinetische Profil wurden in Kleintier-PET und Biodistributionsstudien in LNCaP-Tumor tragenden CB-17 SCID Mäusen evaluiert. Die Verwendung von subzellulären murinen S9 Leber- und Nierenfraktionen ermöglichte die Etablierung eines *ex vivo* Metaboliten-Assay. Des Weiteren erlaubten quantitative Autoradiographiestudien die Evaluierung der Affinität gegenüber murinem PSMA (mPMSA).

Die Erweiterung des Peptidspacers um 4-Amino-L-Phenylalanin in Kombination mit einer stereochemisch optimierten Spacerkonfiguration resultierte in einer Affinität von 1.1 ± 0.1 nM für das Derivat [^{nat}Lu]**PSMA-31**, was einer siebenfachen Steigerung im Vergleich zur Leitstruktur [^{nat}Lu]**PSMA I&T** gleichkommt. Glykosilierung ermöglichte die Reduktion der unspezifischen Gewebebindung von [^{68}Ga]**PSMA-20** sowohl in PET als auch in Biodistributionsstudien im Vergleich zur Referenz [^{68}Ga]**PSMA I&T**. Die schnelle Distribution *in vivo* bei gleichzeitiger Reduktion der renalen Anreicherung bestätigte, dass Glykosilierung eine effiziente Methode für die Entwicklung von Bildgebungsagenzien ist. Die Erhöhung der Plasmaproteinbindung durch die Linkermodifikation mit 4-Iod-D-Phenylalanin (> 97%) ermöglichte einer Steigerung der Tumoraufnahme von 8.5 ± 1.1% ID/g nach 1 h auf 14.01 ± 1.3 % ID/g nach 24 h für das Derivat [^{177}Lu]**PSMA-41**. Der Übergang vom EuK-

Zusammenfassung

Bindemotiv hin zum EuE-Bindemotiv in Kombination mit Substituenten im Linker und Peptidspacer basierend auf 2,4-Dinitrobenzoesäure erhöhte die Internalisierung auf den am höchsten gemessenen Wert von 359.5 ± 22.6% für [^{177}Lu]**PSMA-61**. Diese Verbesserung kommt im Vergleich mit [^{177}Lu]**PSMA I&T** einer fast fünffachen Steigerung gleich.

Weitere Optimierungsschritte führten zum Design der mit Trimesinsäure modifizierten Verbindung **PSMA-66**. Im Vergleich mit der Referenz [^{177}Lu]**PSMA I&T** führten die finalen Modifikationen zu einer verbesserten nanomolaren Affinität (3.8 ± 0.8 nM vs. 7.9 ± 2.4 nM), zu einer drastisch erhöhten Internalisierung (297.8 ± 2.0% vs. 75.5 ± 1.6%), einer verlängerten intrazellulären Retention (90.1 ± 3.5% vs. 62.8 ± 0.4%, 60 min Inkubation), einer niedrigeren unspezifischen Gewebebindung *in vivo*, einer leicht reduzierten renalen Aufnahme (117.5 ± 6.9% ID/g vs. 128.9 ± 16.7% ID/g) und einer mehr als zweifach erhöhten Tumoraufnahme (10.0 ± 0.4 vs. 4.7 ± 1.0% ID/g) in der Biodistributionsstudie des Liganden [^{177}Lu]**PSMA-66**. Die erhöhte Affinität in Kombination mit einer höheren Internalisierungsrate und einer verlängerten Zellretention sollten in der klinischen Anwendung zu einer erhöhten Tumoraufnahme und verlängerten Retention im Tumorgewebe führen. Gleichzeitig sollte es hierdurch zu einer Steigerung der therapeutischen Effizienz einer Endoradiotherapie kommen. Obwohl **PSMA-66** in den präklinischen Studien eine hohe Nierenaufnahme zeigte, handelt es sich bei diesem PSMA Liganden um eine hochpotente Verbindung mit verbesserten pharmakokinetischen Profil. Im Rahmen erster klinischer Untersuchungen wird zu belegen sein, ob die erfolgreiche präklinische Optimierung auch zu einer verbesserten *in vivo* Eignung hinsichtlich Bildgebung und Endoradiotherapie des rezidivierenden Prostatakarzinoms führen wird.

Abschließend ermöglichte die Verwendung subzellulärer S9-Fraktionen im etablierten *ex vivo* Metabolitenassay die Reduktion benötigter Labortiere für die schnelle und effiziente Beurteilung der metabolischen Stabilität von PSMA Liganden. Die Ergebnisse bestätigten den vorteilhaften Effekt von D-Aminosäuren gegenüber L-Aminosäuren hinsichtlich der metabolischen Stabilität. Es war zusätzlich möglich zu zeigen, dass der S9-Assay im Vergleich mit einer Blutplasmainkubation validere Daten zur Metabolisierung liefert. Um die bisherigen Ergebnisse zu validieren sind weitere präklinische Untersuchungen notwendig. Der im Rahmen dieser Arbeit etablierte S9-Assay kann daher eine wertvolle Plattform zur einfachen und umfangreichen Evaluierung der metabolischen Stabilität darstellen und helfen ungünstige Modifikationen schon früh zu identifizieren und zu eliminieren.

I. INTRODUCTION

1. Background

"Illness is the night side of life, a more onerous citizenship. Everyone who is born holds dual citizenships, in the kingdom of the well and in the kingdom of the sick. Although we all prefer to use the good passport, sooner or later each of us is obliged, at least for a spell, to identify ourselves as citizens of that other place"

-Susan Sontag, Illness as Metaphor-

1.1 Cancer: Origin and evolution

Besides metabolic and infectious diseases, cancer remains one the most common reasons for death worldwide and the lifetime risk for a diagnosis of cancer is one in three [1-4]. Particularly in developed affluent countries, in which the demographic population-age is high, cancer is the second leading cause for death since the incidence of cancer correlates with age. Regarding public healthcare systems, the associated high costs of diagnosis and treatment of malignant diseases are considered as a major problem [5,6].

From an evolutionary perspective, cancer development and progression arises from a natural competitive Darwinian selection among populations of dividing cells, which is an unavoidable consequence of fluctuating intrinsic and extrinsic factors [7,8]. Together with a changing microenvironment, these driving factors result in a consecutive accumulation of genetic and epigenetic incidents (mutations), which allow cancer cells to acquire a variety of multifaceted phenotypic abilities such as proliferative self-renewal and expansion throughout the cancer-harboring organism [9,10].

All cells originate from a progenitor cell, which is the fertilized egg in humans. The acquired somatic mutations of the deoxyribonucleic acid (DNA) lead over time to genetic instability and contribute to the origin of phenotypically abnormal tumor progenitor cells (see Figure 1). Not all acquired somatic alterations contribute to the development of cancer. While some just increase the mutational burden and are referred as passenger mutations, driver mutations are fundamentally associated with progressive oncogenesis, such as the recurrent fusion of TMPRSS2 and ETS genes in prostate cancer [11].

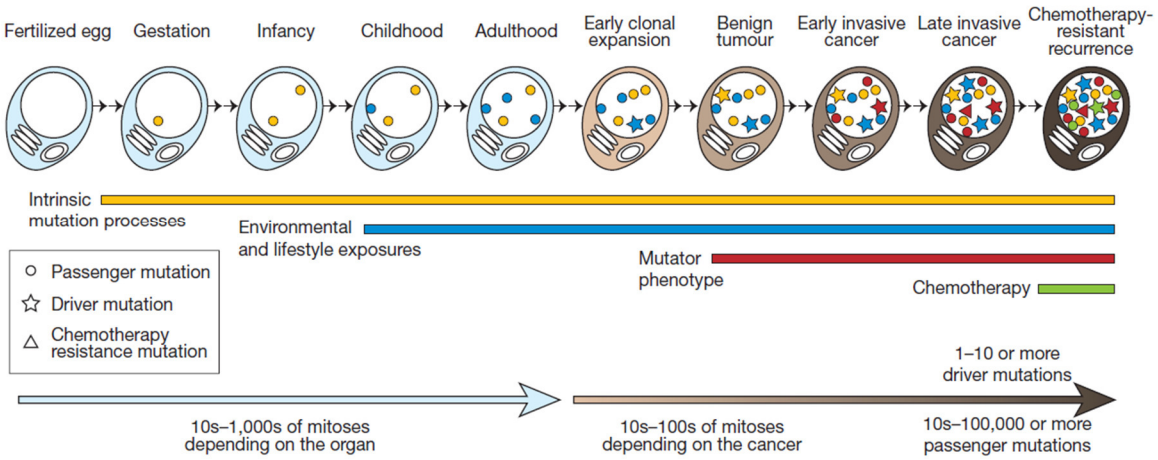

Figure 1. Lineage of mitotic cell division from the fertilized egg to a chemoresistant cancer cell showing the course of acquired somatic mutations by the cancer cell and the involved processes. Intrinsic mutations may be acquired during normal cell division or through exogenous mutagens, while the cell maintains a phenotypical normal state. During progression to cancer, early processes like DNA repair defects increase the mutational burden. While passenger mutations have no effect on cancer development, driver mutations will induce cancerous phenotypes [12].

Somatic DNA aberrations may be a result of several origins, involving hormonal factors [13], inflammation [14], viral infections [15], epigenetic methylation [16], free radical induced DNA damage [17], dietary habits [18], ionizing radiation-exposure [19], chemical exposure [20], skin exposure to ultraviolet light [21] or detrimental lifestyle habits [22,23] amongst others. It is estimated that adult epithelial cancer such as prostate cancer requires five to seven somatic driver mutations within a cancerogenic cell to confer the ability to spread into distant regions and to develop the characteristic trait of metastatic behavior [24-27].

Whether tumorigenesis is the consequence of gradually acquired genetic mutations or more distinct incidents of genome rearrangements is currently unclear (see Figure 2). Chromothripsis characterizes single catastrophic events of massive genome shattering and reassembly and is described for pediatric medulloblastoma due to loss of TP53 [28-30], whereas chromoplexy is associated with punctuated tumor evolution and may involve a wide range of DNA rearrangements such as deletion of NKX3-1 or FOXP1 in prostate cancer [31]. The primary result of these genetic alteration is the unrestrained proliferation and subsequent clonal expansion with gradually increasing genomic instability [10,32].

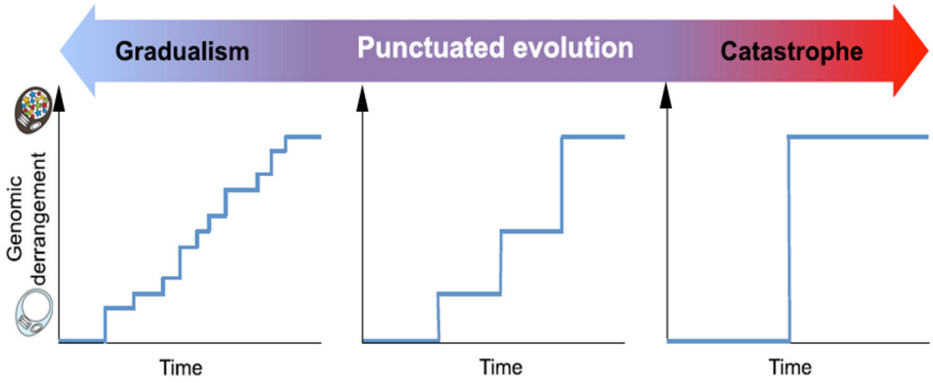

Figure 2. Continuum model of genomic derangement of prostate cancer. Oncogenic mutations may accumulate continuously in cancer genomes (left), through punctuated progression (middle, chromoplexy), or in a single catastrophic event (right, chromothripsis) [31].

Nevertheless, the clonal expansion of cancer cells is subject to extensive selection pressure emanated from the immune system and the tumor microenvironment. Genetic aberrations alone are not always sufficient to manifest clinical development of cancer, since driver mutations give only a 'fitness advantage' of 0.4 to 1.0% as it was stochastically quantified for glioblastoma, pancreatic cancer and colorectal cancer [26,33]. The surrounding microenvironment is essentially involved and displays ambivalent characteristics. Injection of cancer cells into developing embryos can suppress the malignant behavior and convert the phenotype to near normal state [34-36]. On the other side, activated stoma cells (e.g. through radiation) can induce the formation of cancer in nontumorgenic cell lines [37,38]. In this context, increased levels of transforming growth factor-β (TGFβ) and stromal-cell-derived factor 1 (SDF1 or CXCL12) are considered to be among the primary essential molecular signals which contribute to swift stromal remodeling and formation of a 'niche' for cancer cells and increased myofibroblast differentiation [39,40]. Association of myofibroblasts has been observed in premalignant prostatic intraepithelial neoplasia (PIN) with rising numbers as the tumor progresses [41,42] and specific genomic signatures of cancer-associated myofibroblast are of prognostic value to predict clinical outcome [43].

A high grade of mutations will ultimately lead to a change of antigens presented by the affected cells and thereby initiate immune-recognition by the innate and adaptive immune system. Infiltrating immune cells affect tumor growth in a paradoxical way and display the central role of inflammation in tumorigenesis [44]. While the infiltration of natural killer (NK) cells is associated with favorable prognosis in gastric and colorectal carcinoma [45,46], high numbers of macrophages, CD4+ and CD8+ T-cells correlate with poor prognosis in PCa [47-50]. Macrophages interact with the surrounding stromal cells through expression of several regulatory factors such as tumor necrosis factor-α (TNF-α), TGFβ, VEGF and interleukins 1 (IL-1) and 6 (IL-6) [51], thereby promoting the transformation of the tumor microenvironment. Interestingly, long-

term utilization of non-steroidal anti-inflammatory drugs (NSAIDs) reduces the relative risk to develop non-viral-associated solid tumors of epithelial origin [52,53].

1.2 Prostate Cancer: From benign to castration resistance and metastasis

Whole genome sequencing (WGS) of tumors dissected from prostate cancer patients revealed that characteristic mutation signatures are recurring and relate to different stages of the disease [31,54]. It was reported that benign prostatic hyperplasia (BPH) and PIN exhibit 13.4% differentially expressed genes while the difference between PIN and localized PCa is only 1.2%, indicating that early events are crucial determinants of further progress as shown in Figure *3* [55]. The deletion of the tumor suppressor gene (TSG) NKX3-1 [56], mutation of glutathione S-transferase π [57] and partial deletion of chromosome 21, which triggers the fusion of TMPRSS2 and ETS transcription factor ERG [58], are considered to be among the earliest events [11,31,59]. NKX3-1 regulates androgen receptor signaling and suppresses the TMPRSS2-ERG fusion gene, whereas the latter triggers loss of PTEN [60], a further TSG, and promotes the overexpression of androgen receptors (AR), the MYC oncogene-bearing chromosome 8q and CXCR4 [61]. Genetic TMPRSS2-ERG fusion has been observed in approx. 50% of localized PCa and infrequently in PIN [55,62]. Interestingly, whereas ETS-fusion positive PCa cells resembled chromoplexy, ETS-fusion negative PCa cells resembled chromothrypsis with extensive chromosomal rearrangements [31].

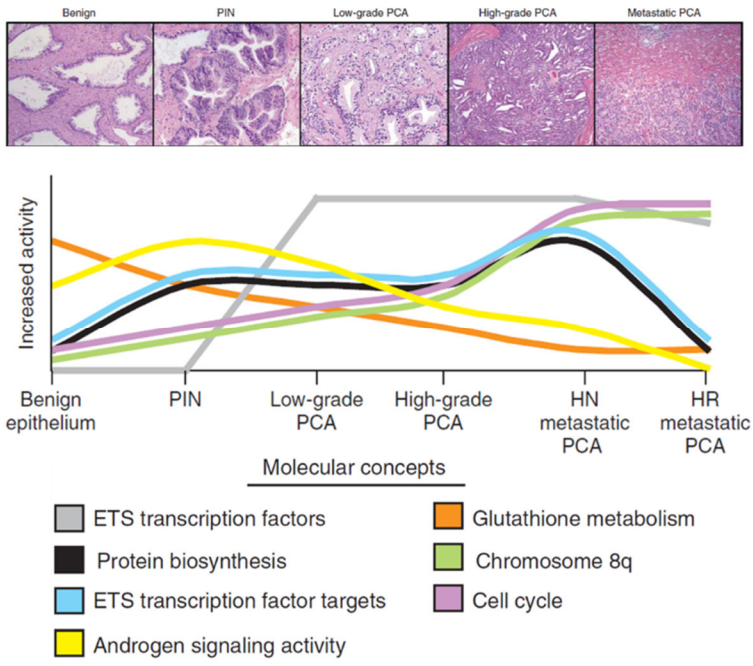

Figure 3. Molecular concept model of PCa progression from benign to hormone refractory (HR) metastatic PCa. The relative expression of enriched concepts identified by expression profiling of specific cell populations was used to develop a molecular theory of PCa progression [55].

The transition of PIN to low-grade PCa is accompanied by loss of additional TSG's like TP53 [31] and the steadily increasing role of androgen receptor signaling, which leads to enhanced proliferation. The increased biosynthesis is observable through enlarged nucleoli during that state [63]. According to a comprehensive analysis of 333 primary PCa samples, the most frequent genomic aberrations are ETS family gene fusion, PTEN deletion, SPOP and FOXA-1 mutations [64].

Androgen ablation therapy is initially highly effective but treatment failure and biochemical recurrence are imminent after several months or years [65,66]. Therefore, the progression to androgen independent PCa remains a central cornerstone. A genetic mutation to circumvent androgen ablation is the amplification of the AR gene, which is recurrently found in progressed PCa but only rarely seen in primary cancers before endocrine treatment [67,68]. Other mechanisms involve hypersensitivity to androgen signaling [69], enhanced conversion of dihydrotestosterone through increased activity of 5α-reductase [70], promiscuous ligand-binding in which antagonists or endocrine steroids act as agonists [71,72] or dysregulation of co-regulators influencing AR signaling [73]. Among other effects, androgen depletion and AR gene mutations are reported to enhance mesenchymal-epithelial transition (MET) through upregulation of adhesion molecules like N-cadherin and cadherin-11 [74,75], thereby increasing the migratory properties of metastatic cells.

The transition from localized to metastatic castration resistant prostate cancer (mCRPC) arises from a complex interacting dynamic network involving several components and ongoing mutations [31]. Nevertheless, the most frequent genomic aberrations in the mutational landscape of mCRPC are mutations of the AR gene, loss of PTEN and TP53 and fusion of ETS genes with TMPRSS2 [27]. In this respect it is noteworthy, that TMPRSS2-ERG fusion gen partly mediates down-regulation of PSMA expression at the transcript level [76].

Precise genomic information support the selection of patients for explicit therapy regimes according to their individual stage of disease to enhance treatment response [54,77-79] or to predict disease progression [80-84]. However, transcriptional mutations lead to altered expression profiles of proteins, which represent the working components of cancer progression. Thus, proteins may serve as diagnostic marker or targets for the development of new therapeutic agents [85]. In this respect, the PSMA represents an outstanding target due to its expression profile.

2. Prostate-specific membrane antigen

"If you know the enemy and know yourself, you need not fear the result of a hundred battles. If you know yourself but not the enemy, for every victory gained you will also suffer a defeat. If you know neither the enemy nor yourself, you will succumb in every battle"

-Sun Tsu-

2.1 Structure, function and expression

2.1.1 Structure

PSMA is expressed on prostate cancer cell membranes as a non-covalently associated homodimer [86]. The entire protein contains a transmembrane region (24 amino acids (AA)), an *N*-terminal cytoplasmatic sequence (19 AA) and a large extracellular domain (707 AA) (see Figure 4) [86,87].

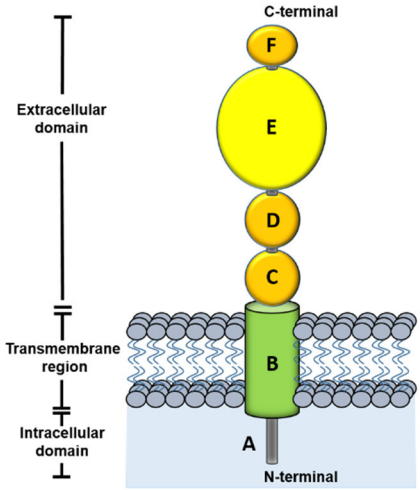

Figure 4. Schematic structure of PSMA. The structure of PSMA includes a short intracellular domain (A), a hydrophobic transmembrane region (B) and the large extracellular domain (ED). The ED structure contains two proline- and glycine rich domains (C and D) with unknown function and the catalytic domain (E), which contains the binding site for small PSMA inhibitors. To the C-terminal domain (F), with unknown function, is a helical dimerization domain localized.

The extracellular domain has nine available *N*-linked glycosylation sides, of which none is able to interact directly with a bound substrate due to the broad distance. Glycosylation affects further the secretion of the cleavable extracellular domain, membrane expression and enzymatic activity [87-90]. Each monomer of the extracellular dimer contains three domains. An exopeptidase-like protease domain, a helical domain, which is involved in forming the interface of the dimer and the substrate binding cavity, and the apical domain, a substantial piece of the substrate binding cavity [91]. The surface of the protein and the enzymatic active core is connected through an approx. 20 Å deep funnel [92].

The large cavity at the interface of the three domains (1,110 $Å^2$) accommodates the binuclear, substrate binding, zinc-site with predominantly polar residues (66-70%). The two zinc atoms

are coordinated by two histidines (His337/553), Glu425 and Asp453 residues and a water molecule [91,93]. This water molecule inherits hydroxide character through the interaction with one of the zinc-ions and is deprotonated through a glutamate residue, which is involved in the catalytic process after substrate binding. Crystal structure analysis with 2-(phosphonomethyl)pentanedioic acid (2-PMPA) in complex with PSMA revealed that the water molecule is replaced by the phosphonate moiety of 2-PMPA, which strongly interacts with the zinc ion [94].

2.1.2 Physiological and pathophysiological function

PSMA belongs to the type II transmembrane proteins, which serve as transport or binding proteins or have hydrolytic activity. The enzymatic activity of PSMA is located at the extracellular domain [95] and the protein was physiologically found to be expressed predominantly at the apical side in the brain, kidney, prostate and brush border membrane of the intestine among other sites [96,97].

In the brain, PSMA mediates the conversion of *N*-acetyl-aspartyl glutamate (NAAG), which is a neuro-transmitter, to NAA and free glutamate and therefore called NAALDase. In the small intestine, it is referred as folate hydrolase (FOLH1) or glutamate carboxypeptidase II (GCPII), since it is cleaving glutamates from poly-γ-glutamated folate in an exopeptidase-like manner (see Figure 5) [96,98-102]. In order to perform enzymatic folate hydrolase and NAALDase activity, dimerization of PSMA is necessary [103,104].

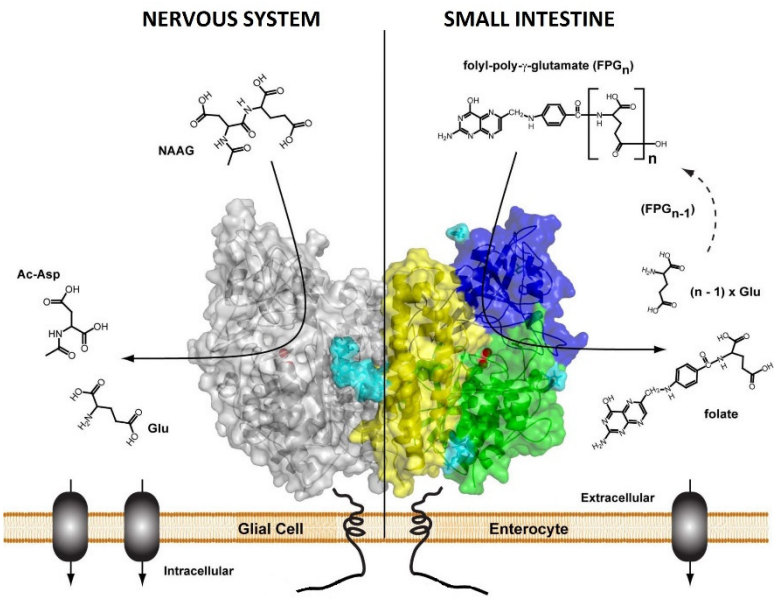

Figure 5. Crystal structure of PSMA tethered to the cellular plasma membrane. One monomer shown in semitransparent surface representation (green – protease domain; blue – apical domain; yellow – C-terminal domain) and the second monomer is colored gray. *N*-linked sugar moieties are colored cyan, and the active-site Zn^{2+} ions are shown as red spheres. **Left panel:** NAAG catabolism in the mammalian nervous system. **Right panel:** Folate hydrolase at the plasma membrane of enterocytes.

Clathrin coated pits mediate constitutive and spontaneous internalization of PSMA. Upon binding of a ligand and internalization, the ligand-PSMA complex accumulates in the endosome

[105]. The MXXXL motif in the cytoplasmatic tail of PSMA is necessary for internalization. Deletion of either the first or the last position of the peptidic sequence, abolishes internalization, whereas the amino acids in between are to some extent dispensable [106]. In the process of internalization, the cytoplasmatic tail of PSMA binds Filamin a (FLNa), an actin cross-linking protein, at the plasma membrane. The association with FLNa leads to the localization of PSMA in the recycling endosomal compartment. Without FLNa, PSMA accumulates in vesicles distributed throughout the cytoplasm [95].

Dependent on the ligand, binding can increase the internalization rate in a dose dependent manner [105]. Incubation of PSMA with the natural substrate NAAG has no effect on the internalization rate, whereas coincubation with the murine antibody (mAb) J591 increases the internalization process [105,106]. These results indicate that the substrate itself has impact on the internalization kinetics and PSMA might function as a transporter for a putative ligand.

Three alternatively spliced variants of PSMA are known, PSM', PSM-C and PSMA-D. The ratio between the alternatively spliced variant PSMA and PSM' (PSMA/PSM') was shown to correlate with the Gleason score in PCa patients [107]. Normal prostate cells predominantly express the transcripts of the truncated form PSM', which lacks intracellular and transmembrane domains and resides in the cytoplasm. This truncated form is less glycosylated and thus likely lacks enzymatic activity, since it was reported that the glycosylation pattern influences the enzymatic activity of the carboxypeptidase and the folate hydrolase [89,90]. Folate is necessary for cell growth, in this respect the ratio between PSMA and PSM' increases in cancerous cells, which may enables sufficient supply of folate via PSMA overexpression and provides growth advantage [108] as folate receptors are present on the membrane of epithelial cells [108].

Little is known about the precise mechanisms of PSMA function in PCa and its regulation. Since PSMA is predominantly expressed in the neovasculature of solid tumors, the association with angiogenesis is plausible [109-113]. Conway et al. reported that PSMA enzyme activity is necessary for laminin-specific endothelial cell invasion via β_1-integrin activation and thus increased cell adhesion and migration. On the other side, PSMA activity is not necessary for endothelial cell viability or morphogenesis [114]. Non-PSMA expressing mice develop normally, which implies that PSMA is not essential for physiological angiogenesis but rather participates in pathological response mechanisms [114,115]. A lack of PSMA does also not affect normal retinal angiogenesis, whereas PSMA expression may induce avascular growth [116].

The proposed mechanism for angiogenesis presumes that the endothelial cell activation and adhesion is a consequence of laminin digestion through matrix metalloproteinase-2 (MMP-2) and MMP-9. In the following step, the laminin-fragments are further processed by PSMA in a

downstream-cascade to enable angiogenesis [114,117]. The PSMA generated laminin peptides, especially LQE, activate endothelial cells and their migration via direct $\alpha_2\beta_1$- and $\alpha_3\beta_1$-integrin binding and concomitant phosphorylation of focal adhesion kinase (FAK), thereby increasing cell adhesion in a dose dependent manner and enhancing angiogenesis [118].

Further investigation showed that PSMA is able to activate the GTPases RAS, RAC1, MAPK, p38 and ERK1/2. Phosporylation of p38 and ERK1/2 is able to activate NF-κB and thus induces the transcriptional upregulation of interleukin 6 (IL-6) and the chemokine CCL5, both known for their involvement in the regulation of proliferation, apoptosis and angiogenesis [119]. Recent work indicates, that PSMA associates in a macromolecular complex with FLNa, β_1-integrin, phosphor-p130CAS, phosphor c-Src and the epidermal growth factor receptor (EGFR) [120]. The associated complex activates the β_1-integrin and phosphorylates c-SRc and thereby EGFR. The hereby triggered signal activates the PI3K-AKT/mTOR/BAD and MAPK pathway and induces proliferation and resistance to apoptosis among other mechanisms [120,121]. Interestingly, a recent phase II study using everolimus (mTOR inhibitor) and bicalutamide (anti-androgen) showed promising results in castration resistant PCa patients [122].

Information about the interaction of androgen receptor signaling and PSMA expression are currently scarce. The PSMA encoding gene is located on chromosome 11p11-p12 and a homologues gene on 11q14 [87]. No androgen response elements within the promotor region of PSMA was found, indicating primarily no direct regulation but maybe in an indirect way through the cAMP second messenger way, since the promotor region of PSMA contains a cAMP response element [87]. The down-regulation of PSMA expression in the LNCaP cell line through 5-α-dihydrotestosterone (DHT) and testosterone is another indicating factor for a distinct relationship of PSMA and AR-signaling [123]. DHT reduced the expression level 8 to 10 fold and testosterone 3 to 4 fold after 24 h coincubation in LNCaP cells [123]. Similar findings were obtained in clinical studies, in which PSMA levels were rising following androgen ablation therapy [124].

2.1.3 Physiological and pathophysiological expression

PSMA was discovered through the anti-prostate monoclonal antibody 7E11-C5.3, which was profound binding to malignant prostate tissue [123]. Besides the prostate, physiological expression of PSMA exists in the duodenal mucosa, proximal renal tubules, colonic crypt neuroendocrine cells, lactating breast, salivary and submaxillary glands [125-127]. Expression of PSMA was likewise detected in non-neoplastic reparative and regenerative tissues such as the vessels of proliferative endometrium, on vessels of the granulation tissue of the heart valve and pleura and to some extent in keloids [128]. Neurological disorders, like schizophrenia, Alzheimer, multiple sclerosis and amyotrophic lateral sclerosis, displayed often dysregulated PSMA levels [129-131].

Information about the PSMA expression in benign and malignant prostate tissue are somewhat contradictory. While benign prostate tissue reveals only decreased or absent luminal PSMA expression [123], the number of PSMA-positive cells are increasing from PIN to adenocarcinoma and metastases [132-134]. Immunostaining of basal cells revealed only rarely positive results. Perner et al. [135] reported that PSMA levels in hormone refractory metastases were lower compared to lymph node lesions, whereas Bostwick et al. showed that hormone refractory metastases inherit the highest PSMA levels [132]. In contrary to others, Schmittgen et al. reported that malignant PSMA overexpression was only modest in magnitude compared to normal prostate tissue [107].

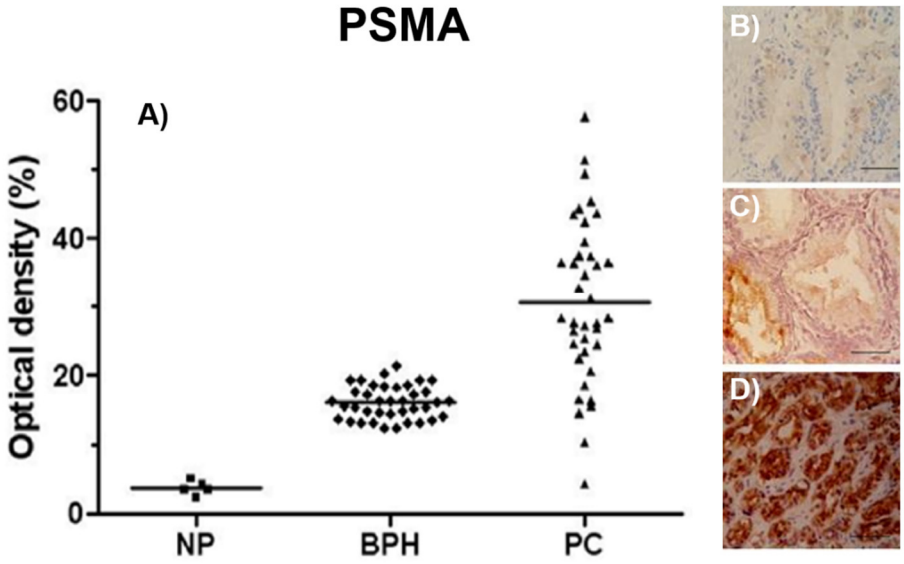

Figure 6. Distribution of tissue PSMA-immunostaining intensity (measured as average optical density) according to normal prostate (NP), benign prostatic hyperplasia (BPH) and prostatic carcinoma (PC) (A). H&E stained slides of PSMA in NP (B), BPH (C) and PC (D) [133].

Immunostaining revealed that the PSMA expression is homogenously distributed on PCa samples [136] (see Figure 6 [133]). However, heterogeneous PSMA staining was likewise reported for high grade carcinoma [125] and low Gleason score (GS) tumors showed a greater degree of heterogeneity and less association with PSMA [132,137].

Several solid tumors, including pancreatic carcinoma, melanoma, lung cancer, transitional cell carcinoma of urinary bladder and soft tissue sarcoma, express PSMA mRNA and the protein PSMA in their angiogenic microvessels in the neovascular endothelium [110-113]. The differentiated malignant cells, however, did not stain for PSMA nor did the endothelial cells of normal vessels in nearby benign tissue.

PSMA overexpression is significantly associated with time to PSA recurrence [135] and may be used as independent biomarker to predict biochemical recurrence after prostatectomy [137].

Overexpression of PSMA reduced the biochemical recurrence time from 43.8 months in PSMA non-overexpressing patients to 34.8 months in PSMA overexpressing patients [137].

Some regulating factors of PSMA expression are known. The genetic expression is influenced by the PSMA promotor gene and PSMA enhancer (PSME) [87]. PSME was shown to be upregulated in prostate cancer and down regulated through indirect androgen signaling [138]. Intracellular Ca^{2+} ions activate transcription factors which upregulate PSMA. Coincidentally, CaT-like calcium channels are upregulated in prostate cancer cells and correlate with the malignancy of the disease [139]. Downregulation of PSMA was reported for the TMPRSS2-ETS fusion gene but not for the normal ERG gene, which is partially mediated by androgen receptor signaling on the transcriptional level [76].

2.2 Design of PSMA inhibitors

Mainly phosphine, thiol and urea-based PSMA-targeting motifs are described in the literature with emphasis on urea-based motifs due to the straightforward synthesis and high obtainable affinity [140,141]. The stereochemical configuration of the binding motif exerts immense influence on the binding affinity, in which the L-amino acids are superior to D-configuration [140,142,143]. This observation implies that stereochemistry plays a fundamental role in substrate binding.

Thiol-based inhibitors, like 2-(3-mercaptopropyl)pentanedioic acid (2-MPPA), demonstrated high affinity towards PSMA and were used as orally bioavailable PSMA inhibitors for neuropathic pain [144]. Further modifications of 2-MPPA in the P1' position (Figure 7 C) through introduction of benzoic acid derivatives, additionally increased binding potency [145,146]. Hydroxamate and sulfonamide-derivatives were investigated due to a bidentate binding of zinc ions in MMPs. Nevertheless, they showed only moderate binding capacity towards PSMA [147,148].

2-PMPA was one of the first potent PSMA inhibitors based on phosphinic acid [149]. The pentanedioic acid moiety within 2-PMPA was used for fluorination with ^{18}F for PET-imaging and resulted in a PET imaging agent with limited suitability[150,151]. Phosphoramidate based inhibitors demonstrated that besides the affinity towards PSMA, the mode of inhibition may be used to increase the internalization rate and thereby the effective uptake *in vivo*. Pseudo-irreversible mode of inhibition correlated with increased internalization capacity, whereas slowly reversible and rapidly reversible binding modes demonstrated less internalization. Based on these findings, the authors concluded that the induced conformational changes upon binding contribute to the interactions of the cytoplasmatic tail of PSMA with clathrin and the clathrin adaptor protein-2 (AP-2) [152,153].

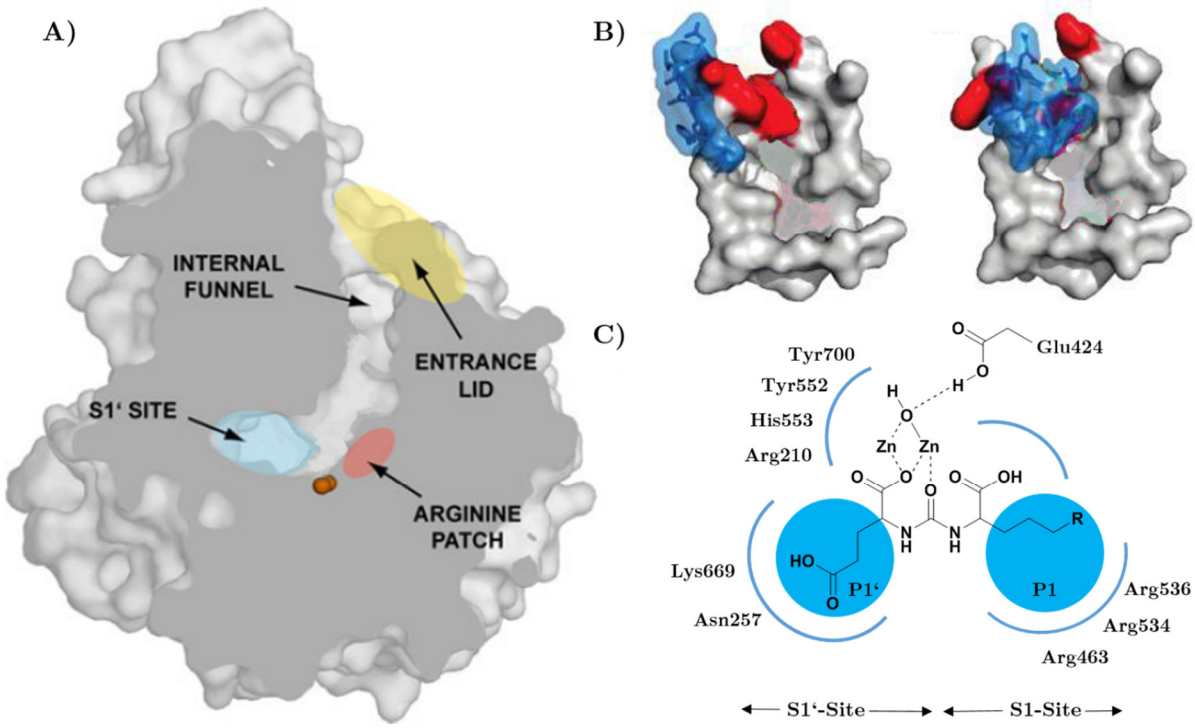

Figure 7. Cross section image of PSMA (PDB code 4P45) (A). The protein structure is colored as gray surface. Zinc ions are shown as orange spheres. Approximate positions of the arginine patch (red), S1' site (cyan) and entrance lid (yellow) are depicted [154]. Opened and closed entrance lid (blue) configuration of PSMA (B). Open lid configuration uncovers arene binding site (red) for lipophilic interactions with small ligands [155]. (C) Suggested binding mode of urea-based ligands to PSMA. The modification sites P1 and P1' are highlighted in blue [156].

The minimum requirements for effective binding of urea containing ligands were determined to be at least one glutamate moiety in the S1' pocket plus a second residue bearing a carboxyl group in addition to a further functionality (see Figure 7 C)[140]. The S1 pocket appears to be more promiscuous towards structural changes and can accommodate hydrophobic and hydrophilic groups through interaction with an accessory hydrophobic pocket [94,142,157,158]. The ureido linkage between the P1 and P1' moieties interacts with the zinc-ion, the side chains of His-553 and the activated water molecule through the ureido carbonyl oxygen. Although the glutamic acid residue at the P1' site enables high affinity and specificity, allyl, alkenyl, furanyl and thiophenyl moieties among others can bioisosterically replace this position [159,160].

L-glutamate within the S1' pocket is bound via its α-carboxylate group, forms a salt bridge with Arg-210 and interacts with the hydroxyl group of Tyr-552 and Tyr-700 [93]. The γ-carboxylate group creates a strong salt bridge with Lys-699 and a hydrogen bond with Asn-257 (Figure 7 C). Whereas the S1' pocket is indispensable for high affinity binding, the S1 pocket is to some extent more tolerant towards modifications and does not add substantial gain regarding substrate affinity [87,94].

The binding cavity additionally contains a patch of three arginine residues (Arg-463/534/536) within the S1 pocket (Figure 7 C). This patch is conserved among the species and may participates in the correct orientation of substrates via interaction with the negatively charged Glu-residues [161]. Overall, the cavity displays a positively charged character.

The funnel region of PSMA contains the arene binding site [155], which allows further affinity improvement upon simultaneous addressing of the catalytic center and the arene binding site (see Figure 7 A). However, in order to address the lipophilic pocket the entrance lid (amino acids Trp-541 to Gly-548, Figure 7 B) towards the enzyme needs to be in an open conformation, thus the ligands have to prevent the closure via steric hindrance.

Since the arene binding pocket requires open lid configuration, the linker between the binding motif and further functionality groups are of considerable importance and have been shown to highly influence the binding potency, mode of inhibition and internalization rate of PSMA [155,162,163].

While the interaction between the catalytic center and glutamate urea moieties are rather rigid, more distal ligand-protein interactions display highly dynamic behavior and may be cautiously considered [155]. Conformational structure activity analysis of PSMA inhibitors indicated that binding potency is entropy driven and a high conformational flexibility of the substrates provokes entropic penalty. In this respect, restricted ligands are more likely to exhibit higher potency compared to their more flexible analogs [164,165]. The same conclusion was found for the linker region of elongated PSMA inhibitors containing further functionality groups outside the enzymatic pharmacophore [163,166].

3. PSMA-targeting radiopharmaceuticals in prostate cancer management

"We must accept finite disappointment, but never lose infinite hope."

- Martin Luther King, Jr.-

3.1. PSMA imaging

The accurate diagnosis and staging of prostate cancer is essential for the effective treatment of patients. Current guidelines recommend in the first line sonography-guided needle biopsy for histological verification [167]. If the results are negative but PCa still suspected, MRI and CT evolved to standard procedures to facilitate confirmation [168]. Upon diagnosis, PCa-patients are stratified to certain risk groups according to several prognostic markers. The PSA serum level, Gleason Score (GS), TNM-staging and the digital-rectal examination (DRE) are the most important indicative parameter for the consecutive medical care. However, widespread screening is associated with overdiagnosis and overtreatment and therefore is population-based screening not recommended. On the other hand, morphological imaging using computer tomography (CT) or magnetic resonance imaging (MRI) modalities remain insufficient to accurately detect lymphatic spread with high sensitivity during primary staging since most of the metastatic lymph nodes are smaller than 8 mm in average [169,170]. In this context, metabolic PET-imaging agents like [^{18}F]FDG, [^{11}C]choline, [^{18}F]fluorocholine, or [^{11}C]acetate initially offered the possibility for higher detection rates but partially failed to prove their eligibility due to either unsuitably low sensitivity or misleading uptake in non-malignant tissue with false-negative results [169,171-174].

Radiolabeled PSMA inhibitors revealed significant potential in the past regarding diagnosis and staging of PCa patients. PSMA-imaging improved the localization of the metastasis compared with CT or MRT and rendered bone scintigraphy and cross-sectional imaging redundant [169].

3.1.1 SPECT

Single photon emission computed tomography (SPECT) is based upon detection of γ-emitting isotopes through γ-cameras, which detect and record the emitted photons to produce a digital image of the distribution of the radioisotope within the animal or human body. Single or dual-head γ-cameras are often mounted on a rotating gantry to allow tomographic or cross-sectional imaging, usually covering an angle of 360°. Commonly used radionuclides for SPECT-imaging are listed in Table 1.

Table 1. Selected SPECT isotopes (photon emitters) and their physical properties. IT: isomeric transition; EC: electron capture [175].

Radionuclide	Half-life	Decay mode (%)	E_γ (keV)	Production
^{99m}Tc	6.01 h	IT (99.99)	140.51	Generator ^{99}Mo/^{99m}Tc
^{123}I	13.22 h	EC (100)	158.97	Cyclotron
^{111}In	67.31 h	EC (100)	171.28, 245.35	Cyclotron
^{67}Ga	78.28 h	EC (100)	93.31, 184.58, 300.22	Cyclotron

Most cameras used for detection are based on a large-area rectangular sodium iodide NaI(Tl) scintillation crystal, a collimator, a light guide and an array of 30 to 100 photo multiplier (PM). NaI(Tl) crystals were developed to work in the range of 80 to 300 keV, hence sufficiently suited to detect the 141 keV γ-photons emitted in the decay of ^{99m}Tc [176]. The collimator is used to determine the direction of the γ-photons and consist usually of a lead, tungsten or platinum plate with a large number of holes. The collimator has the largest influence on the spatial resolution, which depends on the length and diameter of the holes. The γ-photons absorptive material of the collimators allows γ-photons to pass only within a certain direction towards the detector and thereby reduces the amount of potential radiation and hence increase resolution. Depending on the imaging-purpose, several collimators are available to either increase the sensitivity or spatial resolution, e.g. pinhole-collimators are primarily used for magnification-imaging of small areas or laboratory animals, while parallel-hole collimators are most commonly employed for cardiac imaging [177].

The PM tubes detect the scintillation of the NaI(Tl)-crystal and convert the signal into position logic circuits to determine the location of the scintillation event. The thickness of the crystal is a trade-off between intrinsic spatial resolution and detection efficiency. For low energy γ-emitters, such as ^{99m}Tc, 6 mm thick detector crystals are sufficient, whereas most modern cameras system utilize 9.5 mm thick crystal plates [178]. Light guides are used to increase the light collection efficiency through improvement of the uniformity of light collection as a function of position. The output-signals of each PM tube are used to reconstruct a three-dimensional image.

The system spatial resolution is further highly influenced through the reconstruction process of the image. Novel algorithms like the maximum-likelihood expectation-maximization (ML-EM) or the ordered-subset expectation-maximization (OSEM) outbalance the trade-off between low signal to noise rations and high spatial resolution [178]. The resolution of a SPECT-system is approx. 0.4 mm for preclinical scanner [179], while clinical systems achieve 5 to 12 mm [178,180].

3.1.2 Positron emission tomography

Positron emission tomography (PET) is a technique in nuclear medicine to detect quantitatively the spatial and temporal distribution of radioisotopes upon injection within a human or animal body. In contrast to other imaging modalities like CT or MRI, PET and SPECT are particularly useful to determine biochemical functions and are therefore often associated with the term "molecular imaging" [181]. The fundamental principle of PET relies on the decay of positron emitting radionuclides, which results in the transformation of a proton to a neutron, a positron (β^+) and a neutrino (ν).

$$ {}^{A}_{Z}X_N \rightarrow {}^{A}_{Z-1}X_{N+1} + \beta^+ + \nu $$

After emission from the nucleus, the positron loses its kinetic energy due to collision with atoms of the surrounding matter within a few millimeter from the emission site (energy-dependent). The thermalized positron forms with an electron (β^-) of the surrounding matter a "positronium" intermediate. In the following annihilation reaction, the masses of the electron and positron are converted to energy and appear in the form of two at almost 180 degrees to each other emitted 0.511 MeV annihilation photons (γ-photons) [178].

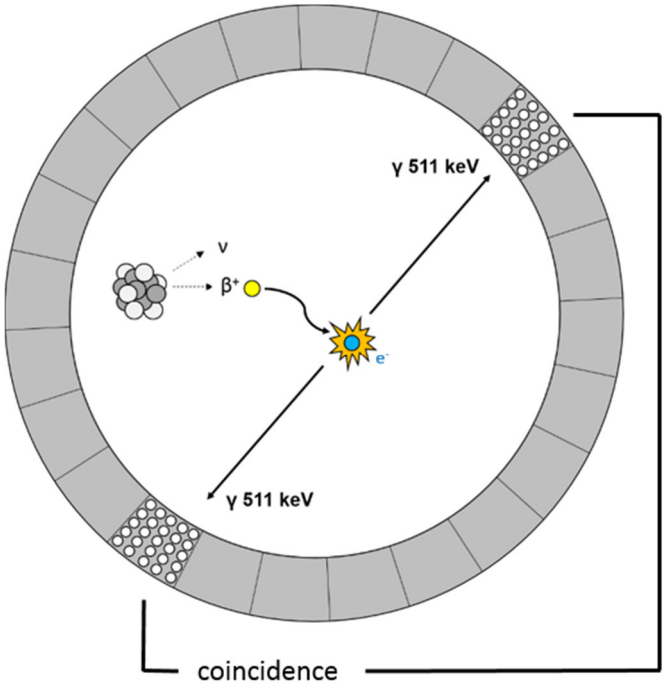

Figure 8. Schematic PET scanner representation. The radioisotope decays by β^+-emission. Following annihilation of the formed positronium results in two 511 keV γ-photons, being emitted at almost 180 degrees to each other, which are detected by two opposite detector units electronically connected via a coincidence circuit.

In contrast to SPECT, PET-systems do not require collimators. Annihilation coincidence detection (ACD) allows near-simultaneous detection of the origin of the two "back-to-back" annihilation-photons and results in higher sensitivity compared to SPECT (see Figure 8) [178].

Due to the relative high energy of the 511 keV γ-photons, NaI(Tl) scintillator crystals are less suitable for PET. $Bi_3Ge_4O_{12}$ (BGO), LSO:Ce and Lu_2SiO_5:Ce crystals are more commonly used in PET-detectors [178]. The arrangement of multiple opposing detectors enables fast measurement and the detection of dynamic processes within the body [182]. However, the precision depends on the exact parallel measurement of coincidence events in a coincidence-timing window and thus PET-systems inherit a finite timing resolution.

The spatial resolution of PET-system is primarily determined by the size of the individual detector components (depth-of-interaction effect) and the radionuclide itself. Since only the position of annihilation is detected, the distance between positron-emission and annihilation restricts the exact localization. Maximum energies from emitted positrons are in the range of 0.5 to 5.0 MeV with an extrapolated range of 0.1 to 2.0 cm in water [178]. Yet, the average travel distance of a positron between origin and point of annihilation is significantly smaller than the maximum energy would allow due to a wide spectrum of emission-energies and interactions with surrounding matter. The positron range is inversely proportional to the density of the surrounding tissue. Thus, the average distance in soft tissue is greater than in a dense proximity like bone. A list of common radionuclides used in PET is depicted in Table 2.

Table 2. Selected positron-emitting radionuclides used for PET imaging. EC: electron capture [175].

Radionuclide	Half-life	Decay Mode (%)	Mean $E_{\beta+}$ (MeV)
^{68}Ga	67.71 min	EC + β^+ (100) β^+ (89)	0.83
^{11}C	20.38 min	EC + β^+ (100) β^+ (99.8)	0.39
^{15}O	2.03 min	EC + β^+ (100) β^+ (99.9)	0.74
^{18}F	109.77 min	EC + β^+ (100) β^+ (97)	0.25
^{64}Cu	12.70 h	EC + β^+ (61.5) β^+ (18); β^-(39)	0.28
^{86}Y	14.74 h	EC + β^+ (100) β^+ (32)	0.66
^{89}Zr	78.41 h	EC + β^+ (100) β^+ (23)	0.40
^{124}I	4.18 d	EC + β^+ (100) β^+ (23)	0.82
^{44}Sc	3.97 h	EC + β^+ (100) β^+ (94)	0.63

The raw dynamic PET data (sinogram) may be reconstructed using the same algorithms as in SPECT [183] and require calibration and several corrections regarding scattered radiation, random coincidences, attenuation and dead time to obtain corrected signals for a three

dimensional picture with quantitative radioactivity values (voxel-intensity; Bq/mL) [178,183]. Further attention has to be paid to the partial-volume-effect (PVE). Small structures, e.g. metastasis, are readily over- or underestimated, since the PVE distributes the radioactivity signal over a larger ("spill-out") or smaller ("spill-in") volume because of image blurring and image sampling (voxel-size) [184]. The final PET signal in a region of interest (ROI) is expressed as % injected dose per mL (% ID/mL) or the standardized uptake value (SUV), which is normalized by the bodyweight or surface-area and total injected radioactivity.

3.1.3 PSMA ligands for PET and SPECT

Several groups investigated antibodies and small molecules for PSMA-PET and SPECT-imaging of prostate cancer in predominantly preclinical models based on the radionuclides ^{11}C, ^{123}I, ^{125}I, ^{99m}Tc, ^{18}F, ^{111}In, ^{89}Zr and ^{68}Ga among others [185-198].

Inspired by the work of Pomper et al. [185], Eder M. et al. developed [^{68}Ga]DKFZ-PSMA-11 (Glu-NH-CO-NH-Lys(Ahx)-[^{68}Ga]HBED-CC), the currently most widely used PSMA targeted imaging agent for clinical PET-imaging of prostate cancer [199]. The high affinity and internalization rate combined with a favorable pharmacokinetic profile and fast background clearance, rendered [^{68}Ga]DKFZ-PSMA-11 as a valuable tracer for primary staging and diagnosis of recurrent prostate cancer [200-202]. A retrospective analysis revealed, that [^{68}Ga]DKFZ-PSMA-11 demonstrates high sensitivity (65.9%) and specificity (98.9%) for lymph node staging in primary to intermediate and high risk PCa patients with a median PSA level of 11.6 ng/mL [202]. Direct comparison with [^{18}F]fluorocholine in a small retrospective study demonstrated the superiority of [^{68}Ga]DKFZ-PSMA-11 especially in patients with low PSA-levels (< 2.8 ng/mL) [203].

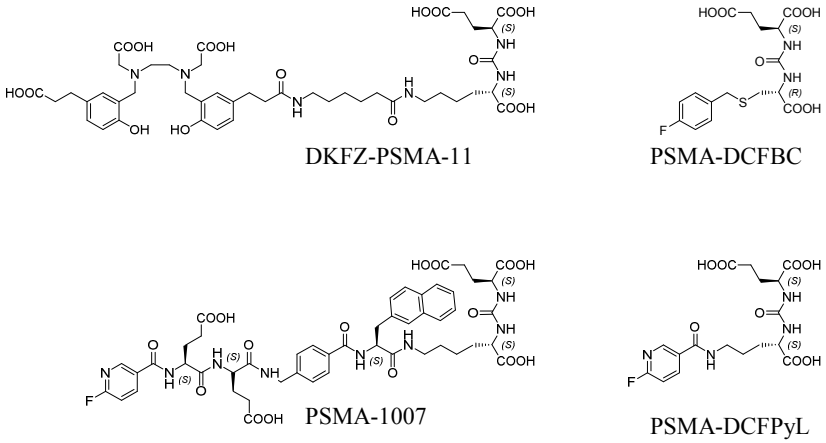

Figure 9. Structural representation of selected PSMA imaging agents for PET.

PSMA I&T (PSMA for Imaging & Therapy) developed by Wirtz et al. was introduced as theranostic tracer in 2015 [204] (Figure 10). Utilization of 2-(4,7,10-tris(carboxymethyl)-1,4,7,10-tetraazacyclododecan-1-yl)pentanedioic acid (DOTAGA) as chelating unit in **PSMA I&T** enables not only ^{68}Ga-complexation but also allows the introduction of further radionuclides (e.g. ^{177}Lu, ^{90}Y, ^{111}In or ^{213}Bi, to mention only a few). The incorporation of D-amino acids into the peptidic scaffold, among other modifications, resulted in high metabolic stability and favorable pharmacokinetic properties *in vivo* [194]. The complexation with ^{111}In enabled successful application in preoperative SPECT/CT imaging and consecutive radioguided surgery [196].

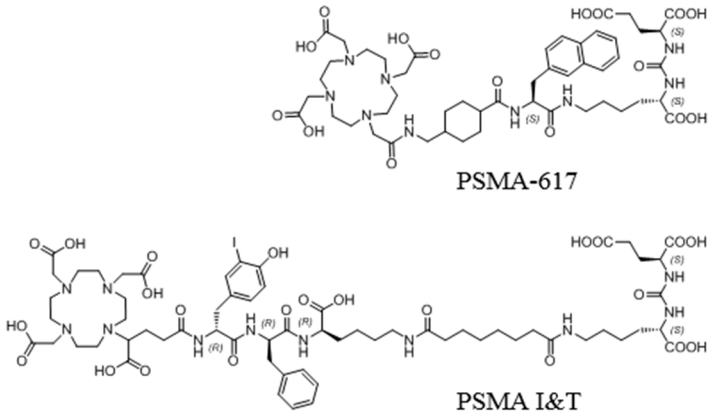

Figure 10. Structural representation of the selected theranostic PSMA inhibitors PSMA I&T and PSMA-617.

Another theranostic (employable for therapy and diagnostic) agent is **PSMA-617** (Figure 10). The preclinical investigation in mice demonstrated remarkably low kidney uptake and high accumulation in LNCaP-xenografts. While the low renal uptake was not completely transferable to human application, **PSMA-617** proved its eligibility through sensitive tumor lesion detection and imaging with high contrast [205-207].

As a result of the preferable physicochemical properties of ^{18}F (109.8 min, 0.25 MeV, $\beta^+ = 99.4\%$) compared to ^{68}Ga (67.7 min, 0.83 MeV, $\beta^+ = 89\%$), several ^{18}F-based compounds have been reported of which ^{18}F-DCFBC and its successor ^{18}F-DCFPyL are of currently greater interest [190,195,208] (see Figure 9). The preliminary comparison of [^{18}F]DCFPyL and [^{68}Ga]DKFZ-PSMA-11 in a small group of patients, rendered [^{18}F]DCFPyL superior due to better tumor to background ratios and higher sensitivity in lesion detection [209].

PSMA-1007 (Figure 9) was recently introduced for ^{18}F-PET imaging. The primary structure is similar to PSMA-617 (Figure 10) but it contains a 4-(aminomethyl) benzoic acid residue and two glutamic acids instead of the 1,4,7,10-tetraazacyclododecane-1,4,7,10-tetraacetic acid (DOTA) chelator and a cyclohexane-derivative as linker. The preclinical evaluation showed high and fast tumor-uptake and exceptional high internalization [210]. Compared to [^{68}Ga]DKFZ-

PSMA-11, the clearance kinetics of [^{18}F]PSMA-1007 were slower in humans with less urinary clearance and a higher absorbed dose in the liver [211].

3.2 Endoradiotherapy of prostate cancer

About 10 to 20% of PCa patients develop mCRPC within approx. 5 years of follow-up [212]. Conventional therapy includes surgery, androgen ablation, radiation therapy, chemotherapy and lately radionuclide-therapy with $^{223}RaCl_2$. However, the overall survival prolongation applying monotherapy remained only modest compared to placebo (approx. 5 months). Albeit the synergistic combination of several drugs seems to be more effective, adverse events are frequently occurring and hamper further treatment [213,214].

The endoradiotherapy of mCRPC using theranostic PSMA tracer became highly attractive owing to high lesion uptake, minimal severe or long-term side effects besides xerostomia [215], the possibility to monitor tracer distribution and an overall beneficial influence on survival prolongation [215,216].

Currently, [^{177}Lu]**PSMA I&T** and [^{177}Lu]**PSMA-617** (see Figure 10) are used for endoradiotherapeutic approaches. Because of the possibility to radiolabel both ligands with a variety of radionuclides due to the chelator DOTA and its derivative DOTAGA, the treatment may be conducted with either α- or β-emitting radionuclides. A list of commonly used radionuclides for endoradiotherapy is depicted in Table 3.

Table 3. Physical properties of currently used therapeutic isotopes [175,217,218]. Italic indicates alternative therapeutic radionuclides with possible application.

Radionuclide	Half-life	Decay	Mean E_{β^-} (MeV)	Mean tissue range (mm)
^{177}Lu	6.65 d	β	0.13	0.5
^{67}Cu	*61.83 h*	*β*	*0.14*	*0.4*
^{90}Y	64.0 h	β	0.93	4.1
^{188}Re	*17.0 h*	*β*	*0.76*	*3.8*
^{211}At	7.2 h	α	6.79	< 0.1
^{213}Bi	46 min	α	8.32	< 0.1
^{223}Ra	*11.4 d*	*α*	*6.70*	*< 0.1*
^{111}In	*2.8 d*	*EC/Auger*	*0.02*	*0.02 – 0.1*

Comparing both ligands in human applications, the clinical efficacy and toxicity profiles are quite similar. [^{177}Lu]**PSMA-617** shows a slightly prolonged whole body residence time with a higher effective half-life in the kidneys and parotid and lacrimal glands. [^{177}Lu]**PSMA I&T**

demonstrated an initially higher metastasis-uptake but [^{177}Lu]**PSMA-617** remained effectively longer at the tumor-site. However, the differences regarding uptake and the resulting doses in the metastasis were found to be insignificant. Most common side-effects are fatigue and mild dryness of mouth [215]. Apart from rarely occurring anemia [219], no relevant hemato- or nephrotoxicity was reported so far and in general the radioligand-therapy was well tolerated [219,220].

Although the therapy with ^{177}Lu-labeled PSMA ligands seems to be highly effective, not all patients respond to this treatment modality. The utilization of α-emitting radionuclides seems to intensify lesion radiation, presumably due to the markedly higher linear energy-transfer of α-particles [175].

An initial report about two mCRPC patients receiving [^{225}Ac]**PSMA-617** treatment, clearly indicated the high potential of α-emitter radiotherapy. In both patients, PSMA-positive lesions disappeared and indicated complete remission. However, a relevant side effect of [^{225}Ac]**PSMA-617** treatment in both patients was moderate to severe xerostomia [221].

4. Objectives

"Those who have not been trained in chemistry or medicine may not realize how difficult the problem of cancer treatment really is. It is almost- not quite, but almost- as hard as finding some agent that will dissolve away the left ear, and leave the right ear unharmed. So slight is the difference between a cancer cell and its normal ancestors"

-William Woglom-

The exceptional target characteristics of PSMA in PCa enabled the development of selective and highly affine radiopharmaceuticals for diagnostic and endoradiotherapeutic approaches. Several PSMA inhibitors have demonstrated their successful applicability in preclinical studies and were thus transferred to human applications [207,215,222-224]. Among these, predominantly **PSMA I&T** [196,225], developed in our group, and **PSMA-617** [206] are currently used for peptide radioligand therapy (PRLT) in mCRPC. A still remaining drawback regarding PRLT is the unwanted uptake in healthy tissue in which especially the salivary glands and the kidneys, the latter due to its physiological PSMA expression, are of concern [219]. Based on the previous work in our group, the goal of this thesis was the exploration of possible strategies to improve the pharmacokinetic traits of novel PSMA ligands for PET imaging and endoradiotherapeutic treatment of PCa and thus to extend the currently known structure activity relationship (SAR).

Fundamental aspects such as affinity, internalization, specificity, selectivity, lipophilicity, metabolic stability and specific activity (A_S) have to be considered during the course of tracer development. However, little attention has been paid in the recent literature regarding plasma protein binding of PSMA ligands [226]. As shown in recent reports for xenobiotics, the interaction of PSMA inhibitors with HSA should exert considerable influence on their pharmacokinetics regarding metabolic stability, clearance and thus *in vivo* half-life [227-230]. Therefore, a further goal of this work was the establishment of a fast an efficient chromatographic albumin-binding assay and to investigate the influence of several structural modifications on HSA binding.

The metabolic stability *in vivo* remains one of the most critical aspects during the preclinical tracer development. As demonstrated by Wirtz et al., the utilization of D-amino acids compared to L-configured peptides not only improved tumor uptake, but also the overall tracer disposition *in vivo* [193]. Current preclinical protocols are either employing simple blood incubation methods or the utilization of animals with subsequent tissue extraction and chromatographic analysis to assess metabolic stability [204,210]. In order to reduce the consumption of laboratory animals and to obtain less individual and representative data with high reproducibility, subcellular

fractions from extracted mice organs were used to establish an efficient S9-assay for metabolite detection via radio-RP-HPLC. The established S9-assay was further used to assess the influence of stereochemistry on metabolite formation in this work.

A central feature for most PSMA tracer in preclinical *in vivo* studies is the immense renal uptake compared to tumor accumulation [156]. An exception regarding this renal behavior was displayed by **PSMA-617**, which demonstrated moderate uptake and fast clearance from the kidneys [206]. This favorable trait, however, could not be confirmed in humans or at least to a lower degree. Further interspecies differences were recently found for [^{18}F]PSMA-1007, for which urinary tract excretion occurred in rodents but unexpectedly less strong in humans [211]. Previous work from our group regarding CXCR4 ligands, disclosed marked interspecies differences between murine and human receptor affinity [231,232]. These observations led to the question if murine PSMA displays differences regarding affinity in comparison to human PSMA and was therefore investigated in quantitative autoradiographic studies.

II. MATERIAL AND METHODS

"Science is what scientists do, and there are as many scientific methods as there are individual scientists"

-Percy Williams Bridgman-

1. General information

The Fmoc-(9-fluorenylmethoxycarbonyl-) and all other protected amino acid analogs were purchased from Bachem (Bubendorf, Switzerland) or Iris Biotech (Marktredwitz, Germany). The 2-chlorotrityl chloride (2-CTC) resin was obtained from PepChem (Tübingen, Germany). Chematech (Dijon, France) delivered the chelator DOTAGA-anhydride. PSMA-DKFZ-617 was purchased from ABX advanced chemical compounds (Radeberg, Germany). All necessary solvents and other organic reagents were purchased from either Alfa Aesar (Karlsruhe, Germany), Sigma-Aldrich (Munich, Germany) or VWR (Darmstadt, Germany). Solid phase synthesis of the peptides was carried out by manual operation using an Intelli-Mixer syringe shaker (Neolab, Heidelberg, Germany). Analytical reversed-phase high performance liquid chromatography (RP-HPLC) was performed on a Nucleosil 100 C18 column (5 µm, 125 × 4.0 mm, CS GmbH, Langerwehe, Germany) using a Shimadzu gradient RP-HPLC System (Shimadzu Deutschland GmbH, Neufahrn, Germany). Analysis of the peptides was performed by applying different gradients of 0.1% (*v*/*v*) trifluoroacetic acid (TFA) in H_2O (solvent A) and 0.1% TFA together with (*v*/*v*) in acetonitrile (MeCN) (solvent B) with a constant flow of 1 mL/min (specific gradients are cited in the text). The Shimadzu SPD 20 A prominence UV/VIS detector (Shimadzu Deutschland GmbH) was used at λ = 220 nm and 254 nm. HSA binding was determined using a Chiralpak HSA (5 µm, 50 x 3 mm) analytical column connected to a Chiralpak HSA (5 µm, 10 x 3 mm) guard cartridge (Daicel Chemical Industries) purchased from Chiral Technologies Europe (Illkirch, France). Non-linear regression for the HSA binding was performed using OriginPro 2016G (Northampron, USA). Retention times t_R as well as the capacity factors K' are cited in the text. Preparative RP-HPLC of the peptides was achieved on a Shimadzu RP-HPLC system using a Multospher 100 RP 18-5 column (250 × 20 mm, CS GmbH) with a constant flow of 5 mL/min. Analytical and preparative Radio RP-HPLC of the radioiodinated reference ligand was performed using a Nucleosil 100 C18 column (5 µm, 125 × 4.0 mm). Radioactivity was detected through connection of the outlet of the UV-photometer to a NaI(Tl) well-type scintillation counter from EG&G Ortec (Munich, Germany). The ^{68}Ga-and ^{177}Lu-labeled compounds were analyzed as published previously [224,233]. Electrospray ionization mass spectrometry (ESI-MS) spectra were acquired on an expression^{L} CMS mass spectrometer (Advion Ltd., Harlow, UK) and on a Varian 500-MS IT mass spectrometer (Agilent Technologies, Santa Clara, USA). For the

Bradford-Assay a V-630 UV-Vis spectrophotometer from JASCO Germany GmbH (Gross-Umstadt, Germany) was used and centrifugation of the S9-fractions was performed in an Avanti JXN-26 centrifuge from Beckman Coulter GmbH (Krefeld, Germany). The centrifugation of the radioactive S9-metabolite assays was performed using a Heraeus PICO 17 centrifuge from Thermo Fisher Scientific Messtechnik GmbH (Munich, Germany). NMR Data were obtained applying 300 K using an AV 300 (300 MHz) or an AV 400 (400 MHz) from *Bruker* (Billerica, USA). The incubation of the S9-fractions for *ex vivo* metabolite analysis was performed in a Biometra UNO Thermoblock (*Biometra*, Göttingen, Deutschland).

2. PSMA inhibitor synthesis

2.1 Synthesis protocols (SP)

SP-1: 2-CTC-resin loading: 2-CTC-resin (1.6 mmol/g) is loaded with Fmoc-AA-OH (1.5 eq.) in anhydrous dichloromethane (DCM) with *N*,*N*-Diisopropylethylamine (DIPEA) (4.5 eq.) at room temperature (RT) for 2 h. The remaining tritylchloride is capped by addition of 2 mL/g methanol (MeOH) for 15 min. After that, the resin is filtered and thoroughly washed with DCM (2×), with dimethylformamide (DMF) (2×) and MeOH (2×), respectively and stored under vacuum overnight. The loading is determined using the weight differences:

$$\frac{(m_{total} - m_{net\ weight}) \times 1000}{(M_{AS} - M_{HCl}) \times m_{weight\ of\ resin}} = mmol/g$$

Formula 1. Determination of resin-loading: m_{total}: mass of loaded resin (Fmoc-AA-OH and HCl); M_{As}: molar mass of amino acid; m_{net} weight: mass of used resin; M_{HCl}: molar mass of hydrochloric acid

SP-2: Peptide synthesis via TBTU/HOBt coupling: A solution of Fmoc-AA-OH (2.0 eq.), *N,N,N′,N′*-Tetramethyl-O-(benzotriazol-1-yl)uronium tetrafluoroborate (TBTU) (2.0 eq.), *N*-Hydroxybenzotriazole (HOBt) (2.0 eq.), DIPEA (4.5 eq.) in DMF (8 ml/g resin) was added to the resin-bound free amine peptide and shaken for 2 h at RT and washed with DMF (6×). The coupling with secondary or aromatic amines was performed employing a different protocol. Fmoc-AA-OH (3.0 eq.) was dissolved in DMF (8 mL/g resin) together with 1-[Bis(dimethylamino)methylene]-1*H*-1,2,3-triazolo[4,5-b]pyridinium 3-oxid hexafluoro-phosphate (HATU) (3.0 eq.), 1-Hydroxy-7-azabenzotriazol (HOAt) (3.0 eq.) and DIPEA (6.0 eq.) and stirred for 15 min. The pre-activated solution was added to the resin bound peptide and shaken for 2 h at RT. After completion of the reaction, the resin was washed with DMF (6×). In general, all peptidic scaffolds were synthesized as previously described [224,234].

SP-3: On-resin Fmoc-deprotection: The resin-bound Fmoc-protected peptide was treated with 20% piperidine in DMF (*v*/*v*) for 5 min and a second time for 15 min. Afterwards, the resin was washed thoroughly with DMF (8×).

SP-4: On-resin Dde-deprotection: The *N*-(1-(4,4-dimethyl-2,6-dioxocyclohexylidene)ethyl) (Dde) protected peptide (1.0 eq.) was dissolved in a solution of 2.0% hydrazine monohydrate ($N_2H_4 \cdot H_2O$) in DMF (*v*/*v*). After 15 min, the deprotected peptide, if bound to resin, was washed with DMF (6×) or precipitated in diethyl ether (Et_2O) to give the crude product. If Fmoc- and Dde-protecting groups were present and only Dde-deprotection was necessary, the resin-loaded peptide was treated with a solution containing $NH_2OH \cdot HCl$ (630 mg), imidazole (460 mg), DCM (0.5 mL), DMF (0.5 mL) and *N*-methyl-2-pyrrolidone (NMP) (2.5 mL) for 3 h at RT. Afterwards, the resin-loaded peptide was washed with DMF (6×).

SP-5: On-resin Alloc/Allyl-deprotection: The Alloc/Allyl-protecting group was removed from the resin-bound peptide using a solution of DCM (6.0 mL) containing triisopropylsilane (TIPS) (50.0 eq.) and (triphenyl)palladium(0) ($Pd(PPh_3)_4$) (0.3 eq.). The resin was treated with this solution for 1.5 h at RT. Finally, the resin was washed with DCM (3×) to remove the $Pd(PPh_3)_4$.

SP-6: *t*Bu/Boc deprotection: Removal of the *tert*-butyl (*t*Bu)/*tert*-butyloxycarbonyl (Boc)-protecting groups was carried out by dissolving the crude product in TFA (approx. 500 µL) and stirring for 40 min at RT. Afterwards, the TFA was almost completely removed using nitrogen stream. After precipitation in Et_2O, the crude product was centrifuged and the supernatant removed. The dried pellet was further used for the following synthesis-steps.

SP-7.1: *A) Peptide cleavage from the resin with preservation of side-chain protecting groups*: The fully protected, resin-bound peptide was dissolved in a mixture of DCM/trifluoroethanol (TFE)/acetic acid (AcOH) (6/3/1; *v*/*v*/*v*) and shaken for 30 min. The solution was filtered off and the resin was dissolved in another cleavage solution for another 30 min. The fractions were combined and the solvent was concentrated under reduced pressure. The filtrate was redissolved in toluene and concentrated under reduced pressure to remove the AcOH. Precipitation in water or Et_2O resulted in the crude, side chain protected peptide.

SP-7.2: *B) Peptide cleavage from the resin with concurrent deprotection of all acid labile protecting groups:* The fully protected, resin-bound peptide was dissolved in a mixture of TFA/TIPS/water (95/2.5/2.5; *v*/*v*/*v*) and shaken for 30 min. The solution was filtered off and the resin was treated in the same way for another 30 min. Afterwards, the fractions were combined and the solvent was concentrated under a constant flow of nitrogen. The crude peptide was precipitated in Et_2O and left to dry overnight.

SP-8: Deacetylation of carbohydrate-moieties**:** Deacetylation was accomplished by dissolving the PSMA inhibitor in MeOH containing KCN (0.5 eq.) [235] with concomitant stirring overnight at RT. The final product was purified by RP-HPLC.

SP-9: Preparation of non-radioactive metal-complexed PSMA inhibitors:

SP-9.1: *^{nat}Ga-compounds:* For the preparation of the $^{nat}Ga^{III}$-complexes, a 2.0 mM aqueous (aq.) solution of the PSMA inhibitor (50 µL) and a 2.0 mM aq. solution of $Ga(NO_3)_3$ (50 µL) were mixed and heated at 40°C for 30 min. The chelate formation was assessed using RP-HPLC and ESI-MS. The resulting 1.0 mM solution was diluted and used for *in vitro IC_{50}* determination and HSA binding.

SP-9.2: *^{nat}Lu-compounds:* The corresponding $^{nat}Lu^{III}$-complexes were prepared from a 2.0 mM aqueous solution of the PSMA inhibitor with a 2.5 molar excess of $LuCl_3$ (20 mM aq. solution) and heated to 95°C for 30 min. After cooling, the $^{nat}Lu^{III}$-chelate formation was confirmed using RP-HPLC and ESI-MS. The resulting 1.0 mM aqueous solutions of the respective ^{nat}Lu-complexes were then diluted and used in the *in vitro IC_{50}* studies without further processing.

2.2 Synthesis of building blocks

2.2.1 Building blocks for the linker and binding motif

Di-*tert*-butyl(((*S*)-6-amino-1-(*tert*-butoxy)-1-oxohexan-2-yl)carbamoyl)-L-glutamate ((O*t*Bu)KuE(O*t*Bu)$_2$) (1): The synthesis of the *tert*-butyl-protected Lys-urea-Glu binding motif (EuK) was synthesized as previously described by solution phase synthesis [234]. In short, a solution of DCM containing L-di-*tert*-butyl-glutamate · HCl (2.0 g, 7.71 mmol, 1.0 eq.) was cooled on ice for 30 min and afterwards treated with trimethylamine (TEA) (2.69 mL, 19.28 mmol, 2.5 eq.) and 4-(dimethylamino)pyridine (DMAP) (3.3 mg, 0.3 mmol, 0.04 eq.). After additional stirring for 5.0 min, 1,1'-carbonyldiimidazole (CDI) (1.38 g, 8.84 mmol, 1.1 eq.) was dissolved in DCM and slowly added over a period of 30 min. The reaction mixture was further stirred overnight and enabled to warm to RT. The reaction was stopped using saturated (sat.) $NaHCO_3$ solution (8 mL) with concomitant washing steps of water (2×) and brine (2×) and dried over sat. Na_2SO_4 solution. The remaining solvent was removed *in vacuo* and the crude product (*S*)-Di-*tert*-butyl 2-(1*H*-imidazole-1-carboxamido)pentanedioate used without further purification. RP-HPLC (10 to 90% B in 15 min): t_R = 12.2 min; K' = 5.8. Calculated monoisotopic mass ($C_{17}H_{27}N_3O_5$): 353.4; found: *m/z* = 376.1 $[M+Na]^+$. The crude product (*S*)-Di-*tert*-butyl 2-(1*H*-imidazole-1-carboxamido)pentanedioate (2.72 g, 7.71 mmol, 1.0 eq.) was dissolved in 1,2-dichloroethane (DCE) and cooled on ice for 30 min. To this solution was added TEA (2.15 mL, 15.42 mmol,

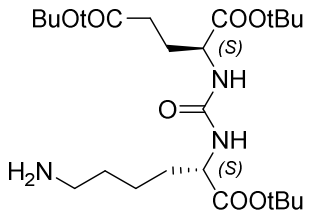

Chemical Formula: $C_{24}H_{45}N_3O_7$
Molecular Weight: 487,64

2.0 eq.) and H-Lys(Cbz)-O*t*Bu · HCl (2.87 g, 7.71 mmol, 1.0 eq.) and the solution stirred overnight at 40°C. The remaining solvent was evaporated and the crude product purified using silica gel flash-chromatography with an eluent mixture containing ethyl acetate (EtOAc)/hexane/TEA (500/500/0.8; *v*/*v*/*v*). After removal of the solvent, (9*R*,13*S*)-tri-*tert*-butyl-3,11-dioxo-1-phenyl-2-oxa-4,10, 12-triazapentadecane-9,13,15-tricarboxylate was obtained as colorless oil. RP-HPLC (40 to 100% B in 15 min): t_R = 14.5 min; K' = 6.25. Calculated monoisotopic mass ($C_{32}H_{51}N_3O_9$) = 621.8; found: *m/z* = 622.3 $[M+H]^+$. To synthesize (O*t*Bu)KuE(O*t*Bu)$_2$ **(1),** (9*R*,13*S*)-tri-*tert*-butyl-3,11-dioxo-1-phenyl-2-oxa-4,10, 12-triazapentadecane-9,13,15-tricarboxylate (3.4 g, 5.47 mmol, 1.0 eq.) was dissolved in ethanol (EtOH) (75 mL) and palladium on activated charcoal (0.34 g, 0.57 mmol, 0.1 eq.) (10 %) was given to this solution. The reaction mixture containing flask was initially purged with hydrogen stream and the solution allowed to stir overnight at RT under light hydrogen-pressure (balloon). The crude product was purified through celite and the solvent evaporated *in vacuo*. The desired product **1** was obtained as a waxy solid (1.9 g, 3.89 mmol, 71.6% yield). RP-HPLC (10 to 90% B in 15 min): t_R = 12.6 min; K' = 6.4. Calculated monoisotopic mass ($C_{24}H_{45}N_3O_7$) = 487.6; found: m/z = 488.3 $[M+H]^+$, 510.3 $[M+Na]^+$.

(*S*)-5-(*tert*-butoxy)-4-(3-((*S*)-1,5-di-*tert*-butoxy-1,5-dioxopentan-2-yl)ureido)-5-oxopentanoic acid ((O*t*Bu)EuE(O*t*Bu)$_2$) (2): The synthesis of the *tert*-butyl-protected Glu-urea-Glu binding motif (EuE) was similarly synthesized as described for **1** [234] using H-L-Glu(OBzl)-O*t*Bu · HCl instead of H-L-Lys(Cbz)-O*t*Bu · HCl. The desired product was obtained as waxy and strongly hygroscopic solid (4.10 g, 8.39 mmol, 84% yield). RP-HPLC (10 to 90% B in 15 min): t_R = 11.3 min; K' = 7.69. Calculated monoisotopic mass ($C_{23}H_{49}N_2O_9$) = 488.3; found: m/z = 489.4 $[M+H]^+$, 516.4 $[M+Na]^+$.

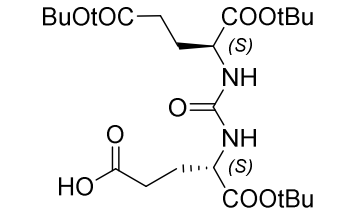

Chemical Formula: $C_{23}H_{40}N_2O_9$
Molecular Weight: 488,58

Di-pentafluorophenyl suberate (Sub(OPfp)$_2$) (3): To a solution of suberic acid (2.0 g, 11.5 mmol, 1.0 eq.) in tetrahydrofurane (THF) (30 mL), were added pyridine (2.8 mL, 34.5 mmol, 3.0 eq.), *N,N´* -Diisopropylcarbodiimide (DIC) (7.1 mL, 46.0 mmol, 4.0 eq) in THF (15 mL) and pentafluorophenol (PfpOH) (8.47 g, 46.0 mmol, 4.0 eq.) in THF (15 mL). Progress of the active ester formation was monitored using thin-layer chromatography (TLC) (EtOAc/petroleum ether (PE) (55 to 65°C) (1/9)). After approx. 2 h at RT, the reaction mixture was filtered, and the solvent was evaporated *in vacuo*. The crude product was purified via silica gel flash-chromatography using an eluent mixture of EtOAc/PE (1/9; *v*/*v*). The product was obtained as a yellow crystalline solid (3.96 g, 7.82 mmol, 68% yield). Calculated monoisotopic mass for Sub(OPfp)$_2$ ($C_{20}H_{12}O_4F_{10}$) = 506.1 (Product is not detectable using ESI-MS).

OPfp-Sub-(O*t*Bu)KuE(O*t*Bu)$_2$ (4): The synthesis of **4** was accomplished as previously described [234]. In short, a solution of **1** (400 mg, 0.8 mmol, 1.0 eq.) in THF (100 mL) was treated with DIPEA (274 µl, 1.6 mmol, 2.0 eq.) to adjust the pH. This solution was dropwise given to a second solution containing Sub(OPfp)$_2$ **(3)** (1.6 g, 3.2 mmol, 4.0 eq.) in THF. The mixed solutions were stirred for 2 h at RT and finally concentrated *in vacuo*. The purification of the crude product was achieved through silica gel flash-chromatography applying a stepwise gradient of EtOAc in PE (55 to 65°C) of 10%, 50%, 90% and pure EtOAc (200 mL each). The final product **4** was obtained as a yellowish oil. Calculated monoisotopic mass ($C_{38}H_{56}F_5N_3O_{10}$) = 809.4; found: m/z = 810.6 $[M+H]^+$, 832.4 $[M+Na]^+$.

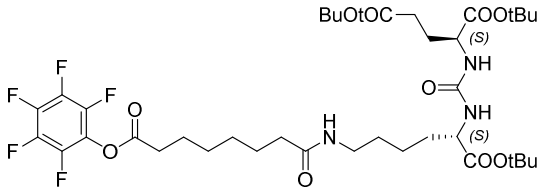

Chemical Formula: $C_{38}H_{56}F_5N_3O_{10}$
Molecular Weight: 809,87

(*S*)-NHFmoc-Asu(O*t*Bu)-OBzl (5): To a solution of (*S*)-Fmoc-Asu(O*t*Bu)-OH (50 mg, 107.0 µmol, 1.0 eq.) in DMF was added HOAt (21.8 mg, 0.16 mmol, 1.5 eq.), HATU (61.0 mg, 161.0 µmol, 1.5 eq.) and DIPEA (73.2 µL, 0.48 mmol, 4.5 eq.). After 15 min of stirring at RT, benzyl alcohol (22.2 µL, 0.32 mmol, 3.0 eq.) was further added and the solution stirred overnight. Finally, the solvent was removed *in vacuo*. Completion of reaction of **5** was analyzed by RP-HPLC (10 to 90% B in 15 min): t_R = 17.1 min; K' = 7.55. Calculated monoisotopic mass for **5** ($C_{34}H_{39}NO_6$) = 557.28; found: m/z = 580.7 $[M+Na]^+$.

(*S*)-NHFmoc-Asu-OBzl (6): *t*Bu deprotection of the crude product **5** was performed with a stirring mixture (*v*/*v*) of TFA (95%) and DCM (5%) at RT for 45 min. After evaporation of the solvent, the crude product **6** was purified using preparative RP-HPLC (60 to 80% B in 15 min): t_R = 9.3 min; K' = 8.9. Calculated monoisotopic mass for **6** ($C_{30}H_{31}NO_6$) = 501.22; found m/z = 524.5 $[M+Na]^+$.

OBzl-(*S*)-Fmoc-Asu[(O*t*Bu)KuE(O*t*Bu)$_2$] (7): To a solution of **6** (51.8 mg, 10.3 µmol, 1.0 eq.) in DMF was added HOBt (20.9 mg, 0.15 mmol, 1.5 eq.), TBTU (36.3 mg, 15.5 µmol, 1.5 eq.) and DIPEA (79.4 µL, 59.7 mg, 0.46 mmol, 4.5 eq.). After 15 min stirring, **1 (**75.6 mg, 15.5 µmol, 1.5 eq.) was added and further stirred for 20 h at RT. The crude product **7** was purified using preparative RP-HPLC (70 to 80% B in 15 min): t_R = 8.9 min; K' = 1.97. Calculated monoisotopic mass for **7** ($C_{54}H_{74}N_4O_{12}$) = 970.53; found: m/z = 971.8 $[M+H]^+$.

(*S*)-Fmoc-Asu[(O*t*Bu)KuE(O*t*Bu)$_2$] (8): For benzyl alcohol (Bzl) deprotection, of **7** (57.2 mg, 65.0 µmol, 1.0 eq.) was dissolved in EtOH (2.0 mL) and palladium on activated charcoal (10%) (5.72 mg, 9.0 µmol, 0.1 eq.) was added. The flask was purged beforehand with hydrogen stream and the solution stirred under light hydrogen-pressure (balloon). After 70 min stirring, the crude product was filtered through celite, the EtOH evaporated *in vacuo* and the

product purified using preparative RP-HPLC (70 to 70.5% B in 15 min): t_R = 6.5 min; *K'* = 0.54. Calculated monoisotopic mass for **5** ($C_{47}H_{68}N_4O_{12}$) = 880.48; found: *m/z* = 881.8 $[M+H]^+$.

OPfp-(*S*)-Fmoc-Asu[(O*t*Bu)KuE(O*t*Bu)$_2$] (9): To a solution of **8** (13.6 mg, 15.4 µmol, 1.0 eq.) in dry DMF was added DIC (4.77 µL, 1.94 mg, 30.8 µmol, 2.0 eq.) and PfpOH (5.67 mg, 30.8 µmol, 2.0 eq.). After 5 min stirring, pyridine (2.49 µL, 31.0 µmol, 2.0 eq.) was added and the solution was allowed to stir overnight at RT. Completion of reaction of **9** was analyzed by RP-HPLC (10 to 90% B in 15 min): t_R = 17.2 min; *K'* = 7.6. Calculated monoisotopic mass for **9** ($C_{53}H_{67}F_5N_4O_{12}$) = 1046.47; found: *m/z* = 1069.8 $[M+Na]^+$.

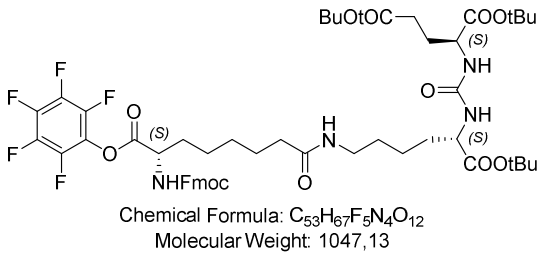

Di-pentafluorophenyl glutarate (Glut(OPfp)$_2$) (10): To glutaric acid (2.0 g, 15.1 mmol, 1.0 eq.) in THF (15 mL) was added pyridine (3.7 mL, 45.4 mmol, 3.0 eq.), DIC (9.5 mL, 60.5 mmol, 4.0 eq.) in THF (10 mL) and PfpOH (11.1 g, 60.5 mmol, 4.0 eq.) in THF (10 mL). After 2 h, the solvent was removed *in vacuo*, the crude product dissolved in petrol ether (PE) and filtered and finally purified using silica gel flash chromatography (PE/EtOAc; 95/5; *v/v*). The final product was obtained as white crystalline solid (6.1 g, 14.7 mmol, 87%). RP-HPLC (10 to 100% B in 15 min): t_R = 17.5 min *K'* = 7.75. Calculated monoisotopic mass ($C_{19}H_{36}N_4O_6$) = 416.3; found: *m/z* = 417.1 $[M+H]^+$.

f(4-I)[(O*t*Bu)KuE(O*t*Bu)$_2$] (11): A solution of Fmoc-D-4-iodo-Phe (0.5 g, 0.97 mmol, 1.2 eq.), HOAt (0.2 g, 1.22 mmol, 1.5 eq.), DIC (0.2 mL, 0.16 g, 1.22 mmol, 1.5 eq.) and DIPEA (0.6 mL, 3.65 mmol, 4.5 eq.) in 15 mL THF was stirred at RT for 1 h. After addition of **1** (395.0 mg, 0.81 mmol, 1.0 eq.) in THF (5 mL), the reaction mixture was stirred overnight. Water (20 mL) was added and extracted with EtOAc (3×) (25 mL), followed by water (3×) (20 mL) and brine (25 mL). The organic phase was dried over $MgSO_4$ and the solvent was evaporated *in vacuo* yielding quantitative (quant.) Fmoc-f(4-I)[(O*t*Bu)KuE(O*t*Bu)$_2$] as a white solid. Finally, Fmoc-f(4-I)[(O*t*Bu)KuE(O*t*Bu)$_2$] was dissolved in DMF (25 mL) together with piperidine (5.0 mL) and stirred for 2 h. The crude product was purified using RP-PRP-HPLC (58% B isocratic). RP-HPLC (10 to 90% B in 20 min): t_R = 15.6 min. *K'* = 8.2. Calculated monoisotopic mass ($C_{33}H_{53}IN_4O_8$) = 760.3; found: *m/z* = 761.4 $[M+H]^+$, 783.4 $[M+Na]^+$, 799.4 $[M+K]^+$, 593.3 [M -3 *t*Bu +H]$^+$, 649.3 [M-2 *t*Bu +H]$^+$, 705.3 [M –t*Bu* +H]$^+$.

OPfp-Glut-f(4-I)[(O*t*Bu)KuE(O*t*Bu)$_2$] (12): At 0°C **11** (270 mg, 0.35 mmol, 1.0 eq.) and DIPEA (122 µL, 0.71 mmol, 2.0 eq.) in THF (20 mL) were slowly added to **10** (660 mg, 1.42 mmol, 4.0 eq.) dissolved in THF (10 mL). After 2 h at RT, the solvent was removed *in vacuo* and the crude product was purified using silica gel flash chromatography (PE/EtOAc: 10/1→1/10). RP-HPLC (10 to 90% B in 15 min): t_R = 18.0 min K' = 9.6. Calculated monoisotopic mass ($C_{44}H_{58}F_5IN_4O_{11}$) = 1,040.3; found: m/z = 1,041.2 $[M+H]^+$, 1,063.6 $[M+Na]^+$.

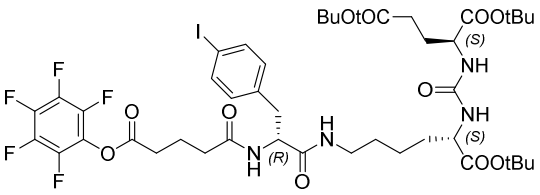

Chemical Formula: $C_{44}H_{58}F_5IN_4O_{11}$
Molecular Weight: 1040,86

α-Amino-L-Gly(Fmoc)-OH (L-Agl(Fmoc)-OH) (13): Boc-L-Agl(Fmoc)-OH (300 mg, 0.72 mmol, 1.0 eq.) was treated with TFA for 15 min at RT. The TFA was afterwards evaporated using a nitrogen stream. The crude product was diluted in water and *t*-BuOH (1/1; *v*/*v*) and lyophilized *in vacuo* overnight and used without further purification. Calculated monoisotopic mass ($C_{17}H_{16}N_2O_4$) = 312.11; found: m/z = 313.5 $[M+H]^+$.

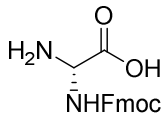

Chemical Formula: $C_{17}H_{16}N_2O_4$
Molecular Weight: 312,33

Agl(Fmoc)-Glut-[(O*t*Bu)KuE(O*t*Bu)$_2$] (14): To a solution of **1** (400 mg, 0.86 mmol, 1.0 eq.) in DMF was added **10** (407.6 mg, 0.86 mmol, 1.0 eq.) and the solution stirred overnight at RT. In the next step, **13** (268.9 mg, 0.86 mmol, 1.0 eq.) dissolved in DMF and DIPEA (147.7 µL, 0.86 mmol, 1.0 eq.) were given to this reaction mixture and again stirred overnight at RT. The crude product was purified using RP-HPLC (30 to 90% B in 15 min): t_R = 11.6 min. K' = 4.8. Calculated monoisotopic mass ($C_{46}H_{65}N_5O_{13}$) = 895.46; found: m/z = 896.6 $[M+H]^+$.

OPfp-Agl(Fmoc)-Glut-[(O*t*Bu)KuE(O*t*Bu)$_2$] (15): To a solution of **14** (7.0 mg, 6.41 µmol, 1.0 eq.) in DMF was given PfpOH (2.36 mg, 12.82 µmol, 2.0 eq.), DIC (2.0 µL, 12.82 µmol, 2.0 eq.) and pyridine (1.1 µL, 12.82 µmol, 2.0 eq.). The solution was allowed to stir for 24 h and the *in situ* activated active ester was used without any purification for further coupling steps. RP-HPLC (10 to 90% B in 15 min): t_R = 15.3 min. K' = 6.7. Calculated monoisotopic mass ($C_{52}H_{64}F_5N_5O_{13}$) = 1,061.44; found: m/z = 1,062.7 $[M+H]^+$.

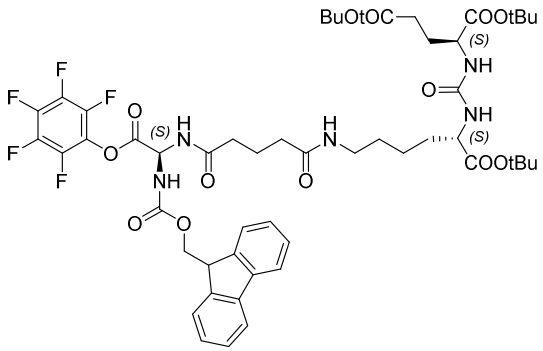

Chemical Formula: $C_{52}H_{64}F_5N_5O_{13}$
Molecular Weight: 1062,10

Fmoc-D-Phe(4-NHDde)-OH (16) and Fmoc-L-Phe(4-NHDde)-OH (17): Into two separate flasks containing either Fmoc-D-Phe(4-NHBoc)-OH (200 mg, 0.39 mmol, 1.0 eq.) or Fmoc-L-Phe(4-NHBoc)-OH (200 mg, 0.39 mmol, 1.0 eq.) was given TFA (1.5 mL) and the mixtures were allowed to stirr for 15 min at RT. Afterwards, the TFA was evaporated using nitrogen stream. The crude products of were diluted with water and *t*-BuOH (1/1; *v*/*v*) and lyophilized overnight without further purification. Afterwards, Dde-OH (284.3 mg, 1.56 mmol, 4.0 eq.) and DIPEA (272.5 µL, 1.56 mmol, 4.0 eq.) dissolved in DMF were added to the lyophilized educts and the reactions were allowed to stir overnight at RT. Analytical RP-HPLC (10 to 90% B in 15 min): t_R = 12.9 min. K' = 5.5. Calculated monoisotopic mass ($C_{34}H_{34}N_2O_6$) = 566.24; found: m/z = 567.4 $[M+H]^+$.

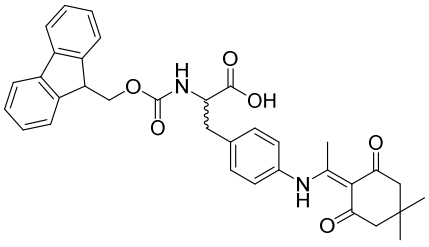

Chemical Formula: $C_{34}H_{34}N_2O_6$
Molecular Weight: 566,65

Dde-D-Phe(4-NHFmoc)-OH (18): To a flask containing Boc-D-Phe(4-NHFmoc)-OH (200 mg, 0.39 mmol, 1.0 eq.) was given TFA (1.5 mL) and the solution was stirred for 15 min at RT. Afterwards, the TFA was evaporated using nitrogen stream. The crude product was diluted with water and *t*-BuOH (1/1; *v*/*v*) and lyophilized overnight without further purification. Afterwards, Dde-OH (284.3 mg, 1.56 mmol, 4.0 eq.) and DIPEA (272.5 µL, 1.56 mmol, 4.0 eq.) dissolved in DMF were added to the lyophilized educt and the reaction was allowed to stir overnight at RT. RP-HPLC (10 to 90% B in 15 min): t_R = 12.5 min. K' = 5.3. Calculated monoisotopic mass ($C_{34}H_{34}N_2O_6$) = 566.24; found: m/z = 567.6 $[M+H]^+$.

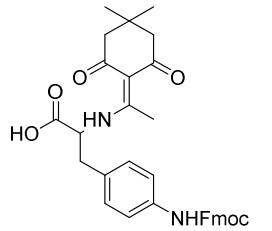

Chemical Formula: $C_{34}H_{34}N_2O_6$
Molecular Weight: 566,65

Pentafluorophenyl 4'-(pentyloxy)-[1,1'-biphenyl]-4-carboxylate (OPfp-PBP) (19): To a solution of DMF containing 4'-(pentyloxy)-[1,1'-biphenyl]-4-carboxylic acid (PBP) (100 mg, 0.35 mmol, 1.0 eq.) was given DIC (109 µL, 703 µmol, 2.0 eq.), pyridine (56.6 µL, 703 µmol, 2.0 eq.) and PfpOH (129 mg, 703 µmol, 2.0 eq.). The solution was stirred for 24 h at RT. Afterwards the crude product was purified by RP-HPLC (10 to 90% B in 15 min): t_R = 17.7 min. K' = 7.9. Calculated monoisotopic mass ($C_{24}H_{19}F_5O_3$) = 450.13; found: m/z = not possible to detect with ESI-MS.

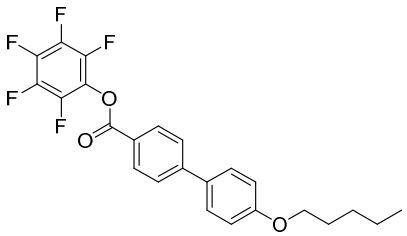

Chemical Formula: $C_{24}H_{19}F_5O_3$
Molecular Weight: 450,41

1-(*tert*-butyl) 5-(perfluorophenyl) (4'-(pentyloxy)-[1,1'-biphenyl]-4-carbonyl)-D-glutamate (PBP-D-Glu(OPfp)-O*t*Bu) (20): To a solution containing **19** (159 mg, 352 µmol, 1.0 eq.) and DIPEA (89 µL, 528 µmol, 1.5 eq.) in DMF was added D-Glu(O*t*Bu)-OH (107 mg, 528 µmol, 1.5 eq.). The solution was stirred overnight at RT. Afterwards, DIC (109 µL, 703 µmol, 2.0 eq.), pyridine (56.6 µL, 703 µmol, 2.0 eq.) and PfpOH (129 mg, 703 µmol, 2.0 eq.) dissolved in DMF were added and the reaction solution stirred overnight at RT. The crude product of **20** was purified using RP-HPLC (60 to 90% B in 15 min): $t_R = 14.2$ min $K' = 6.1$. Calculated monoisotopic mass ($C_{33}H_{34}F_5NO_6$) = 635.63; found: $m/z = 636.9$ $[M+H]^+$.

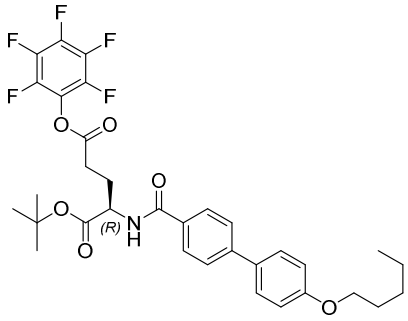

Chemical Formula: $C_{33}H_{34}F_5NO_6$
Molecular Weight: 635,63

Fmoc-D-Asp-OAll (21): To a solution containing Fmoc-D-Asp(*t*Bu)-OH (1.0 g, 1.0 mmol, 1.0 eq.) dissolved in DCM were added DMAP (6.11 mg, 0.05 mmol, 0.05 eq.) and 1-ethyl-3-(3-dimethylaminopropyl)carbodiimide (EDC)·HCl (288 mg, 1.5 mmol, 1.5 eq.). The solution was cooled on ice and stirred for 30 min. Afterwards, allyl alcohol (683 µL, 10 mmol, 10.0 eq.) was slowly added over a period of 10 min and the mixture was allowed to stir for 21 h. The completeness of the reaction was assessed using TLC. The reaction mixture was washed with water and an aq. solution of HCl (5%). The aq. fraction was extracted with DCM. The combined organic phases were once again washed with sat. saline over $MgSO_4$ and filtered to remove the $MgSO_4$. The crude product was purified using flash chromatography (PE/EtOAc = 20/1 → 10/1 → 1/1). TLC (PE/EtOAc; 4/1; *v*/*v*): $R_f = 0.48$ [UV].

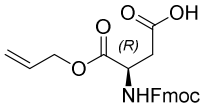

Chemical Formula: $C_{22}H_{21}NO_6$
Molecular Weight: 395,41

^{1}H-NMR ($CDCl_3$, 298 K, 400 MHz): (ppm) = 7.77 (d, ^3J = 7.5 Hz, 2H, H-4'*), 7.61 (dd, ^3J = 7.5 Hz, ^4J = 4.2 Hz, 2H, H-7'*), 7.40 (*virt.* t, ^3J = 7.5 Hz, 2H, H-5'), 7.31 (*virt.* t, ^3J = 7.5 Hz, 2H, H-6'), 5.91 (ddt, $^3J_{trans}$ = 17.0, $^3J_{cis}$ = 10.6, ^3J = 5.7 Hz, 1H, CH_2-C*H*=CH_2), 5.83 (d, ^3J = 8.4 Hz, 1H, N*H*), 5.34 (dd, ^2J = 0.8, $^3J_{trans}$ = 17.0 Hz, 1H, CH_2-CH=CH-H_Z), 5.25 (dd, ^2J = 0.8, $^3J_{cis}$ = 10.4 Hz, 1H, CH_2-CH=CH-H_E), 4.77 – 4.56 (m, 3H, Asp-α-C*H*, CH_2-CH=CH_2), 4.43 (dd, ^2J = 10.5, ^3J = 7.2 Hz, 1H, H-1'), 4.35 (dd, ^2J = 10.5, ^3J = 7.2 Hz, 1H, H-1'***), 4.25 (t, ^3J = 7.2 Hz, 1H, H-2'), 2.98 (dd, ^2J = 16.9, ^3J = 4.3 Hz, 1H, Asp-β-CH-*H*), 2.79 (dd, ^2J = 16.9, ^3J = 4.2 Hz, 1H, Asp-β-CH-*H*), 1.46 (s, 9H, C(CH_3)$_3$).

^{13}C-NMR ($CDCl_3$, 298 K, MHz): (ppm) = 170.8, 170.1, 144.1, 143.9, 141.4, 131.7, 127.9, 127.2, 125.3, 120.1, 119.0, 82.0, 67.4, 66.5, 50.8, 47.3, 38.0, 34.6, 29.8, 28.2.

Synthesis of the PfpOH activated thioglycosides Galactose(OAc)$_4$-MPA-OPfp (22), Mannose(OAc)$_4$-MPA-OPfp (23), Fucose(OAc)$_4$- MPA-OPfp (24) and Cellobiose(OAc)$_7$-MPA-OPfp (25): Synthesis of the PfpOH activated thioglycoside-derivatives of galactose (**22**), mannose (**23**), fucose (**24**) and cellobiose (**25**) was carried out as previously published [236-238] and the substances kindly provided by the laboratory of Prof. Wester. In short for **22**, β-D-galactose pentaacetate (0.5 g, 1.5 mmol, 1.0 eq.) in dry DCM was treated with 3-mercaptopropionic acid (3-MPA) (534 µL, 4.0 mmol, 6.0 eq.) and $BF_3 \cdot Et_2O$ (565 µL, 5.0 mmol, 6.5 eq.) and stirred overnight at RT. The yellowish reaction mixture was extracted with 1.0 N HCl (2×). The aq. phases were additionally extracted with DCM. The combined organic phases were dried over $MgSO_4$ and the solvent evaporated *in vacuo*. The crude thiolated product Galacto(OAc)$_4$-MPA-mercaptopropionate was purified using silica gel flash-chromatography applying a acidified mixture of EtOAc, PE and AcOH (5/5/0.1; *v*/*v*/*v*). In the next step, Galacto(OAc)$_4$-MPA-mercaptopropionate (357 mg, 0.82 mmol, 1.0 eq.) in THF was treated with DIC (506 µL, 3.28 mmol, 4.0 eq.), PfpOH (602 mg, 3.28 mmol, 4.0 eq.) and DIPEA (280 µL, 1.64 mmol, 2.0 eq.). The reaction mixture was allowed to stir overnight at RT and the solvent evaporated *in vacuo*. The crude product **22** was purified using silica gel flash-chromatography applying a mixture of EtOAc and PE (EtOAc/PE; 3/7; *v*/*v*) and obtained as waxy solid (259 mg, 0.43 mmol, 53% yield). The synthesis of **23**, **24** and **25** was accomplished in similarity to **22** using α-D-mannose pentaacetate for **23**, L-fucose tetracetate for **24** and α-D-cellobiose octaacetate for **25**.

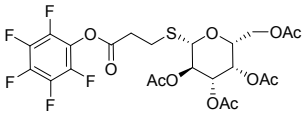
Chemical Formula: $C_{23}H_{23}F_5O_{11}S$
Molecular Weight: 602,48

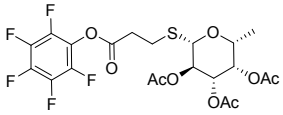
Chemical Formula: $C_{21}H_{21}F_5O_9S$
Molecular Weight: 544,44

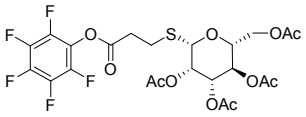
Chemical Formula: $C_{23}H_{23}F_5O_{11}S$
Molecular Weight: 602,48

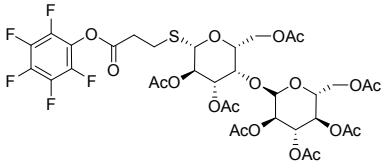
Chemical Formula: $C_{35}H_{39}F_5O_{19}S$
Molecular Weight: 890,73

Pentafluorophenyl benzoate (OPfp-BA) (26): To a solution containing benzoic acid (20.0 mg, 164 µmol, 3.0 eq.) in DMF was added DIC (8.4 µL, 54.5 µmol, 1.0 eq.), pyridine (8.7 µL, 0.11 mmol, 2.0 eq.) and PfpOH (20.0 mg, 0.11 mmol, 2.0 eq.) and the reaction mixture was allowed to stir overnight. The crude product was purified using RP-HPLC (10 to 90% B in 15 min): t_R = 7.57 min K' = 2.8. Calculated monoisotopic mass ($C_{13}H_5F_5O_2$) = 288.60; found: not detectable in ESI-MS

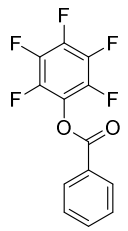
Chemical Formula: $C_{13}H_5F_5O_2$
Molecular Weight: 288,17

NHS-2,4-dinitrobenzoate (NHS-DNBA) (27): To a solution of 2,4-dinitrobenzoic acid (DNBA) (10.0 mg, 47.1 µmol, 1.0 eq.) in dry THF was given *N*, *N*'-dicyclohexylcarbodiimide (DCC) (9.7 mg, 47.1 µmol, 1.0 eq.) and *N*-hydroxysuccinimide (NHS) (10.8 mg, 94.3 µmol, 2.0 eq.) and the reaction mixture was allowed to stir overnight. The crude product was purified using RP-HPLC. RP-HPLC (10 to 90% B in 15 min): t_R = 10.21 min K' = 4.1. Calculated monoisotopic mass ($C_{11}H_7N_3O_8$) = 309.02; found: not detectable in ESI-MS

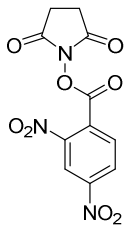

Chemical Formula: $C_{11}H_7N_3O_8$
Molecular Weight: 309,19

4-(hydroxymethyl)phenyl 4-(dimethylamino)benzoate (P-DMBA) (28): To a solution containing 4-(dimethylamino)benzoic acid (DMBA) (20.0 mg, 0.12 mmol, 1.0 eq.) in DMF was given DIC (18.7 µL, 0.12 mmol, 1.0 eq.), HOBt (12.3 mg, 0.18 mmol, 1.5 eq.), TEA (33.6 µL, 0.18 mmol, 1.5 eq.) and 4-(hydroxymethyl)phenol (45.1 mg, 0.48 mmol, 4.0 eq.). The mixture was allowed to stir overnight. The crude product was purified using RP-HPLC. RP-HPLC (10 to 90% B in 15 min): t_R = 12.42 min K' = 5.2. Calculated monoisotopic mass ($C_{16}H_{17}NO_3$) = 271.12; found: m/z = 272.2 $[M+H]^+$.

4-((((4-nitrophenoxy)carbonyl)oxy)methyl)phenyl-4(dimethylamino)benzoate (PNP-P-DMBA) (29): To a solution containing **28** (P-DMBA) (6.0 mg, 22.1 µmol, 1.0 eq.) in dry DCM was given pyridine (3.5 µL, 44.0 µmol, 2.0 eq.), 4-nitrophenyl chloroformate (6.6 mg, 33.0 µmol, 1.5 eq.) and TEA (3.1 µL, 22.0 µmol, 1.0 eq.). The solution turned yellowish after 30 min and was allowed to stir overnight. The crude product was purified using RP-HPLC (10 to 90% B in 15 min): t_R = 15.44 min K' = 6.8. Calculated monoisotopic mass ($C_{23}H_{20}N_2O_7$) = 436.13; found: m/z = 473.5 $[M+H]^+$.

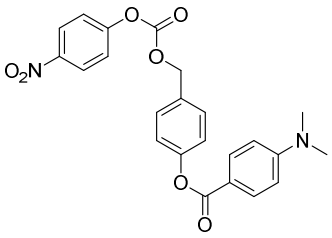

Chemical Formula: $C_{23}H_{20}N_2O_7$
Molecular Weight: 436,42

2.2.2 Building blocks for the arene-binding region

2.2.2.1 Peptides for the synthesis of KuE-based PSMA inhibitors

The necessary peptidic structures for the synthesis of the respective PSMA inhibitors were achieved according to **SP-1** to **SP-7**. The initial starting point was the resin loading according to **SP-1** of a protected amino acid. Resin coupling with further amino acids (**SP-2**) was achieved using standard Fmoc-solid-phase strategy as previously described [225,234]. If peptide cleavage from the resin was necessary for chelator coupling, the peptide sequence was cleaved from the resin either using **SP-7.1** or **SP-7.2** depending on necessary side-group protection. Otherwise, the chelator was directly condensed with the resin-bound peptide. Both procedures will be found in the following sections. Finally, the peptides were consequently purified via RP-HPLC.

DOTAGA-3-iodo-D-Tyr-D-Phe-D-Lys-OH (DOTAGA-y(3-I)fk) (30) : The synthesis of **30** was accomplished via solid phase strategy as previously described [224,234]. RP-HPLC (10 to 90% B in 15 min): t_R = 6.2 min K' = 2.1. Calculated monoisotopic mass ($C_{43}H_{61}IN_8O_{14}$) = 1,040.34; found: m/z = 1,040.5 $[M+H]^+$, m/z = 521.3 $[M+2H]^{2+}$, m/z = 1,063.4 = $[M+Na]^+$.

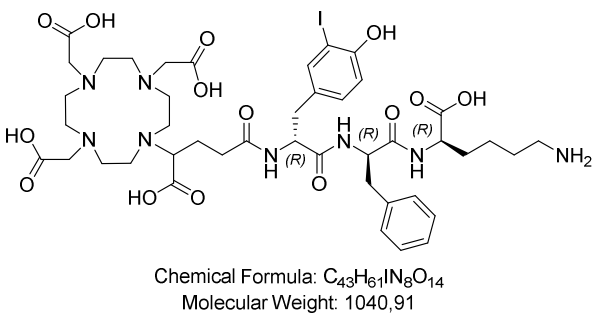

DOTAGA-3-iodo-D-Tyr-D-Phe-L-Lys-OH (DOTAGA-y(3-I)fK) (31): The synthesis of **31** was performed according to **30** as previously published [225,234]. RP-HPLC (10 to 90% B in 15 min): t_R = 6.2 min K' = 2.1. Calculated monoisotopic mass ($C_{43}H_{61}IN_8O_{14}$) = 1,040.34; found: m/z = 1,040.6 $[M+H]^+$, m/z = 521.3 $[M+2H]^{2+}$, m/z = 1,063.4 = $[M+Na]^+$.

DOTAGA-3-iodo-L-Tyr-D-Phe-D-Lys-OH (DOTAGA-Y(3-I)fk) (32): The synthesis of **32** was performed according to **30** as previously published [225,234]. RP-HPLC (10 to 90% B in 15 min): t_R = 6.2 min K' = 2.1. Calculated monoisotopic mass ($C_{43}H_{61}IN_8O_{14}$) = 1,040.34; found: m/z = 1,040.5 $[M+H]^+$, m/z = 521.3 $[M+2H]^{2+}$, m/z = 1,063.4 = $[M+Na]^+$.

DOTAGA-3-iodo-D-Tyr-L-Phe-L-Lys-OH (DOTAGA-y(3-I)FK) (33): The synthesis of **33** was performed according to **30** as previously published [225,234]. RP-HPLC (10 to 90% B in 15 min): t_R = 6.2 min K' = 2.1. Calculated monoisotopic mass ($C_{43}H_{61}IN_8O_{14}$) = 1,040.34; found: m/z = 1,040.4 $[M+H]^+$, m/z = 521.3 $[M+2H]^{2+}$, m/z = 1,063.4 = $[M+Na]^+$.

DOTAGA-3-iodo-D-Tyr-L-Phe-D-Lys-OH (DOTAGA-y(3-I)Fk) (34): The synthesis of **34** was performed according to **30** as previously published [225,234]. RP-HPLC (10 to 90% B in 15 min): t_R = 6.2 min K' = 2.1. Calculated monoisotopic mass ($C_{43}H_{61}IN_8O_{14}$) = 1,040.34; found: m/z = 1,040.4 $[M+H]^+$, m/z = 521.3 $[M+2H]^{2+}$, m/z = 1,063.5 = $[M+Na]^+$.

DOTAGA-3-iodo-L-Tyr-D-Phe-L-Lys-OH (DOTAGA-Y(3-I)fK) (35): The synthesis of **35** was performed according to **30** as previously published [225,234]. RP-HPLC (10 to 90% B in 15 min): t_R = 6.2 min K' = 2.1. Calculated monoisotopic mass ($C_{43}H_{61}IN_8O_{14}$) = 1,040.34; found: m/z = 1,040.5 $[M+H]^+$, m/z = 521.3 $[M+2H]^{2+}$, m/z = 1,063.3 = $[M+Na]^+$.

DOTAGA-3-iodo-L-Tyr-L-Phe-L-Lys-OH (DOTAGA-Y(3-I)FK) (36): The synthesis of **36** was performed according to **30** as previously published [225,234]. RP-HPLC (10 to 90% B in 15 min): t_R = 6.2 min K' = 2.1. Calculated monoisotopic mass ($C_{43}H_{61}IN_8O_{14}$) = 1,040.34; found: m/z = 1,040.6 $[M+H]^+$, m/z = 521.3 $[M+2H]^{2+}$, m/z = 1,063.4 = $[M+Na]^+$.

DOTAGA-3-iodo-D-Tyr-D-Phe-D-Lys(Dde)-D-Lys-OH (DOTAGA-y(3-I)fk(Dde)k) (37): 37 was similarly synthesized as already published for **30** [225,234]. After resin loading with Fmoc-D-Lys(Boc)-OH according to **SP-1**, the resin bound amino acid was Fmoc-deprotected according to **SP-3** and coupled with Fmoc-D-Lys(Dde)-OH and the following Fmoc-protected amino acids Fmoc-D-Phe-OH and Fmoc-D-Tyr(3-I)-OH according to **SP-2** with subsequent Fmoc-deprotection. Coupling with DOTAGA-anhydride was achieved using DOTAGA-anhydride (5.0 eq.) and DIPEA (10 eq.) for 24 h at RT. The final product **37** was cleaved from the resin according to **SP-7.2** and purified via RP-HPLC. RP-HPLC (10 to 90% B in 15 min): t_R = 7.46 min K' = 2.7. Calculated monoisotopic mass ($C_{59}H_{85}IN_{10}O_{17}$) = 1,332.51; found: m/z = 1,333.6 $[M+H]^+$, m/z = 667.4 $[M+2H]^{2+}$.

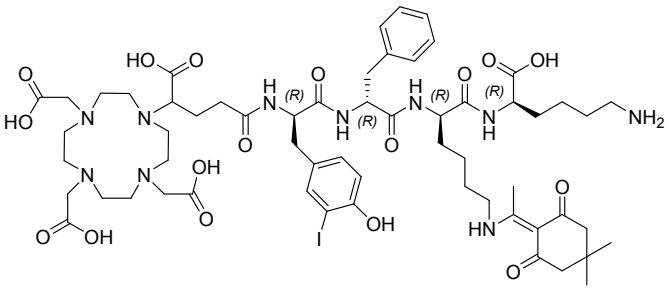

Chemical Formula: $C_{59}H_{85}IN_{10}O_{17}$
Molecular Weight: 1333,29

DOTAGA-3-iodo-D-Tyr-D-Phe-N^6-D-Lys(N^2-Dde)-D-Lys-OH (DOTAGA-y(3-I)f-N^6-k(N^2-Dde)k) (38): The synthesis of **38** was accomplished according to the procedure of **37** utilizing Dde-D-Lys(Fmoc)-OH [225,234]. RP-HPLC (10 to 90% B in 15 min): t_R = 7.33 min K' = 2.67. Calculated monoisotopic mass ($C_{59}H_{85}IN_{10}O_{17}$) = 1,332.51; found: m/z = 1,333.8 $[M+H]^+$, m/z = 667.3 $[M+2H]^{2+}$.

DOTAGA-3-iodo-D-Tyr-D-Lys(Dde)-D-Phe-D-Lys-OH(DOTAGA-y(3-I) k(Dde)fk) (39): The synthesis of **39** was accomplished according to the procedure of **37** utilizing Fmoc-D-Lys(Dde)-OH [225,234]. RP-HPLC (10 to 90% B in 15 min): t_R = 7.55 min K' = 2.78. Calculated monoisotopic mass ($C_{59}H_{85}IN_{10}O_{17}$) = 1,332.51; found: m/z = 1,333.8 $[M+H]^+$, m/z = 667.4 $[M+2H]^{2+}$.

DOTAGA-3-iodo-D-Tyr-N^6-D-Lys(N^2-Dde)-D-Phe-D-Lys-OH (DOTAGA-y(3-I)-N^6-k(N^2-Dde)fk) (40): The synthesis of **40** was accomplished according to the procedure of **37** utilizing Dde-D-Lys(Fmoc)-OH [225,234]. RP-HPLC (10 to 90% B in 15 min): t_R = 7.47 min K' = 2.74. Calculated monoisotopic mass ($C_{59}H_{85}IN_{10}O_{17}$) = 1,332.51; found: m/z = 1,333.5 $[M+H]^+$, m/z = 667.4 $[M+2H]^{2+}$.

DOTAGA-D-Lys(Dde)-3-iodo-D-Tyr-D-Phe-D-Lys-OH (DOTAGA-k(Dde)y(3-I)fk) (41): The synthesis of **41** was accomplished according to the procedure of **37** utilizing Fmoc-D-Lys(Dde)-OH [225,234]. RP-HPLC (10 to 90% B in 15 min): t_R = 7.61 min K' = 2.81. Calculated monoisotopic mass ($C_{59}H_{85}IN_{10}O_{17}$) = 1,332.51; found: m/z = 1,333.8 $[M+H]^+$, m/z = 667.3 $[M+2H]^{2+}$.

DOTAGA-N^6-D-Lys(N^2-Dde)-3-iodo-D-Tyr-D-Phe-D-Lys-OH (DOTAGA-N^6-k(N^2-Dde)y(3-I)fk) (42): The synthesis of **42** was accomplished according to the procedure of **37** utilizing Dde-D-Lys(Fmoc)-OH [225,234]. RP-HPLC (10 to 90% B in 15 min): t_R = 7.39 min K' = 2.69. Calculated monoisotopic mass ($C_{59}H_{85}IN_{10}O_{17}$) = 1,332.51; found: m/z = 1,333.8 $[M+H]^+$, m/z = 667.4 $[M+2H]^{2+}$.

DOTAGA-L-Phe(4-NHDde)-3-iodo-D-Tyr-D-Phe-D-Lys-OH (DOTAGA-F(4-NHDde)-y(3-I)fk)(43): The synthesis of **43** was accomplished in similarity to **37** using Fmoc-L-Phe(4-NHDde)-OH (**17**) [225,234]. The final crude product was purified via RP-HPLC. RP-HPLC (10 to 90% B in 15 min): t_R = 8.67 min K' = 3.33. Calculated monoisotopic mass ($C_{62}H_{83}IN_{10}O_{17}$) = 1,366.50; found: m/z = 1,367.7 $[M+H]^+$, m/z = 684.7 $[M+2H]^{2+}$.

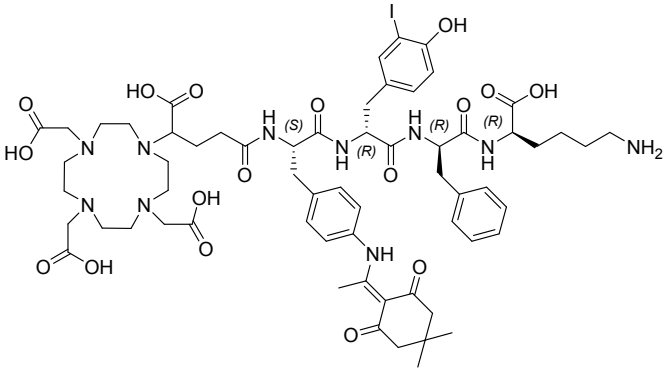

DOTAGA-D-Phe(4-NHDde)-3-iodo-D-Tyr-D-Phe-D-Lys-OH (DOTAGA-f(4-NHDde)y(3-I)fk) (44): The synthesis of **44** was accomplished in similarity to **37** using Fmoc-D-Phe(4-NHDde)-OH (**16**) [225,234]. The final crude product was purified via RP-RP-HPLC. RP-RP-HPLC (10 to 90% B in 15 min): t_R = 7.63 min K' = 2.82. Calculated monoisotopic mass ($C_{62}H_{83}IN_{10}O_{17}$) = 1,366.50; found: m/z = 1,367.6 $[M+H]^+$, m/z = 684.8 $[M+2H]^{2+}$.

DOTAGA-D-Phe(4-NHBoc)-3-iodo-D-Tyr-D-Phe-L-Lys-OH (DOTAGA-f(NHBoc)y(3-I)fK) (45): The synthesis of **45** was accomplished in similarity to **37** using Fmoc-D-Phe(4-NHBoc)-OH [225,234] and Fmoc-L-Phe(4-NHDde)-OH as starting point. Dde-deprotection was achieved via **SP-5** with concomitant cleavage from the resin using **SP-7.1**. The final crude product was purified via RP-HPLC. RP-HPLC (10 to 90% B in 15 min): t_R = 8.1 min K' = 3.1. Calculated monoisotopic mass ($C_{57}H_{79}IN_{10}O_{17}$) = 1,302.50; found: m/z = 1,303.3 $[M+H]^+$, m/z = 652.3 $[M+2H]^{2+}$.

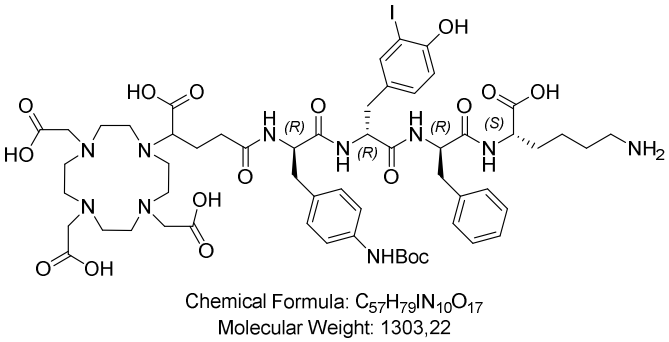

DOTAGA-D-Phe(4-NHBoc)-3-iodo-D-Tyr-L-Phe-L-Lys-OH (DOTAGA-f(4-NHBoc)y(3-I)FK) (46): The synthesis of **46** was accomplished in similarity to **45** using Fmoc-D-Phe(4-NHBoc)-OH [225,234]. The final crude product was purified via RP-HPLC. RP-HPLC (10 to 90% B in 15 min): t_R = 8.1 min K' = 3.1. Calculated monoisotopic mass ($C_{57}H_{79}IN_{10}O_{17}$) = 1,302.50; found: m/z = 1,303.4 $[M+H]^+$, m/z = 652.3 $[M+2H]^{2+}$.

DOTAGA-L-Phe(4-NHBoc)-3-iodo-D-Tyr-D-Phe-L-Lys-OH (DOTAGA-F(4-NHBoc)y(3-I)fK) (47): The synthesis of **47** was accomplished in similarity to **45** using Fmoc-L-Phe(4-NHBoc)-OH [225,234]. The final crude product was purified via RP-HPLC. RP-HPLC (10 to 90% B in 15 min): t_R = 8.1 min K' = 3.1. Calculated monoisotopic mass ($C_{57}H_{79}IN_{10}O_{17}$) = 1,302.50; found: m/z = 1,303.4 $[M+H]^+$, m/z = 652.3 $[M+2H]^{2+}$.

DOTAGA-D-Tyr-D-2-Nal-D-Lys (DOTAGA-y-2-nal-k) (48): The synthesis of **48** was achieved as already described for **37** and using **SP-7.2** for cleavage from the resin [225,234]**.** RP-HPLC (20 to 70% B in 15 min): t_R = 10.7 min K' = 4.13. Calculated monoisotopic mass ($C_{47}H_{64}N_8O_{14}$) = 964.5; found: m/z = 965.8 $[M+H]^+$, 987.8 $[M+Na]^+$.

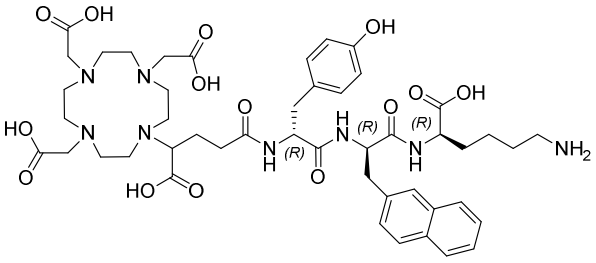

DOTAGA-L-Phe(4-NHBoc)-D-Tyr(*t*Bu)-D-2-Nal-D-Lys (DOTAGA-F(4-NHBoc)y(*t*Bu)-2-nal-k) (49): The synthesis of **49** was accomplished as described for **45** using Fmoc-D-Lys(NHDde)-OH as starting point [225,234]. RP-HPLC (10 to 90% B in 15 min): t_R = 9.6 min K' = 3.8. Calculated monoisotopic mass ($C_{65}H_{90}N_{10}O_{17}$) = 1,282.65; found: m/z = 1,283.2 $[M+H]^+$, 642.6 $[M+2H]^{2+}$.

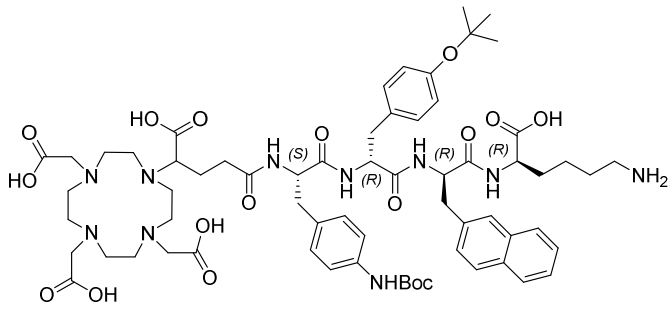

DOTAGA-D-Phe(4-NHBoc)-D-Tyr(*t*Bu)-D-2-Nal-D-Lys (DOTAGA-f(4-NHBoc)y(*t*Bu)-2-nal-k) (50): The synthesis of **50** was accomplished as described for **45** using Fmoc-D-Lys(NHDde)-OH as starting point [225,234]. RP-HPLC (10 to 90% B in 15 min): t_R = 9.6 min K' = 3.8. Calculated monoisotopic mass ($C_{65}H_{90}N_{10}O_{17}$) = 1,282.65; found: m/z = 1,283.3 $[M+H]^+$, 642.6 $[M+2H]^{2+}$.

DOTAGA-D-Phe(4-NHBoc)-D-Tyr(*t*Bu)-D-2-Nal-L-Lys (DOTAGA-f(4-NHBoc)y(*t*Bu)-2-nal-K) (51): The synthesis of **51** was accomplished as described for **45** using Fmoc-L-Lys(NHDde)-OH as starting point [225,234]. RP-HPLC (10 to 90% B in 15 min): t_R = 9.6 min K' = 3.8. Calculated monoisotopic mass ($C_{65}H_{90}N_{10}O_{17}$) = 1,282.65; found: m/z = 1,283.3 $[M+H]^+$, 642.6 $[M+2H]^{2+}$.

DOTAGA-L-Phe(4-NHBoc)-D-Tyr(*t*Bu)-D-2-Nal-L-Lys (DOTAGA-F(4-NHBoc)y(*t*Bu)-2-nal-K) (52): The synthesis of **52** was accomplished as described for **45** using Fmoc-L-Lys(NHDde)-OH as starting point [225,234]. RP-HPLC (10 to 90% B in 15 min): t_R = 9.6 min K' = 3.8. Calculated monoisotopic mass ($C_{65}H_{90}N_{10}O_{17}$) = 1,282.65; found: m/z = 1,283.3 $[M+H]^+$, 642.6 $[M+2H]^{2+}$.

DOTA-D-Phe(4-NHBoc)-D-Tyr(*t*Bu)-D-2-Nal-D-Lys (DOTA-f(4-NHBoc)y(*t*Bu)-2-nal-k) (53): The synthesis of **53** was achieved as described for **45** [225,234]. After resin loading using Fmoc-D-Lys(NHDde)-OH as first amino acid, according to **SP-1**, the peptide was further synthesized applying **SP-2**. The chelating moiety DOTA was coupled using a solution containing DOTA · 6 H_2O (4.0 eq.), EDCI (5.0 eq.), NHS (5.0 eq.) and DIPEA (8.0 eq.) in water, which was allowed to stir for 30 min prior to the addition to the peptide-loaded resin. The mixed reaction solution was further allowed to stir for 18 h at RT. After cleavage, the peptide was purified by RP-HPLC. RP-HPLC (10 to 90% B in 15 min): t_R = 9.2 min K' = 3.6. Calculated monoisotopic mass ($C_{62}H_{86}N_{10}O_{15}$) = 1,210.63; found: m/z = 1,211.4 $[M+H]^+$, 606.5 $[M+2H]^{2+}$.

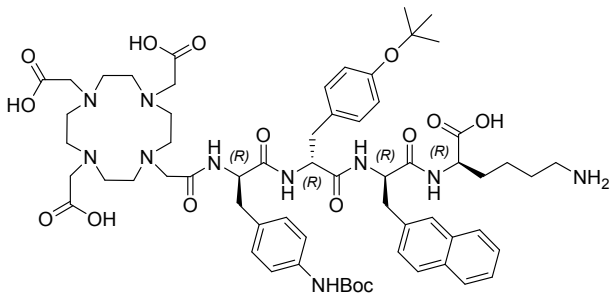

Chemical Formula: $C_{62}H_{86}N_{10}O_{15}$
Molecular Weight: 1211,43

(z)-(2-(((4-fluorobenzylidene)amino)oxy)acetyl)-D-lysine (4-FBA-AOA-D-Lys) (54): 2-CTC resin was loaded with Fmoc-D-Lys(NHBoc)-OH according to **SP-1**. After Fmoc-deprotection applying **SP-3**, 2-(*tert*-Butyloxycarbonyl-aminooxy)-acetic acid (Boc-AOAc-OH) (2.0 eq.) was coupled to H-D-Lys(NHBoc) using **SP-2**. The protecting groups were removed using **SP-7.2**. The TFA was evaporated using nitrogen stream. The resulting yellowish oily crude product was directly treated with an aq. MeCN mixture (H_2O/MeCN; 7/3; *v*/*v*) containing 4-fluorobenzaldehyde (10 eq.) and allowed to stir for 15 min at RT. After removal of the solvent *in vacuo*, the crude product was purified via RP-HPLC. RP-HPLC (10 to 90% B in 15 min): t_R = 6.1 min K' = 2.05. Calculated monoisotopic mass ($C_{15}H_{20}FN_3O_4$) = 325.14; found: m/z = 326.4 $[M+H]^+$.

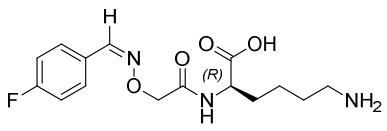

Chemical Formula: $C_{15}H_{20}FN_3O_4$
Molecular Weight: 325,34

(2-((((Z)-4-fluorobenzylidene)amino)oxy)acetyl)-D-phenylalanyl-D-lysine (4-FBA-AOA-D-Phe-D-Lys) (55): The synthesis of **55** was achieved in similarity to **54** employing the same final reaction mixture to couple the amino-oxy group with 4-fluorobenzaldehyde. RP-HPLC (10 to 90% B in 15 min): t_R = 8.34 min K' = 3.17. Calculated monoisotopic mass ($C_{24}H_{29}FN_4O_5$) = 472.21; found: m/z = 473.7 $[M+H]^+$.

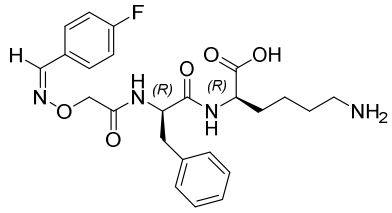

Chemical Formula: $C_{24}H_{29}FN_4O_5$
Molecular Weight: 472,52

4-FBA-AOA-3-iodo-D-Tyr-D-Phe-D-Lys (56): The synthesis of **56** was achieved in similarity to **54** employing the same final reaction mixture to couple the amino-oxy group with 4-fluorobenzaldehyde. RP-HPLC (10 to 90% B in 15 min): t_R = 9.34 min K' = 3.67. Calculated monoisotopic mass ($C_{34}H_{39}FIN_5O_7$) = 775.19; found: m/z = 775.4 $[M+H]^+$.

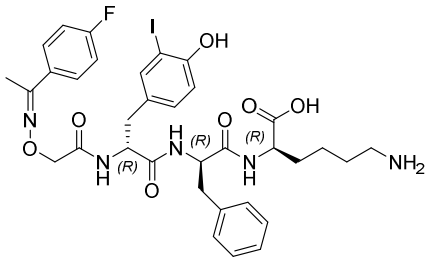

Chemical Formula: $C_{34}H_{39}FIN_5O_7$
Molecular Weight: 775,62

Succinimidyl-4-tributylstannyl-benzoate ($SnBu_3$-BA-NHS) (57): The synthesis for **57** and in general for the radioiodination-precursor was achieved as previously described [234,239-241]. Briefly, 4-iodobenzoic acid (500 mg, 2.0 mmol, 1.0 eq.) were dissolved in DCM (10 mL) under nitrogen atmosphere with NHS (278 mg, 2.4 mmol, 1.2 eq.) and DCC (374 mg, 1.81 mmol, 0.9 eq.). The reaction solution was allowed to stir overnight and after completion of reaction, the precipitate filtered off. The resulting filtrate was evaporated *in vacuo* and the resulting product succinimidyl-4-iodobenzoate (I-BA-NHS) was washed with a mixture of DCM and hexane (1/1; *v*/*v*). In the next step, I-BA-NHS (100 mg, 0.29 mmol, 1.0 eq.) was dissolved in dry toluene under nitrogen atmosphere together with hexabutylditin (234 µL, 0.46 mmol, 1.6 eq.) and $Pd(PPh_3)_4$ (10.7 mg, 9.1 µmol, 0.02 eq.). The solution was heated under reflux overnight and turned black. The solvent was removed *in vacuo* and the resulting oily product purified using silica gel flash chromatography with a mixture of EtOAc and hexane (3/7; *v*/*v*) to yield as a colorless oil. TLC (EtOAc/hexane; 3/7; *v*/*v*): R_f = 0.46.

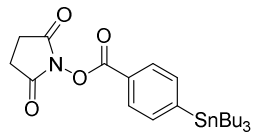

Chemical Formula: $C_{23}H_{35}NO_4Sn$
Molecular Weight: 508,25

(9*H*-fluoren-9-yl)methyl(2-hydroxyethyl)carbamate (Fmoc-2-Amet) (58): The synthesis of **58** was achieved as previously published [242]. 2-ethanolamine (2-Amet) (30.2 µL, 500 µmol, 1.0 eq.) were dissolved in a solution containing of a Na_2CO_3-solution (10%, *m/v*) (5 mL) and DCM (3 mL).. To this solution was given 9-Fluorenylmethyl chloroformate (144 mg, 555 µmol, 1.11 eq.) with subsequent stirring for 28 h at RT. Next, the reaction solution was extracted (3×) with EtOAc (25 mL). The combined organic phases were washed with saline (25 mL) and HCl-solution (1.0 M) (25 mL) and dried over Na_2SO_4. The remaining solvent was removed *in vacuo* and the crude product purified via flash chromatography (PE/EtOAc = 1/2 → 1/4) yielding Fmoc-2-Amet as a white solid (127 mg, 0.45 mmol, 90%). TLC (PE/EtOAc ; 1/2 ; *v/v*): R_f = 0.57 [UV; $KMnO_4$].

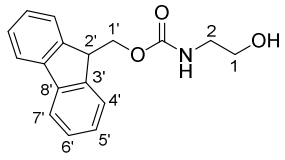

Chemical Formula: $C_{17}H_{17}NO_3$
Molecular Weight: 283,33

^{1}H-NMR ($CDCl_3$, 298 K, 400 MHz): δ (ppm) = 7.77 (d, ^{3}J = 7.5 Hz, 2H, H-4'), 7.60 (d, ^{3}J = 7.5 Hz, 2H, H-7'), 7.41 (virt. t, ^{3}J = 7.5, 7.3 Hz, 2H, H-5'), 7.32 (virt. t, ^{3}J = 7.5, 7.3 Hz, 2H, H-6'), 5.12 (s, 1H, 1H, OH), 4.44 (d, ^{3}J = 6.5 Hz, 2H, H-1'), 4.22 (t, ^{3}J = 6.5 Hz, 1H, H-2'), 3.78 – 3.69 (m, 2H, H-1), 3.41 – 3.32 (m, 2H, H-2).

^{13}C-NMR ($CDCl_3$, 298 K, 101 MHz): δ (ppm) = 157.2 (1C, C=O), 144.0 (2C, C-3'), 141.5 (2 C, C-8'), 127.8 (2 C, C-4'), 127.2 (2 C, C-5'), 125.1 (2 C, C-6'), 120.1 (2 C, C-7'), 66.9 (1C, C-1'), 62.4 (1C, C-1), 47.4 (1C, C-2'), 43.7 (1C, C-2').

4-(2-((((9*H*-fluoren-9-yl) methoxy)carbonyl)amino)ethoxy)-4-oxobutanoic acid (Fmoc-AE-Suc) (59): To a solution of DMF containing **58** (50 mg, 176.5 µmol, 1.0 eq.) was given succinic anhydride (123.6 mg, 1.24 mmol, 7.0 eq.) and DIPEA (277 µL, 1.59 mmol, 9.0 eq.). The solution was stirred for 24 h at RT. After completion of reaction the solvent was removed *in vacuo* and the crude product purified via RP-HPLC (10 to 90% B in 15 min): t_R = 13.1 min K' = 5.55. Calculated monoisotopic mass ($C_{21}H_{21}NO_6$) = 383.14 found: *m/z* = 384.0 $[M+H]^+$.

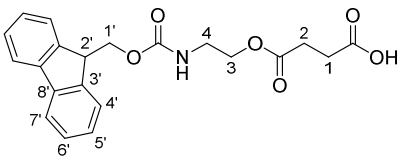

Chemical Formula: $C_{21}H_{21}NO_6$
Molecular Weight: 383,40

^{1}H-NMR (DMSO-d_6, 298 K, 400 MHz): 12.24 (s, 1H, COOH), 7.89 (d, ^3J = 7.5 Hz, 2H, H-4'*), 7.69 (d, ^3J = 7.5 Hz, 2H, H-7'*), 7.42 (*virt.* t, ^3J = 7.5, 6.9 Hz, 2H, H-5'**), 7.34 (*virt.* t, ^3J = 7.5 Hz, 2H, H-6'**), 4.32 (d, ^3J = 6.9 Hz, 1H, H-1'), 4.22 (t, ^3J = 6.9 Hz, 1H, H-2'), 4.02 (t, ^3J = 5.7 Hz, 2H, H-3), 3.22 (*virt.* q, ^3J = 5.7 Hz, 2H, H-4), 2.55 – 2.43 (m, 4H, H-1, H-2).
^{13}C-NMR (DMSO-d_6, 298 K, 101 MHz): 173.39 (1C, COOH*), 172.09 (1C, COOR*), 156.23 (1C, NH-(C=O)-O), 143.87 (2C, C-3'*), 140.74 (2 C, C-8'*), 127.62 (2 C, C-4'**), 127.07 (2 C, C-5'**), 125.14 (2 C, C-6'**), 120.12 (2 C, C-7'**), 65.42 (1C, C-1'), 62.74 (1C, C-3), 46.72 (1C, C-4***), 31.31 (1C, C-2'***), 28.70 (1C, C-1****), 28.64 (1C, C-2****).

2.3 Synthesis of EuK-based PSMA inhibitors

2.3.1 Stereoisomers of PSMA I&T

DOTAGA-y(3-I)fk(Sub-KuE) (PSMA I&T) (PSMA-1): The synthesis of **PSMA-1** was performed as already published [225]. Briefly, to a solution of DMF containing **30** (5.0 mg, 4.8 µmol, 1.0 eq.), **4** (5.8 mg, 7.2 µmol, 1.5 eq.) and DIPEA (3.3 µL, 21.6 µmol, 4.0 eq.) were added. The solution was allowed to stir overnight at RT. After completion of reaction, the solvent was reduced to approx. 300 µL and precipitated in Et_2O, centrifuged and the supernatant removed. With the resulting pellet was processed according to **SP-6** for *t*Bu-removal. The final product was purified via RP-HPLC (10 to 45% B in 15 min): t_R = 10.5 min K' = 4.25. Calculated monoisotopic mass ($C_{63}H_{92}IN_{11}O_{23}$) = 1,497.54; found: m/z = 1,498.3 $[M+H]^+$, 750.1 $[M+2H]^{2+}$.

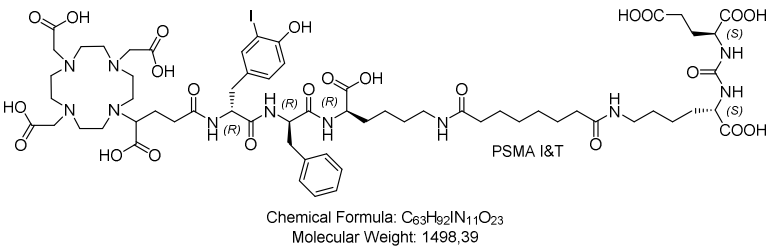

DOTAGA-y(3-I)fK(Sub-KuE) (PSMA-2): The synthesis of **PSMA-2** was accomplished in concordance to **PSMA-1** using of **31** (5.0 mg, 4.8 µmol, 1.0 eq.), **4** (1.5 eq.) and DIPEA (4.0 eq.). RP-HPLC (10 to 50% B in 15 min): t_R = 10.64 min K' = 4.32. Calculated monoisotopic mass ($C_{63}H_{92}IN_{11}O_{23}$) = 1,497.54; found: m/z = 1,498.3 $[M+H]^+$, 750.1 $[M+2H]^{2+}$.

DOTAGA-Y(3-I)fk(Sub-KuE) (PSMA-3): The synthesis of **PSMA-3** was accomplished in concordance to **PSMA-1** using **32** (5.0 mg, 4.8 µmol, 1.0 eq.), **4** (1.5 eq.) and DIPEA (4.0 eq.). RP-HPLC (15 to 40% B in 15 min): t_R = 12.58 min K' = 5.29. Calculated monoisotopic mass ($C_{63}H_{92}IN_{11}O_{23}$) = 1,497.54; found: m/z = 1,498.3 $[M+H]^+$, 750.1 $[M+2H]^{2+}$.

DOTAGA-y(3-I)FK(Sub-KuE) (PSMA-4): The synthesis of **PSMA-4** was accomplished in concordance to **PSMA-1** using **33** (5.0 mg, 4.8 µmol, 1.0 eq.), **4** (1.5 eq.) and DIPEA (4.0 eq.). RP-HPLC (10 to 40% B in 15 min): t_R = 13.14 min K' = 5.57. Calculated monoisotopic mass ($C_{63}H_{92}IN_{11}O_{23}$) = 1,497.54; found: m/z = 1,498.3 $[M+H]^+$, 750.1 $[M+2H]^{2+}$.

DOTAGA-y(3-I)Fk(Sub-KuE) (PSMA-5): The synthesis of **PSMA-5** was accomplished in concordance to **PSMA-1** using **34** (5.0 mg, 4.8 µmol, 1.0 eq.), **4** (1.5 eq.) and DIPEA (4.0 eq.). RP-HPLC (10 to 50% B in 15 min): t_R = 10.52 min K' = 4.26. Calculated monoisotopic mass ($C_{63}H_{92}IN_{11}O_{23}$) = 1,497.54; found: m/z = 1,498.3 $[M+H]^+$, 750.1 $[M+2H]^{2+}$.

DOTAGA-Y(3-I)fK(Sub-KuE) (PSMA-6): The synthesis of **PSMA-6** was accomplished in concordance to **PSMA-1** using **35** (5.0 mg, 4.8 µmol, 1.0 eq.), **4** (1.5 eq.) and DIPEA (4.0 eq.). RP-HPLC (10 to 40% B in 15 min): t_R = 11.62 min K' = 4.81. Calculated monoisotopic mass ($C_{63}H_{92}IN_{11}O_{23}$) = 1,497.54; found: m/z = 1,498.3 $[M+H]^+$, 750.1 $[M+2H]^{2+}$.

DOTAGA-Y(3-I)FK(Sub-KuE) (PSMA-7): The synthesis of **PSMA-7** was accomplished in concordance to **PSMA-1** using **36** (5.0 mg, 4.8 µmol, 1.0 eq.), **4** (1.5 eq.) and DIPEA (4.0 eq.). RP-HPLC (10 to 50% B in 15 min): t_R = 10.7 min K' = 4.35. Calculated monoisotopic mass ($C_{63}H_{92}IN_{11}O_{23}$) = 1,497.54; found: m/z = 1,498.3 $[M+H]^+$, 750.1 $[M+2H]^{2+}$.

2.3.2 PSMA inhibitors with a free amino group

DOTAGA–y(3-I)fk(L-Asu[KuE]) (PSMA-8): To a solution of DMF containing **30** (5.0 mg, 4.8 µmol, 1.0 eq.), **9** (7.5 mg, 7.2 µmol, 1.5 eq.) and DIPEA (3.3 µL, 21.6 µmol, 4.0 eq.) were added. The reaction solution was allowed to stir overnight at RT. After completion of reaction, the solvent was removed *in vacuo* and the crude product treated with a mixture of piperidine in DMF (20/80; *v*/*v*) for 15 min to achieve Fmoc-deprotection. The solvent was reduced to approx. 300 µL via evaporation *in vacuo*, precipitated in Et_2O and centrifuged. With the resulting pellet was processed according to **SP-6** for *t*Bu-removal. The final product was purified via RP-HPLC (10 to 90% B in 15 min): t_R = 6.09 min K' = 2.05. Calculated monoisotopic mass ($C_{63}H_{93}IN_{12}O_{23}$) = 1,512.55; found: m/z = 1,513.9 $[M+H]^+$, 757.8 $[M+2H]^{2+}$.

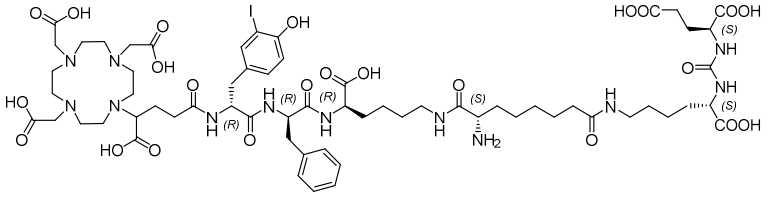

DOTAGA-y(3-I)fkk(Sub-KuE) (PSMA-9): The synthesis of **PSMA-9** was achieved similarly to **PSMA-1**. Briefly, into a solution of DMF (960 µL) containing **37** (5.0 mg, 3.75 µmol, 1.0 eq.), was given **4** (6.1 mg, 7.5 µmol, 2.0 eq.) and DIPEA (2.6 µL, 15.0 µmol, 4.0 eq.). After completion of reaction, the mixture was treated with $N_2H_4 \cdot H_2O$ (40 µL) for Dde-deprotection on the basis of **SP-4**. The reaction mixture was allowed to stir for 15 min at RT and subsequently precipitated in Et_2O, centrifuged and the supernatant removed. In the next step, the dried pellet was treated with TFA according to **SP-6** for *t*Bu-

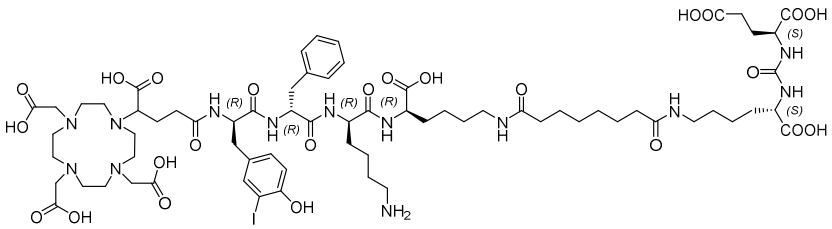

removal. The crude product was purified via RP-HPLC (10 to 90% B in 15 min): t_R = 7.83 min $K^{'}$ = 2.92. Calculated monoisotopic mass ($C_{69}H_{104}IN_{13}O_{24}$) = 1,625.64; found: m/z = 1,626.9 $[M+H]^+$, 814.4 $[M+2H]^{2+}$, 1,648.9 $[M+Na]^+$.

DOTAGA-y(3-I)f-N^6-kk(Sub-KuE)) (PSMA-10): The synthesis of **PSMA-10** was achieved using **38** (5.0 mg, 3.75 µmol, 1.0 eq.) and applying the same procedure as described for **PSMA-9.** The crude product was purified using RP-HPLC (10 to 50% B in 15 min): t_R = 9.75 min $K^{'}$ = 3.86. Calculated monoisotopic mass ($C_{69}H_{104}IN_{13}O_{24}$) = 1,625.64; found: m/z = 1,626.9 $[M+H]^+$, 814.4 $[M+2H]^{2+}$, 1,648.9 $[M+Na]^+$.

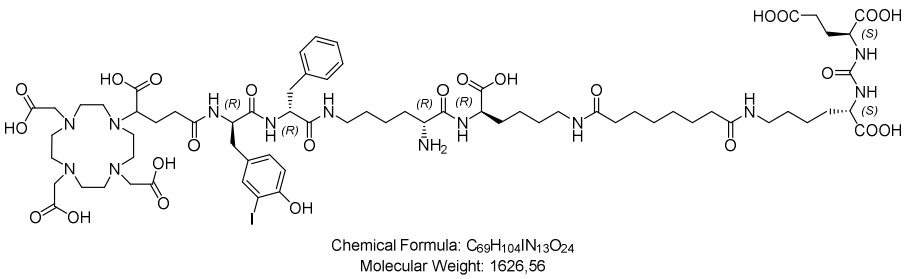

DOTAGA-y(3-I)kfk(Sub-KuE) (PSMA-11): The synthesis of **PSMA-11** was achieved using **39** (5.0 mg, 3.75 µmol, 1.0 eq.) and applying the same procedure as described for **PSMA-9**. The crude product was purified using RP-HPLC (10 to 40% B in 15 min): t_R = 11.63 min $K^{'}$ = 4.82. Calculated monoisotopic mass ($C_{69}H_{104}IN_{13}O_{24}$) = 1,625.64; found: m/z = 1,626.5 $[M+H]^+$, 814.4 $[M+2H]^{2+}$.

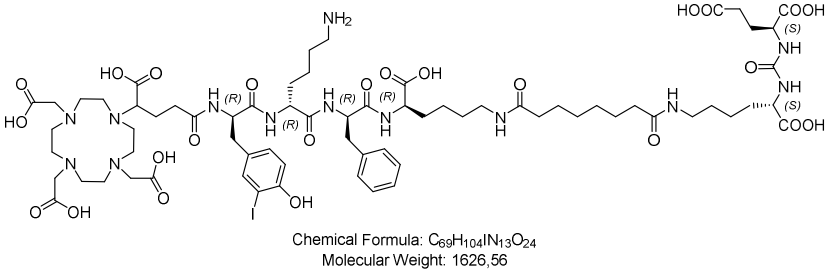

DOTAGA-y(3-I)-N^6-kfk(Sub-KuE) (PSMA-12): The synthesis of **PSMA-12** was achieved using **40** (5.0 mg, 3.75 µmol, 1.0 eq.) and applying the same procedure as described for **PSMA-9**. The crude product was purified using RP-HPLC (10 to 90% B in 15 min): t_R = 7.92 min $K^{'}$ = 2.96. Calculated monoisotopic mass ($C_{69}H_{104}IN_{13}O_{24}$) = 1,625.64; found: m/z = 1,626.6 $[M+H]^+$, 814.4 $[M+2H]^{2+}$.

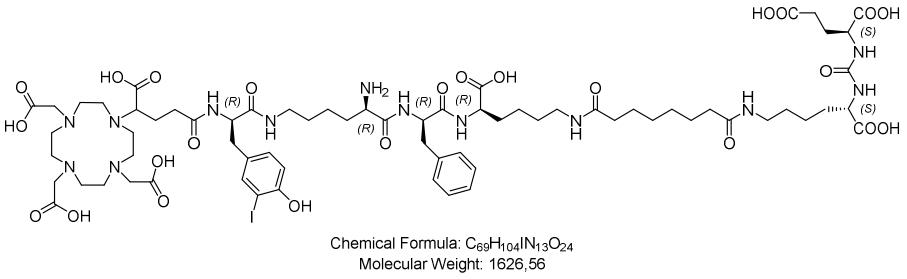

DOTAGA-ky(3-I)fk(Sub-KuE) (PSMA-13): The synthesis of **PSMA-13** was achieved using **41** (5.0 mg, 3.75 µmol, 1.0 eq.) and applying the same procedure as described for **PSMA-9**. The final crude product was purified using RP-HPLC (10 to 90% B in 15 min): t_R = 7.95 min K' = 2.97. Calculated monoisotopic mass ($C_{69}H_{104}IN_{13}O_{24}$) = 1,625.64; found: m/z = 1,626.5 $[M+H]^+$, 814.3 $[M+2H]^{2+}$.

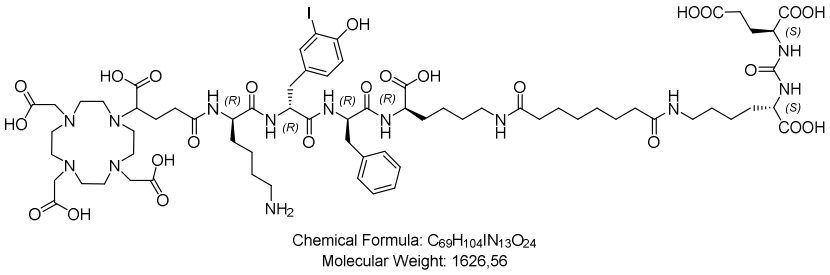

DOTAGA-N^6-ky(3-I)fk(Sub-KuE) (PSMA-14): The synthesis of **PSMA-13** was achieved using **42** (5.0 mg, 3.75 µmol, 1.0 eq.) and applying the same procedure as described for **PSMA-9**. The crude product was purified using RP-HPLC (10 to 90% B in 15 min): t_R = 7.85 min K' = 2.93. Calculated monoisotopic mass ($C_{69}H_{104}IN_{13}O_{24}$) = 1,625.64; found: m/z = 1,626.5 $[M+H]^+$, 814.4 $[M+2H]^{2+}$.

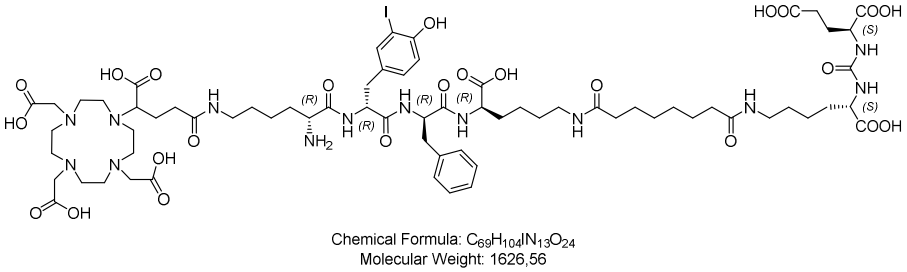

DOTAGA-F(4-NH$_2$)y(3-I)fk(Sub-KuE) (PSMA-15): The synthesis of **PSMA-15** was achieved using **43** (5.0 mg, 3.66 µmol, 1.0 eq.) and applying the same procedure as described for **PSMA-9**. The crude product was purified using RP-HPLC (10 to 60% B in 15 min): t_R = 7.9 min K' = 2.95. Calculated monoisotopic mass ($C_{72}H_{102}IN_{13}O_{24}$) = 1,659.62; found: m/z = 1,660.5 $[M+H]^+$, 831.3 $[M+2H]^{2+}$.

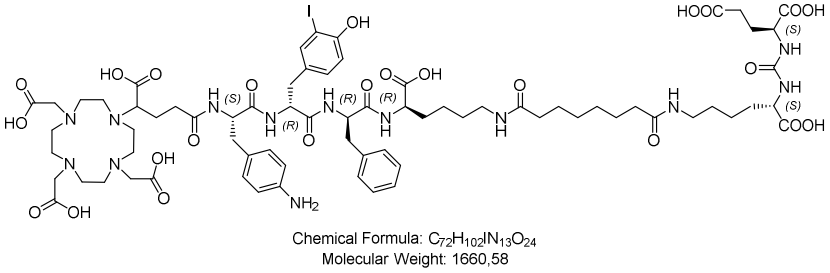

DOTAGA-f(4-NH$_2$)y(3-I)fk(Sub-KuE) (PSMA-16): The synthesis of **PSMA-16** was achieved using **44** (5.0 mg, 3.66 µmol, 1.0 eq.) and applying the same procedure as described for **PSMA-9**. The crude product was purified using RP-HPLC (10 to 60% B in 15 min): t_R = 8.4 min K' = 3.2. Calculated monoisotopic mass ($C_{72}H_{102}IN_{13}O_{24}$) = 1,659.62; found: m/z = 1,660.6 $[M+H]^+$, 831.1 $[M+2H]^{2+}$.

DOTAGA-f(4-NH₂)y(3-I)fK(Sub-KuE) (PSMA-17): The synthesis of **PSMA-17** was achieved using **45** (5.0 mg, 3.66 µmol, 1.0 eq.) and applying the same procedure as described for **PSMA-1**. The final crude product was purified using RP-HPLC (10 to 60% B in 15 min): t_R = 7.8 min K' = 2.9. Calculated monoisotopic mass ($C_{72}H_{102}IN_{13}O_{24}$) = 1,659.62; found: *m/z* = 1,660.0 $[M+H]^+$, 831.0 $[M+2H]^{2+}$.

DOTAGA-f(4-NH₂)y(3-I)FK(Sub-KuE) (PSMA-18): The synthesis of **PSMA-18** was achieved using **46** (5.0 mg, 3.66 µmol, 1.0 eq.) and applying the same procedure as described for **PSMA-1**. The final crude product was purified using RP-HPLC (10 to 60% B in 15 min): t_R = 8.3 min K' = 3.15. Calculated monoisotopic mass ($C_{72}H_{102}IN_{13}O_{24}$) = 1,659.62; found: *m/z* = 1,660.2 $[M+H]^+$, 831.2 $[M+2H]^{2+}$.

DOTAGA-F(4-NH₂)y(3-I)fK(Sub-KuE) (PSMA-19): The synthesis of **PSMA-19** was achieved using **46** (5.0 mg, 3.66 µmol, 1.0 eq.) and applying the same procedure as described for **PSMA-1**. The final crude product was purified using RP-HPLC (10 to 60% B in 15 min): t_R = 8.0 min K' = 3.0. Calculated monoisotopic mass ($C_{72}H_{102}IN_{13}O_{24}$) = 1,659.62; found: *m/z* = 1,660.0 $[M+H]^+$, 831.0 $[M+2H]^{2+}$.

2.3.3 Carbohydrated PSMA inhibitors

DOTAGA–y(3-I)fk(L-Asu[KuE]-MPA-Galactose) (PSMA-20): The synthesis of

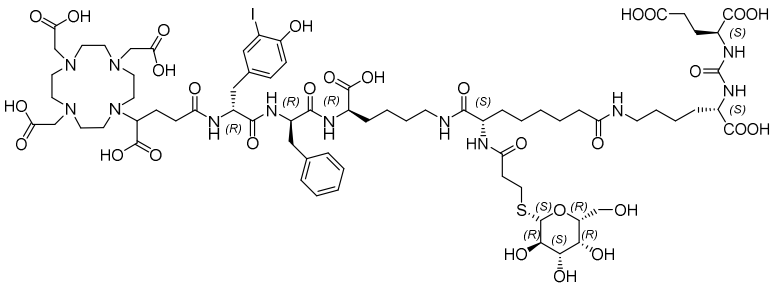

PSMA-20 was accomplished using **PSMA-8** (3.0 mg, 1.98 µmol, 1.0 eq.) and **22** (3.58 mg, 5.95 µmol, 3.0 eq.) dissolved in DMF. To this solution was added DIPEA (1.0 µL, 5.95 µmol, 3.0 eq.) and the solution was allowed to stir overnight at RT. After completion of reaction, the reaction mixture was reduced *in vacuo* to approx. 300 µL and precipitated in Et_2O, centrifuged and the supernatant removed. The dried pellet was treated with TFA according to **SP-6** for *t*Bu-removal. After precipitation in Et_2O, centrifugation and removal of the supernatant, the resulting pellet was deacetylated according to **SP-8**. The final product was purified using RP-HPLC (10 to 60% B in 15 min): t_R = 9.28 min K' = 3.64. Calculated monoisotopic mass ($C_{72}H_{107}IN_{12}O_{29}S$) = 1,762.60; found: *m/z* = 1,763.6 $[M+H]^+$.

DOTAGA-y(3-I)fk(L-Asu[KuE]-MPA-Mannose) (PSMA-21): The synthesis of **PSMA-21** was accomplished as already described for **PSMA-20** using **PSMA-8** (3.0 mg, 1.98 µmol, 1.0 eq.) and **23** (3.58 mg, 5.95 µmol, 3.0 eq.) dissolved in DMF. The final product was purified using RP-HPLC (10 to 60% B in 15 min): t_R = 7.98 min K' = 2.99. Calculated monoisotopic mass ($C_{72}H_{107}IN_{12}O_{29}S$) = 1,762.60; found: m/z = 1,764.1 $[M+H]^+$.

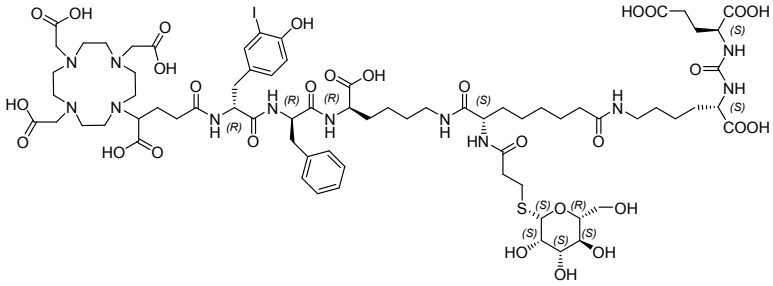

DOTAGA-y(3-I)fk(L-Asu[KuE]-MPA-Fucose) (PSMA-22): The synthesis of **PSMA-22** was accomplished as already described for **PSMA-20** using **PSMA-8** (3.0 mg, 1.97 µmol, 1.0 eq.) **24** (3.3 mg, 6.03 µmol, 3.1 eq.) dissolved in DMF. The final product was purified using RP-HPLC (10 to 60% B in 15 min): t_R = 8.17 min K' = 3.09. Calculated monoisotopic mass ($C_{72}H_{107}IN_{12}O_{28}S$) = 1,746.61; found: m/z = 1,764.1 $[M+H]^+$.

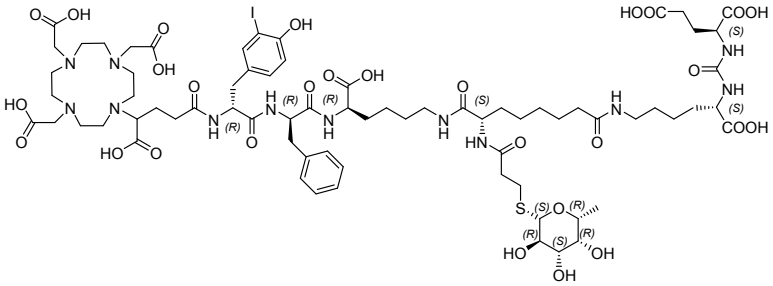

DOTAGA–y(3-I)fk(L-Asu[KuE]-MPA-Cellobiose) (PSMA-23): The synthesis of **PSMA-23** was accomplished as already described for **PSMA-20** using **PSMA-8** (3.0 mg, 1.98 µmol, 1.0 eq.) and **25** (2.7 mg, 3.0 µmol, 1.5 eq.) dissolved in DMF. The final product was purified using RP-HPLC (10 to 60% B in 15 min): t_R = 9.01 min K' = 3.51. Calculated monoisotopic mass ($C_{78}H_{117}IN_{12}O_{34}S$) = 1,924.66; found: m/z = 1,926.8 $[M+H]^+$.

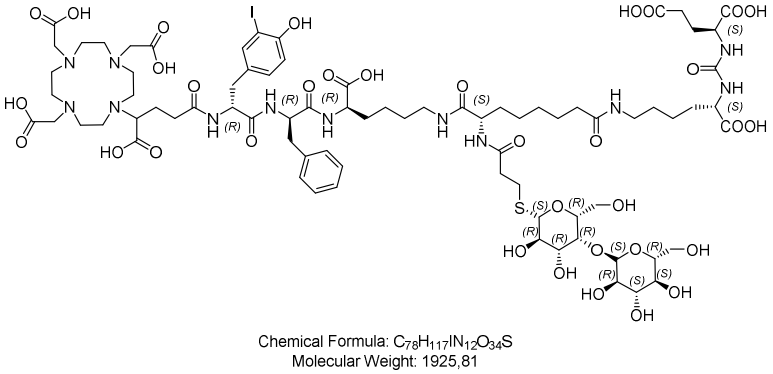

F-BA-AOAc-k(Agl[MPA-Galactose]-Glut-KuE) (PSMA-24): The synthesis of

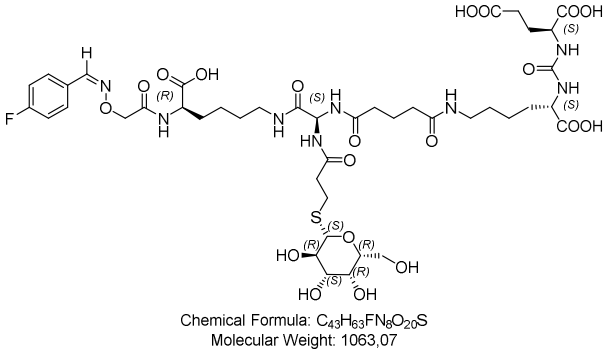

PSMA-24 was accomplished using **54** (5.0 mg, 15.36 µmol, 1.0 eq.) and **15** (24.5 mg, 23.1 µmol, 1.5 eq.) dissolved in DMF (800 µL). To this solution was given DIPEA (10.7 µL, 61.5 µmol, 4.0 eq.) and the solution was stirred overnight at RT. After completion of reaction, piperidine (200 µL) was given to this reaction mixture with further stirring for 15 min to cleave the Fmoc-protecting group. In the next step, the solvent was reduced *in vacuo* to approx. 300 µL and precipitated in Et_2O, centrifuged and the supernatant removed. The crude product was redissolved in DMF and **22** (37.0 mg, 61.5 µmol, 4.0 eq.) was added together with DIPEA (10.7 µL, 61.47 µmol, 4.0 eq.). The reaction mixture was allowed to stir for 24 h at RT. After completion of reaction, the solvent was reduced *in vacuo* to approx. 500 µL and the crude product was precipitated in Et_2O, centrifuged and the supernatant removed. With the dried pellet was proceeded according to **SP-6** and **SP-8**. The final product was purified using RP-HPLC (10 to 70% B in 15 min): t_R = 9.28 min $K^{\prime}$ = 3.64. Calculated monoisotopic mass ($C_{43}H_{63}FN_8O_{20}S$) = 1,062.39; found: m/z = 1,063.2 $[M+H]^+$.

F-BA-AOAc-fk(Agl[MPA-Galactose]-Glut-KuE) (PSMA-25): The synthesis of

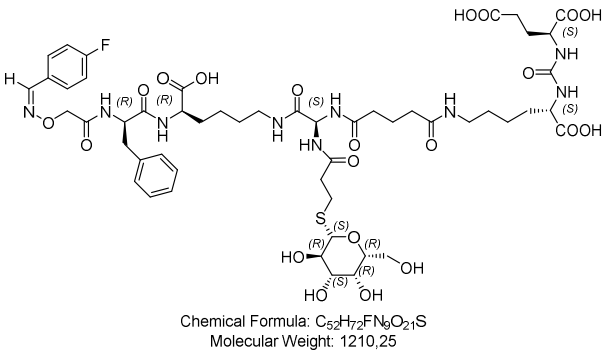

PSMA-25 was achieved as described for **PSMA-24** using **55** (5.0 mg, 10.6 µmol, 1.0 eq.), **15** (16.9 mg, 15.9 µmol, 1.5 eq.) and DIPEA (7.4 µL, 42.3 µmol, 4.0 eq.) dissolved in DMF. The final product was purified using RP-HPLC (10 to 70% B in 15 min): t_R = 9.28 min $K^{\prime}$ = 3.64. Calculated monoisotopic mass ($C_{52}H_{72}FN_9O_{21}S$) = 1,209.45; found: m/z = 1,210.2 $[M+H]^+$.

F-BA–AOAc–y(3-I)fk(Agl[MPA-Galactose]-Glut-KuE) (PSMA-26): The synthesis of

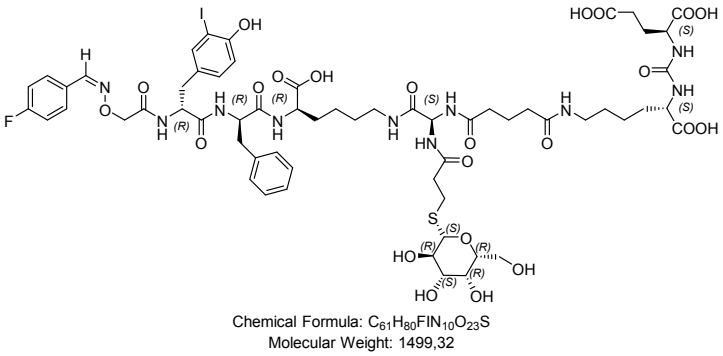

PSMA-26 was performed as described for **PSMA-24** using **56** (5.0 mg, 6.44 µmol, 1.0 eq.), **15** (10.3 mg, 9.7 µmol, 1.5 eq.) and DIPEA (4.5 µL, 25.8 µmol, 4.0 eq.) in DMF. The final product was purified using RP-HPLC (10 to 70% B in 15 min): t_R = 10.54 min $K^{\prime}$ =

4.27. Calculated monoisotopic mass ($C_{61}H_{80}FIN_{10}O_{23}S$) = 1,498.41; found: m/z = 1,499.9 $[M+H]^+$.

2.3.4 Combination of carbohydration and a free amino group

DOTAGA-f(4-NH₂)y(3-I)fk(L-Asu[KuE]-MPA-Galactose) (PSMA-27): The

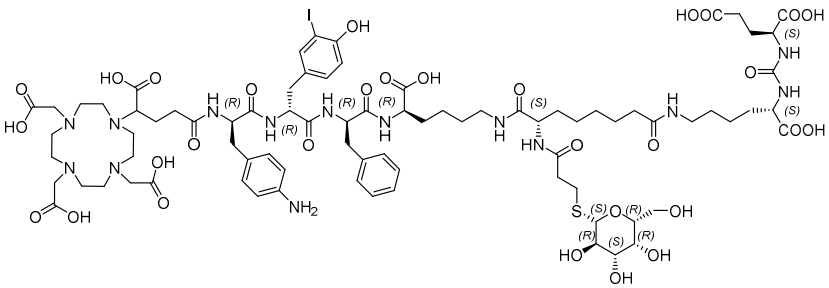

synthesis of **PSMA-27** was accomplished as described for **PSMA-20** using **44** (5.0 mg, 3.7 µmol, 1.0 eq.), **9** (5.8 mg, 5.5 µmol, 1.5 eq.) and DIPEA (2.6 µL, 14.6 µmol, 4.0 eq.) dissolved in DMF and the reaction mixture was allowed to stir for 16 h at RT. The Dde-deprotection of D-Phe(4-NHDde) was performed as described in **SP-4**. The final product was purified using RP-HPLC (10 to 90% B in 15 min): t_R = 11.51 min K' = 4.75. Calculated monoisotopic mass ($C_{81}H_{117}IN_{14}O_{30}S$) = 1,924.68; found: m/z = 1,926.1 $[M+H]^+$.

DOTAGA-f(4-NH₂)y(3-I)fk(Agl[MPA-Galactose]-Glut-KuE) (PSMA-28): The

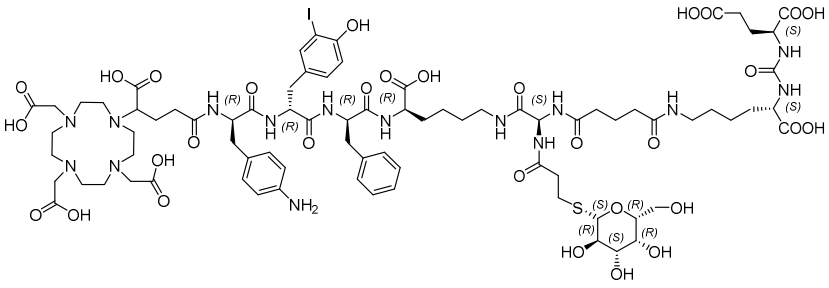

synthesis of **PSMA-28** was achieved in similarity to **PSMA-24** using **44** (5.0 mg, 3.7 µmol, 1.0 eq.), **15** (5.8 mg, 5.5 µmol, 1.5 eq.) and DIPEA (2.6 µL, 14.6 µmol, 4.0 eq.) dissolved in DMF and the reaction mixture was allowed to stir overnight at RT. The Dde-deprotection of D-Phe(4-NHDde) was performed as described in **SP-4**. The final product was purified using RP-HPLC (10 to 90% B in 15 min): t_R = 8.37 min K' = 3.19. Calculated monoisotopic mass ($C_{80}H_{114}IN_{15}O_{31}S$) = 1,939.66; found: m/z = 1,941.7 $[M+H]^+$.

DOTAGA-f(4-NH-MPA-Galactose)y(3-I)fk(Agl[MPA-Galactose]-Glut-KuE) (PSMA-29): The synthesis of **PSMA-29** was achieved in similarity to **PSMA-28** using **44** (5.0 mg, 3.7 µmol, 1.0 eq.), **15** (5.8 mg, 5.5 µmol, 1.5 eq.) and DIPEA (2.6 µL, 14.6 µmol, 4.0 eq.) dissolved in DMF (960 µL).

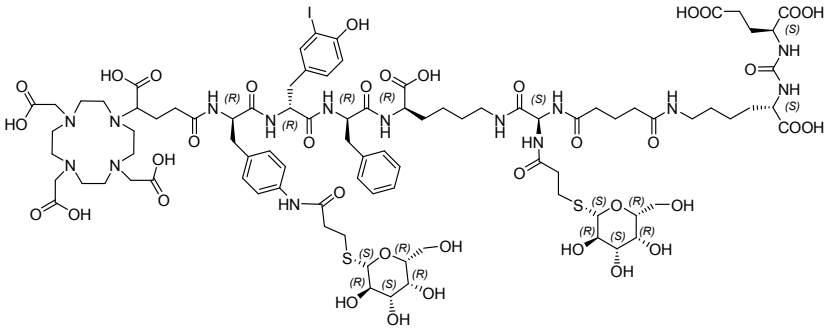

The reaction mixture was allowed to stir overnight at RT. After completion of reaction, $N_2H_4 \cdot H_2O$ (40 µL) was given to the reaction mixture to achieve Fmoc- and Dde-deprotection. In the next step, the solvent was reduced *in vacuo* to approx. 500 µL and precipitated in Et_2O, centrifuged and the supernatant removed. The dried pellet was dissolved in DMF with **22** (22.1 mg, 36.6 µmol, 10 eq.) and DIPEA (6.4 µL, 36.6 µmol, 10 eq.) was added. The reaction mixture was allowed to stir for 48 h at 40°C. After completion of reaction, the reaction mixture was stepwise treated according to **SP-8** and afterwards according to **SP-6**. The final product was purified using RP-HPLC (5 to 25% B in 15 min): t_R = 16.44 min K' = 7.22. Calculated monoisotopic mass ($C_{89}H_{128}IN_{15}O_{37}S_2$) = 2,189.71; found: m/z = 1,096.9 $[M+2H]^{2+}$.

2.3.5 Peptide sequence modifications of EuK-based peptides

DOTAGA-y-2-nal-k(Sub-KuE) (PSMA-30): The synthesis of **PSMA-30** was accomplished as described for **PSMA-1** using **48** (5.0 mg, (5.2 µmol, 1.0 eq.), **4** (6.3 mg, 7.8 µmol, 1.5 eq.) and DIPEA (3.6 µL, 20.7 µmol, 4.0 eq.) dissolved in DMF. The final product was purified using RP-HPLC (25 to 55% B in 15 min): t_R = 12.5 min K' = 2.07. Calculated monoisotopic mass ($C_{67}H_{95}N_{11}O_{23}$) = 1,421.66; found: m/z = 1,422.8 $[M+H]^+$, 712.1 $[M+2H]^{2+}$.

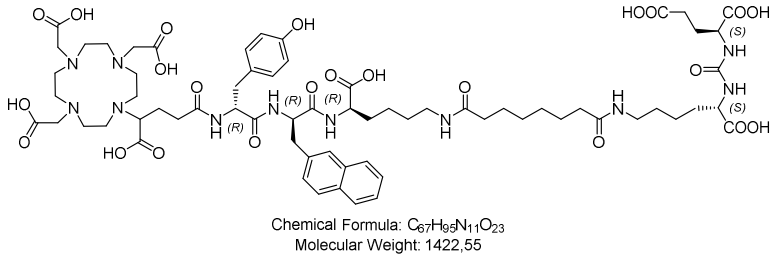

DOTAGA-F(4-NH₂)y-2-nal-k(Sub-KuE) (PSMA-31): The synthesis of **PSMA-31** was achieved as described for **PSMA-1** using **49** (5.0 mg, 3.9 µmol, 1.0 eq.) and **4** (4.7 mg, 5.8 µmol, 1.5 eq.) with DIPEA (2.7 µL, 15.6 µmol, 4.0 eq.) dissolved in DMF. The final product was purified using RP-HPLC (10 to 60% B in 15 min): t_R = 8.0 min K' = 3.0. Calculated monoisotopic mass ($C_{76}H_{105}N_{13}O_{24}$) = 1,583.74; found: m/z = 1,584.4 $[M+H]^+$, 793.1 $[M+2H]^{2+}$.

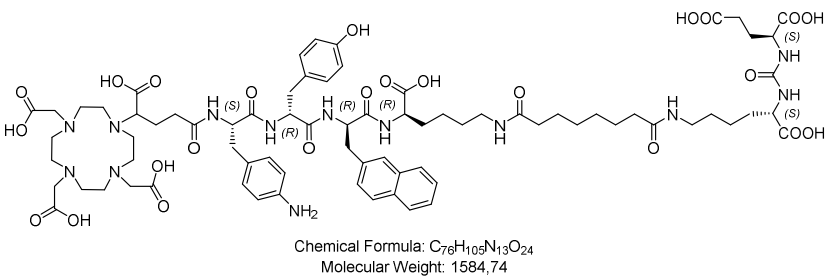

DOTAGA-f(4-NH₂)y-2-nal-k(Sub-KuE) (PSMA-32): The synthesis of **PSMA-32** was achieved as described for **PSMA-31** using **50** (5.0 mg, 3.9 µmol, 1.0 eq.), **4** (4.7 mg, 5.8 µmol, 1.5 eq.) and DIPEA (2.7 µL, 15.6 µmol, 4.0 eq.) dissolved in DMF. The final product was purified using RP-HPLC (10 to 60% B in 15 min): t_R = 8.7 min K' = 3.4. Calculated monoisotopic mass ($C_{76}H_{105}N_{13}O_{24}$) = 1,583.74; found: m/z = 1,584.4 $[M+H]^+$, 793.2 $[M+2H]^{2+}$.

DOTAGA-f(4-NH₂)y-2-nal-K(Sub-KuE) (PSMA-33): The synthesis of **PSMA-33** was achieved as described for **PSMA-31** using **51** (5.0 mg, 3.9 µmol, 1.0 eq.), **4** (4.7 mg, 5.8 µmol, 1.5 eq.) and DIPEA (2.7 µL, 15.6 µmol, 4.0 eq.) dissolved in DMF. The final product was purified using RP-HPLC (10 to 60% B in 15 min): t_R = 8.1 min K' = 3.1. Calculated monoisotopic mass ($C_{76}H_{105}N_{13}O_{24}$) = 1,583.74; found: m/z = 1,584.7 $[M+H]^+$, 793.1 $[M+2H]^{2+}$.

DOTAGA-F(4-NH₂)y-2-nal-K(Sub-KuE) (PSMA-34): The synthesis of **PSMA-34** was achieved as described for **PSMA-31** using **52** (5.0 mg, 3.9 µmol, 1.0 eq.), **4** (4.73 mg, 5.8 µmol, 1.5 eq.) and DIPEA (2.7 µL, 15.6 µmol, 4.0 eq.) dissolved in DMF. The final product was purified using RP-HPLC (10 to 60% B in 15 min): t_R = 8.2 min K' = 3.1. Calculated monoisotopic mass ($C_{76}H_{105}N_{13}O_{24}$) = 1,583.74; found: m/z = 1,585.4 $[M+H]^+$, 793.2 $[M+2H]^{2+}$.

2.3.6 Linker modification of EuK-based peptides

DOTAGA–y(3-I)fk(L-Asu[KuE]-BA) (PSMA-35): The synthesis of **PSMA-35** was achieved by dissolving **PSMA-8** (3.0 mg, 3.3 µmol, 1.0 eq.) in DMF and addition of **26** (3.8 mg, 13.2 µmol, 4.0 eq.) and DIPEA (2.3 µL, 13.2 µmol, 4.0 eq.). The solution was stirred for 18 h at RT and the final product purified by RP-HPLC (10 to 90% B in 15 min): t_R = 8.49 min K' = 3.25. Calculated monoisotopic mass ($C_{70}H_{97}IN_{12}O_{24}$) = 1,616.58; found: m/z = 1,619.2 $[M+H]^+$, 809.7 $[M+2H]^{2+}$.

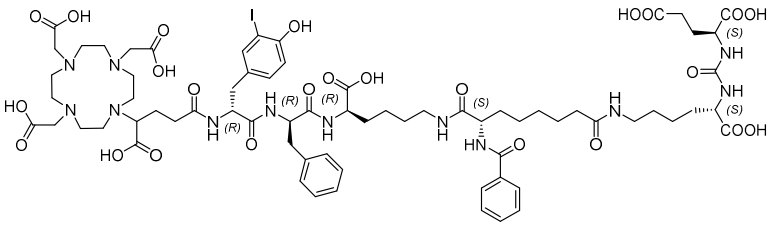
Chemical Formula: $C_{70}H_{97}IN_{12}O_{24}$
Molecular Weight: 1617,51

DOTAGA–y(3-I)fk(L-Asu[KuE]-2,4-DNBA) (PSMA-36): The synthesis of **PSMA-36** was achieved by dissolving **PSMA-8** (3.0 mg, 3.3 µmol, 1.0 eq.) in DMF and addition of **27** (4.1 mg, 13.2 µmol, 4.0 eq.) and DIPEA (2.3 µL, 13.2 µmol, 4.0 eq.). The solution was stirred for 10 h at RT and the final product purified by RP-HPLC (10 to 50% B in 15 min): t_R = 12.12 min K' = 5.06. Calculated monoisotopic mass ($C_{70}H_{95}IN_{14}O_{28}$) = 1,706.55; found: m/z = 1,707.8 $[M+H]^+$, 854.7 $[M+2H]^{2+}$.

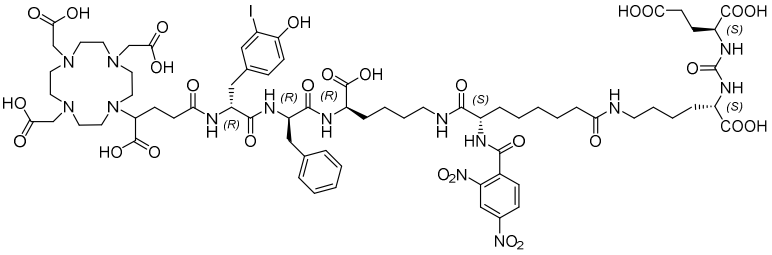
Chemical Formula: $C_{70}H_{95}IN_{14}O_{28}$
Molecular Weight: 1707,50

DOTAGA-y(3-I)fk(L-Asu[KuE]-DMBA) (PSMA-37): The synthesis of **PSMA-37** was performed using **PSMA-8** (3.0 mg, 3.3 µmol, 1.0 eq.), **29** (5.8 mg, 13.2 µmol, 4.0 eq.) and DIPEA (2.3 µL, 13.2 µmol, 4.0 eq.) dissolved in DMF. The solution was stirred for 24 h at 40°C and the final product purified by RP-HPLC (10 to 90% B in 15 min): t_R = 9.44 min K' = 3.72. Calculated monoisotopic mass ($C_{80}H_{108}IN_{13}O_{27}$) = 1,809.65; found: m/z = 1,812.2 $[M+H]^+$, 917.7 $[M+H+Na]^{2+}$, 1,664.3 [M - 3,5-dimethylbenzoic acid]$^+$, 1,514.2 [M-P-DMBA]$^+$.

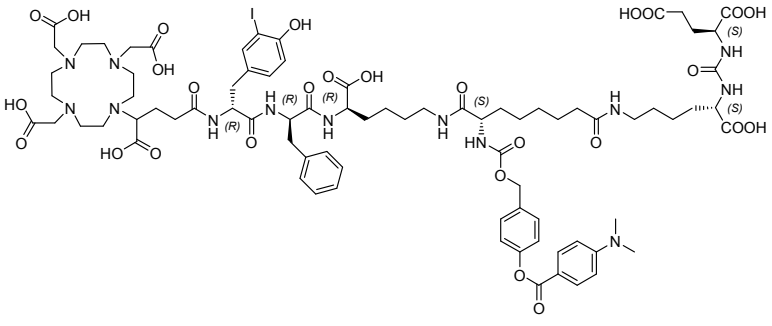
Chemical Formula: $C_{80}H_{108}IN_{13}O_{27}$
Molecular Weight: 1810,71

DOTAGA-f(4-NH₂)y(3-I)fk(Agl[PBP]-Glut-KuE) (PSMA-38): The synthesis of

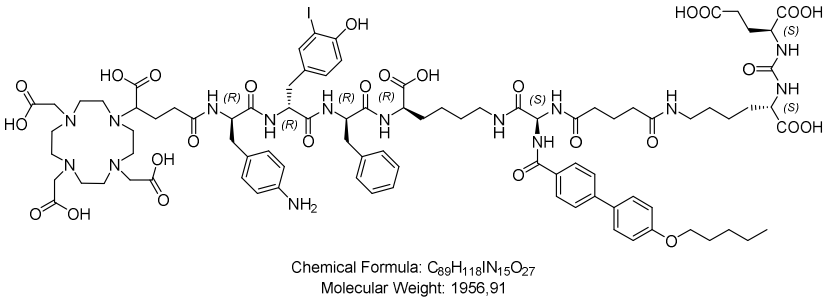

PSMA-38 was performed by dissolving **44** (5.0 mg, 3.7 µmol, 1.0 eq.), **9** (5.7 mg, 5.5 µmol, 1.5 eq.) and DIPEA (2.5 µL, 14.6 µmol, 4.0 eq.) in DMF (800 µL). The solution was stirred for 24 h at RT. After completion of reaction, piperidine (200 µL) was added and the solution further stirred for 15 min. In the next step, the reaction mixture was precipitated in Et_2O, centrifuged and the supernatant removed. The dried pellet was dissolved in DMF (960 µL) and **19** (6.6 mg, 14.6 µmol, 4.0 eq.) was added together with DIPEA (5.0 µL, 29.3 µmol, 8.0 eq.). The solution was stirred for 48 h at RT. The final Dde- and *t*Bu-deprotection was achieved according to **SP-4** and **SP-6**. The final product was purified by RP-HPLC (10 to 90% B in 15 min): t_R = 9.00 min K' = 3.5. Calculated monoisotopic mass ($C_{89}H_{118}IN_{15}O_{27}$) = 1,955.74; found: m/z = 1,956.9 $[M+H]^+$, 979.0 $[M+2H]^{2+}$.

DOTAGA-f(4-NH₂)y(3-I)fk(Agl[*C⁴*-e-PBP]-Glut-KuE) (PSMA-39): The synthesis of

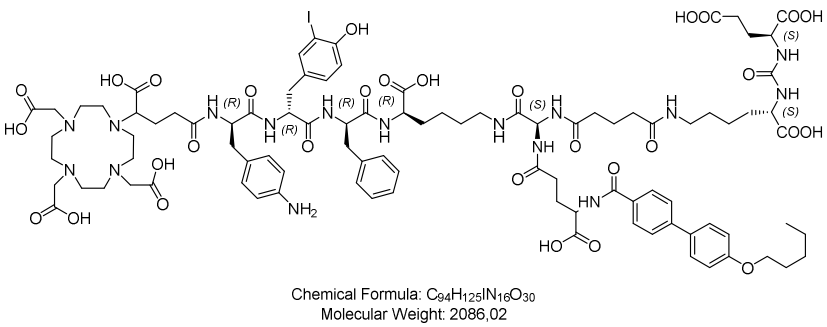

PSMA-39 was performed as described for **PSMA-38** using **20** (9.3 mg, 14.6 µmol, 4.0 eq.) for the last coupling step instead of **19**. The final product was purified by RP-HPLC (10 to 90% B in 15 min): t_R = 8.9 min K' = 3.5. Calculated monoisotopic mass ($C_{94}H_{125}IN_{16}O_{30}$) = 2,084.78; found: m/z = 1,043.5 $[M+2H]^{2+}$.

DOTAGA-f(4-NH₂)y(3-I)fk(Glut-f[4-I]-KuE) (PSMA-40): The synthesis of **PSMA-40** was performed as described for **PSMA-16** using **44** (5.0 mg, 3.7 µmol, 1.0 eq.), **12** (7.6 mg, 7.3 µmol, 2.0 eq.) and DIPEA (2.5 µL, 14.6 µmol, 4.0 eq.) dissolved in DMF (800 µL). The final product was purified by RP-HPLC (10 to 90% B in 15 min): t_R = 8.9 min K' = 3.5. Calculated monoisotopic mass ($C_{78}H_{104}I_2N_{14}O_{25}$) = 1,890.54; found: m/z = 1,891.4 $[M+H]^+$, 946.7 $[M+2H]^{2+}$.

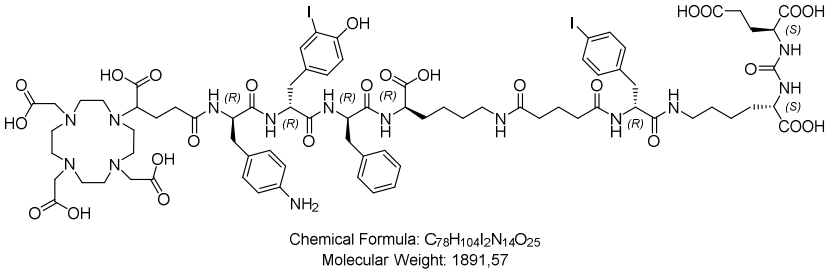

DOTAGA-f(4-NH₂)y-2-nal-k(Glut-f[4-I]-KuE) (PSMA-41): The synthesis of **PSMA-41** was achieved as described for **PSMA-15** using **50** (5.0 mg, 3.9 µmol, 1.0 eq.), **12** (8.1 mg, 7.8 µmol, 2.0 eq.) and DIPEA (2.7 µL, 15.6 µmol, 4.0 eq.) in DMF. The final product was purified by RP-HPLC (10 to 60% B in 15 min): t_R = 10.3 min K' = 4.2. Calculated monoisotopic mass ($C_{82}H_{107}IN_{14}O_{25}$) = 1,814.66; found: m/z = 1,815.6 $[M+H]^+$, 908.4 $[M+2H]^{2+}$.

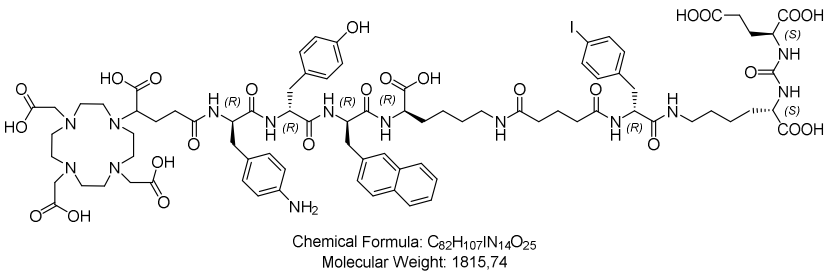

DOTAGA-f(4-NH₂)y-2-nal-K(Glut-f[4-I]-KuE) (PSMA-42): The synthesis of **PSMA-42** was achieved as described for **PSMA-41** using **51** (5.0 mg, 3.9 µmol, 1.0 eq.), **12** (8.1 mg, 7.8 µmol, 2.0 eq.) and DIPEA (2.7 µL, 15.6 µmol, 4.0 eq.) in DMF. The final product was purified by RP-HPLC (10 to 60% B in 15 min): t_R = 9.7 min K' = 3.9. Calculated monoisotopic mass ($C_{82}H_{107}IN_{14}O_{25}$) = 1,814.66; found: m/z = 1,815.1 $[M+H]^+$, 908.3 $[M+2H]^{2+}$.

DOTAGA-y-2-nal-K(Glut-f[4-I]-KuE) (PSMA-43): The synthesis of **PSMA-43** was accomplished as described for **PSMA-15** using **48** (4.0 mg, 4.1 µmol, 1.0 eq.), **12** (8.6 mg, 8.3 µmol, 2.0 eq.) and DIPEA (2.9 µL, 16.6 µmol, 4.0 eq.) in DMF. The final product was purified by RP-HPLC (10 to 60% B in 15 min): t_R = 10.79 min K' = 4.40. Calculated monoisotopic mass ($C_{73}H_{97}IN_{12}O_{24}$) = 1,652.58; found: m/z = 1,653.7 $[M+H]^+$, 827.4 $[M+2H]^{2+}$.

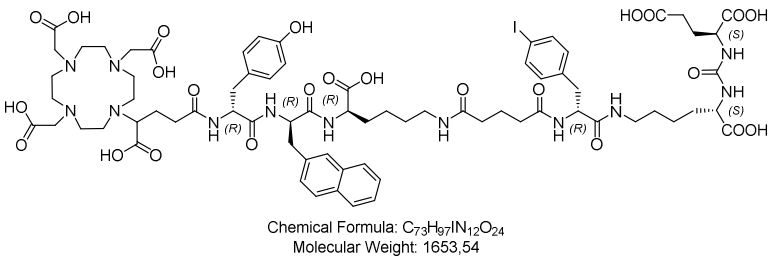

2.3.7 Exchange of DOTAGA to DOTA

DOTA-f(4-NH₂)-y-2-nal-k(Sub-KuE) (PSMA-44): The synthesis of **PSMA-44** was achieved as described for **PSMA-1** using **53** (5.0 mg, 4.1 µmol, 1.0 eq.), **4** (5.0 mg, 6.2 µmol, 1.5 eq.) and DIPEA (2.8 µL, 16.1 µmol, 4.0 eq.) dissolved in DMF. The final product was purified using RP-HPLC (10 to 60% B in 15 min): t_R = 8.0 min K' = 3.0. Calculated monoisotopic mass ($C_{73}H_{101}N_{13}O_{22}$) = 1,511.72; found: m/z = 1,512.9 $[M+H]^+$, 757.1 $[M+2H]^{2+}$.

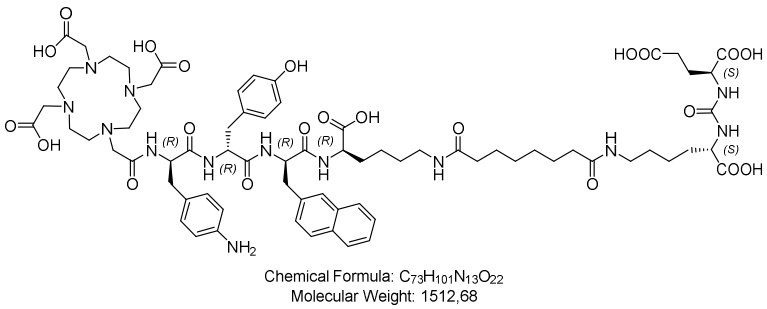

2.3.8 Synthesis of the precursor for radio-iodination

(SnBu$_3$-BA)(O*t*Bu)KuE(O*t*Bu)$_2$ (PSMA-45): The synthesis of **PSMA-45** was achieved as described previously [234,239-241]. Briefly, **57** (19.0 mg, 39.0 µmol, 1.0 eq.), **1** (19.8 mg, 0.39 mmol, 1.0 eq.) and TEA (26.3 µL, 0.19 mmol, 4.8 eq.) were dissolved in DCM. The reaction mixture was stirred for 4 h at RT. Afterwards, the reaction solution was diluted with DCM and washed with water. The combined organic phases were dried over Na_2SO_4, filtered and evaporated *in vacuo* to obtain the final product as a colorless oil. RP-HPLC (10 to 90% B in 15 min): t_R = 23.8 min; K' = 13.9. Calculated monoisotopic mass ($C_{43}H_{75}N_3O_8Sn$): 880.8/881.8/882.8; found: m/z = 902.2/903.3/904.3 $[M+Na]^+$.

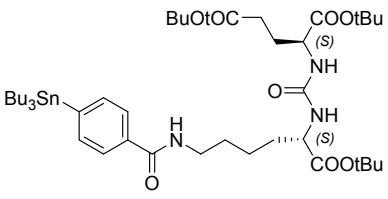

Chemical Formula: $C_{43}H_{75}N_3O_8Sn$
Molecular Weight: 880,80

2.4 Synthesis of EuE-based PSMA inhibitors

2.4.1 Peptide sequence modifications of EuE-based peptides

The general synthesis for the EuE-based PSMA inhibitors **PSMA-46** to **PSMA-57** was accomplished using a combined standard solid-phase Fmoc-strategy according to **SP-1** to **SP-7.1** with concomitant conjugation to the chelator DOTAGA-anhydride in either solution-phase or on solid phase. The initial resin loading with Fmoc-D-Orn(NHDde)-OH was performed as described in **SP-1**. After Fmoc-deprotection according to **SP-3**, **2** (1.5 eq.) was coupled to D-Orn(NHDde) according to **SP-2**. In the next step, the Dde-protecting group was cleaved according to **SP-4** and the free amino group treated with succinic anhydride (7.5 eq.) and DIPEA (7.5 eq.) dissolved in DMF. The reaction mixture was allowed to react overnight at RT. Next, Fmoc-D-Lys-OAll·HCl (1.5 eq.) was coupled according to **SP-2** and Fmoc-deprotected as described in **SP-3**. The following conjugations with the Fmoc-protected amino acids were conducted as described in **SP-2**. Before the peptides were cleaved from the resin according to **SP-7.1**, Alloc/Allyl-deprotection was achieved according to **SP-5**. The *N*-terminal Fmoc-deprotected and from the resin cleaved peptides were conjugated to the chelator using DOTAGA-anhydride (2.0 eq.) and DIPEA (9.0 eq.) over 24 h at RT in 500 µL DMF or directly conjugated to DOTAGA-anhydride on solid-phase without prior cleavage from the resin. After completion of reaction with DOTAGA-anhydride in solution phase, the reaction mixture was precipitated in Et_2O, centrifuged and the supernatant removed. To remove the *t*Bu/*t*Boc-protecting groups, the dried pellet was treated as described in **SP-6**. If the conjugation was achieved on solid phase, the PSMA inhibitor was directly cleaved from the resin according to **SP-7.2**. The final products were purified via RP-HPLC.

DOTAGA-y-2-nal-k(Suc-N^5-orn-C^4-EuE) (PSMA-46): RP-HPLC (10 to 60% B in 15 min): t_R = 7.8/8.2 min K' = 2.9/3.1. Calculated monoisotopic mass ($C_{67}H_{92}N_{12}O_{26}$) = 1,480.62; found: m/z = 1,481.7 $[M+H]^+$, 741.2 $[M+2H]^{2+}$.

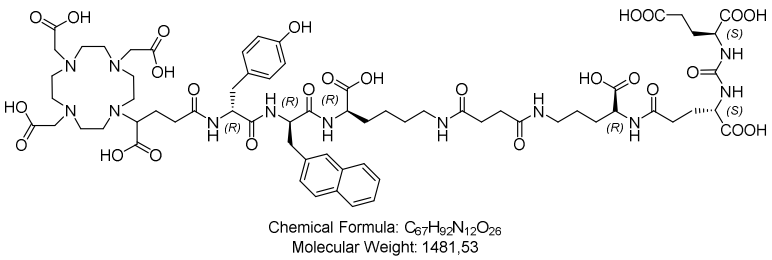

DOTAGA-F(4-NH_2)y(3-I)fk(Suc-N^5-orn-C^4-EuE) (PSMA-47): RP-HPLC (10 to 60% B in 15 min): t_R = 7.5 min K' = 2.75. Calculated monoisotopic mass ($C_{72}H_{99}IN_{14}O_{27}$) = 1,718.58; found: m/z = 1,719.8 $[M+H]^+$, 860.5 $[M+2H]^{2+}$.

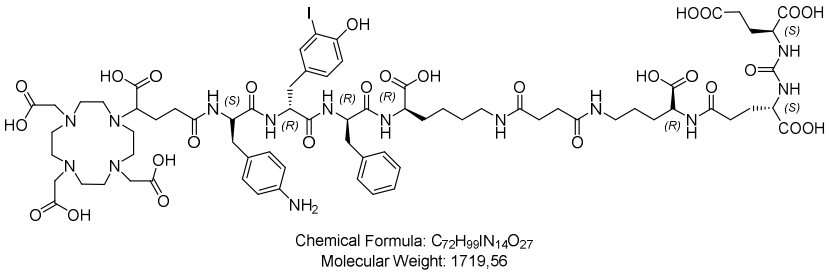

DOTAGA-f(4-NH_2)y(3-I)fk(Suc-N^5-orn-C^4-EuE) (PSMA-48): RP-HPLC (10 to 60% B in 15 min): t_R = 6.7 min K' = 2.35. Calculated monoisotopic mass ($C_{72}H_{99}IN_{14}O_{27}$) = 1,718.58; found: m/z = 1,719.9 $[M+H]^+$, 860.4 $[M+2H]^{2+}$.

DOTAGA-F(4-NH_2)y-2-nal-k(Suc-N^5-orn-C^4-EuE) (PSMA-49): RP-HPLC (10 to 60% B in 15 min): t_R = 7.2 min K' = 2.6. Calculated monoisotopic mass ($C_{76}H_{102}N_{14}O_{27}$) = 1,642.70; found: m/z = 1,643.6 $[M+H]^+$, 822.5 $[M+2H]^{2+}$.

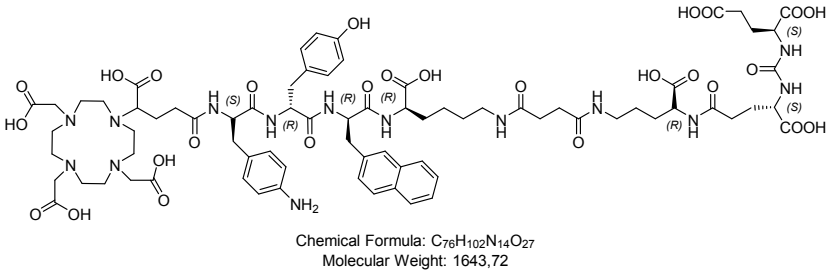

DOTAGA-f(4-NH_2)-y-2-nal-k(Suc-N^5-orn-C^4-EuE) (PSMA-50): RP-HPLC (10 to 60% B in 15 min): t_R = 7.1 min K' = 2.55. Calculated monoisotopic mass ($C_{76}H_{102}N_{14}O_{27}$) = 1,642.70; found: m/z = 1,642.8 $[M+H]^+$, 822.8 $[M+2H]^{2+}$.

DOTAGA-f(4-NH_2)-y-2-nal-K(Suc-N^5-orn-C^4-EuE) (PSMA-51): RP-HPLC (10 to 60% B in 15 min): t_R = 7.1 min K' = 2.55. Calculated monoisotopic mass ($C_{76}H_{102}N_{14}O_{27}$) = 1,642.70; found: m/z = 1,643.3 $[M+H]^+$, 822.3 $[M+2H]^{2+}$.

DOTAGA-F(4-NO$_2$)-y-2-nal-k(Suc-*N*^{5}-orn-*C*^{4}-EuE) (PSMA-52): RP-HPLC (10 to 60% B in 15 min): t_R = 9.71 min K' = 3.86. Calculated monoisotopic mass ($C_{76}H_{100}N_{14}O_{29}$) = 1,672.68; found: m/z = 1,673.0 $[M+H]^+$.

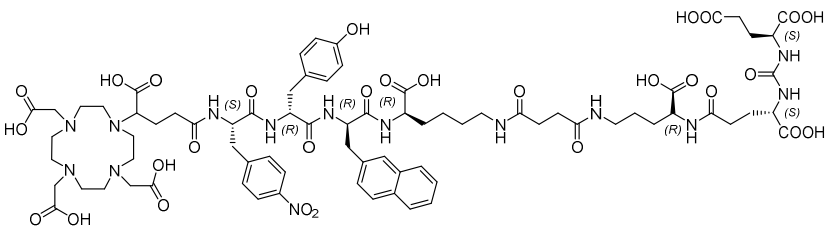

2,4-DNBA-Dap(DOTAGA)-y-2-nal-k(Suc-*N*^{5}-orn-*C*^{4}-EuE) (PSMA-53): The synthesis of **PSMA-53** was achieved as described in chapter **II 2.4.1** with minor modifications. After coupling of Fmoc-L-Dap(NHDde), Dde-deprotection was achieved as described in **SP-4**. Next, the free amino group was conjugated to 2,4-dintrobenzoic acid (2,4-DNBA) using 2,4-DNBA (2.0 eq.), HOBt (2.0 eq.), TBTU (2.0 eq.) and DIPEA (4.0 eq.) in DMF. After completion of reaction, Fmoc-deprotection was achieved using **SP-3**, the peptide cleaved from the resin utilizing **SP-7.1** and further proceeded as described in chapter **II 2.4.1**. RP-HPLC (10 to 60% B in 15 min): t_R = 11.71 min K' = 4.86. Calculated monoisotopic mass ($C_{77}H_{100}N_{16}O_{32}$) = 1,760.67; found: m/z = 1,762.1 $[M+H]^+$.

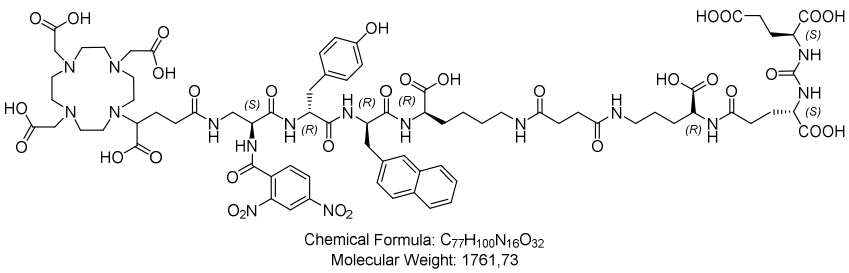

DOTAGA-Yy-2-nal-k(Suc-*N*^{5}-orn-*C*^{4}-EuE) (PSMA-54): RP-HPLC (10 to 60% B in 15 min): t_R = 8.71 min K' = 3.36. Calculated monoisotopic mass ($C_{76}H_{101}N_{13}O_{28}$) = 1,643.69; found: m/z = 1,644.8 $[M+H]^+$.

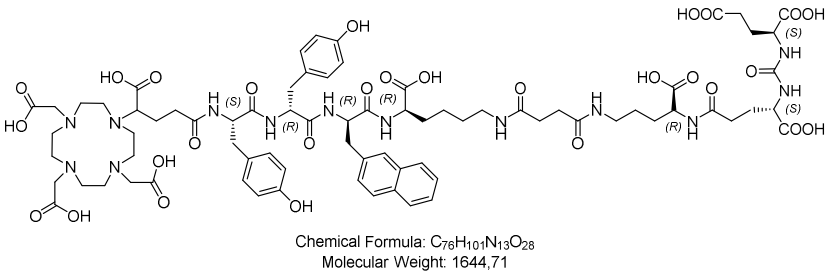

DOTAGA-2-Nal-y-2-nal-k(Suc-*N*^{5}-orn-*C*^{4}-EuE) (PSMA-55): RP-HPLC (10 to 60% B in 15 min): t_R = 10.5 min K' = 4.25. Calculated monoisotopic mass ($C_{80}H_{103}N_{13}O_{27}$) = 1,677.71; found: m/z = 1,679.0 $[M+H]^+$.

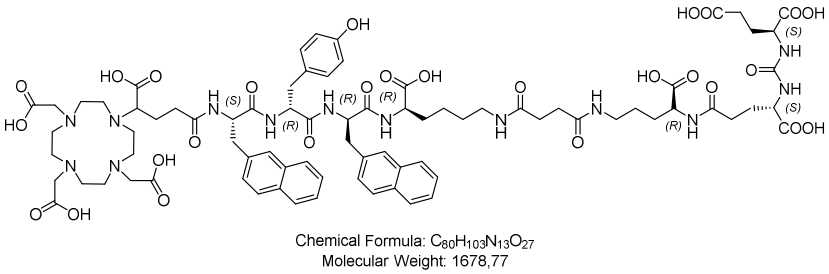

DOTAGA-K(PBP)y-2-nal-k(Suc-*N*^{5}-orn-*C*^{4}-EuE) (PSMA-56): The synthesis of

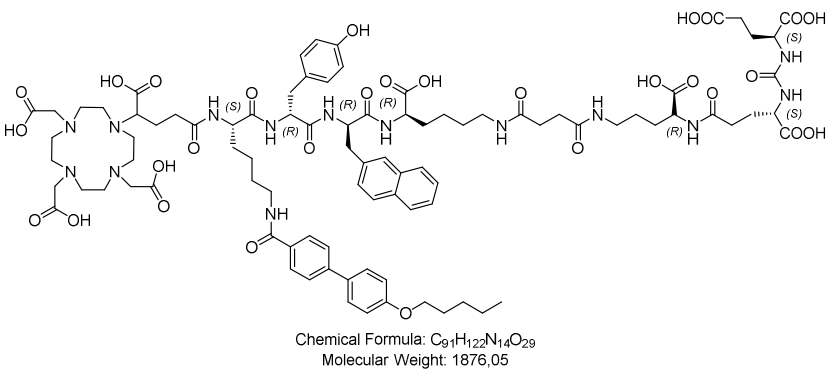

PSMA-56 was achieved as described in chapter **II 2.4.1** with minor modifications. After coupling of Fmoc-L-Lys(NHDde), the free amino group was conjugated to **19** (2.0 eq.) using DIPEA (4.0 eq.) in DMF solution. After completion of reaction, Fmoc-deprotection was achieved applying **SP-3**, the peptide was cleaved from the resin utilizing **SP-7.1** and further proceeded as described in chapter **II 2.4.1**. RP-HPLC (10 to 70% B in 15 min): t_R = 13.0 min K' = 5.5. Calculated monoisotopic mass ($C_{91}H_{122}N_{14}O_{29}$) = 1,874.85; found: m/z = 1,876.3 $[M+H]^+$.

DOTAGA-K(*C*^{4}-e-PBP)y-2-nal-k(Suc-*N*^{5}-orn-*C*^{4}-EuE) (PSMA-57): The synthesis of

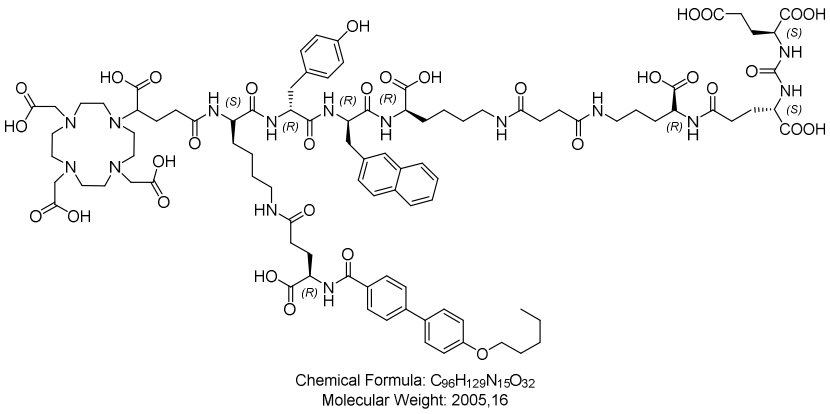

PSMA-57 was achieved as described in chapter **II 2.4.1** with minor modifications. After coupling of Fmoc-L-Lys(NHDde), the free amino group was conjugated to **20** (2.0 eq.) using DIPEA (4.0 eq.) in DMF solution. After completion of reaction, Fmoc-deprotection was achieved using **SP-3** and the peptide cleaved from the resin utilizing **SP-7.1** and further proceeded as described in chapter **II 2.4.1**. RP-HPLC (10 to 60% B in 15 min): t_R = 14.1 min K' = 6.05. Calculated monoisotopic mass ($C_{96}H_{129}N_{15}O_{32}$) = 2,003.89; found: m/z = 1,003.30 $[M+2H]^{2+}$.

2.4.2 Linker modifications of EuE-based peptides

The synthesis of the PSMA inhibitors **PSMA-58** to **PSMA-61** were achieved in a similar manner as described in chapter **II 2.4.1**. The initial resin loading with Fmoc-D-Orn(NHDde)-OH was the starting point and performed as described in **SP-1**. After Fmoc-deprotection according to **SP-3**, **2** (1.5 eq.) was coupled to D-Orn(NHDde) according to **SP-2**. In the next step, the Dde-protecting group was cleaved according to **SP-4** and the free amino group was conjugated with either Fmoc-Gly-OH (1.5 eq.) for **PSMA-58** and **PSMA-59**, Fmoc-Abz-OH (1.5 eq.) for **PSMA-60** or Fmoc-D-Asp(OAll)-OH (1.5 eq.) for **PSMA-61** and **PSMA-62** using HOBt (2.0 eq.), TBTU (2.0 eq.) and DIPEA (4.0 eq.) in DMF. After

completion of reaction, Fmoc-deprotection was accomplished as described in **SP-3**. All further reaction steps are described for each PSMA inhibitor separately in the following sections.

DOTAGA-F(4-NH₂)y-2-nal-e(r-G-*N*⁵-orn-*C*⁴-EuE) (PSMA-58): After Fmoc-deprotection of glycine, the resin bound peptide was further conjugated with Fmoc-D-Arg(Pbf)-OH (1.5 eq.) and Fmoc-D-Glu(OAll)-OH (1.5 eq.) according to **SP-2**. All further reactions steps were performed as described in chapter **II 2.4.1**. RP-HPLC (10 to 70% B in 15 min): t_R = 7.5 min K' = 2.75. Calculated monoisotopic mass ($C_{79}H_{108}N_{18}O_{28}$) = 1,756.76; found: m/z = 1,758.5 $[M+H]^+$.

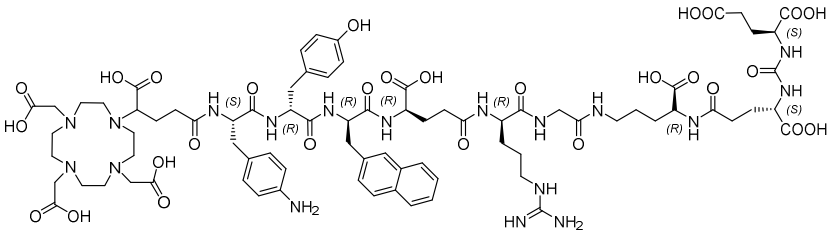

DOTAGA-F(4-NH₂)y-2-nal-e(e-G-*N*⁵-orn-*C*⁴-EuE) (PSMA-59): After Fmoc-deprotection of glycine, the resin bound peptide was further conjugated with Fmoc-D-Glu(O*t*Bu)-OH (1.5 eq.) and Fmoc-D-Glu(OAll)-OH (1.5 eq.) according to **SP-2**. All further reactions steps were performed as described in chapter **II 2.4.1**. RP-HPLC (10 to 70% B in 15 min): t_R = 7.5 min K' = 2.75. Calculated monoisotopic mass ($C_{78}H_{103}N_{15}O_{30}$) = 1,729.70; found: m/z = 1,730.6 $[M+H]^+$.

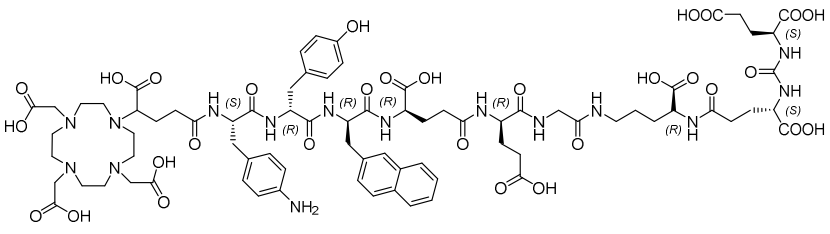

DOTAGA-F(4-NH₂)y-2-nal-e(Abz-*N*⁵-orn-*C*⁴-EuE) (PSMA-60): After Fmoc-deprotection of 4-aminobenzoic acid, the resin bound peptide was further conjugated with Fmoc-D-Glu(OAll)-OH (1.5 eq.) according to **SP-2**. All further reactions steps were performed as described in chapter **II 2.4.1**. RP-HPLC (10 to 60% B in 15 min): t_R = 8.6 min K' = 3.3. Calculated monoisotopic mass ($C_{78}H_{98}N_{14}O_{27}$) = 1,662.67; found: m/z = 1,663.7 $[M+H]^+$.

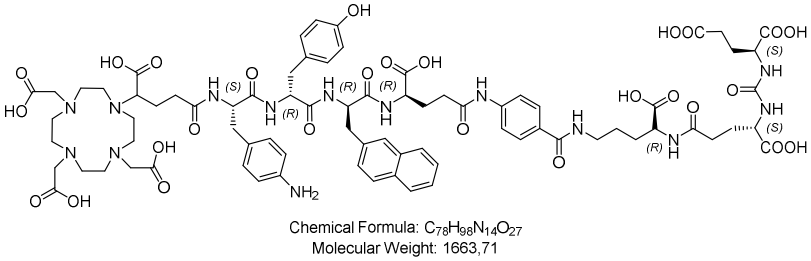

DOTAGA-F(4-NH$_2$)y-2-nal-k(d[*N*^{5}-orn-*C*^{4}-EuE]-2,4-DNBA) (PSMA-61): 2,4-DNBA was coupled to the Alloc-deprotected aspartic acid using 2,4-DNBA (1.5 eq.), HOBt (2.0 eq.), TBTU (2.0 eq.) and DIPEA (4.0 eq.) in DMF. After completion of reaction, Fmoc-deprotection was conducted according to **SP-3**. All further reactions steps were performed as described in chapter **II 2.4.1**. RP-HPLC (10 to 90% B in 15 min): t_R = 6.40 min K' = 2.2. Calculated monoisotopic mass ($C_{83}H_{105}N_{17}O_{32}$) = 1,851.71; found: m/z = 1,852.5 $[M+H]^+$, 926.7 $[M+2H]^{2+}$.

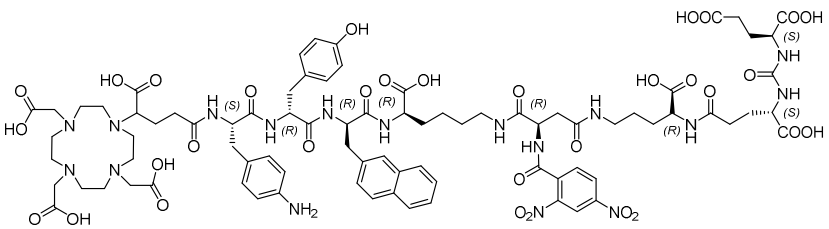

DOTAGA-F(4-NH$_2$)y-2-nal-k(d[*N*^{5}-orn-*C*^{4}-EuE]-TMA) (PSMA-62): The synthesis of **PSMA-62** was accomplished in similarity to **PSMA-61** except for the conjugation of the trimesic acid (TMA). The Allyl-protected D-aspartic acid was not Allyl-deprotected and instead the synthesis continued with Fmoc-D-Lys-OAll·HCl and the following amino acids as described in chapter **II 2.4.1**. After conjugation with DOTAGA-anhydride on solid phase using DOTAGA-anhydride (2.0 eq.) and DIPEA (2.0 eq.) over 48 h at RT, the resin bound peptide was Allyl-deprotected using **SP-5**. The free amino group of the aspartic acid residue was coupled with TMA using a solution containing TMA (20.0 eq.), PfpOH (4.0 eq.), DIC (4.0 eq.) and DIPEA (4.0 eq.) dissolved in DMF. This solution was allowed to stir 24 h at RT beforehand and was subsequently given to the peptide bound resin. The reaction mixture was stirred for 6 h at RT and the final crude product cleaved from the resin applying **SP-7.2**. RP-HPLC (10 to 70% B in 15 min): t_R = 7.48 min K' = 2.74. Calculated monoisotopic mass ($C_{85}H_{107}N_{15}O_{32}$) = 1,849.72; found: m/z = 1,850.5 $[M+H]^+$, 925.7 $[M+2H]^{2+}$.

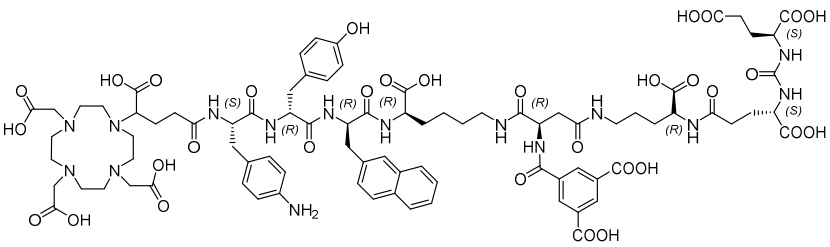

DOTAGA-F(4-NH$_2$)y-2-nal-k(Suc-*N*^{5}-orn-2-nal-*C*^{4}-EuE) (PSMA-63): The synthesis of **PSMA-63** was performed as described in chapter **II 2.4.1** with minor modifications. After initial resin loading

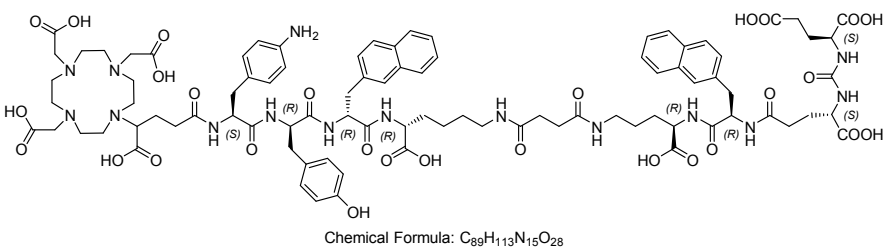

with Fmoc-D-Orn(Dde)-OH according to **SP-1** and concomitant Fmoc-deprotection via **SP-3**, Fmoc-D-2-Nal-OH was coupled as described in **SP-2** and Fmoc-deprotected. The next step was the conjugation of (O*t*Bu)EuE(O*t*Bu)$_2$ using **2** (1.5 eq.), HOBt (2.0 eq.), TBTU (2.0 eq.) and DIPEA (4.0 eq.) dissolved in DMF. Next, the Dde-protecting group was cleaved applying **SP-4**. Afterwards, succinic anhydride (7.5 eq.) and DIPEA (7.5 eq.) were dissolved in DMF and allowed to react with the resin-bound peptide overnight at RT. All further reactions steps were performed as described in chapter **II 2.4.1**. RP-HPLC (10 to 60% B in 15 min): t_R = 10.0 min K' = 4.0. Calculated monoisotopic mass ($C_{89}H_{113}N_{15}O_{28}$) = 1,839.79; found: m/z = 1,841.5 $[M+H]^+$.

2.4.3 Linker and Spacer modified EuE-based inhibitors

DOTAGA-F(4-NO$_2$)y-2-nal-k(Suc-*N*^{5}-orn-2-nal-*C*^{4}-EuE) (PSMA-64): The synthesis of **PSMA-64** was achieved as described for **PSMA-63**. RP-HPLC (10 to 60% B in 15 min): t_R = 11.4 min K' = 4.7. Calculated monoisotopic mass ($C_{89}H_{111}N_{15}O_{30}$) = 1,869.76: found: m/z = 1,871.8 $[M+H]^+$.

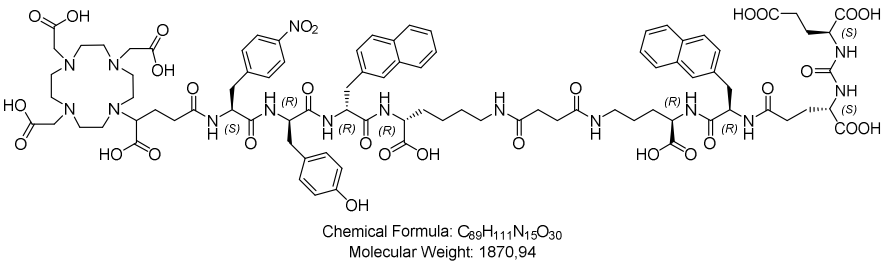

2,4-DNBA-Dap(DOTAGA)y-2-nal-e(Abz-*N*^{5}-orn-*C*^{4}-EuE) (PSMA-65): The synthesis of **PSMA-65** was achieved as described for **PSMA-53** and **PSMA-60**. RP-HPLC (10 to 60% B in 15 min): t_R = 10.2 min K' = 4.1. Calculated monoisotopic mass ($C_{79}H_{96}N_{16}O_{32}$) = 1,780.64; found: m/z = 1,781.3 $[M+H]^+$.

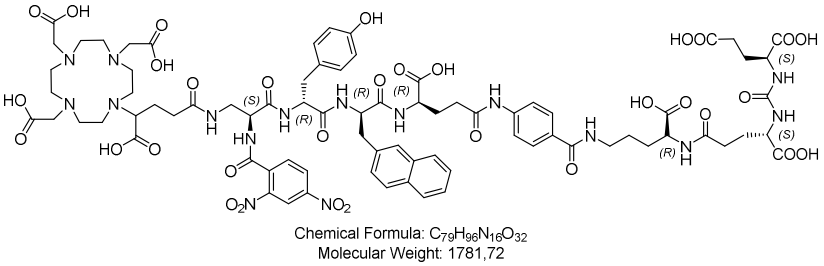

DOTAGA-Dap(TMA)y-2-nal-k(d[*N*^{5}-orn-*C*^{4}-EuE]-TMA) (PSMA-66): The synthesis of **PSMA-66** was accomplished as described for **PSMA-53** and **PSMA-62** with minor modifications. After conjugation of Fmoc-D-Asp(OAll)-OH, the synthesis was continued until the amino acid Fmoc-L-Dap(NHDde) was successfully coupled

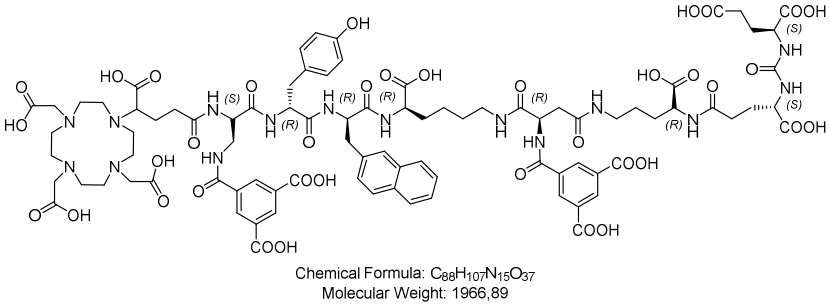

to the resin bound PSMA inhibitor. After Fmoc-deprotection according to **SP-3**, DOTAGA-anhydride was coupled as described for **PSMA-62**. In the following steps, **SP-5** and **SP-4** were subsequently performed to cleave the Dde-protecting group and to remove the Allyl/Alloc-groups. The conjugation of trimesic acid was accomplished as described for **PSMA-62**. The final crude product was cleaved from the resin applying **SP-7.2**. RP-HPLC (10 to 70% B in 15 min): t_R = 7.48 min K' = 2.74. Calculated monoisotopic mass ($C_{88}H_{107}N_{15}O_{37}$) = 1,965.70; found: m/z = 1,966.4 $[M+H]^+$, 984.1 $[M+2H]^{2+}$.

2.4.4 Synthesis of EuE-based peptides with an ester-group

DOTAGA-2-Amet-Suc-F(4-NH$_2$)y-2-nal-k(Suc-*N*^{5}-orn-*C*^{4}-EuE) (PSMA-67): The synthesis of **PSMA-67** was performed as described for **PSMA-49** with minor modifications. After the coupling and Fmoc-deprotection of Fmoc-L-Phe(4-NHBoc)-OH, the resin loaded peptide was treated with a solution containing DIC (3.0 eq.), ethyl isonitrosocyanoacetate (0.8 eq.) and **59** (2.0 eq.) in DMF for 24 h at RT. Next, Fmoc- and Allyl-deprotection was conducted as described in **SP-3** and **SP-5** and the peptide cleaved from the resin according to **SP-7.1**. The final conjugation to the chelator was achieved using DOTAGA-anhydride (4.0 eq.) and DIPEA (6.0 eq.) in dry DMF. The reaction solution was allowed to stir at RT and stopped after 68 h. The final product was purified via RP-HPLC (10 to 60% B in 15 min): t_R = 8.0 min K' = 3.0. Calculated monoisotopic mass ($C_{82}H_{111}N_{15}O_{30}$) = 1,785.76; found: m/z = 1,787.6 $[M+H]^+$.

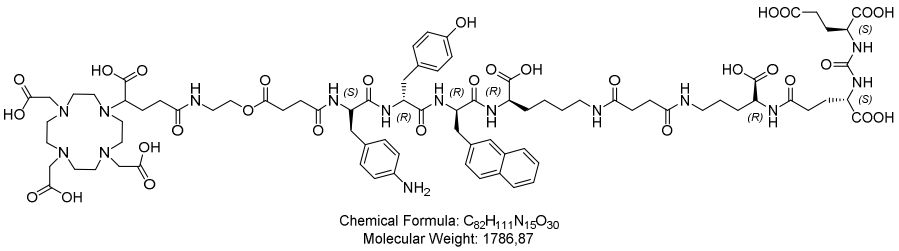

2.5 Control peptides for the S9-metabolite assay

DOTAGA-FFK(Sub-KuE) (PSMA-68): The synthesis of **PSMA-68** was performed as previously described [193]. RP-HPLC (10 to 90% B in 15 min): t_R = 9.7 min K' = 4.1. Calculated monoisotopic mass ($C_{63}H_{93}N_{11}O_{22}$) = 1,355.65; found: m/z = 1,356.2 $[M+H]^+$, 679.2 $[M+2H]^{2+}$.

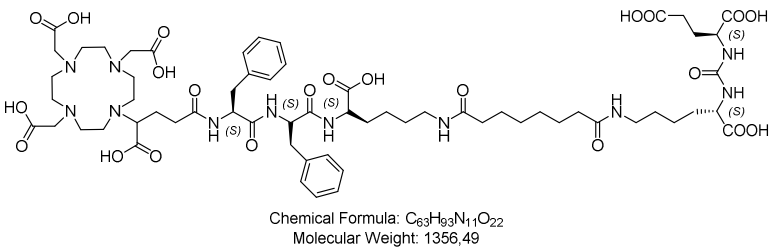

K(DOTA)VDFPANF (S9-positiv-control-peptide (S9-PCP-1)): The synthesis of **S9-PCP-1** was achieved analog to the synthesis of **30**. Loading of the 2-CTC resin was achieved using Fmoc-L-Lys(Dde)-OH (2.7 eq.) as described in **SP-1**. The resin loading was determined to be 0.87 mmol/g. The following Fmoc-protected amino acids were coupled as described in **SP-2 to SP-4**. After conjugation of the last amino acid Fmoc-L-Phe-OH, the resin-bound peptide was Dde-deprotected via **SP-4** and the chelator DOTA attached using DOTA-tris(*t*Bu)ester (1.5 eq.), HOBt (2.0 eq.), TBTU (2.0 eq.) and DIPEA (4.0 eq.) dissolved in DMF. The reaction was allowed to stir for 48 h at RT. After completion of reaction, the peptide was Fmoc-deprotected on the *N*-terminal site via **SP-3** and cleaved from the resin using **SP-7.2**. The final crude product was purified via RP-HPLC (10 to 60% B in 15 min): t_R = 7.85 min K' = 2.93. Calculated monoisotopic mass ($C_{61}H_{90}N_{14}O_{19}$) = 1,322.65; found: *m/z* = 1,323.4 $[M+H]^+$, 662.7 $[M+2H]^{2+}$.

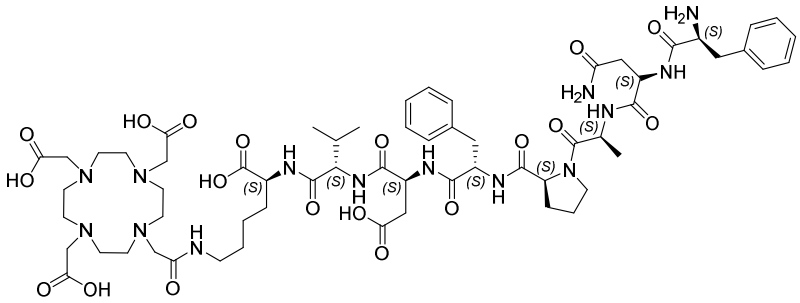

2.6. ^{nat}Ga-and ^{nat}Lu-labeled PSMA inhibitors for affinity and HSA binding studies

2.6.1 ^{nat}Ga-labeled PSMA inhibitors

$^{nat}Ga^{III}$-chelate complexation was conducted as described in **SP-9.1**. The resulting 1.0 mM aq. solutions of the respective ^{nat}Ga-PSMA inhibitors were diluted (serial dilution 10^{-4} to 10^{-11} M in Hank's buffered salt solution (HBSS) with 1% bovine serum albumin (BSA)) and used for the *in vitro* affinity evaluation. For HSA binding, the respective ^{nat}Ga-complexed 10^{-3} M solution was purified via RP-HPLC to remove free metal ions and lyophilized.

[^{nat}Ga]DOTAGA-y(3-I)fk(Sub-KuE) (PSMA I&T) ([^{nat}Ga]PSMA-1): RP-HPLC (25 to 55% B in 15 min): t_R = 11.8 min K' = 5.6. Calculated monoisotopic mass ($C_{63}H_{92}IN_{11}O_{23}Ga$) = 1,565.46.54; found: *m/z* = 1,566.6.3 $[M+H]^+$, 782.7.1 $[M+2H]^{2+}$.

[^{nat}Ga]PSMA-617: RP-HPLC (10 to 45% B in 15 min): t_R = 10.5 min K' = 4.25. Calculated monoisotopic mass ($C_{49}H_{65}IN_9O_{16}Ga$) = 1,107.40; found: *m/z* = 1,108.6 $[M+H]^+$.

[^{nat}Ga]DOTAGA–y(3-I)fk(L-Asu[KuE]-MPA-Galactose) ([^{nat}Ga]PSMA-20): RP-HPLC (10 to 60% B in 15 min): t_R = 7.3 min K' = 2.65. Calculated monoisotopic mass ($C_{72}H_{104}IN_{12}O_{29}SGa$) = 1,828.52; found: *m/z* = 1,830.1 $[M+H]^+$.

[^{nat}Ga]DOTAGA-y(3-I)fk(L-Asu[KuE]-MPA-Mannose) ([^{nat}Ga]PSMA-21): RP-HPLC (10 to 60% B in 15 min): t_R = 8.0 min K' = 3.0. Calculated monoisotopic mass ($C_{72}H_{104}IN_{12}O_{29}SGa$) = 1,828.52; found: m/z = 1,830.1 $[M+H]^+$.

[^{nat}Ga]DOTAGA-y(3-I)fk(L-Asu[KuE]-MPA-Cellobiose) ([^{nat}Ga]PSMA-23): RP-HPLC (10 to 60% B in 15 min): t_R = 7.7 min K' = 2.9. Calculated monoisotopic mass ($C_{78}H_{115}IN_{12}O_{34}SGa$) = 1,991.57; found: m/z = 1,992.4 $[M+H]^+$.

[^{nat}Ga]DOTAGA-y-2-nal-k(Sub-KuE) ([^{nat}Ga]PSMA-30): RP-HPLC (25 to 55% B in 15 min): t_R = 10.8 min K' = 4.4. Calculated monoisotopic mass ($C_{67}H_{92}N_{11}O_{23}Ga$) = 1,489.58; found: m/z = 1,490.9 $[M+H]^+$, 746.1 $[M+2H]^{2+}$.

[^{nat}Ga]DOTAGA-y-2-nal-K(Glut-f[4-I]-KuE) ([^{nat}Ga]PSMA-43): RP-HPLC (25 to 55% B in 15 min): t_R = 11.8 min K' = 5.6. Calculated monoisotopic mass ($C_{73}H_{94}IN_{12}O_{24}Ga$) = 1,720.5; found: m/z = 1,721.5 $[M+H]^+$, 861.4 $[M+2H]^{2+}$.

[^{nat}Ga]DOTAGA-y-2-nal-k(Suc-N^5-orn-C^4-EuE) ([^{nat}Ga]PSMA-46): RP-HPLC (10 to 60% B in 15 min): t_R = 7.8 min K' = 2.9. Calculated monoisotopic mass ($C_{67}H_{89}N_{12}O_{26}Ga$) = 1,546.53; found: m/z = 1,547.4 $[M+H]^+$.

[^{nat}Ga]DOTAGA-F(4-NH_2)y-2-nal-k(Suc-N^5-orn-C^4-EuE) ([^{nat}Ga]PSMA-49): RP-HPLC (10 to 60% B in 15 min): t_R = 7.3 min K' = 2.65. Calculated monoisotopic mass ($C_{76}H_{99}N_{14}O_{27}Ga$) = 1,708.62; found: m/z = 1,709.6 $[M+H]^+$, 855.5 $[M+2H]^{2+}$.

[^{nat}Ga]DOTAGA-f(4-NH_2)-y-2-nal-k(Suc-N^5-orn-C^4-EuE) ([^{nat}Ga]PSMA-50): RP-HPLC (10 to 60% B in 15 min): t_R = 7.3 min K' = 2.65. Calculated monoisotopic mass ($C_{76}H_{99}N_{14}O_{27}Ga$) = 1,708.62; found: m/z = 1,709.5 $[M+H]^+$, 855.3 $[M+2H]^{2+}$.

[^{nat}Ga]DOTAGA-f(4-NH_2)-y-2-nal-K(Suc-N^5-orn-C^4-EuE) ([^{nat}Ga]PSMA-51): RP-HPLC (10 to 60% B in 15 min): t_R = 7.2 min K' = 2.6. Calculated monoisotopic mass ($C_{76}H_{99}N_{14}O_{27}Ga$) = 1,708.62; found: m/z = 1,709.4 $[M+H]^+$, 855.5 $[M+2H]^{2+}$.

2.6.2 ^{nat}Lu-labeled PSMA inhibitors

$^{nat}Lu^{III}$-chelate complexation was conducted as described in **SP-9.2**. The resulting 1.0 mM aq. solutions of the respective ^{nat}Lu-PSMA inhibitors were diluted (serial dilution 10^{-4} to 10^{-11} M in HBSS with 1% BSA) and used for the *in vitro* affinity evaluation. For HSA binding, the respective ^{nat}Lu-complexed 10^{-3} M solution was purified via RP-HPLC to remove free metal ions and lyophilized.

[^{nat}Lu]DOTAGA-y(3-I)fk(Sub-KuE) (PSMA I&T) ([^{nat}Lu]PSMA-1): RP-HPLC (10 to 45% B in 15 min): t_R = 10.5 min K' = 4.25. Calculated monoisotopic mass ($C_{63}H_{92}IN_{11}O_{23}Lu$) = 1,669.46; found: m/z = 1,498.3 $[M+H]^+$, 750.1 $[M+2H]^{2+}$.

[^{nat}Lu]PSMA-617: RP-HPLC (10 to 45% B in 15 min): t_R = 10.5 min K' = 4.25. Calculated monoisotopic mass ($C_{49}H_{65}IN_9O_{16}Lu$) = 1,213.42; found: m/z = 1,498.3 $[M+H]^+$, 750.1 $[M+2H]^{2+}$.

[^{nat}Lu]DOTAGA-y(3-I)fk(L-Asu[KuE]) ([^{nat}Lu]PSMA-8): RP-HPLC (10 to 40% B in 15 min): t_R = 9.72 min K' = 3.86. Calculated monoisotopic mass ($C_{63}H_{90}IN_{12}O_{23}Lu$) = 1,684.47; found: m/z = 1,685.6 $[M+H]^+$, 843.5 $[M+2H]^{2+}$.

[^{nat}Lu]DOTAGA-y(3-I)fkk(Sub-KuE) ([^{nat}Lu]PSMA-9): RP-HPLC (10 to 50% B in 15 min): t_R = 10.27 min K' = 4.14. Calculated monoisotopic mass ($C_{69}H_{101}IN_{13}O_{24}Lu$) = 1,797.56; found: m/z = 1,798.7 $[M+H]^+$, 900.1 $[M+2H]^{2+}$.

[^{nat}Lu]DOTAGA-y(3-I)f-N^6-kk(Sub-KuE)) ([^{nat}Lu]PSMA-10): RP-HPLC (10 to 50% B in 15 min): t_R = 10.12 min K' = 4.06. Calculated monoisotopic mass ($C_{69}H_{101}IN_{13}O_{24}Lu$) = 1,797.56; found: m/z = 1,798.7 $[M+H]^+$, 900.1 $[M+2H]^{2+}$.

[^{nat}Lu]DOTAGA-y(3-I)kfk(Sub-KuE) ([^{nat}Lu]PSMA-11): RP-HPLC (10 to 40% B in 15 min): t_R = 8.67 min K' = 3.33. Calculated monoisotopic mass ($C_{69}H_{101}IN_{13}O_{24}Lu$) = 1,797.56; found: m/z = 1,798.7 $[M+H]^+$, 900.1 $[M+2H]^{2+}$.

[^{nat}Lu]DOTAGA-y(3-I))-N^6-kfk(Sub-KuE) ([^{nat}Lu]PSMA-12): RP-HPLC (10 to 50% B in 15 min): t_R = 9.62 min K' = 3.81. Calculated monoisotopic mass ($C_{69}H_{101}IN_{13}O_{24}Lu$) = 1,797.56; found: m/z = 1,798.7 $[M+H]^+$, 900.1 $[M+2H]^{2+}$.

[^{nat}Lu]DOTAGA-ky(3-I)fk(Sub-KuE) ([^{nat}Lu]PSMA-13): RP-HPLC (10 to 50% B in 15 min): t_R = 9.77 min K' = 3.89. Calculated monoisotopic mass ($C_{69}H_{101}IN_{13}O_{24}Lu$) = 1,797.56; found: m/z = 1,798.7 $[M+H]^+$, 900.1 $[M+2H]^{2+}$.

[^{nat}Lu]DOTAGA-N^6-ky(3-I)fk(Sub-KuE) ([^{nat}Lu]PSMA-14): RP-HPLC (10 to 50% B in 15 min): t_R = 10.07 min K' = 4.04. Calculated monoisotopic mass ($C_{69}H_{101}IN_{13}O_{24}Lu$) = 1,797.56; found: m/z = 1,798.7 $[M+H]^+$, 900.1 $[M+2H]^{2+}$.

[^{nat}Lu]DOTAGA-F(4-NH_2)y(3-I)fk(Sub-KuE) ([^{nat}Lu]PSMA-15): RP-HPLC (10 to 50% B in 15 min): t_R = 10.24 min K' = 4.12. Calculated monoisotopic mass ($C_{72}H_{99}IN_{13}O_{24}Lu$) = 1,831.54; found: m/z = 1,832.7 $[M+H]^+$, 917.4 $[M+2H]^{2+}$.

[^{nat}Lu]DOTAGA-f(4-NH$_2$)y(3-I)fk(Sub-KuE) ([^{nat}Lu]PSMA-16): RP-HPLC (10 to 60% B in 15 min): t_R = 8.6 min K' = 3.3. Calculated monoisotopic mass ($C_{72}H_{99}IN_{13}O_{24}Lu$) = 1,831.54; found: m/z = 1,833.2 $[M+H]^+$, 917.3 $[M+2H]^{2+}$.

[^{nat}Lu]DOTAGA-f(4-NH$_2$)y(3-I)fK(Sub-KuE) ([^{nat}Lu]PSMA-17): RP-HPLC (10 to 60% B in 15 min): t_R = 8.9 min K' = 3.45. Calculated monoisotopic mass ($C_{72}H_{99}IN_{13}O_{24}Lu$) = 1,831.54; found: m/z = 1,832.8 $[M+H]^+$, 917.0 $[M+2H]^{2+}$.

[^{nat}Lu]DOTAGA-f(4-NH$_2$)y(3-I)FK(Sub-KuE) ([^{nat}Lu]PSMA-18): RP-HPLC (10 to 60% B in 15 min): t_R = 9.3 min K' = 3.65. Calculated monoisotopic mass ($C_{72}H_{99}IN_{13}O_{24}Lu$) = 1,831.54; found: m/z = 1,832.2 $[M+H]^+$, 917.0 $[M+2H]^{2+}$.

[^{nat}Lu]DOTAGA-F(4-NH$_2$)y(3-I)fK(Sub-KuE) ([^{nat}Lu]PSMA-19): RP-HPLC (10 to 60% B in 15 min): t_R = 9.0 min K' = 3.5. Calculated monoisotopic mass ($C_{72}H_{99}IN_{13}O_{24}Lu$) = 1,831.54; found: m/z = 1,832.4 $[M+H]^+$, 916.8 $[M+2H]^{2+}$.

.

[^{nat}Lu]DOTAGA–y(3-I)fk(L-Asu[KuE]-MPA-Galactose) ([^{nat}Lu]PSMA-20): RP-HPLC (10 to 60% B in 15 min): t_R = 7.7 min K' = 2.85. Calculated monoisotopic mass ($C_{72}H_{101}IN_{12}O_{29}SLu$) = 1,934.52; found: m/z = 1,935.4 $[M+H]^+$, 968.2 $[M+2H]^{2+}$.

[^{nat}Lu]DOTAGA-y(3-I)fk(L-Asu[KuE]-MPA-Mannose) ([^{nat}Lu]PSMA-21): RP-HPLC (10 to 60% B in 15 min): t_R = 7.4 min K' = 2.7. Calculated monoisotopic mass ($C_{72}H_{101}IN_{12}O_{29}SLu$) = 1,934.52; found: m/z = 1,936.4 $[M+H]^+$, 968.3 $[M+2H]^{2+}$.

[^{nat}Lu]DOTAGA-y(3-I)fk(L-Asu[KuE]-MPA-Fucose) ([^{nat}Lu]PSMA-22): RP-HPLC (10 to 60% B in 15 min): t_R = 8.1 min K' = 3.05. Calculated monoisotopic mass ($C_{72}H_{101}IN_{12}O_{28}SLu$) = 1,918.53; found: m/z = 1,919.9 $[M+H]^+$.

[^{nat}Lu]DOTAGA-y(3-I)fk(L-Asu[KuE]-MPA-Cellobiose) ([^{nat}Lu]PSMA-23): RP-HPLC (10 to 60% B in 15 min): t_R = 7.6 min K' = 2.8. Calculated monoisotopic mass ($C_{78}H_{111}IN_{12}O_{34}SLu$) = 2,096.58; found: m/z = 1,049.8 $[M+2H]^{2+}$.

[^{nat}Lu]DOTAGA-f(4-NH$_2$)y(3-I)fk(L-Asu[KuE]-MPA-Galactose) ([^{nat}Lu]PSMA-27): RP-HPLC (10 to 40% B in 15 min): t_R = 1011 min K' = 4.06. Calculated monoisotopic mass ($C_{81}H_{114}IN_{14}O_{30}SLu$) = 2,096.6; found: m/z = 1,049.7 $[M+2H]^{2+}$.

[^{nat}Lu]DOTAGA-f(4-NH$_2$)y(3-I)fk(Agl[MPA-Galactose]-Glut-KuE) (PSMA-28): ([^{nat}Lu]PSMA-28): RP-HPLC (10 to 90 % B in 15 min): t_R = 5.67 min K' = 1.84. Calculated monoisotopic mass ($C_{80}H_{111}IN_{15}O_{31}SLu$) = 2,111.58; found: m/z = 1,056.9 $[M+2H]^{2+}$.

[^{nat}Lu]DOTAGA-f(4-NH-MPA-Galactose)y(3-I)fk(Agl[MPA-Galactose]-Glut-KuE) ([^{nat}Lu]PSMA-29): RP-HPLC (10 to 90% B in 15 min): t_R = 5.56 min K' = 1.78. Calculated monoisotopic mass ($C_{89}H_{125}IN_{15}O_{37}S_2Lu$) = 2,361.63; found: *m/z* = 1,182.0 $[M+2H]^{2+}$.

[^{nat}Lu]DOTAGA-y-2-nal-k(Sub-KuE) ([^{nat}Lu]PSMA-30): RP-HPLC (25 to 55% B in 15 min): t_R = 11.6 min K' = 4.8. Calculated monoisotopic mass ($C_{67}H_{92}N_{11}O_{23}Lu$) = 1,593.58; found: *m/z* = 1,595.0 $[M+H]^+$, 798.2 $[M+2H]^{2+}$.

[^{nat}Lu]DOTAGA-F(4-NH$_2$)y-2-nal-k(Sub-KuE) ([^{nat}Lu]PSMA-31): RP-HPLC (10 to 60% B in 15 min): t_R = 9.1 min K' = 3.6. Calculated monoisotopic mass ($C_{76}H_{102}N_{13}O_{24}Lu$) = 1,755.66; found: *m/z* = 1,756.6 $[M+H]^+$, 878.8 $[M+2H]^{2+}$.

[^{nat}Lu]DOTAGA-f(4-NH$_2$)y-2-nal-k(Sub-KuE) ([^{nat}Lu]PSMA-32): RP-HPLC (10 to 60% B in 15 min): t_R = 9.0 min K' = 3.5. Calculated monoisotopic mass ($C_{76}H_{102}N_{13}O_{24}Lu$) = 1,755.66; found: *m/z* = 1,756.4 $[M+H]^+$, 879.0 $[M+2H]^{2+}$.

[^{nat}Lu]DOTAGA-f(4-NH$_2$)y-2-nal-K(Sub-KuE) ([^{nat}Lu]PSMA-33): RP-HPLC (10 to 60% B in 15 min): t_R = 9.1 min K' = 3.55. Calculated monoisotopic mass ($C_{76}H_{102}N_{13}O_{24}Lu$) = 1,755.66; found: *m/z* = 1,756.4 $[M+H]^+$, 879.3 $[M+2H]^{2+}$.

[^{nat}Lu]DOTAGA-F(4-NH$_2$)y-2-nal-K(Sub-KuE) ([^{nat}Lu]PSMA-34): RP-HPLC (10 to 60% B in 15 min): t_R = 9.2 min K' = 3.6. Calculated monoisotopic mass ($C_{76}H_{102}N_{13}O_{24}Lu$) = 1,755.66; found: *m/z* = 1,756.9 $[M+H]^+$, 879.2 $[M+2H]^{2+}$.

[^{nat}Lu]DOTAGA-y(3-I)fk(L-Asu[KuE]-BA) ([^{nat}Lu]PSMA-35): RP-HPLC (10 to 50% B in 15 min): t_R = 10.53 min K' = 4.27. Calculated monoisotopic mass ($C_{70}H_{94}IN_{12}O_{24}Lu$) = 1,788.5; found: *m/z* = 1,789.9 $[M+H]^+$.

[^{nat}Lu]DOTAGA-y(3-I)fk(L-Asu[KuE]-2,4-DNBA) ([^{nat}Lu]PSMA-36): RP-HPLC (10 to 60% B in 15 min): t_R = 9.81 min K' = 3.91. Calculated monoisotopic mass ($C_{70}H_{92}IN_{14}O_{28}Lu$) = 1,878.47; found: *m/z* = 1,879.9 $[M+H]^+$.

[^{nat}Lu]DOTAGA-y(3-I)fk(L-Asu[KuE]-DMBA) ([^{nat}Lu]PSMA-37): RP-HPLC (10 to 90% B in 15 min): t_R = 9.08 min K' = 3.54. Calculated monoisotopic mass ($C_{80}H_{105}IN_{13}O_{27}Lu$) = 1,981.57; found: *m/z* = 1,983.5 $[M+H]^+$.

[^{nat}Lu]DOTAGA-f(4-NH$_2$)y(3-I)fk(Agl[PBP]-Glut-KuE) ([^{nat}Lu]PSMA-38): RP-HPLC (10 to 90% B in 15 min): t_R = 9.2 min K' = 3.6. Calculated monoisotopic mass ($C_{89}H_{115}IN_{15}O_{27}Lu$) = 2,127.66; found: m/z = 1,065.2 $[M+2H]^{2+}$.

[^{nat}Lu]DOTAGA-f(4-NH$_2$)y(3-I)fk(Agl[*C^4*-e-PBP]-Glut-KuE) ([^{nat}Lu]PSMA-39): RP-HPLC (10 to 60% B in 15 min): t_R = 12.5 min K' = 5.35. Calculated monoisotopic mass ($C_{94}H_{122}IN_{16}O_{30}Lu$) = 2,256.7; found: m/z = 1,129.7 $[M+2H]^{2+}$.

[^{nat}Lu]DOTAGA-f(4-NH$_2$)y(3-I)fk(Glut-f[4-I]-KuE) ([^{nat}Lu]PSMA-40): RP-HPLC (10 to 60% B in 15 min): t_R = 10.3 min K' = 4.15. Calculated monoisotopic mass ($C_{78}H_{101}I_2N_{14}O_{25}Lu$) = 2,062.46; found: m/z = 1,032.6 $[M+2H]^{2+}$.

[^{nat}Lu]DOTAGA-f(4-NH$_2$)y-2-nal-k(Glut-f[4-I]-KuE) ([^{nat}Lu]PSMA-41): RP-HPLC (10 to 60% B in 15 min): t_R = 9.7 min K' = 3.85. Calculated monoisotopic mass ($C_{82}H_{104}IN_{14}O_{25}Lu$) = 1,986.58; found: m/z = 1,987.5 $[M+H]^+$, 994.3 $[M+2H]^{2+}$.

[^{nat}Lu]DOTAGA-f(4-NH$_2$)y-2-nal-K(Glut-f[4-I]-KuE) ([^{nat}Lu]PSMA-42): RP-HPLC (10 to 60% B in 15 min): t_R = 10.7 min K' = 4.35. Calculated monoisotopic mass ($C_{82}H_{104}IN_{14}O_{25}Lu$) = 1,986.58; found: m/z = 1,987.6 $[M+H]^+$, 994.4 $[M+2H]^{2+}$.

[^{nat}Lu]DOTAGA-y-2-nal-K(Glut-f[4-I]-KuE) ([^{nat}Lu]PSMA-43): RP-HPLC (25 to 55% B in 15 min): t_R = 10.6 min K' = 4.3. Calculated monoisotopic mass ($C_{73}H_{94}IN_{12}O_{24}Lu$) = 1,824.5; found: m/z = 1,826.5 $[M+H]^+$, 913.8 $[M+2H]^{2+}$.

[^{nat}Lu]DOTA-f(4-NH$_2$)y-2-nal-k(Sub-KuE) ([^{nat}Lu]PSMA-44): RP-HPLC (10 to 60% B in 15 min): t_R = 9.0 min K' = 3.5. Calculated monoisotopic mass ($C_{73}H_{98}N_{13}O_{22}Lu$) = 1,683.64; found: m/z = 1,685.1 $[M+H]^+$, 842.9 $[M+2H]^{2+}$.

[^{nat}Lu]DOTAGA-y-2-nal-k(Suc-*N^5*-orn-*C^4*-EuE) ([^{nat}Lu]PSMA-46): RP-HPLC (10 to 60% B in 15 min): t_R = 7.8/8.2 min K' = 2.9/3.1. Calculated monoisotopic mass ($C_{67}H_{89}N_{12}O_{26}Lu$) = 1,652.54; found: m/z = 1,653.9 $[M+H]^+$.

[^{nat}Lu]DOTAGA-F(4-NH$_2$)y(3-I)fk(Suc-*N^5*-orn-*C^4*-EuE) ([^{nat}Lu]PSMA-47): RP-HPLC (10 to 60% B in 15 min): t_R = 7.8 min K' = 2.9. Calculated monoisotopic mass ($C_{72}H_{96}IN_{14}O_{27}Lu$) = 1,890.5; found: m/z = 1,891.8 $[M+H]^+$, 946.6 $[M+2H]^{2+}$.

[^{nat}Lu]DOTAGA-f(4-NH$_2$)y(3-I)fk(Suc-*N^5*-orn-*C^4*-EuE) ([^{nat}Lu]PSMA-48): RP-HPLC (10 to 60% B in 15 min): t_R = 6.9 min K' = 2.45. Calculated monoisotopic mass ($C_{72}H_{96}IN_{14}O_{27}Lu$) = 1,890.5; found: m/z = 1,891.7 $[M+H]^+$, 946.4 $[M+2H]^{2+}$.

[^{nat}Lu]DOTAGA-F(4-NH_2)y-2-nal-k(Suc-N^5-orn-C^4-EuE) ([^{nat}Lu]PSMA-49): RP-HPLC (10 to 60% B in 15 min): t_R = 7.2 min K' = 2.6. Calculated monoisotopic mass ($C_{76}H_{99}N_{14}O_{27}Lu$) = 1,814.62; found: m/z = 1,815.6 $[M+H]^+$, 908.3 $[M+2H]^{2+}$.

[^{nat}Lu]DOTAGA-f(4-NH_2)-y-2-nal-k(Suc-N^5-orn-C^4-EuE) ([^{nat}Lu]PSMA-50): RP-HPLC (10 to 60% B in 15 min): t_R = 7.3 min K' = 2.65. Calculated monoisotopic mass ($C_{76}H_{99}N_{14}O_{27}Lu$) = 1,814.62; found: m/z = 1,815.9 $[M+H]^+$, 908.3 $[M+2H]^{2+}$.

[^{nat}Lu]DOTAGA-f(4-NH_2)-y-2-nal-K(Suc-N^5-orn-C^4-EuE) ([^{nat}Lu]PSMA-51): RP-HPLC (10 to 60% B in 15 min): t_R = 7.3 min K' = 2.65. Calculated monoisotopic mass ($C_{76}H_{99}N_{14}O_{27}Lu$) = 1,814.62; found: m/z = 1,815.9 $[M+H]^+$, 908.5 $[M+2H]^{2+}$.

[^{nat}Lu]DOTAGA-F(4-NO_2)-y-2-nal-k(Suc-N^5-orn-C^4-EuE) ([^{nat}Lu]PSMA-52): RP-HPLC (10 to 60% B in 15 min): t_R = 9.4 min K' = 3.7. Calculated monoisotopic mass ($C_{76}H_{97}N_{14}O_{29}Lu$) = 1,844.6; found: m/z = 1,846.0 $[M+H]^+$.

[^{nat}Lu]2,4-DNBA-Dap(DOTAGA)-y-2-nal-k(Suc-N^5-orn-C^4-EuE) ([^{nat}Lu]PSMA-53): RP-HPLC (10 to 60% B in 15 min): t_R = 8.3 min K' = 3.15. Calculated monoisotopic mass ($C_{77}H_{97}N_{16}O_{32}Lu$) = 1,932.59; found: m/z = 1,933.7 $[M+H]^+$.

[^{nat}Lu]DOTAGA-Yy-2-nal-k(Suc-N^5-orn-C^4-EuE) ([^{nat}Lu]PSMA-54): RP-HPLC (10 to 60% B in 15 min): t_R = 8.4 min K' = 3.2. Calculated monoisotopic mass ($C_{76}H_{98}N_{13}O_{28}Lu$) = 1,815.61; found: m/z = 1,816.8 $[M+H]^+$.

[^{nat}Lu]DOTAGA-2-Nal-y-2-nal-k(Suc-N^5-orn-C^4-EuE) ([^{nat}Lu]PSMA-55): RP-HPLC (10 to 60% B in 15 min): t_R = 10.2 min K' = 4.1. Calculated monoisotopic mass ($C_{80}H_{100}N_{13}O_{27}Lu$) = 1,849.63; found: m/z = 1,851.0 $[M+H]^+$.

[^{nat}Lu]DOTAGA-K(PBP)y-2-nal-k(Suc-N^5-orn-C^4-EuE) ([^{nat}Lu]PSMA-56): RP-HPLC (10 to 70% B in 15 min): t_R = 10.6 min K' = 4.3. Calculated monoisotopic mass ($C_{91}H_{119}N_{14}O_{29}Lu$) = 2,046.77; found: m/z = 1,024.7 $[M+H]^+$.

[^{nat}Lu]DOTAGA-K(C^4-e-PBP)y-2-nal-k(Suc-N^5-orn-C^4-EuE) ([^{nat}Lu]PSMA-57): RP-HPLC (10 to 60% B in 15 min): t_R = 13.8 min K' = 5.9. Calculated monoisotopic mass ($C_{96}H_{126}N_{15}O_{32}Lu$) = 2,175.81; found: m/z = 1,089.3 $[M+2H]^{2+}$.

[^{nat}Lu]DOTAGA-F(4-NH_2)y-2-nal-e(r-G-N^5-orn-C^4-EuE) ([^{nat}Lu]PSMA-58): RP-HPLC (10 to 60% B in 15 min): t_R = 8.0 min K' = 3.0. Calculated monoisotopic mass ($C_{79}H_{105}N_{18}O_{28}Lu$) = 1,928.68; found: m/z = 1,929.7 $[M+H]^+$.

[^{nat}Lu]DOTAGA-F(4-NH_2)y-2-nal-e(e-G-N^5-orn-C^4-EuE) ([^{nat}Lu]PSMA-59): RP-HPLC (10 to 60% B in 15 min): t_R = 7.5 min K' = 2.75. Calculated monoisotopic mass ($C_{78}H_{97}N_{15}O_{30}Lu$) = 1,901.62; found: m/z = 1,902.7 $[M+H]^+$.

[^{nat}Lu]DOTAGA-F(4-NH_2)y-2-nal-e(Abz-N^5-orn-C^4-EuE) ([^{nat}Lu]PSMA-60): RP-HPLC (10 to 60% B in 15 min): t_R = 8.2 min K' = 3.1. Calculated monoisotopic mass ($C_{78}H_{95}N_{14}O_{27}Lu$) = 1,834.59; found: m/z = 1,835.7 $[M+H]^+$.

[^{nat}Lu]DOTAGA-F(4-NH_2)y-2-nal-k(d[N^5-orn-C^4-EuE]-2,4-DNBA) ([^{nat}Lu]PSMA-61): RP-HPLC (10 to 90% B in 15 min): t_R = 8.22 min K' = 3.11. Calculated monoisotopic mass ($C_{83}H_{102}N_{17}O_{32}Lu$) = 2,023.63; found: m/z = 1,013.1 $[M+2H]^{2+}$.

[^{nat}Lu]DOTAGA-F(4-NH_2)y-2-nal-k(d[N^5-orn-C^4-EuE]-TMA) ([^{nat}Lu]PSMA-62): RP-HPLC (10 to 70% B in 15 min): t_R = 7.27 min K' = 2.64. Calculated monoisotopic mass ($C_{85}H_{104}N_{15}O_{32}Lu$) = 2,021.64; found: m/z = 1,012.3 $[M+2H]^{2+}$.

[^{nat}Lu]DOTAGA-F(4-NH_2)y-2-nal-k(Suc-N^5-orn-2-nal-C^4-EuE) ([^{nat}Lu]PSMA-63): RP-HPLC (10 to 60% B in 15 min): t_R = 9.7 min K' = 3.85. Calculated monoisotopic mass ($C_{89}H_{110}N_{15}O_{28}Lu$) = 2,011.71; found: m/z = 1,007.0 $[M+2H]^{2+}$.

[^{nat}Lu]DOTAGA-F(4-NO_2)y-2-nal-k(Suc-N^5-orn-2-nal-C^4-EuE) ([^{nat}Lu]PSMA-64): RP-HPLC (10 to 60% B in 15 min): t_R = 11.2 min K' = 4.6. Calculated monoisotopic mass ($C_{89}H_{108}N_{15}O_{30}Lu$) = 2,041.68; found: m/z = 1,022.0 $[M+2H]^{2+}$.

[^{nat}Lu]2,4-DNBA-Dap(DOTAGA)y-2-nal-e(Abz-N^5-orn-C^4-EuE) ([^{nat}Lu]PSMA-65): RP-HPLC (10 to 60% B in 15 min): t_R = 9.8 min K' = 3.9. Calculated monoisotopic mass ($C_{79}H_{93}N_{16}O_{32}Lu$) = 1,952.56; found: m/z = 1,954.0 $[M+H]^+$.

[^{nat}Lu]DOTAGA-Dap(TMA)y-2-nal-k(d[N^5-orn-C^4-EuE]-TMA) (PSMA-66) RP-HPLC (10 to 70% B in 15 min): t_R = 7.46 min K' = 2.73. Calculated monoisotopic mass ($C_{88}H_{108}N_{15}O_{37}Lu$) = 2,137.62; found: m/z = 1,070.4 $[M+2H]^{2+}$.

[^{nat}Lu]DOTAGA-2-Amet-Suc-F(4-NH_2)y-2-nal-k(Suc-N^5-orn-C^4-EuE) ([^{nat}Lu]PSMA-67): RP-HPLC (10 to 90% B in 15 min): t_R = 7.1 min K' = 2.55. Calculated monoisotopic mass ($C_{82}H_{108}N_{15}O_{30}Lu$) = 1,957.68; found: m/z = 1,958.5 $[M+H]^+$.

2.7. Radiolabeling

^{68}Ga-labeling: The ^{68}Ge/^{68}Ga generator was eluted with aq. HCl (1.0 M), from which a fraction of 1.25 mL, containing approximately 80% of the activity (600 to 800 MBq), was transferred into a reaction vial (ALLTECH, 5 mL). The vial was beforehand loaded with the respective compound (5.0 nmol) and an aq. 2-(4-(2-hydroxyethyl)-1-piperazinyl)-ethanesulfonic acid (HEPES) solution (950 µL, 2.7 M). The reaction vial was heated for 5 min at 95°C with subsequent fixation of the radiolabeled compound on a preconditioned SPE cartridge (C8 light, SepPak). After purging the cartridge with water (10 mL) in advance, the elution of the radiolabeled PSMA inhibitor from the cartridge was achieved with a mixture of EtOH and water (1/1; *v/v*), phosphate buffered saline (PBS) (1.0 mL) and again water (1.0 mL). At the end of radiolabeling, the EtOH was evaporated *in vacuo* and the tracer used without any further purification. Radiochemical purity was controlled using Radio-TLC (1.0 M sodium citrate buffer and 0.06 M NH_4OAc/MeOH buffer (1/1 ; *v/v*)).

^{177}Lu-labeling: The ^{177}Lu-labeled compounds were prepared as previously described [243] with minor modifications and used without further purification. In short, to NH_4OAc-buffer (10 µL, 1.0 M, pH = 5.9) was added the respective tracer (0.75 to 1.0 nmol, 7.5 to 10 µL), $^{177}LuCl_3$ (10 to 40 MBq; A_S > 3000 GBq/mg, 740 MBq/mL, 0.04 M HCl, ITG, Garching, Germany) and finally filled with trace-pure water (up to 100 µL) (Merck, Darmstadt, Germany). The reaction mixture was heated for 40 min at 95°C and the radiochemical purity was determined using radio-TLC.

^{125}I-labeling: Briefly, the stannylated precursor ($SnBu_3$-BA)(O*t*Bu)KuE(O*t*Bu)$_2$ (**PSMA-45**) (approx. 0.1 mg) was dissolved in a solution containing peracetic acid (20 µL), [^{125}I]NaI (5.0 µL, approx. 21.0 MBq) (74 TBq/mmol, 3.1 GBq/mL, 40 mM NaOH, Hartmann Analytic, Braunschweig, Germany), MeCN (20 µL) and AcOH (10 µL). The reaction solution was incubated for 10 min at RT, loaded on a cartridge (C18 Sep Pak Plus, preconditioned with 10 mL MeOH and 10 mL water) and rinsed with water (10 mL). After elution with a 1/1 mix (*v/v*) of EtOH and MeCN (2.0 mL), the solution was evaporated to dryness under a gentle nitrogen stream and treated with TFA (200 µL) for 30 min with subsequent evaporation of TFA. The crude product of ([^{125}I]I-BA)KuE was purified by radio-RP-HPLC (20 to 40% B in 20 min): t_R = 13.0 min; K' = 6.2.

3. *In vitro* methods

"A model is a lie that helps you see the truth"
-Howard Skipper-

3.1 Determination of HSA binding

HSA binding experiments were performed as previously described [244]. The mobile phase consisted of a binary gradient system with a constant total flow rate of 0.5 mL/min. Mobile phase A was a 50 mM pH 6.9 NH_4OAc-solution, mobile phase B was 2-Propanol (RP-HPLC grade, VWR, Germany). The gradient of mobile phase A was 100% from 0 to 3 min and from 3 min to the end of each run mobile phase B was set 20%. At each experimental day, the column was calibrated with nine reference substances to confirm the performance and to establish the non-linear regression. PSMA inhibitors were dissolved in a 0.5 mg/mL concentration in a mixture of 2-Propanol and NH_4OAc-buffer (50 mM pH 6.9) (1/1; *v/v*). For each run, 10 µL of the solution containing the inhibitor was injected into the RP-HPLC system and the retention time measured. The literature HSA binding [%] was obtained from Valko et. al. or Yamazaki et al. [244,245]. Non-linear regression was established with OriginPro 2016G.

3.2 Determination of lipophilicity and blood cell distribution

Lipophilicity: The radiolabeled PSMA inhibitor (0.5 to 1.0 MBq) dissolved in PBS (500 µL, pH = 7.4), was added to n-octanol (500 µL) in a reaction vial (1.5 mL), which was rigorously vortexed for 3 min (n = 6). For quantitative phase separation, the mixture was centrifuged at 6,000 g for 5 min (Biofuge 15, Heraus Sepatech, Osterode, Germany). The activity from samples of each phase (100 µL) were measured in a γ-counter to obtain the $\log P_{(o/w)}$ value.

Blood cell binding: Human blood samples (approx. 1.0 mL) from ethylenediaminetetraacetic acid (EDTA) coated vials were incubated for 15 min with a solution (225 µL) of the respective ^{177}Lu-labeled PSMA inhibitor (1.0 nM) and with either PBS or 2-PMPA solution (25 µL, respectively, 100 µM 2-PMPA) in reaction vials. Separation of the different blood cells was accomplished by stepwise centrifugation. Erythrocytes were gained after centrifugation at 700 g (1,400 rpm, Biofuge 15, Heraus Sepatech, Osterode, Germany) for 5 min. The resulting pellet was rinsed with ice-cold PBS (500 µL) and again centrifuged (700 g, 5 min). Leukocytes were gained by combination of the supernatant and subsequent centrifugation at 3,100 g for 5 min (6,200 rpm). The resulting pellet was washed with ice-cold PBS (500 µL) and the centrifugation repeated. The activities of the pellets (erythrocytes and leukocytes) and the supernatant were measured in a γ-counter. PSMA specific binding was determined by co-incubation with 2-PMPA solution (100 µM).

3.3 Bradford-assay

The Bradford-assay was conducted as already described with minor modifications [246]. To establish a linear regression curve, four different concentrations of BSA-containing solutions were prepared (0.2, 0.5, 0.8 and 1.0 mg/mL) in *buffer-B* (see **chapter II 4.1.2.1**). The blank probe contained only *buffer-B*. The preparation of the probes for measurement was achieved by mixing the respective BSA-containing solution (30 µL) and the *Bradford-reagent* (1.5 mL) in acrylic (PMMA) cuvettes. The cuvettes were kept for 4 min at RT and the extinction measured at $\lambda = 595$ nm. Each concentration was measured in triplicate. The measured values were used to establish the linear regression curve. Analog to the calibration probes, the S9 liver and kidney fractions (30 µL) were mixed with *Bradford-reagent* (1.5 ml) and measured at $\lambda =$ 595 nm to determine the protein concentration of the S9-fractions.

Bradford-reagent: Coomassie Brilliant Blue G (5.0 mg, Sigma Aldrich, Germany) was dissolved in a mixture containing MeOH (5.0 mL), 85% H_3PO_4 (10 mL) and water (85 ml). The mixture was filtered and kept at 4°C under light exclusion.

3.4 Cell experiments

Cell culture: PSMA-positive LNCAP cells (300265; Cell Lines Service GmbH) were cultivated in Dulbecco modified Eagle medium/Nutrition Mixture F-12 (1/1) (DMEM-F12, Biochrom) supplemented with fetal calf serum (FCS) (10%, Biochrom) and kept at 37°C in a humidified CO_2 atmosphere (5%). One day (24 h ± 2 h) prior to all experiments with LNCaP cells, the cultivated cells were harvested using a mixture of trypsin/ethylendiaminetetraacetate (0.05%/ 0.02%) and PBS and centrifuged. After centrifugation, the supernatant was disposed and the cell pellet resuspended in culture medium. Afterwards, cells were counted with a hemocytometer (Neubauer) and seeded in 24-well plates. IC_{50} values were determined transferring 150,000 cells/mL per well into 24-well plates, whereas internalization rates were obtained by transferring 125,000 cells/mL per well into 24-well PLL-coated plates.

3.4.1 Affinity (IC_{50})

After removal of the culture medium, the cells were treated once with HBSS (500 µL, Hank's balanced salt solution, Biochrom, Berlin, Germany, with addition of 1% BSA) and left 15 min on ice for equilibration in HBSS (200 µL, 1% BSA). Next, solutions (25 µL per well) containing either HBSS (1% BSA, control) or the respective ligand in increasing concentration (10^{-10} to 10^{-4} M in HBSS (1% BSA)) were added with subsequent addition of ([^{125}I]I-BA)KuE (25 µL, 2.0 nM) in HBSS (1% BSA). All experiments were performed at least three times for each concentration. After 60 min incubation on ice, the experiment was terminated by removal of the medium and consecutive rinsing with HBSS (200 µL). The media of both steps were combined in one fraction and represent the amount of free radioligand. Afterwards, the cells were lysed with NaOH (250 µL, 1.0 M) and united with the HBSS (200 µL) of the following

washing step. Quantification of bound and free radioligand was accomplished in a γ-counter.

3.4.2 Internalization

Subsequent to the removal of the culture medium, the cells were washed once with DMEM-F12-solution (500 µL, 5% BSA) and left to equilibrate for at least 15 min at 37°C in DMEM-F12-solution (200 µL, 5% BSA). Afterwards, each well was treated with either DMEM-F12-solution (25 µL, 5% BSA) or 2-PMPA-solution (25 µL, 100 µM) for blockade. Next, the respective ^{68}Ga- or ^{177}Lu-labeled PSMA inhibitor (25 µL; 2.0 nM and 10 nM, respectively) was added and the cells incubated at 37°C for 5, 15, 30 and 60 min, respectively. The experiment was terminated by placing the 24-well plate on ice for 3 min and the consecutive removal of the medium. Each well was rinsed with HBSS (250 µL) and the fractions from these first two steps combined, representing the amount of free radioligand. Removal of surface bound activity was accomplished by incubation of the cells with ice-cold 2-PMPA-solution (250 µL, 10 µM in PBS) for 5 min and subsequent rinsing with ice-cold PBS (250 µL). The internalized activity was determined through incubation of the cells in NaOH (250 µL, 1.0 M) and the combination with the fraction of the subsequent washing step with again NaOH (250 µL, 1.0 M). Each experiment (control and blockade) was performed in triplicate for each time point. Free, surface bound and internalized activity was quantified in a γ-counter.

3.4.3 Externalization

Externalization kinetics of the radiolabeled PSMA inhibitors were determined using LNCaP cells, which were similarly prepared as described for the internalization assay. After an initial cell-washing step with DMEM-F12-solution (5% BSA), the cells were left to recondition for at least 15 min at 37°C. Subsequently, the LNCaP cells were incubated with the respective radiolabeled peptide (25 µL, 10.0 nM) at 37°C for 60 min in a total volume of 250 µL in each well. After 60 min, the supernatant with the unbound free fraction was removed and measured in a γ-counter for the calculation of total added radioactivity. An acid wash step was avoided to warrant enzyme integrity during the following externalization and recycling study. To determine the recycling rate, fresh DMEM-F12-solution (250 µL, 5% BSA) was given to the cells to allow re-internalization. In contrast, re-internalization was inhibited by addition of DMEM-F12-solution containing 2-PMPA (225 µL DMEM-F12 (5% BSA) and 25 µL of 100 µM 2-PMPA-solution (PBS)). The cells were then incubated for 0, 20, 40 and 60 min at 37°C. Consequently, the supernatant was removed and the cells were washed with ice-cold HBSS (250 µL). The combination of the supernatant and the volume of the concomitant washing step with HBSS (200 µL) account for externalized radioligand at the investigated time point. Further, the cells were then washed with ice-cold 2-PMPA HBSS solution (250 µL, 10 µM) twice, combined and thus represented the fraction of membrane-bound radioligand. The determination of the internalized fraction was achieved by lysis as described for the

internalization assay with NaOH (250 µL, 1.0 M). The activities of free, externalized, membrane-bound and internalized radioligand were quantified in a γ-counter.

4. *In vivo* experiments

4.1 Animal experiments

All animal experiments were carried out in accordance with the general animal welfare regulations in Germany (Deutsches Tierschutzgesetz, approval #55.2-1-54-2532-71-13). For the tumor model, LNCaP cells (approx. 10^7 cells) were suspended in serum-free DMEM-F12 medium and Matrigel (1/1; *v/v*) (BD Biosciences, Germany) and inoculated onto the right shoulder of male, 6 to 8 weeks old CB-17 SCID mice (Charles River Laboratories, Sulzfeld, Germany). Animals were used after the tumor size reached 4 to 8 mm in diameter for experiments.

4.1.1 *In vivo* metabolism

In vivo metabolism was determined using 20 to 25 MBq of the respective ^{177}Lu-labeled PSMA inhibitors, which were injected into the tail vein of healthy CB17-SCID mice. The animals were subsequently sacrificed after 60 min. Samples of the urine and blood were immediately taken. Kidneys were frozen with liquid nitrogen, homogenized and extracted with 2-PMPA solution (500 µL, 400 µM in PBS) in a reaction vial. After centrifugation (15,000 g for 5 min) of the reaction vial, the suspension was ultra-filtrated and analyzed by radio-RP-HPLC. The blood samples were centrifuged at 6,000 g for 5 min to obtain the plasma. To remove the proteins from the plasma, ice-cold MeCN was added (1/1; *v/v*) to the samples and incubated for 10 min at 4°C. After concomitant centrifugation and ultrafiltration, the samples were analyzed by radio-RP-HPLC. The urine samples were used without any further purification.

4.1.2 *In vitro* S9-metabolism

4.1.2.1 Preparation of the S9-fractions

The preparation of the murine S9-liver and kidney fractions was performed as previously published with minor modifications [247]. Prior to the extractions of the organs, all solutions and instruments were cooled on ice for at least 30 min. Each S9-batch contained four or five male CB-17 SCID mice (> 6 months). The average body weight (BW) before tissue extraction was 32.05 g ± 1.59 g comprising approx. 1.7% kidney and 4.9% liver weight. All animals were sacrificed without fasting by cervical dislocation. Afterwards, the thorax was opened by vertical incisions to expose the heart. The caval vein was severed and the left heart chamber cannulated with a needle, which was connected to isotonic NaCl-solution to perfuse the internal organs and blood vessels to remove the residual blood. After the first perfusion step with isotonic NaCl-solution (30 mL), a second perfusion step with *buffer-A* (30 mL) was conducted. Finally, the livers and kidneys were completely removed and the gall bladder separated from each liver.

To assure complete removal of blood, all samples were in addition punctuated with a syringe, containing *buffer-A*, at different locations and perfused until the organs appeared pale pink. The processed organs were dried with paper towels and weighted. In the next step, the liver and kidney samples were separately cut with a scalpel to small pieces in a mortar and twice as much *buffer-B* added, so that the total weight consisted out of 1/3 tissue and 2/3 *buffer-B*. The heterogeneous solution was homogenized using a pestle for about 10 min. The homogenized solution was transferred into a chilled tube and centrifuged (10,000 g; 20 min; 4°C). After centrifugation, the supernatant was aliquoted into cryo-vials and stored under nitrogen atmosphere utilization.

Buffer-A: HBSS (985.4 mL; with Ca^{2+}/Mg^{2+}, 0.35 g/L $NaHCO_3$, without phenol red) was treated with aq. EDTA-solution (4.6 mL, 0.26 M) and aq. HEPES-solution (10 mL, 1.0 M). The resulting pH was adjusted using NaOH-solution (1.0 M) to reach pH = 7.8.

Buffer-B: Tris·HCl-solution (800 mL, 50 mM) was mixed with KCl-solution (150 mL, 1.0 M), EDTA-solution (4.0 mL, 50.0 mM) and with D/L-Dithiotreitol-solution (10 mL, 100 mM). To this mixture was given sucrose (85.6 g) and the final pH adjusted using KOH-solution (1.0 M) to reach pH = 7.8.

4.1.2.2 S9-metabolism assay procedure

The assay was conducted by mixing DMEM-solution (33.3 vol.%) with the radiolabeled peptide (2.0 nmol/L) and the respective S9-kidney or liver-fraction. The final volume was adjusted to 100 % through the addition of *buffer-B*. The protein concentration in the S9-kidney assay was adjusted to 5 mg/mL and 7.0 mg/mL when conducting the S9-liver assay through the addition of the S9-stock solutions. To exclude other reason than enzymatic metabolism for metabolite formation, the procedure was conducted a second time with heat-denaturized proteins (same protein concentration) by heating the S9-fractions for 10 min at 95°C. After mixing of all components in 0.5 mL micro reaction tubes (Eppendorf, Hamburg Germany), the reaction tubes were placed in a Biometra UNO Thermoblock (Biometra GmbH, Göttingen, Germany) and kept at 37°C. After a respective time point, the reaction tube was placed in an oil bath at 95°C for 10 min to stop the metabolism. Alternatively, MeCN (20 vol.%) was added to the reaction tubes to denaturize the enzymes. Afterwards, the denaturized reaction mixtures were centrifuged in polyether sulfone ultrafiltration vials (low-protein binding, 30 kDa, VWR International GmbH, Darmstadt, Germany) for 30 min at 5,000 rpm (Heraeus PICO 17 centrifuge). Finally, the centrifuged fractions were evaluated via radio-RP-HPLC and compared with the quality control (QC) chromatograms of the radiolabeled peptides. Since all tracer were ^{177}Lu-labeled as described in chapter **II 2.6**, it was accepted that the radiolabeled peptides and hence their metabolites are stable under these conditions.

4.1.3 PET

Imaging experiments were conducted using a Siemens Inveon small animal PET and the data analyzed by the associated Inveon Research Workplace software. Mice were anaesthetized with isoflurane and approx. 4.0 to 17 MBq of the ^{68}Ga-labeled compounds were injected via tail vein (approx. 150 to 300 µL). Dynamic imaging was carried out after on-bed injection for 90 min. The static blockade image was obtained after 1 h p.i. with 15 min acquisition time. PSMA-blockade was achieved by coinjection of 8 mg/kg of 2-PMPA-solution (PBS). All images were reconstructed using an OSEM3D algorithm without scanner and attenuation correction.

4.1.4 Biodistribution

Approximately 4.0 to 12.0 MBq (approx. 150 to 300 µL) of the respective ^{68}Ga- or ^{177}Lu-labeled PSMA inhibitors were injected into the tail vein of LNCaP tumor-bearing male CB-17 SCID mice, which were sacrificed after a specific timeframe (n = 4, respectively). Selected organs were removed, weighted and measured in a γ-counter.

4.1.5 Quantitative autoradiography of murine kidneys

Autoradiographic kidney images of healthy CB-17 SCID mice were achieved using a Microtome Cryostat HM500 OM (Microm International GmbH, Walldorf, Germany) and a Medical CR 35 Bio high-speed image plate scanner (Raytest, Straubenhardt, Germany). Sequential transversal tissue slices of frozen kidneys were obtained in 20 µm thickness at -20°C. The frozen slices were thaw-mounted on circular cover glass inlays and subsequently transferred into 24-well plates, which were afterwards frozen on dry ice and kept refrigerated until further utilization. The frozen 24-well plates were allowed to preincubate on ice for 30 min and were subsequently washed once with ice-cold HBSS (500 µL, 1% BSA) and left to equilibrate for 15 min on ice in HBSS (200 µL, 1% BSA). Next, solutions (25 µL per well) containing either HBSS (1% BSA, control) or the respective ligand in increasing concentration (10^{-10} to 10^{-4} M in HBSS (1% BSA)), were added with subsequent addition of ([^{125}I]I-BA)KuE (25 µL, 2..0 nM) in HBSS (1% BSA). After 60 min incubation on ice, the experiments were terminated by removal of the medium and consecutive rinsing with ice-cold HBSS (200 µL). The circular glass inlays, with the fixed tissue sections, were afterwards removed from the 24-well plates and placed in apposition to phosphor screens (X-Ray Casette 8 x 10, Rego X-Ray Gmbh, Augsburg, Germany) for 14 d. Images were evaluated using AIDA software (Raytest, Straubenhardt, Germany).

III. RESULTS AND DISCUSSION

"Insanity: doing the same thing over and over again and expecting different results"
-Albert Einstein-

1. *In vitro* evaluation

1.1 EuK-based PSMA inhibitors

Based on the reference compound **PSMA I&T** [194], the molecular structure of the PSMA inhibitors was divided into four essential areas (see Figure 11). Earlier results of our group indicated that the chelator and the peptide spacer are highly influencing the pharmacokinetic profile regarding tumor and kidney uptake [193,194]. Further, previously published reports demonstrated that the linker region influences internalization and affinity [163,206]. The EuK scaffold proved to be highly effective in order to increase the affinity towards PSMA and was therefore implemented as binding motif, which displays the fourth essential part [140].

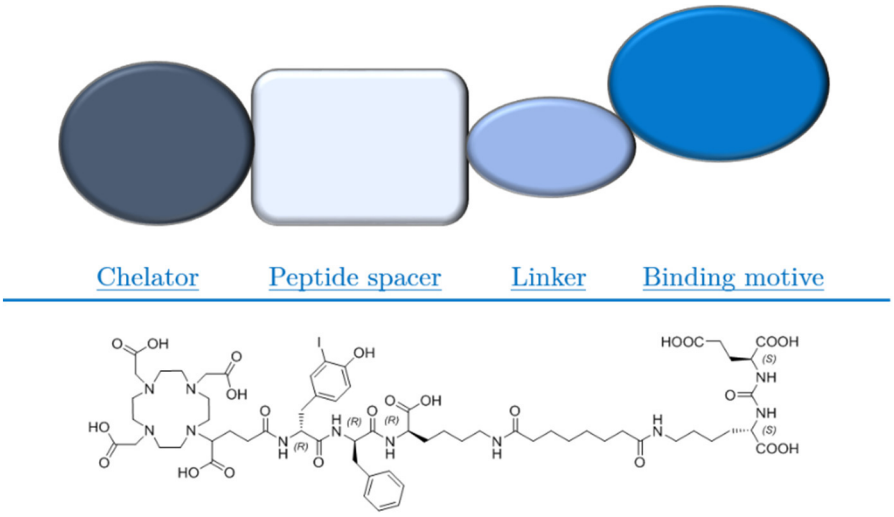

Figure 11. Illustration of the four essential molecular units of PSMA inhibitors evaluated in this study and exemplary **PSMA I&T**

In order to investigate specific effects of modifications within the essential areas, the following sections are divided into EuK- and EuE-based PSMA inhibitors and the respective sub-categories. To improve the comparability, the references **PSMA I&T** and **PSMA-617** are included and were likewise evaluated [194,206,248].

1.1.1 Influence of a free amino group

The pharmacophore of PSMA enables high affinity binding of glutamic acid residues through the interaction with positively charged amino acids of the enzyme [159,249-251]. In this respect, it seems reasonable to avoid modifications within the binding pocket of PSMA, which exhibit repulsive charge characteristics. Huang et al. indicated that the evolution of the PSMA enzyme directed the overall composition of the enzyme towards structures, as for instance the tunnel region, being receptive for negatively charged molecules [252]. However, despite many conducted SAR studies, only little is known about the influence of a free positive charge, emanating from e.g. a free amino group within the peptide spacer and linker region, on the *in vitro* and *in vivo* characteristics of PSMA inhibitors. To investigate this effect and the dependence on the position within the PSMA inhibitor, D-lysine was introduced into **PSMA I&T**, resulting in peptide spacer with alternating order of D-lysine, D-phenylalanine and D-3-iodo-tyrosine (Figure 12). Additionally, L-aminosuberic acid was used to introduce a free amine group into the linker. These modifications facilitated the investigation whether charge induced repulsive effects deteriorate affinity towards PSMA and if the tunnel region is able to encompass such residues.

Table 4. Summary of all parameter *in vitro* investigated for PSMA inhibitors with a free amino group and the reference **PSMA I&T**. The half maximal inhibitory concentration (IC_{50}) of the PSMA inhibitors was determined in a competitive binding assay using LNCaP cell (1.5 * 10^5 cells/well, 1 h, 4°C, HBSS + 1% BSA) and ([^{125}I]I-BA)KuE as radioligand. Internalized activity expressed in [%] as relative cellular uptake to ([^{125}I]I-BA)KuE (1.25 * 10^5 cells/well, PLL-coated plates, c = 0.2 nM for ([^{125}I]I-BA)KuE and c = 1.0 nM for ^{177}Lu-labeled PSMA inhibitors, DMEM/F-12 + 5% BSA, 37°C, 60 min). Data are corrected for non-specific binding (10 µM 2-PMPA). IC_{50} and internalization data are expressed as mean ± SD (n=3). Lipophilicity expressed as log*P* (distribution coefficient in n-octanol/PBS) of radiolabeled PSMA inhibitor. Data for log*P* expressed as mean ± SD (n=6). Albumin binding (HSA) expressed in [%] after logarithmic plotting and calibration (n=1). Spacer sequence describes the *N*- to *C*-terminal peptide spacer structure and the linking unit suberic (Sub) acid or L-aminosuberic (Asu) acid. n.d. = not determined. * = data obtained from Wirtz et al [204].

PSMA inhibitor	Spacer sequence	IC_{50} [nM]	Internalization [%]	log*P*	HSA [%]
[$^{nat/177}$Lu]**PSMA I&T**	-y(3-I)fk-	7.9 ± 2.4*	75.5 ± 1.6*	-4.12 ± 0.11*	78.6
[$^{nat/177}$Lu]**PSMA-8**	-y(3-I)fk(**Asu**)-	31.6 ± 0.8	n.d.	n.d.	16.5
[$^{nat/177}$Lu]**PSMA-9**	-y(3-I)f**k**k(Sub-	6.9 ± 1.9	49.4 ± 2.9	-3.51 ± 0.07	34.5
[$^{nat/177}$Lu]**PSMA-10**	-y(3-I)f-***N*^{6}-k**k(Sub-	414.7 ± 38.5	n.d.	n.d.	25.2
[$^{nat/177}$Lu]**PSMA-11**	-y(3-I)**k**fk(Sub-	4.8 ± 0.6	34.2 ± 1.6	-3.48 ± 0.15	34.9
[$^{nat/177}$Lu]**PSMA-12**	-y(3-I)-***N*^{6}-k**fk(Sub-	35.6 ± 13.2	36.6 ± 2.7	-3.59 ± 0.10	47.4
[$^{nat/177}$Lu]**PSMA-13**	-**k**y(3-I)fk(Sub-	6.9 ± 0.2	40.5 ± 1.9	-3.57 ± 0.06	34.3
[$^{nat/177}$Lu]**PSMA-14**	-***N*^{6}-k**y(3-I)fk(Sub--	8.2 ± 1.0	66.4 ± 0.8	-3.50 ± 0.19	56.0
[$^{nat/177}$Lu]**PSMA-16**	-**f(4-NH$_2$)**y(3-I)fk-	2.3 ± 0.6	122.2 ± 1.6	- 4.11 ± 0.06	82.5

The determined IC_{50} values, internalization capacities as well as the log*P* and HSA binding values are shown in Table 4. Compared to the reference ligand [^{nat}Lu]**PSMA I&T**, only the ligands [^{nat}Lu]**PSMA-8**, [^{nat}Lu]**PSMA-12** and especially [^{nat}Lu]**PSMA-10** showed a pronounced decline of affinity, indicating a negative influence on binding possibly due to charge-repulsion. London et. al showed that "hot-spot"-binding is essentially responsible for protein-peptide interactions and that specific structures are necessary to obtain high affinity [253]. A loss of one "hot-spot" ultimately leads to inferior affinity and might therefore explain the significant lower affinity of [^{nat}Lu]**PSMA-10**. All other compounds exhibited affinities in the range of approx. 2 to 8 nM, being similar to the reference [^{nat}Lu]**PSMA I&T**. Interestingly, the new developed derivatives harboring a *N*-terminal connected D-lysine were throughout more affine than their side-chain coupled analogs. This observation is not transferable on the internalization capacities, in which all derivatives except for [^{nat}Lu]**PSMA-16** exhibited lower cellular uptake compared to the reference. The similar log*P*-values of the derivatives [^{177}Lu]**PSMA-8** to [^{177}Lu]**PSMA-14** are reasonable, since these compounds differ only in their position and conjugation of D-lysine.

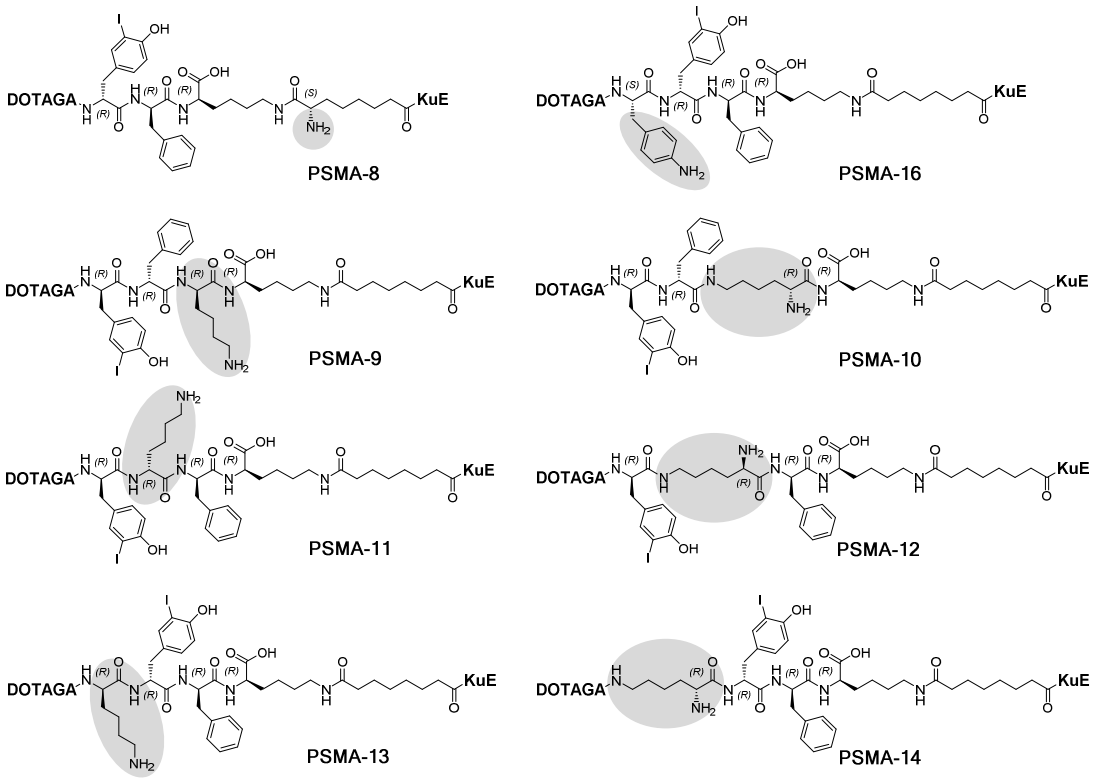

Figure 12. Structural overview of the PSMA ligands (**PSMA-8** to **PSMA-14** and **PSMA-16**) with a positive charge. The into the **PSMA I&T** scaffold introduced structural modifications are highlighted in grey.

The introduction of a free amino group caused in general a decline in human albumin binding (Table 4 and Figure 13) compared to the reference. Especially [^{nat}Lu]**PSMA-8** demonstrated an almost five fold drop compared to [^{nat}Lu]**PSMA I&T**. The derivatives with a free lysine

side chain, [^{nat}Lu]**PSMA-9**, [^{nat}Lu]**PSMA-11** and [^{nat}Lu]**PSMA-13**, displayed similar HSA-binding values of approx. 34%. Whereas in contrast to these inhibitors, the values for all side chain coupled compounds are increasing the broader the distance between the free amino group and binding motif becomes (see Figure 13), indicating that especially the structural parts close to the EuK binding motif are highly influencing albumin binding.

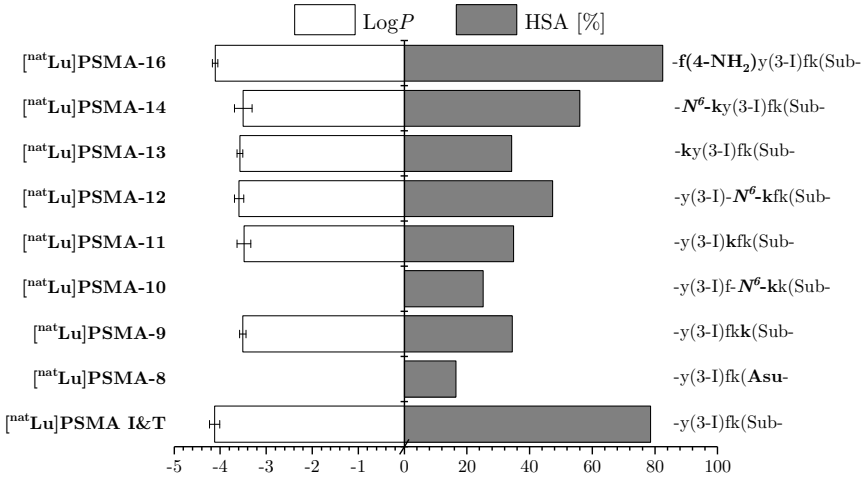

Figure 13. Binding to human serum albumin (HSA binding [%]) and measured log*P* value of the PSMA inhibitors with a free amino group and **PSMA I&T** as reference. Distinct decline in HSA binding was observed the closer the proximity between amino group and EuK-binding motif became, whereas log*P* was less affected.

Valko et al. and others showed that lipophilicity correlates with HSA binding, the obtained data demonstrated that slight differences in structural arrangement are further important components besides lipophilicity, which determine the albumin binding and thus the *in vivo* pharmacokinetics [244,254]. A further implication of these results is that the tunnel region of PSMA is able to encompass free aliphatic amino groups (pH = 7.4 *in vivo*; pk_s = 10.28) within the structure of the inhibitors at distinct positions without loss of affinity. The low binding value of [^{nat}Lu]**PSMA-8** implies that the incorporation of a positive charge in closer proximity (linker area) to the EuK-motif should be avoided. This is in agreement with the findings of Zhang et al., showing that the conjugation of glutamic acid to lysine or ornithine via urea-bridge deteriorates affinity, if the side chain amino group of lysine or ornithine remains unconjugated (Figure 14)[255].

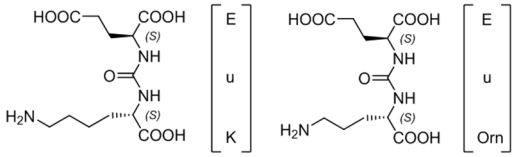

IC_{50} [nM]*	
EuK	381
EuOrn	271
2-PMPA	10

Figure 14. Structural illustration of the PSMA binding motifs EuK and EuOrn and their IC_{50} values towards PSMA. 2-PMPA was included for reference. * Data were obtained by Zhang et al [254].

The internalization capacities of the new developed compounds became slightly inferior compared to **PSMA I&T**. If the negative effect of a positive charge on the internalization rate is specific for PSMA inhibitors or just the outcome of this limited investigation remains not fully explored. Other reports demonstrated amplifying effects of positive charges on internalization as in the case of e.g. bombesin analogs [256].

The exception within this group is [$^{nat/177}$Lu]**PSMA-16**, displaying the highest affinity, internalization and HSA binding. The utilization of 4-amino-D-phenylalanine as fourth amino acid within the peptide spacer supports the conclusion that a positive charge and not the amino group itself partially reduces HSA binding, since the compounds [^{nat}Lu]**PSMA-13** and [^{nat}Lu]**PSMA-14**, holding D-lysine at the fourth position within the peptide spacer, display lower HSA binding values than [^{nat}Lu]**PSMA-16** and the aromatic amino group of **PSMA-16** remains unlikely to be charged at physiological pH (anilinium $pk_s = 4.58$).

Blood cell binding was investigated for [$^{nat/177}$Lu]**PSMA-16** and compared to [$^{nat/177}$Lu]**PSMA I&T** (Figure 15)**.**

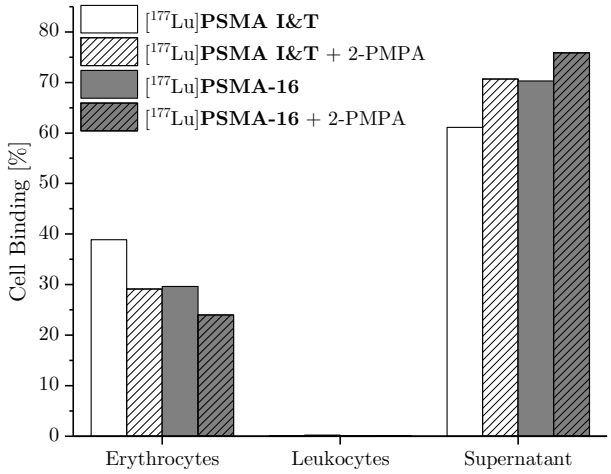

Figure 15. Blood cell binding of [^{177}Lu]**PSMA I&T** and [^{177}Lu]**PSMA-16**. Samples of 1.0 mL blood were incubated with approx. 1.0 MBq of the radiolabeled PSMA inhibitors and additonally for blockade with 100 µM 2-PMPA; Blood samples were stepwise centrifuged at 700 rpm for 5 min with two subsequent washing steps (PBS) to separate red blood cell fraction (erythrocytes). The combined supernatant was centrifuged at 6200 rpm for 5 min and again washed twice to obtain the white cell fraction (leukocytes) and separated from the supernatant. Equal volumes of each fraction were measured in a γ-counter.

In contrast to the reference [^{177}Lu]**PSMA I&T,** the 2-PMPA blockade was less pronounced for [^{177}Lu]**PSMA-16** and indicates that the binding to the red blood cells occurs predominantly in an unspecific manner for both investigated ligands. The higher fraction in the supernatant of [^{177}Lu]**PSMA-16** may be a consequence of the higher albumin binding (78.6% vs. 82.5%; ^{nat}Lu-analogs respectively).

The introduction of the aromatic residue in [^{nat}Lu]**PSMA-16** increased the internalization capacity compared to [^{nat}Lu]**PSMA I&T**. According to the current literature, it is not clear why some structural modifications increase the internalization rate and others not. Liu et al. stated that the mode of inhibition induces conformational changes of the protein, which either benefit or hinder the interaction of the cytoplasmatic tail of PSMA with clathrin and the clathrin adaptor protein-2 (AP- 2) complex [152,153].

The obtained data showed that the introduction of a positive charge within the PSMA inhibitor is in general possible. High affinity towards PSMA was maintained for most of the investigated inhibitors. However, internalization was negatively affected, which renders such modifications disadvantageous. On the other side, the reducing effect of a positive charge on HSA binding may be useful for imaging agents suffering from high plasma protein binding.

1.1.2 Influence of carbohydration

Therapeutic approaches with [^{177}Lu]**PSMA I&T** demonstrated efficiency, tolerability and high safety potential in patients receiving four to eight cycles of 7.4 GBq [215]. First dosimetric studies revealed, that tumor lesions received the highest doses followed by the kidneys and salivary glands [257]. The findings for the kidneys can be explained by the physiologic expression of PSMA and the renal elimination of the radiolabeled compound. Although the occasional occurring renal and hematological toxicities after endoradiotherapy in neuroendocrine tumors (NET) are usually reversible, there is legitimate concern about chronic toxicity especially in patients with relatively long survival rates as stated by Prasad et al. [215,257,258].

Carbohydration proved to be a reasonable modification to optimize compounds suffering from poor *in vivo* distribution patterns, mostly due to elevated lipophilicity with subsequent high hepatic and intestinal uptake [259]. On the other hand, attachment of sugar moieties often leads to accelerated renal clearance with overall lower kidney accumulation and was therefore evaluated [238,260-262].

The initial effort to find a suitable position for carbohydration of **PSMA I&T** uncovered the suberic acid linker area between the binding motif and the peptidic spacer as possible attachment site (Figure 16).

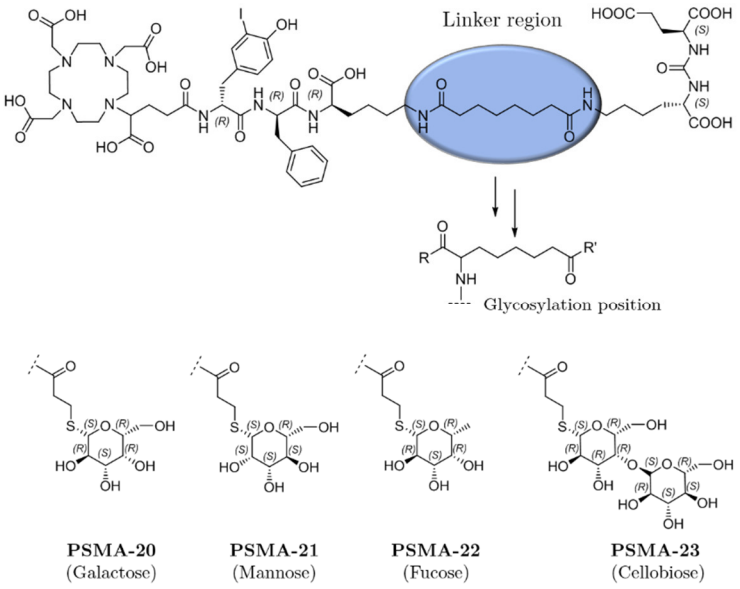

Figure 16. Illustration of the introduced conjugation-position (amino group) for carbohydration. The blue circle indicates the arbitrary linker region.

Compared to the reference ligand **PSMA I&T**, the monosaccharide-derivatives **PSMA-20** and **PSMA-21** displayed higher affinities towards PSMA irrespective of the complexed metal ion (^{nat}Ga or ^{nat}Lu), as shown in Table 5. The carbohydrate compounds showed the same trend as the reference ligand **PSMA I&T**, in which the ^{nat}Lu-labeled compounds possessed higher affinities as their respective ^{nat}Ga analogs, indicating the influence of the free carboxylic acid group of the chelator [224]. The different stereochemistry of **PSMA-20** and **PSMA-21** had almost no effect on affinity. The fucose derivative [^{nat}Lu]**PSMA-22** showed an IC_{50} value of 8.2 ± 0.5 nM, which is in the range of **PSMA I&T** but inferior to the others and was therefore not further evaluated.

The results in Table 5 demonstrated the tolerability of the enzyme PSMA against bulky hydrophilic moieties in close proximity to the S1' binding pocket. **PSMA I&T** was developed with the intention to interact in a bidentate mode with both, the PSMA-pharmacophore and the remote arene-binding site. The occurrence of bidentate binding might compensates the steric requirement of the sugar moieties. Moreover, the tunnel region of PSMA was reported to be partially tolerant towards structural modifications [158,263], which might explains that even the disaccharide-analog [^{nat}Lu]**PSMA-23** exhibited a moderately high affinity (IC_{50} = 12.5 ± 2.3 nM).

Table 5. Summary of all *in* parameter *vitro* investigated for carbohydrated PSMA inhibitors and the reference **PSMA I&T**. The half maximal inhibitory concentration (IC_{50}) of the PSMA inhibitors was determined in a competitive binding assay using LNCaP cell (1.5 * 10^5 cells/well, 1 h, 4°C, HBSS + 1% BSA) and ([^{125}I]I-BA)KuE as radioligand. Internalized activity expressed in [%] as relative cellular uptake to ([^{125}I]I-BA)KuE (1.25 * 10^5 cells/well, PLL-coated plates, c = 0.2 nM for ([^{125}I]I-BA)KuE and c = 1.0 nM for ^{177}Lu-labeled PSMA inhibitors, DMEM/F-12 + 5% BSA, 37°C, 60 min). Data are corrected for non-specific binding (10 µM 2-PMPA). IC_{50} and internalization data are expressed as mean ± SD (n=3). Lipophilicity expressed as log*P* (distribution coefficient in n-octanol/PBS) of radiolabeled PSMA inhibitors. Data for log*P* expressed as mean ± SD (n=6). Albumin binding (HSA) expressed in [%] after logarithmic plotting and calibration (n=1). n.d. = not determined. * = data obtained from Wirtz et al. [204].

PSMA inhibitor	Sugar-moiety	IC_{50} [nM]	Internalization [%]	log*P*	HSA [%
[$^{nat/68}$Ga]**PSMA I&T**	-	9.4 ± 2.9	59.2 ± 1.7	-4.31 ± 0.32	52.0
[$^{nat/177}$Lu]**PSMA I&T**		7.9 ± 2.4	75.5 ± 1.6	-4.12 ± 0.11	78.6
[$^{nat/68}$Ga]**PSMA-20**	Galactose	7.9 ± 3.9	18.7 ± 4.1	-4.15 ± 0.07	7.7
[$^{nat/177}$Lu]**PSMA-20**		5.8 ± 0.6	60.2 ± 2.8	-3.95 ± 0.12	23.3
[$^{nat/68}$Ga]**PSMA-21**	Mannose	7.1 ± 0.3	8.4 ± 0.2	-4.01 ± 0.08	7.6
[$^{nat/177}$Lu]**PSMA-21**		5.9 ± 0.5	35.3 ± 2.9	-3.85 ± 0.04	25.1
[$^{nat/68}$Ga]**PSMA-23**	Cellobiose	10.8 ± 1.7	4.0 ± 0.6	n.d.	6.9
[$^{nat/177}$Lu]**PSMA-23**		12.5 ± 2.3	22.3 ± 1.2	-4.04 ± 0.10	19.9

Whereas lipophilicity was only negligibly affected and resulted in log*P* values ≤ -3.85 for all investigated compounds, carbohydration had immense impact on the internalization rate. Compared to **PSMA I&T**, all carbohydrated compounds exhibited lower internalization values with the tendency of the ^{68}Ga-labeled inhibitors to internalize less by the factor of approximately four than their respective ^{177}Lu–analogs as shown in Figure 17 (**PSMA-20**), which is in concordance with previous reports [224,234]. Differences in the stereochemistry of **PSMA-20** and **PSMA-21** resulted in a slightly higher internalization rate of the galactose derivative. However, the highest obtained value of the ^{68}Ga-labeled compounds by [^{68}Ga]**PSMA-20** is still more than three times lower than for [^{68}Ga]**PSMA I&T** after 60 min.

Apparently, the sterically demanding carbohydrates interfere with the internalization process of PSMA and display the intolerability of bulky hydrophilic moieties within the tunnel region regarding this process. This finding is in contrast to previously published carbohydrated somatostatin derivatives, in which all carbohydrated compounds demonstrated higher internalization capacities than the reference [260].

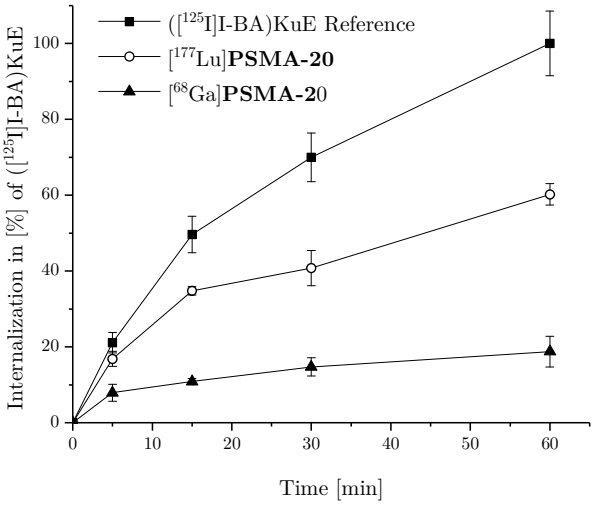

Figure 17. Relative cellular uptake kinetics of ^{177}Lu-and ^{68}Ga-labeled PSMA-20 in comparison to ([^{125}I]I-BA)KuE in LNCaP cells (37 °C, DMEM/F-12 + 5% BSA). Relative binding to ([^{125}I]I-BA)KuE was corrected for non-specific binding (10 µM 2-PMPA). All data are expressed as mean ± SD (n=3)

HSA binding of the carbohydrated compounds ranged from 6.9% for [^{nat}Ga]**PSMA-23** to 25.1% for [^{nat}Lu]**PSMA-21**. For each compound, albumin binding of the ^{nat}Ga-labeled analog was lower than for its ^{nat}Lu-analog, indicating again the influence of the metal-chelator complex. The disaccharide derivative **PSMA-23** exhibited the lowest measured values, irrespective of the complexed metal. Overall, carbohydration reduced considerably albumin binding in comparison to the reference **PSMA I&T**.

The albumin binding value is especially interesting for possible therapeutic applications, since the relationship between increased plasma protein binding and elongated *in vivo* half-life often results in higher enrichment of the compound within the target-tissue, as demonstrated for a radiolabeled folic acid compound [229]. In contrast, low plasma protein binding might be beneficial in terms of low background activity for high contrast PET imaging. Due to a higher unbound fraction in the blood pool, clearance of the remaining activity in the vascular system will occur faster, if the renal glomerular filtration is considered as the primarily contributing elimination process [264]. This feature of low plasma protein binding improves imaging contrast of radiolabeled PSMA tracer with high accumulation at the target side in combination with fast background clearance.

The influence of carbohydration on blood cell binding is shown in Figure 18. [^{177}Lu]**PSMA-20** and [^{177}Lu]**PSMA I&T** were incubated in human blood samples and stepwise centrifuged. Approx. 1.0 MBq of the respective radiolabeled PSMA ligands were incubated in the presence of 2-PMPA solution (100 µM) to differentiate between specific and unspecific binding. Binding to erythrocytes for [^{177}Lu]**PSMA I&T** was reduced from 38.9% to 29.2% by simultaneous

incubation with 2-PMPA. The resulting difference was not visible in the leukocyte fraction (0.1% vs. 0.2%) but in the supernatant, which increased from 61.1% to 70.7%. Regarding [^{177}Lu]**PSMA-20**, incubation with 2-PMPA had only minimal effect on the erythrocyte binding and increased, in contrary to the reference, the value from 26.0% to 29.5%. The difference was also found in the supernatant fraction.

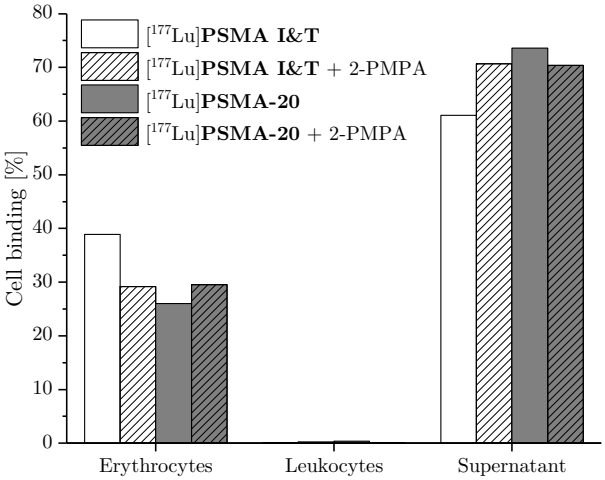

Figure 18. Blood cell binding of [^{177}Lu]**PSMA I&T** and [^{177}Lu]**PSMA-20**. Samples of 1.0 mL blood were incubated with approx. 1.0 MBq of the respective radiolabeled PSMA inhibitors with or without 100 µM 2-PMPA (blockade). Blood samples were stepwise centrifuged at 700 rpm for 5 min with two subsequent washing steps (PBS) to separate red blood cell fraction (erythrocytes). The combined supernatant was centrifuged at 6,200 rpm for 5 min and again washed twice to obtain the white cell fraction (leukocytes) and separated from the supernatant. Equal volumes of each fraction were measured in a γ-counter.

As a proof of concept, three small carbohydrated compounds where synthesized to investigate if the concept of carbohydration is transferable on PSMA inhibitors lacking the peptidic spacer and which are primarily designed for radiolabeling via oxime ligation with [^{18}F]fluorobenzaldehyde. The laborious synthesis of the linker structure incorporated in **PSMA-20** starting from Fmoc-L-Asu(O*t*Bu)-OH (chapter **III 1.1.3**), led to the structural change of the linker to a glycine/glutaric acid linkage as shown in Figure 19, which was more feasible to synthesize.

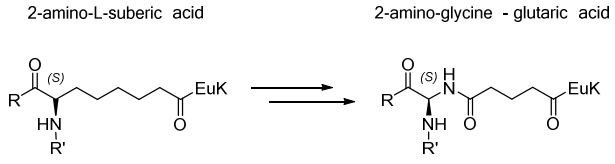

Figure 19. Transition from the L-aminosuberic acid-based linker to the synthetically more feasible 2-amino-glycine/glutaric acid linkage. R indicates peptide spacer and chelator; R' indicates sugar moiety.

Table 6. Summary of all parameter *in vitro* investigated for small carbohydrated PSMA inhibitors and the reference **PSMA I&T**. The half maximal inhibitory concentration (IC_{50}) of the PSMA inhibitors was determined in a competitive binding assay using LNCaP cell (1.5 * 10^5 cells/well, 1 h, 4°C, HBSS + 1% BSA) and ([^{125}I]I-BA)KuE as radioligand. IC_{50} data are expressed as mean ± SD (n=3). Albumin binding (HSA) expressed in [%] after logarithmic plotting and calibration (n=1). Spacer sequence describes the *N*- to *C*-terminal peptide spacer structure. * = data obtained from Wirtz et al. [204].

PSMA inhibitor	**Spacer sequence**	IC_{50} [nM]	**HSA** [%]
[^{nat}Ga]**PSMA I&T**		9.4 ± 2.9*	59.0
PSMA-24	F-BA-AOAc-k-	3.7 ± 0.8	30.4
PSMA-25	F-BA-AOAc-fk-	21.1 ± 0.8	n.d.
PSMA-26	F-BA-AOAc-y(3-I)fk-	3.5 ± 0.3	n.d.

The results given in Table 6 show that **PSMA-24** to **PSMA-26** inherited high affinities towards PSMA, in contrast to **PSMA-25**. The albumin binding of **PSMA-24** was found to be in the range of other investigated carbohydrated compounds (Table 5) and confirmed that carbohydration reduces binding of PSMA inhibitors to human albumin. The results further indicate that an extended peptide spacer in combination with a chelator is not necessary to induce high affinity towards PSMA. The observed high affinities render **PSMA-24** and **PSMA-26** as potential tracer for PCa imaging.

1.1.3 Combination of carbohydration and a positive charge

The combination of a fourth amino acid in the peptide spacer and carbohydration offered the possibility to evaluate if the additional amino acid 4-amino-D-phenylalanine is able to outbalance the observed low internalization rate upon carbohydration (chapter **III 1.1.2**) and if combinatorial inhibitor development is feasible and transferable.

Table 7. Summary of all parameter *in vitro* investigated for carbohydrated PSMA inhibitors and the reference **PSMA I&T** and **PSMA-16**. The half maximal inhibitory concentration (IC_{50}) of the PSMA inhibitors was determined in a competitive binding assay using LNCaP cell (1.5 * 10^5 cells/well, 1 h, 4°C, HBSS + 1% BSA) and ([^{125}I]I-BA)KuE as radioligand. Internalized activity expressed in [%] as relative cellular uptake to ([^{125}I]I-BA)KuE (1.25 * 10^5 cells/well, PLL-coated plates, c = 0.2 nM for ([^{125}I]I-BA)KuE and c = 1.0 nM for ^{177}Lu-labeled PSMA inhibitors, DMEM/F-12 + 5% BSA, 37°C, 60 min). Data are corrected for non-specific binding (10 µM 2-PMPA). IC_{50} and internalization data are expressed as mean ± SD (n=3). Lipophilicity expressed as log*P* (distribution coefficient in n-octanol/PBS) of radiolabeled PSMA inhibitors. Data for log*P* expressed as mean ± SD (n=6). Albumin binding (HSA) expressed in [%] after logarithmic plotting and calibration (n=1). Peptide sequence describes the *N*- to *C*-terminal structural composition without the chelator. n.d. = not determined. * = data obtained from Wirtz et al. [204].

PSMA inhibitor	Peptide sequence	IC_{50} [nM]	Internalization [%]	log*P*	HSA [%]
[$^{nat/177}$Lu]**PSMA I&T**	-y(3-I)fk(Sub-KuE)	7.9 ± 2.4*	75.5 ± 1.6*	- 4.12 ± 0.11*	78.6
[$^{nat/177}$Lu]**PSMA-16**	**-f(4-NH$_2$)**y(3-I)fk(Sub-KuE)	2.3 ± 0.6	122.2 ± 1.6	- 4.11 ± 0.06	82.5
[$^{nat/177}$Lu]**PSMA-27**	-(4-NH$_2$)y(3-I)fk(**L-Asu**[KuE]-MPA-**Galactose**)	5.4 ± 0.2	n.d.	n.d.	n.d.
[$^{nat/177}$Lu]**PSMA-28**	-f(4-NH$_2$)y(3-I)fk(**Agl**[MPA-**Galactose**]-Glut-KuE)	3.9 ± 0.3	31.8 ± 5.1	- 3.80 ± 0.12	29.4
[$^{nat/177}$Lu]**PSMA-29**	-f(4-NH-MPA-**Galactose**)y(3-I)fk(Agl[MPA-**Galactose**]-Glut-KuE)	5.7 ± 1.2	30.6 ± 1.6	- 3.80 ± 0.12	20.7

The carbohydrated compounds [^{nat}Lu]**PSMA-27** to [^{nat}Lu]**PSMA-29** showed IC_{50} values in the range of approx. 4.0 to 6.0 nM, demonstrating that the combination of 4-amino-L-phenylalanin and carbohydration is feasible regarding affinity as shown in Table 7. The exchange of the linker structure from Fmoc-L-Asu(O*t*Bu)-OH to a glycine/glutaric acid linkage increased even slightly the affinity towards PSMA when comparing [^{nat}Lu]**PSMA-27** to [^{nat}Lu]**PSMA-28**. Although the sole introduction of the fourth amino acid was beneficial for internalization, the effect was not transferable to the new developed compounds. Indicating that the influence of the sugar-moiety within the linker region on internalization is stronger than the alteration in the peptide spacer. These results lead to the conclusion, that structural modification influence affinity and internalization in different ways, which impedes the tracer development. Regarding HSA binding, the impact of carbohydration was again observable in a drastic decrease of albumin binding and was in concordance to the other carbohydrated PSMA compounds (chapter **III 1.1.2**).

The possibility to carbohydrate the peptide spacer was demonstrated with [^{nat}Lu]**PSMA-29**, in which the aromatic amino group of 4-amino-D-phenylalanin was conjugated with the galactose-derivative **22**. The high affinity of [^{nat}Lu]**PSMA-29** indicates that the tunnel region is able to incorporate large hydrophilic groups. This is in agreement with the findings of Huang et al., who showed that bulky residues, even exceeding the crystallographic determined axial dimensions of the tunnel region, are acceptable in the substrate tunnel [252,265]. However, due to the confined length of the tunnel region of PSMA (ca. 20 Å), it is arguable if the modifications of the peptide spacer at the *N*-terminal site are still located within the tunnel region of PSMA or if they interact with the topographical exosite of the enzyme.

1.1.4 Influence of the stereochemistry

The configuration of the amino acids used in the binding motif are crucial in order to warrant high affinity towards PSMA [140]. Especially D-isomers of binding motives, appeared to be less potent than their L-analogs [143]. However, the conducted investigations were focused predominantly on the binding motif itself, the influence of stereochemistry of pharmacophore-distant structures in PSMA inhibitors is less well characterized.

Based on the positive results after introduction of the fourth amino acid 4-amino-D-phenylalanine into the peptide spacer (**chapter III 1.1.1**), four stereoisomers of **PSMA-16** (Figure 20) were developed and either single or combined stereochemical alterations of the amino acids investigated and compared to the reference ligands **PSMA I&T** and **PSMA-617** [206].

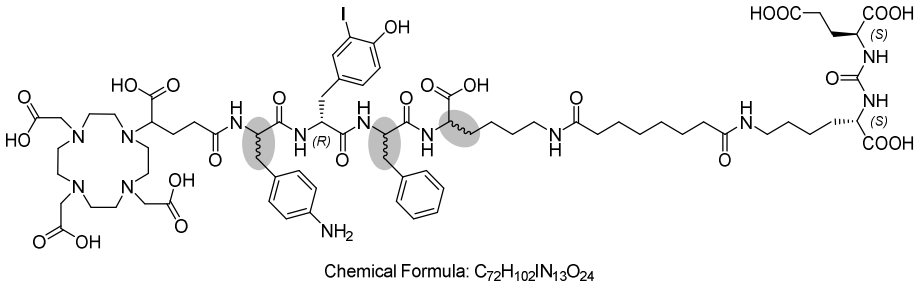

Figure 20. Molecular structure of the PSMA inhibitors **PSMA-15** to **PSMA-19**. Stereochemical centers, which were subject to D- to L amino acid change, are highlighted in grey.

The results in Table 8 show that the configuration of a single amino acid within the whole molecule influenced every measured *in vitro* parameter. The transfer from D- to L-4-amino-phenylalanine in [^{177}Lu]**PSMA-15** increased the internalization rate compared to [$^{nat/177}$Lu]**PSMA-16** and elevated HSA binding to almost 92%. Exchange of D- to L-lysine in [$^{nat/177}$Lu]**PSMA-17** had also a positive effect on internalization, but on the other hand lowered the albumin binding. Exchange of lysine and phenylalanine to the L-isomer in [$^{nat/177}$Lu]**PSMA-**

18 diminished the beneficial effect of the fourth amino acid and lowered the *in vitro* parameter to the level of the reference ligand [$^{nat/177}$Lu]**PSMA I&T**.

A complete D- to L-transfer was avoided due to the possible emanating metabolic instability *in vivo*, which was shown in earlier studies of our group [193,266]. The influence of D- and L-configuration on the metabolic stability is discussed in chapter **III 2.2**.

Table 8. Summary of all parameter *in vitro* investigated for the stereoisomeric PSMA inhibitors **PSMA-15** to **PSMA-19** and the references **PSMA I&T** and **PSMA-617**. The half maximal inhibitory concentration (IC_{50}) of the PSMA inhibitors was determined in a competitive binding assay using LNCaP cell (1.5 * 10^5 cells/well, 1 h, 4°C, HBSS + 1% BSA) and ([^{125}I]I-BA)KuE as radioligand. Internalized activity expressed in [%] as relative cellular uptake to ([^{125}I]I-BA)KuE (1.25 * 10^5 cells/well, PLL-coated plates, c = 0.2 nM for ([^{125}I]I-BA)KuE and c = 1.0 nM for ^{177}Lu-labeled PSMA inhibitors, DMEM/F-12 + 5% BSA, 37°C, 60 min). Data are corrected for non-specific binding (10 µM 2-PMPA). IC_{50} and internalization data are expressed as mean ± SD (n=3). Lipophilicity expressed as log*P* (distribution coefficient in n-octanol/PBS) of radiolabeled PSMA inhibitors. Data for log*P* expressed as mean ± SD (n=6). Albumin binding (HSA) expressed in [%] after logarithmic plotting and calibration (n = 1). Spacer sequence describes the *N*- to *C*-terminal peptide spacer configuration. n.d. = not determined. * = data obtained from Wirtz et al. [204].

PSMA inhibitor	Spacer sequence	IC_{50} [nM]	Internalization [%]	log*P*	HSA [%]
[$^{nat/177}$Lu]**PSMA I&T**	-y(3-I)fk-	7.9 ± 2.4*	75.5 ± 1.6*	-4.12 ± 0.11*	78.6
[$^{nat/177}$Lu]**PSMA-617**		3.8 ± 1.7	160.1 ± 1.5	n.d.	74.7
[$^{nat/177}$Lu]**PSMA-16**	-f(4-NH_2)y(3-I)fk-	2.3 ± 0.6	122.2 ± 1.6	- 4.11 ± 0.06	82.5
[$^{nat/177}$Lu]**PSMA-15**	-**F(4-NH_2)**y(3-I)fk-	2.8 ± 0.3	166.9 ± 2.4	n.d.	91.9
[$^{nat/177}$Lu]**PSMA-17**	-f(4-NH_2)y(3-I)f**K**-	2.5 ± 0.9	129.5 ± 11.0	n.d.	68.5
[$^{nat/177}$Lu]**PSMA-18**	-f(4-NH_2)y(3-I)**FK**-	9.5 ± 0.7	75.0 ± 2.0	n.d.	78.1
[$^{nat/177}$Lu]**PSMA-19**	-**F(4-NH_2)**y(3-I)f**K**-	8.2 ± 4.8	158.8 ± 4.8	n.d.	89.6

The first and last position in L-configuration of the peptide spacer seemed to be favorable and were therefore evaluated ([$^{nat/177}$Lu]**PSMA-19)**. Compared to [$^{nat/177}$Lu]**PSMA-15**, the internalization rate remained high for [$^{nat/177}$Lu]**PSMA-19**, however the affinity was reduced more than threefold. The results of this limited study imply that either the first or the last amino acid in L-configuration exhibits a beneficial effect on the *in vitro* parameters. They further imply, that stereochemistry plays a fundamental role regarding PSMA inhibitor development and that simple alterations may induce drastic effects.

To evaluate the influence of increased internalization on the retention of [^{177}Lu]**PSMA-15** and [^{177}Lu]**PSMA-16** in LNCaP cells more precisely, the externalization kinetics of the two ligands were determined and compared to the reference ligands [^{177}Lu]**PSMA I&T** and [^{177}Lu]**PSMA-617**.

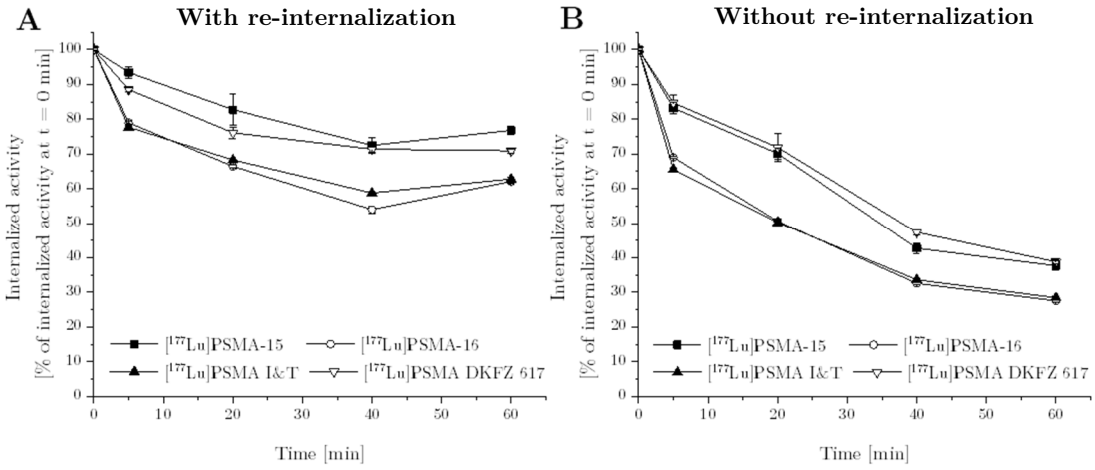

Figure 21. Externalization kinetics of selected ^{177}Lu-labeled PSMA inhibitors from LNCaP cells. 1.25 * 10^5 cells/well were incubated 1 h with the respective radioligand (c = 1.0 nM) at 37 °C in DMEM-medium (5% BSA). Then, the supernatant was removed and once washed with DMEM-medium (5% BSA, 37 °C). Afterwards, either **A**) only DMEM-medium (5% BSA) or **B**) competition DMEM-medium (5% BSA, 10 µM 2-PMPA) were added for replacement. The total cellular internalized activity at t = 0 min was corrected for non-specific binding (10 µM 2-PMPA) and normalized to 100%. All data are expressed as mean ± SD (n=3).

Without the presence of the PSMA inhibitor 2-PMPA (Figure 21 A), re-internalization was allowed and resulted in the highest measured value of 76.8% remaining intracellular activity after 1 h for [^{177}Lu]**PSMA-15**, followed by 70.9% for [^{177}Lu]**PSMA-617**. Although the *in vitro* internalization capacity is higher for [^{177}Lu]**PSMA-16** than for [^{177}Lu]**PSMA I&T**, almost no difference was seen in the intracellular fraction after 1 h (62.1% vs. 62.8%; respectively). Competition with 100 µM 2-PMPA solution resulted in a drastic clearance from the tumor cells for all evaluated ligands (Figure 21 B), demonstrating the importance of re-internalization within this biological system. However, the remaining intracellular activity was approx. 10% higher for [^{177}Lu]**PSMA-15** and [^{177}Lu]**PSMA-617** in comparison to the other two ligands.

High internalization, and the associated re-internalization, should lead to a pronounced retention of the radiolabeled ligand at the target side *in vivo* and is considered as key component next to affinity for PSMA inhibitors to enable high tumor uptake and maintenance *in vivo* after intravenous injection [156,194]. This is especially important in terms of endoradiotherapy, since the efficiency of treatment is essentially time and dose dependent [267-269].

1.1.5 Influence of the peptide sequence

The investigations of Wirtz et al. showed that exchange of the amino acid sequence of the peptide spacer, in particular the transfer of 3-iodo-D-tyrosine to D-tyrosine and D-phenylalanine to D-2-naphtylalanine (Figure 22), resulted in higher affinity and internalization for **PSMA-30** compared to the reference compound **PSMA I&T** (Table 9) [204]. The altered peptide sequence was designed to optimize the interactions with the lipophilic pockets of PSMA. A further improvement is the avoidance of iodine in the new developed structure, since reports showed that cleavage and deiodination of 3-iodo-tyrosine occur *in vivo*, even if the extent can only be marginal [270-273].

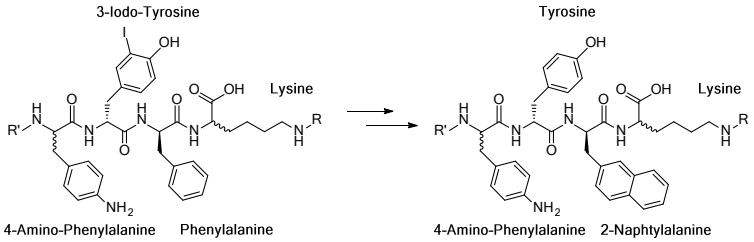

Figure 22. Structural illustration of the peptide spacer transition. 3-iodo-tyrosine was altered to tyrosine and phenylalanine to 2-naphtlylalanine. R = sub(KuE); R' = chelator (DOTAGA).

To assess whether the positive results after peptide spacer extension (chapter **III 1.1.1**) and stereochemical optimization (**III 1.1.4**) are combinable with the new amino acid sequence in **PSMA-30**, the new ligands **PSMA-31** to **PSMA-34** were synthesized and evaluated.

Table 9. Summary of all parameter *in vitro* investigated for the stereoisomeric PSMA inhibitors **PSMA-31** to **PSMA-34** and the references **PSMA I&T**, **PSMA-30** and **PSMA-15**. The half maximal inhibitory concentration (IC_{50}) of the PSMA inhibitors was determined in a competitive binding assay using LNCaP cell (1.5 * 10^5 cells/well, 1 h, 4°C, HBSS + 1% BSA) and ([^{125}I]I-BA)KuE as radioligand. Internalized activity expressed in [%] as relative cellular uptake to ([^{125}I]I-BA)KuE (1.25 * 10^5 cells/well, PLL-coated plates, c = 0.2 nM for ([^{125}I]I-BA)KuE and c = 1.0 nM for ^{177}Lu-labeled PSMA inhibitors, DMEM/F-12 + 5% BSA, 37°C, 60 min). Data are corrected for non-specific binding (10 µM 2-PMPA). IC_{50} and internalization data are expressed as mean ± SD (n=3). Lipophilicity expressed as log*P* (distribution coefficient in n-octanol/PBS) of radiolabeled PSMA inhibitors. Data for log*P* expressed as mean ± SD (n=6). Albumin binding (HSA) expressed in [%] after logarithmic plotting and calibration (n=1). Configuration describes the *N*- to *C*-terminal structural composition of the peptide spacer without the chelator. n.d. = not determined. * = data obtained from Wirtz et al. [204].

PSMA inhibitor	Configuration	IC_{50} [nM]	Internalization [%]	log*P*	HSA [%]
[$^{nat/177}$Lu]**PSMA I&T**	-y(3-I)fk-	7.9 ± 2.4*	75.5 ± 1.6*	-4.12 ± 0.11*	78.6
[$^{nat/177}$Lu]**PSMA-30**	-y-2-nal-k-	2.1 ± 0.8*	77.3 ± 0.7*	- 4.11 ± 0.06*	82.6
[$^{nat/177}$Lu]**PSMA-15**	-**F(4-NH$_2$)**y(3-I)fk-	2.8 ± 0.3	166.9 ± 2.4	n.d.	91.9
[$^{nat/177}$Lu]**PSMA-31**	-**F(4-NH$_2$)**y-2-nal-k-	1.1 ± 0.1	108.8 ± 2.5	- 3.74 ± 0.16	83.2
[$^{nat/177}$Lu]**PSMA-32**	-f(4-NH$_2$)y-2-nal-k-	5.8 ± 1.0	111.3 ± 11.1	n.d.	n.d.
[$^{nat/177}$Lu]**PSMA-33**	-f(4-NH$_2$)y-2-nal-**K**-	8.8 ± 3.4	177.7 ± 5.9	n.d.	88.2

[$^{nat/177}$Lu]**PSMA-34**	**-F(4-NH$_2$)**y-2-nal-**K**-	6.5 ± 1.3	183.2 ± 7.9	n.d.	77.4

The results in Table 9 illustrate that the introduction of 4-amino-phenylalanine and the influence of the stereochemistry are not simply transferable and that each modification has to be evaluated separately. Comparing [^{nat}Lu]**PSMA-30** and [^{nat}Lu]**PSMA-31**, an almost twofold increase in affinity occurred through the extension of the peptide spacer with 4-amino-L-phenylalanine, enabling the highest affinity measured in the context of this work. However, only a moderate increase of the cellular uptake was observable. This is in contrast to [^{177}Lu]**PSMA-15**, in which the internalization increased more than twofold after the same peptide spacer extension. The application of two L-configured amino acids was again beneficial regarding internalization and resulted in 183.2% for [^{177}Lu]**PSMA-34**. The impact on affinity was highly dependent on the respective configuration and did not correlate with the results for the PSMA ligands with the -y(3-I)fk- scaffold (Table 8).

In this context, the introduction of 4-amino-phenyalanin proved to enhance the overall *in vitro* parameter for the investigated PSMA inhibitors. It further implies that the extension and variation of the peptide spacer probably enables further improvement with so far unexploited potential.

1.1.6 Influence of the linker

Wirtz et al. and others showed that the linker region highly influences the pharmacokinetic parameter and thus the biodistribution of PSMA inhibitors [155,162,163,204]. Whereas the findings of Zhang et al. disclosed the influence of spacer length on affinity through a bidentate binding mode, Benešová et al. emphasized the importance of aromatic moieties between the pharmacophore and the chelator to increase the internalization rate. However, the only investigations regarding linker influence on plasma protein binding were conducted in our group, which showed that the introduction of 4-iodo-D-phenylalanine into the linker region of **PSMA-30** increases plasma-protein binding (PPB) of **PSMA-43** (Figure 23) [204].

Figure 23. Illustration of the effect of linker-modification with 4-iodo-D-phenylalanine on PPB. Suberic acid was replaced through glutaric acid and 4-iodo-D-phenylalanin to ensure similar structure length. R = peptide spacer and chelator.

As a consequence of the restrained glomerular filtration of compounds with high PPB, an increase of biological half-life *in vivo* is achievable which in turn enables prolonged addressing of target expressing tissues.

Due to the limited information about the transferability and extension of this modification, several compounds were synthesized and evaluated in comparison to the references **PSMA I&T**, **PSMA-30** and **PSMA-43**. Further, the feasible possibility to conjugate structures via acetylation of **PSMA-8** was used to assess the degree of steric freedom within the linker region regarding affinity and internalization of the PSMA inhibitors.

Table 10. Summary of all parameter *in vitro* investigated for the stereoisomeric PSMA inhibitors **PSMA-35** to **PSMA-43** and the references **PSMA I&T**, **PSMA-30** and **PSMA-43** [204]. The half maximal inhibitory concentration (IC_{50}) of the PSMA inhibitors was determined in a competitive binding assay using LNCaP cell (1.5 * 10^5 cells/well, 1 h, 4°C, HBSS + 1% BSA) and ([^{125}I]I-BA)KuE as radioligand. Internalized activity expressed in [%] as relative cellular uptake to ([^{125}I]I-BA)KuE (1.25 * 10^5 cells/well, PLL-coated plates, c = 0.2 nM for ([^{125}I]I-BA)KuE and c = 1.0 nM for ^{177}Lu-labeled PSMA inhibitors, DMEM/F-12 + 5% BSA, 37°C, 60 min). Data are corrected for non-specific binding (10 µM 2-PMPA). IC_{50} and internalization data are expressed as mean ± SD (n=3). Lipophilicity expressed as log*P* (distribution coefficient in n-octanol/PBS) of radiolabeled PSMA inhibitors. Data for log*P* expressed as mean ± SD (n=6). Albumin binding (HSA) expressed in [%] after logarithmic plotting and calibration (n=1). Configuration describes simplified the *N*- to *C*-terminal structural composition of the peptide spacer and linker without the chelator. n.d. = not determined. * = data taken from Wirtz et al. [204].

PSMA inhibitor	Configuration	IC_{50} [nM]	Internalization [%]	log*P*	HSA [%]
[$^{nat/177}$Lu]**PSMA I&T**	-y(3-I)fk-	7.9 ± 2.4*	75.5 ± 1.6*	-4.12 ± 0.11*	78.6
[$^{nat/177}$Lu]**PSMA-30**	-y-2-nal-k-	2.1 ± 0.8*	77.3 ± 0.7*	- 4.11 ± 0.06*	82.6
[$^{nat/177}$Lu]**PSMA-43**	-y-2-nal-k- || -f(4-I)-	6.1 ± 1.6*	118. 6 ± 0.5*	-3.05 ± 0.02*	96.6
[$^{nat/177}$Lu]**PSMA-40**	-f(4-NH_2)y(3-I)fk- || -f(4-I)-	7.0 ± 1.0	119.1 ± 7.3	-3.66 ± 0.06	96.5
[$^{nat/177}$Lu]**PSMA-41**	-f(4-NH_2)y-2-nal-k- || -f(4-I)-	6.8 ± 3.2	155.1 ± 7.9	-3.47 ± 0.24	97.6
[$^{nat/177}$Lu]**PSMA-42**	-f(4-NH_2)y-2-nal-**K**- || -f(4-I)-	4.6 ± 0.8	153.9 ± 10.1	n.d.	96.9
[$^{nat/177}$Lu]**PSMA-38**	-f(4-NH_2)y(3-I)fk- || -**PBP**-	122 ± 59	4.0 ± 1.7	-2.93 ± 0.12	> 99
[$^{nat/177}$Lu]**PSMA-39**	-f(4-NH_2)y(3-I)fk- || -***C*^{4}-e-PBP**-	622 ± 152	2.1 ± 0.6	-1.51 ± 0.05	> 99
[$^{nat/177}$Lu]**PSMA-35**	-y(3-I)fk- || -**BA**-	23.0 ± 8.4	n.d.	n.d.	n.d.
[$^{nat/177}$Lu]**PSMA-36**	-y(3-I)fk- || -**2,4-DNBA**-	5.3 ± 1.0	189.8 ± 37.5	n.d.	82.5
[$^{nat/177}$Lu]**PSMA-37**	-y(3-I)fk- || -**DMBA**-	10.6 ± 0.4	n.d.	n.d.	n.d.

Table 10 shows that the insertion of 4-iodo-D-phenylalanine into the linker increases HSA binding with only minor influence on internalization or affinity (**PSMA-40** to **PSMA-42**). The introduction of 4-amino-phenylalanine into the peptide spacer increased the hydrophilicity, internalization and affinity of [^{177}Lu]**PSMA-41** compared to [^{177}Lu]**PSMA-43**, proving the overall beneficial effect of this peptide spacer extension.

However, the exchange of 4-iodo-D-phenylalanine ([^{nat}Lu]**PSMA-41)** to the more lipophilic modifications 4'-(pentyloxy)-[1,1'-biphenyl]-4-carboxylic acid ([^{nat}Lu]**PSMA-38**) and its D-glutamate derivative ([^{nat}Lu]**PSMA-39**) shown in Figure 24, impaired affinity and internalization drastically, albeit it was possible to achieve HSA binding-values of > 99%.

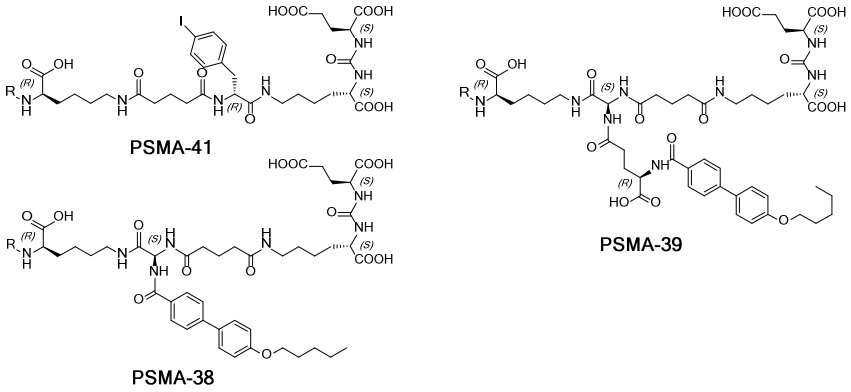

Figure 24. Illustration of the linker-modified PSMA inhibitors **PSMA-41**, **PSMA-38** and **PSMA-39**. R = DOTAGA-f(4-NH_2)y(3-I)f- .

The additional glutamate residue in [^{nat}Lu]**PSMA-39** lowered the affinity more than fivefold compared to [^{nat}Lu]**PSMA-38**, indicating that the available space in the enzyme at this position is either limited or the interaction with the enzyme unfavorable. It further implies, that through greater lipophilicity of the linker, HSA binding of the PSMA ligands becomes stronger which is in agreement with the general findings of Valko et al. [244]. The poor *in vitro* parameter (affinity and internalization) may also be attributable to the immense albumin binding. The applied *in vitro* assays in this work contain 1.0 to 5.0% BSA, which is able to bind endogenous ligands and xenogeneic drugs in large magnitude at multiple drug binding sites [226,227]. The interaction with albumin affects the free drug concentration and thus attenuates the drug potency in the respective *in vitro* system. Even if the investigated compounds exhibit affinities several magnitudes higher towards the target than to albumin or other serum proteins, target occupancy (PSMA) is influenced by the equilibrium towards albumin due to its abundance in the *in vitro* assays and will thus negatively influence the apparent results [227]. Shift-assays (alternating plasma protein concentrations in the *in vitro* system) are readily conducted during drug-development in order to correct the affinity for plasma protein binding [274]. However, albumin and other possible plasma proteins are ubiquitary distributed *in vivo* and

thus ultimately influence the pharmacokinetics of xenogeneic drugs. Validity of such shift-assays regarding *in vivo* efficacy seems doubtful and emphasizes the necessity of preclinical studies [226].

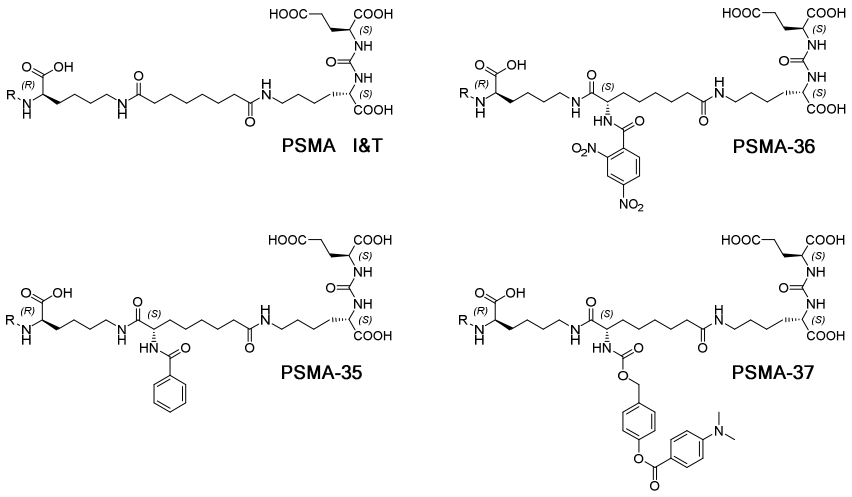

Figure 25. Illustration of **PSMA I&T** and the linker-modified PSMA inhibitors **PSMA-35**, **PSMA-36** and **PSMA-37**. R = DOTAGA-y(3-I)f- .

Comparing [^{nat}Lu]**PSMA I&T** and [^{nat}Lu]**PSMA-35** (Figure 25), the introduction of benzoic acid lowered the affinity almost threefold and was regarded unfavorable. In contrary, the more polar 2,4-dinitrobenzoic acid-residue in [$^{nat/177}$Lu]**PSMA-36** not only increased affinity, but also elevated considerably the cell uptake in comparison to [$^{nat/177}$Lu]**PSMA I&T** and exhibited almost no influence on HSA binding (Table 10). Although the moiety in [^{nat}Lu]**PSMA-37** is sterically more demanding than the benzoic acid in [^{nat}Lu]**PSMA-35**, the compound still exhibited high affinity towards PSMA. Lipophilic protein ligand interactions are in general nonselective [275]. Selectivity may be achieved through spatially separated hydrophobic groups as described by Zhang et al. [155]. In this context, the higher affinity of [^{nat}Lu]**PSMA-37** in comparison to [^{nat}Lu]**PSMA-35** must be an unselective apolar interaction with the protein and thus implies that this particular position is receptive for sterically demanding hydrophobic structures.

The molecular recognition of nitro-groups as in [$^{nat/177}$Lu]**PSMA-36** depends on the intrinsic electronic characteristics of the nitro group itself and the hydrogen donation properties of the interacting structure. Considering that the oxygen atoms in nitro groups are relatively weak hydrogen bond acceptors, it is arguable if both nitro-groups of [^{nat}Lu]**PSMA-36** are involved in specific interactions or if the electron deficiency of the aromatic structure additionally supports binding [155,276]. However, electron-deficient aromatic systems are prone for strong π-stacking interactions with electron-rich arenes [277,278].

1.1.7 Influence of the chelator

In order to investigate if the exchange of the macrocyclic chelator DOTAGA to its analog DOTA influences the *in vitro* characteristics beneficially in combination with 4-amino-D-phenylalanine as illustrated in Figure 26, compound **PSMA-44** (DOTA-analog) was synthesized and evaluated in comparison to **PSMA-32** (DOTAGA-analog).

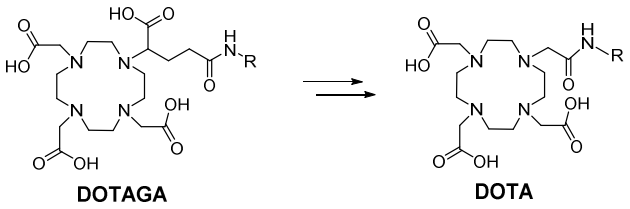

Figure 26. Illustration of the DOTAGA- to DOTA transfer in combination with 4-amino-D-phenylalanine in the peptide spacer of the PSMA inhibitor. R indicates peptide spacer linker and binding motif.

The results in Table 11 confirm the superiority of DOTAGA in [$^{nat/177}$Lu]**PSMA-32** over DOTA in [$^{nat/177}$Lu]**PSMA-44** as chelating agent concerning affinity and internalization and are in agreement with the findings of Wirtz and Eder et al. [193,204]. The additional carboxylic acid of DOTAGA not only improves the *in vitro* characteristics but also increases hydrophilicity, which is assumed to accelerate the renal *in vivo* clearance of the radiolabeled compounds [279].

Table 11. Summary of all parameter *in vitro* investigated for the DOTA-conjugated PSMA inhibitor **PSMA-44** and the references **PSMA I&T** and **PSMA-23**. The half maximal inhibitory concentration (IC_{50}) of the PSMA inhibitors was determined in a competitive binding assay using LNCaP cell (1.5 * 10^5 cells/well, 1 h, 4°C, HBSS + 1% BSA) and ([^{125}I]I-BA)KuE as radioligand. Internalized activity expressed in [%] as relative cellular uptake to ([^{125}I]I-BA)KuE (1.25 * 10^5 cells/well, PLL-coated plates, c = 0.2 nM for ([^{125}I]I-BA)KuE and c = 1.0 nM for ^{177}Lu-labeled PSMA inhibitors, DMEM/F-12 + 5% BSA, 37°C, 60 min). Data are corrected for non-specific binding (10 µM 2-PMPA). IC_{50} and internalization data are expressed as mean ± SD (n=3). Lipophilicity expressed as log*P* (distribution coefficient in n-octanol/PBS) of radiolabeled PSMA inhibitors. Data for log*P* expressed as mean ± SD (n=6). Albumin binding (HSA) expressed in [%] after logarithmic plotting and calibration (n=1). Spacer sequence describes the *N*- to *C*-terminal structural composition of the chelator and peptide spacer. n.d. = not determined. * = data obtained from Wirtz et al. [204].

PSMA inhibitor	Spacer sequence	IC_{50} [nM]	Internalization [%]	log*P*	HSA [%]
[$^{nat/177}$Lu]**PSMA I&T**	**DOTAGA**-y(3-I)fk-	7.9 ± 2.4*	75.5 ± 1.6*	-4.12 ± 0.11*	78.6
[$^{nat/177}$Lu]**PSMA-32**	**DOTAGA**-f(4-NH_2)-y-2-nal-k-	5.8 ± 1.0	111.3 ± 11.1	n.d.	n.d.
[$^{nat/177}$Lu]**PSMA-44**	**DOTA**-f(4-NH_2)-y-2-nal-k-	8.8 ± 3.2	98.8 ± 4.2	-2.95 ± 0.03	75.9

Recent findings of our and others groups emphasized the importance of the chelating agent and the complexed radionuclide itself [156,193,280]. The chelator and its coordination chemistry influences not only the affinity but also the internalization capacity and metabolic stability as shown for **PSMA I&S**. The change of L-amino acids in the chelator to its D-isomers improved tremendously the metabolic stability and subsequently the *in vivo* biodistribution in mice, which enabled first clinical trials with positive results [188].

Pinpointing the exact SAR of the used chelator remains difficult and laborious. Wüstemann et al. supposed that the chelating entity plays an essential role regarding internalization whereas the binding motif and the linking unit are primarily involved in PSMA-targeting [156]. His results further suggest that internalization correlates to some degree with lipophilicity.

The influence of the chelator is not only seen for PSMA inhibitors but also for other targets and especially for CXCR4-directed compounds, in which the chelator-metal complex induces affinity variation over several magnitudes [281-283]. The influence of the chelator may not only be limited regarding affinity and internalization but it was also shown that it may changes the mode of binding, as the introduction of DOTA into a pan-somatostatin analog switched its antagonistic to a full agonistic behavior [284].

1.1.8 Influence of the binding motif

The binding motif itself displays the primary essential part in order to gain affinity towards PSMA. Currently, several different binding motifs have been described, of which the most feature common elements like a pentanedioic acid to mimic glutamate within the S1' binding pocket, a zinc-ion interacting structure and a moiety, which can reside within the S1 binding pocket or extend the ligand structure to the surface of the protein [140,142,158-160,285]. The glutamate mimic and zinc binding structures are, however, not sufficient to achieve high affinity [140,285]. The additional introduction of an L-glutamate or L-lysine into the P1 position is able to increase the affinity through salt bridge formation and other interactions (Figure 7 C). It further enables utilization of the side chains for derivatization [166,239].

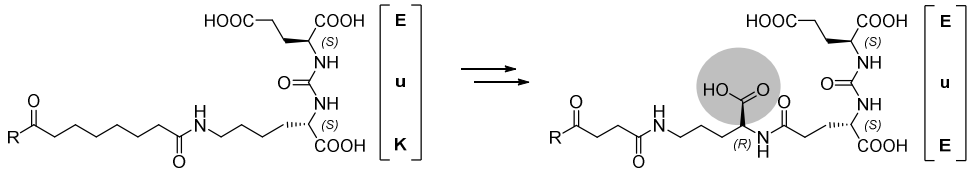

Figure 27. Transition from the EuK-based binding motif to the EuE-based scaffold. The scaffold switch enables the introduction of an additional carboxylic group (highlighted in grey).

The exchange of L-lysine (EuK) to L-glutamate (EuE) at the P1 position and the subsequent conjugation to D-ornithine and glutamic acid allowed the introduction of an additional carboxylic group while maintaining a similar linker length as shown in Figure 27.

The influence of the additional carboxylic group on the *in vitro* parameter of [$^{nat/177}$Lu]**PSMA-46** is shown in Table 12. The comparison demonstrates, that the affinity of [^{nat}Lu]**PSMA-46** is slightly lower than for its EuK analog [^{nat}Lu]**PSMA-30**. On the other side, cell uptake upon EuK to EuE switch increased almost threefold. At the same time higher hydrophilicity and lower HSA binding was achieved compared to references [^{nat}Lu]**PSMA I&T** and [^{nat}Lu]**PSMA-46**.

Table 12. Summary of all parameter *in vitro* investigated for the EuE based PSMA inhibitors **PSMA-46** and the references **PSMA I&T** and **PSMA-30**. The half maximal inhibitory concentration (IC_{50}) of the PSMA inhibitors was determined in a competitive binding assay using LNCaP cell (1.5 * 10^5 cells/well, 1 h, 4°C, HBSS + 1% BSA) and ([^{125}I]I-BA)KuE as radioligand. Internalized activity expressed in [%] as relative cellular uptake to ([^{125}I]I-BA)KuE (1.25 * 10^5 cells/well, PLL-coated plates, c = 0.2 nM for ([^{125}I]I-BA)KuE and c = 1.0 nM for ^{177}Lu-labeled PSMA inhibitors, DMEM/F-12 + 5% BSA, 37°C, 60 min). Data are corrected for non-specific binding (10 µM 2-PMPA). IC_{50} and internalization data are expressed as mean ± SD (n=3). Lipophilicity expressed as log*P* (distribution coefficient in n-octanol/PBS) of radiolabeled PSMA inhibitors. Data for log*P* expressed as mean ± SD (n=6). Albumin binding (HSA) expressed in [%] after logarithmic plotting and calibration (n=1). Structure describes simplified the *N*- to *C*-terminal structural composition of the peptide spacer and the binding motif. n.d. = not determined. * = data obtained from Wirtz et al. [204].

PSMA inhibitor	Structure	IC_{50} [nM]	Internalization [%]	log*P*	HSA [%]
[$^{nat/177}$Lu]**PSMA I&T**	-y(3-I)fk- || **-KuE**	7.9 ± 2.4*	75.5 ± 1.6*	-4.12 ± 0.11*	78.6
[$^{nat/177}$Lu]**PSMA-30**	-y-2-nal-k- || **-KuE**	2.1 ± 0.8*	77.3 ± 0.7*	-4.11 ± 0.06*	82.6
[$^{nat/177}$Lu]**PSMA-46**	-y-2-nal-k- || **-EuE**	3.2 ± 1.1	216.2 ± 9.2	-4.21 ± 0.08	57.7
[^{nat}Ga]**PSMA-46**	-y-2-nal-k- || **-EuE**	5.2 ± 2.7	n.d.	n.d.	n.d.

These results indicate that while the additional carboxylic group has only little impact on affinity, the internalization becomes dramatically affected as shown in Figure 28. It further shows that the additional negative charge inhibits albumin binding, which might be beneficial to accelerate the *in vivo* clearance and thus enable high contrast imaging.

Whether 'affinity' or 'internalization' is the more important parameter regarding the tumor uptake *in vivo* remains difficult to assess. Some reports emphasize that higher internalization correlates with increased tumor uptake and longer retention [156,286]. This is also supported by the findings of Young et al., in which the exchange of the chelator from HBED-CC to THP (tris(hydroxypyridinone)) lowered the affinity towards PSMA more than tenfold [287]. However, the conducted biodistribution studies in mice revealed similar tumor uptake and even slightly superior pharmacokinetics compared to **PSMA-HBED-CC** (**PSMA-11**) [199].

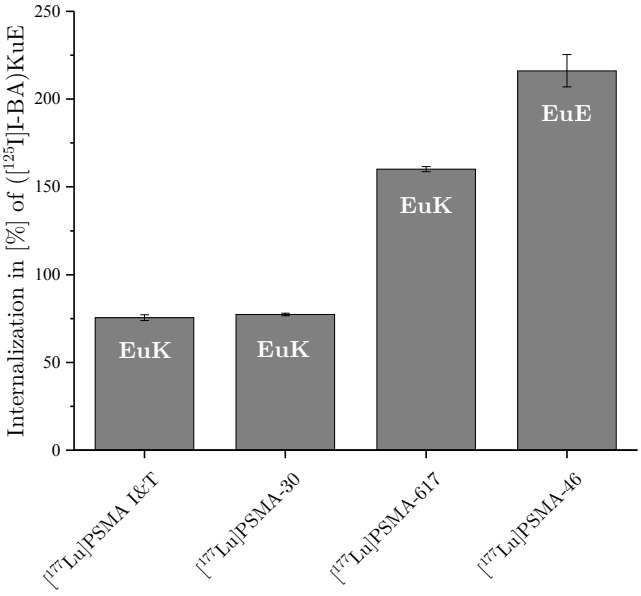

Figure 28. Illustration of the effect on internalization through the exchange of the binding scaffold from EuK to EuE. Whereas peptide sequence change had only little impact on internalization (**[^{177}Lu]PSMA-30** vs. **[^{177}Lu]PSMA I&T**), introduction of EuE increased cell uptake more than twofold (**[^{177}Lu]PSMA-46)**.

The results of Liu et al. imply that the mode of inhibition correlates with the internalization rate for phosphoramidate-based inhibitors. While pseudo irreversible inhibition was associated with high internalization, moderate and rapidly reversible compounds showed less intracellular uptake [152]. The group suggested that hydrophobic functionalities at the P1 site are necessary for π-stacking or lipophilic interactions with nearby aromatic residues of the enzyme while an additional carboxyl group at the P1 site interacts through salt-bridge formation with Arg536 (Figure 29). Yet, without crystallographic evaluation, it is arguable if the additional carboxyl group in **PSMA-46** interacts with an arginine residue in similar manner as described by Liu et al..

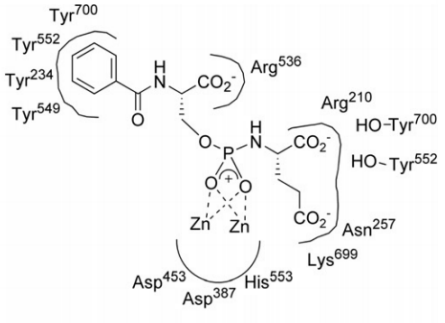

Figure 29. Proposed mechanism of the phosphoramidate peptidomimetic interaction with the pharmacophore of PSMA by Liu et al. [150].

1.2 EuE-based inhibitors

The extended information about the SAR of EuK-based PSMA inhibitors from the preceding chapters allowed the synthesis of new and improved compounds primarily based on the superior EuE binding scaffold. In order to broaden the knowledge about specific structural changes and their transferability, modifications of the peptide spacer and linker region were pursued and evaluated.

1.2.1 Influence of the stereochemistry

The stereochemical configuration and arrangement of the peptide sequence had enormous influence on the biological parameter affinity, internalization and HSA binding (chapter **III 1.1.1** and **1.1.5**). The combination of these modifications with EuE as binding motif (chapter **III 1.1.8**) was evaluated and compared to the references **PSMA I&T** and **PSMA-46**.

Table 13. Summary of all parameter *in vitro* investigated for the EuE-based PSMA inhibitors **PSMA-47** to **PSMA-51** and the references **PSMA I&T** and **PSMA-46**. The half maximal inhibitory concentration (IC_{50}) of the PSMA inhibitors was determined in a competitive binding assay using LNCaP cell (1.5 * 10^5 cells/well, 1 h, 4°C, HBSS + 1% BSA) and ([^{125}I]I-BA)KuE as radioligand. Internalized activity expressed in [%] as relative cellular uptake to ([^{125}I]I-BA)KuE (1.25 * 10^5 cells/well, PLL-coated plates, c = 0.2 nM for ([^{125}I]I-BA)KuE and c = 1.0 nM for ^{177}Lu-labeled PSMA inhibitors, DMEM/F-12 + 5% BSA, 37°C, 60 min). Data are corrected for non-specific binding (10 µM 2-PMPA). IC_{50} and internalization data are expressed as mean ± SD (n=3). Lipophilicity expressed as log*P* (distribution coefficient in n-octanol/PBS) of radiolabeled PSMA inhibitors. Data for log*P* expressed as mean ± SD (n=6). Albumin binding (HSA) expressed in [%] after logarithmic plotting and calibration (n=1). Structure describes simplified the *N*- to *C*-terminal structural composition of the peptide spacer and binding motif. n.d. = not determined. * = data obtained from Wirtz et al. [204]. ** indicates n=6.

PSMA inhibitor	Structure	IC_{50} [nM]	Internalization [%]	log*P*	HSA [%]
[$^{nat/177}$Lu]**PSMA I&T**	-y(3-I)fk- || **-KuE**	7.9 ± 2.4*	75.5 ± 1.6*	-4.12 ± 0.11*	78.6
[$^{nat/177}$Lu]**PSMA-46**	-y-2-nal-k- || **-EuE**	3.2 ± 1.1	216.2 ± 9.2	-4.21 ± 0.08	57.7
[$^{nat/177}$Lu]**PSMA-47**	**-F(4-NH$_2$)**y(3-I)fk- || **-EuE**	2.4 ± 0.3	5.7 ± 0.2**	-4.02 ± 0.2	83.2
[$^{nat/177}$Lu]**PSMA-48**	-f(4-NH$_2$)y(3-I)fk- || **-EuE**	2.6 ± 0.8	181.3 ± 4.1	-4.01 ± 0.08	61.2
[$^{nat/177}$Lu]**PSMA-49**	**-F(4-NH$_2$)**y-2-nal-k- || **-EuE**	2.5 ± 0.6	245.0 ± 4.2	-4.01 ± 0.11	74.2
[^{nat}Ga]**PSMA-49**	**-F(4-NH$_2$)**y-2-nal-k- || **-EuE**	3.3 ± 0.6	n.d.	n.d.	85.1
[$^{nat/177}$Lu]**PSMA-50**	-f(4-NH$_2$)y-2-nal-k- || **-EuE**	2.5 ± 0.6	207.3 ± 8.5	-4.02 ± 0.25	71.7
[^{nat}Ga]**PSMA-50**	-f(4-NH$_2$)y-2-nal-k- || **-EuE**	3.1 ± 0.2	n.d.	n.d.	84.4

[$^{nat/177}$Lu]**PSMA-51**	-f(4-NH_2)y-2-nal-**K**- || -**EuE**	2.3 ± 0.2	216.2 ± 4.3	-4.06 ± 0.08	50.9
[^{nat}Ga]**PSMA-51**	-f(4-NH_2)y-2-nal-**K**- || -**EuE**	3.1 ± 0.7	n.d.	n.d.	41.5

The findings in Table 13 confirmed the superiority of the peptide sequence -y-2-nal-k- over -y(3-I)fk- irrespective of the extension with 4-amino-phenylalanine (**PSMA-49** vs. **PSMA-47** and **PSMA-50** vs. **PSMA-48**) or the binding motif. L-configuration of 4-amino-phenylalanine in [^{177}Lu]**PSMA-49** asserted as the most potent modification regarding cellular uptake, which was more than threefold higher as for [^{177}Lu]**PSMA I&T** (245 ± 4.2% vs. 75.5 ± 1.6%, respectively). L-configuration of lysine or complete D-configuration in the peptide spacer, however, moderated the positive effect of the peptide spacer extension and impeded the *in vitro* characteristics. Interestingly, whereas the L-isomer of 4-amino-phenylalanine in [^{177}Lu]**PSMA-49** improved internalization, the positive effect was completely diminished upon utilization of -y(3-I)fk- in the peptide spacer-scaffold of [^{177}Lu]**PSMA-47** as shown in Figure **30**. All EuE-based ligands showed high affinities in the range of approx. 2 to 3 nM. The influence on albumin binding varied significantly, displaying values in the range of 41% to 85%.

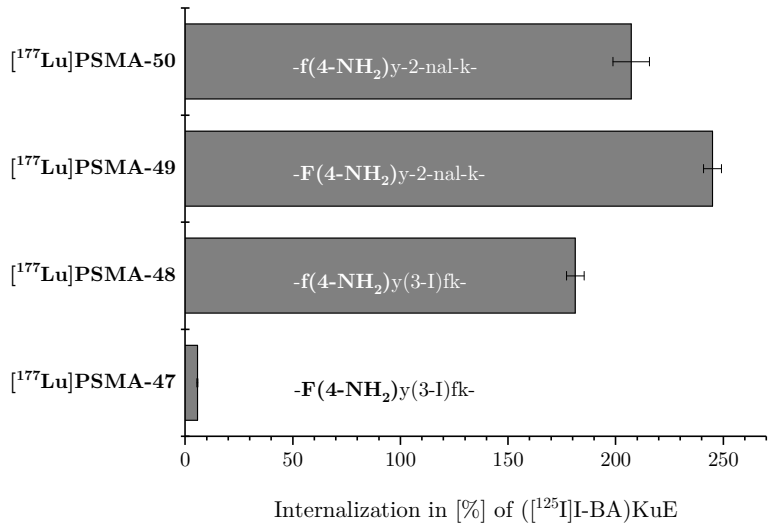

Figure 30. Illustration of peptide sequence- and stereochemistry influence on cellular uptake of selected EuE-based PSMA inhibitors.

As already observed in the previous chapters, even small modifications are able to exert enormous impact on the *in vitro* behavior of the PSMA ligands. Stereochemistry of the binding motif plays a fundamental role regarding affinity [140,142,143]. It is now also clear, that not only the configuration within or in close proximity to the binding motif is important, but also distant modifications can exert drastic influence on the *in vitro* parameter as in the case of **PSMA-47**.

1.2.2 Influence of the peptide spacer extension

The extension of the peptide spacer from three to four amino acids with 4-amino-L-phenylalanine proved to be beneficial (chapter **III 1.1.1** and **1.2.1**). Based on these findings it was reasonable to investigate the influence of the extension with other substitutions. The results of the combination with EuE as binding motif and -y-2-nal-k- as lead sequence of the peptide spacer are listed in Table 14.

Table 14. Summary of all parameter *in vitro* investigated for the EuE-based PSMA inhibitors **PSMA-52** to **PSMA-57** and **PSMA-67** and the references **PSMA I&T** and **PSMA-49**. The half maximal inhibitory concentration (IC_{50}) of the PSMA inhibitors was determined in a competitive binding assay using LNCaP cell (1.5 * 10^5 cells/well, 1 h, 4°C, HBSS + 1% BSA) and ([^{125}I]I-BA)KuE as radioligand. Internalized activity expressed in [%] as relative cellular uptake to ([^{125}I]I-BA)KuE (1.25 * 10^5 cells/well, PLL-coated plates, c = 0.2 nM for ([^{125}I]I-BA)KuE and c = 1.0 nM for ^{177}Lu-labeled PSMA inhibitors, DMEM/F-12 + 5% BSA, 37°C, 60 min). Data are corrected for non-specific binding (10 µM 2-PMPA). IC_{50} and internalization data are expressed as mean ± SD (n=3). Lipophilicity expressed as log*P* (distribution coefficient in n-octanol/PBS) of radiolabeled PSMA inhibitors. Data for log*P* expressed as mean ± SD (n=6). Albumin binding (HSA) expressed in [%] after logarithmic plotting and calibration (n=1). Spacer sequence describes simplified the *N*- to *C*-terminal structural composition of the peptide spacer. n.d. = not determined. * = data obtained from Wirtz et al. [204].

PSMA inhibitor	Spacer sequence	IC_{50} [nM]	Internalization [%]	log*P*	HSA [%]
[$^{nat/177}$Lu]**PSMA I&T**	-y(3-I)fk- **|| -KuE**	7.9 ± 2.4*	75.5 ± 1.6*	-4.12 ± 0.11*	78.6
[$^{nat/177}$Lu]**PSMA-49**	-F(4-NH_2)y-2-nal-k-	2.5 ± 0.6	245.0 ± 4.2	-4.01 ± 0.11	74.2
[$^{nat/177}$Lu]**PSMA-52**	**-F(4-NO_2)**y-2-nal-k-	3.4 ± 0.2	229.9 ± 8.0	-4.11 ± 0.07	95.4
[$^{nat/177}$Lu]**PSMA-53**	**-2,4-DNBA-Dap**-y-2-nal-k-	3.2 ± 0.5	293.6 ± 10.0	-4.08 ± 0.04	95.9
[$^{nat/177}$Lu]**PSMA-54**	-**Y**y-2-nal-k-	2.6 ± 0.4	199.1 ± 18.3	-4.27 ± 0.02	89.1
[$^{nat/177}$Lu]**PSMA-55**	-**2-Nal**-y-2-nal-k-	6.3 ± 1.8	223.6 ± 9.3	-4.11 ± 0.05	98.4
[$^{nat/177}$Lu]**PSMA-56**	-**K(PBP)**y-2-nal-k-	339.0 ± 39.1	25.6 ± 1.0	-2.23 ± 0.22	> 99
[$^{nat/177}$Lu]**PSMA-57**	-**K(*C*^{4}-e-PBP)**y-2-nal-k-	54.3 ± 2.3	27.1 ± 0.7	-2.12 ± 0.16	> 99
[$^{nat/177}$Lu]**PSMA-67**	-**2-Amet**-F(4-NH_2)y-2-nal-k-	4.5 ± 0.6	261.7 ± 4.8	-4.00 ± 0.22	74.7

The substitution of 4-amino-L-phenylalanine was primarily conducted with L-configured aromatic residues due to the reported lipophilic interactions with the arene binding site of PSMA and the identified favorable effect of L-isomers (**PSMA-49** vs. **PSMA-50**; chapter **III 1.2.1**) [155].

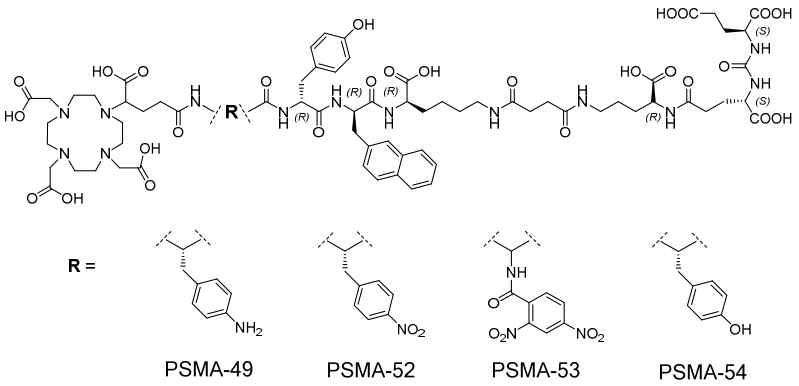

Figure 31. Illustration of the reference **PSMA-49** and the peptide spacer-modified PSMA inhibitors **PSMA-52**, **PSMA-53** and **PSMA-54**.

The substitution with L-tyrosine in [$^{nat/177}$Lu]**PSMA-54** resulted in similar *in vitro* characteristics compared to the reference ligand [$^{nat/177}$Lu]**PSMA-49**, however, internalization was reduced upon introduction of L-tyrosine. The utilization of 4-nitro-L-phenylalanine in [^{177}Lu]**PSMA-52** instead of L-tyrosine ([^{177}Lu]**PSMA-54)** was more favorable regarding internalization. Although affinity and intracellular uptake were slightly lower for [$^{nat/177}$Lu]**PSMA-52** compared to [$^{nat/177}$Lu]**PSMA-49**, it was noteworthy that the albumin binding increased to 95.4% for [^{177}Lu]**PSMA-52**, indicating a positive effect of the nitro group on albumin binding. The differences between **PSMA-49** and **PSMA-52** are probably caused through the changed electrostatic interactions of the aromatic systems (4-nitro-L-phenylalanine vs. 4-amino-L-phenylalanine). While the aromatic amino residue in **PSMA-49** possesses primarily electron donating function, the nitro-group in **PSMA-52** is a pure electron acceptor, which results in an electron deficient arene. Due to the influence of high HSA binding and the associated possible *in vitro* impairment, **PSMA-52** seemed promising for further modifications

PSMA-53 was developed to amplify the effect of electron-deficiency within the peptide spacer extension and resembled to some extent the compounds developed by Zhang et al. (dinitrophenyl-substituted EuK-based PSMA inhibitors)[155]. Utilization of 2,4-dinitrobenzoic acid increased the internalization to 293.6 ± 10.0%, while affinity and HSA binding remained similar compared to [$^{nat/177}$Lu]**PSMA-52**. Considering the positive effect on internalization after incorporation of 2,4-dinitrobenzoic acid into the linker region ([^{177}Lu]**PSMA-36**) and into the peptide spacer ([^{177}Lu]**PSMA-53**), the internalization process of PSMA seems to be receptive for electron deficient aromatic systems. Although the utilization of 2,4-dinitrobenzoic acid were found to be favorable regarding internalization, the reported toxicity of dinitro-substituted arenes is concerning and impedes the further application of nitro-substituted PSMA ligands [288-291].

PSMA-55 to **PSMA-57** are characterized through the introduction of an extended aromatic system to increase the hydrophobic interactions with the arene binding site and to elevate albumin binding (Figure 32). In comparison to [^{nat}Lu]**PSMA-49**, L-2-nal in [^{nat}Lu]**PSMA-55** decreased the affinity almost threefold. In contrast, the influence of L-2-nal on internalization remained moderate, while the interaction with albumin increased. Further amplification of the lipophilic interaction with albumin was achieved through the introduction of the residues PBP and *Cγ*-e-PBP in **PSMA-56** and **PSMA-57**, respectively. High HSA binding was accomplished but only on the expense of affinity and internalization for both ligands.

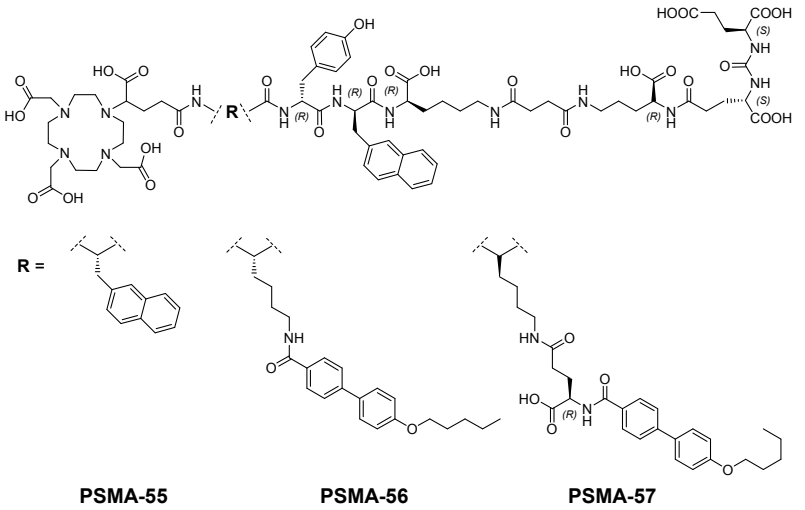

Figure 32. Illustration of the peptide spacer-modified PSMA inhibitors **PSMA-55**, **PSMA-56** and **PSMA-57**.

PSMA-67 (Figure 33) was developed to increase the metabolic degradation through the introduction of an ester-conjugation, which is discussed in chapter **III 2.2.5**. The introduction of 2-aminoethanol and succinic acid is associated with an extension of the distance between the peptide spacer and the chelator.

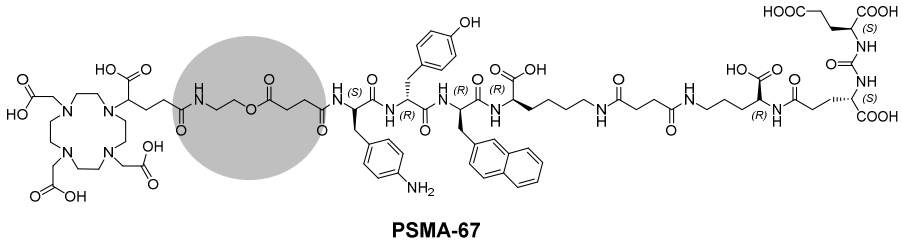

Figure 33. Illustration the ester-based PSMA inhibitor **PSMA-67**. The modified linkage is highlighted in grey.

Compared to the reference **PSMA-49,** the introduction of the new conjugation had only little impact on the *in vitro* parameter. While affinity and HSA binding was lowered, the internalization of [^{177}Lu]**PSMA-67** was increased. The results indicate that elongation of the inhibitor scaffold is conceivable for further modifications.

1.2.3 Influence of the linker

The combination of -F(4-NH_2)y-2-nal-k- in the peptide spacer (**PSMA-49**) and the EuE binding motif was evaluated in combination with several further modifications within the linker.

Table 15. Summary of all parameter *in vitro* investigated for the EuE-based PSMA inhibitors **PSMA-58** to **PSMA-63** and the references **PSMA I&T**, **PSMA-36** and **PSMA-49**. The half maximal inhibitory concentration (IC_{50}) of the PSMA inhibitors was determined in a competitive binding assay using LNCaP cell (1.5 * 10^5 cells/well, 1 h, 4°C, HBSS + 1% BSA) and ([^{125}I]I-BA)KuE as radioligand. Internalized activity expressed in [%] as relative cellular uptake to ([^{125}I]I-BA)KuE (1.25 * 10^5 cells/well, PLL-coated plates, c = 0.2 nM for ([^{125}I]I-BA)KuE and c = 1.0 nM for ^{177}Lu-labeled PSMA inhibitors, DMEM/F-12 + 5% BSA, 37°C, 60 min). Data are corrected for non-specific binding (10 µM 2-PMPA). IC_{50} and internalization data are expressed as mean ± SD (n=3). Lipophilicity expressed as log*P* (distribution coefficient in n-octanol/PBS) of radiolabeled PSMA inhibitors. Data for log*P* expressed as mean ± SD (n=6). Albumin binding (HSA) expressed in [%] after logarithmic plotting and calibration (n=1). Configuration describes simplified the *N*- to *C*-terminal structural composition of the linker and binding motif. n.d. = not determined. * = data obtained from Wirtz et al. [204].

PSMA inhibitor	Configuration	IC_{50} [nM]	Internalization [%]	log*P*	HSA [%]
[$^{nat/177}$Lu]**PSMA I&T**	-k(Sub-**KuE)**	7.9 ± 2.4*	75.5 ± 1.6*	-4.12 ± 0.11*	78.6
[$^{nat/177}$Lu]**PSMA-36**	-k(L-Asu(**KuE**))-**2,4-DNBA**	5.3 ± 1.0	189.8 ± 37.5	n.d.	82.5
[$^{nat/177}$Lu]**PSMA-49**	-k(Suc-N^5-orn-C^4-**EuE**)	2.5 ± 0.6	245.0 ± 4.2	-4.01 ± 0.11	74.2
[$^{nat/177}$Lu]**PSMA-58**	-e(**r**-G-N^5-orn-C^4-**EuE**)	7.4 ± 1.2	86.7 ± 2.4	-3.97 ± 0.61	66.1
[$^{nat/177}$Lu]**PSMA-59**	-e(**e**-G-N^5-orn-C^4-**EuE)**	3.7 ± 0.6	197.4 ± 9.9	-4.03 ± 0.05	98.3
[$^{nat/177}$Lu]**PSMA-60**	-e(**Abz**-N^5-orn-C^4-**EuE**)	6.6 ± 1.5	267.4 ± 7.9	-3.85 ± 0.13	98.5
[$^{nat/177}$Lu]**PSMA-61**	-k(**d**[N^5-orn-C^4-**EuE**]-**2,4-DNBA**)	4.5 ± 0.4	359.5 ± 22.6	-4.07 ± 0.05	63.3
[$^{nat/177}$Lu]**PSMA-62**	-k(**d**[N^5-orn-C^4-**EuE**]-**TMA**)	4.0 ± 0.2	343.9 ± 6.0	-4.12 ± 0.05	n.d.
[$^{nat/177}$Lu]**PSMA-63**	-k(Suc-N^5-orn-**2-nal**-C^4-**EuE**)	8.5 ± 0.7	28.6 ± 0.2	-3.52 ± 0.22	> 99

Introduction of a positive charge through D-arginine in [^{nat}Lu]**PSMA-58** (Figure 34), had similar impact on affinity and HSA binding as observed for the compound [^{nat}Lu]**PSMA-8** (chapter **III 1.1.1**). Compared to the reference ligand [$^{nat/177}$Lu]**PSMA-49**, albumin binding, affinity and especially internalization were negatively affected as shown in Table 15. These data, in relation to the *in vitro* characteristics of [$^{nat/177}$Lu]**PSMA-8**, show that positive charges in the linker region should be avoided.

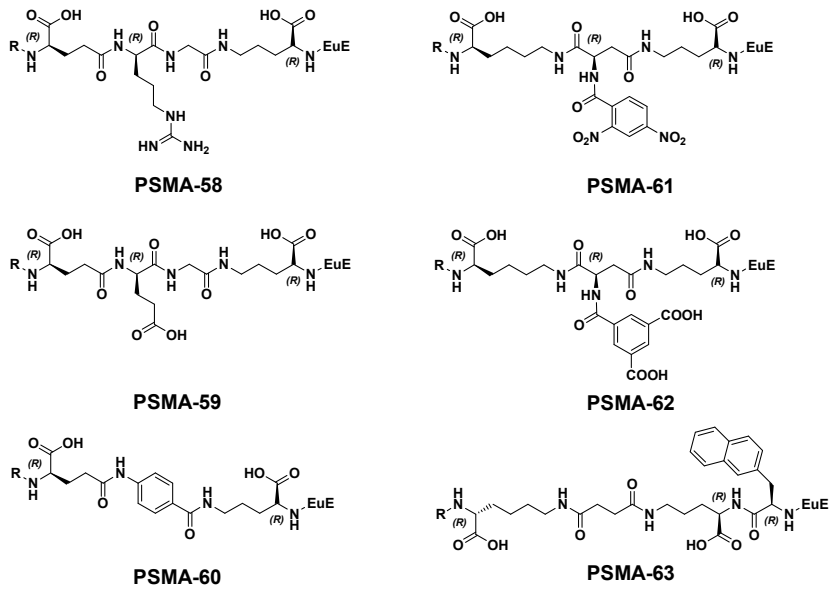

Figure 34. Illustration of the linker-modified PSMA inhibitors **PSMA-58** to **PSMA-63**. R = DOTAGA-F(4-NH_2)y-2-nal-.

Utilization of D-glutamic acid in [$^{nat/177}$Lu]**PSMA-59** impeded affinity and internalization too, yet in a lower extent than the introduction of D-arginine. While the positive charge in [^{nat}Lu]**PSMA-58** decreased albumin binding, it is known that higher lipophilicity (alkyl/aromatic groups) in combination with a negative charge are able to increase HSA binding. The introduction of Abz into the linker increased the lipophilic interactions with PSMA and beneficially affected the internalization of [^{177}Lu]**PSMA-60**. The increased lipophilicity also resulted in elevated HSA binding.

PSMA-61 was developed due to the positive results of **PSMA-36**, which displayed the highest intracellular uptake of all EuK-based compounds (chapter **III 1.1.6**). The favorable influence of the 2,4-dinitrobenzoic acid modification on internalization was also seen for [^{177}Lu]**PSMA-61**, exhibiting an almost fivefold higher value than [^{177}Lu]**PSMA I&T**. Substitution of the nitro groups through carboxylic acid residues in [$^{nat/177}$Lu]**PSMA-62** was possible and affected only slightly internalization. Utilization of trimesic acid instead of 2,4-dinitrobenzoic acid also increased the affinity, while HSA binding was similar for both derivatives. The findings for [$^{nat/177}$Lu]**PSMA-59** to [$^{nat/177}$Lu]**PSMA-62** illustrate that a negative charge alone without a connected aromatic system is not sufficient to increase internalization. According to the results in Table 15, hydrophobic interactions have greater impact on internalization than a negative charge, since the sole introduction of Abz proved to be more favorable than glutamic acid (Figure 35). The comparison of [^{177}Lu]**PSMA-60** and [^{177}Lu]**PSMA-61** also points out that electron deficient arenes in the linker region are highly advantageous for internalization. The beneficial effect becomes greater as electron deficiency becomes stronger (Figure 35).

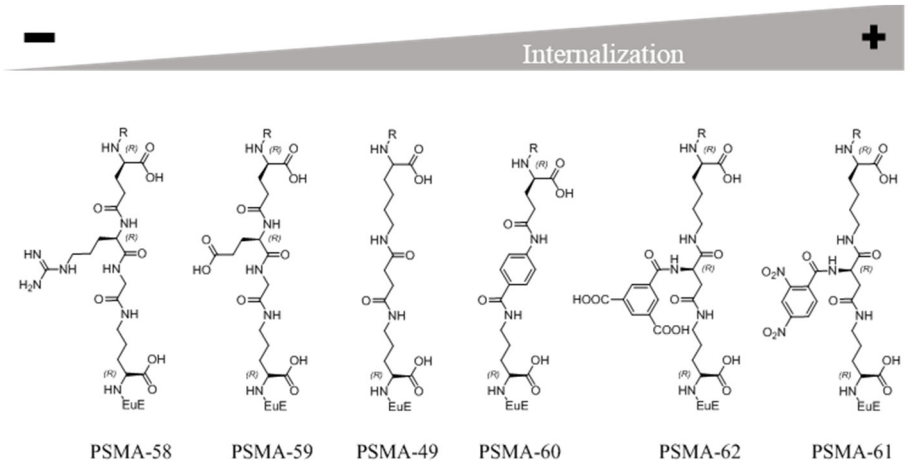

Figure 35. Illustration of the influence of several linker-modifications on internalization of PSMA inhibitors. R = DOTAGA-F(4-NH_2)y-2-nal-.

The introduction of D-2-nal into the linker region of **PSMA-63** demonstrated the possibility to achieve high albumin binding (> 99%), which in contrast lowered the affinity and diminished the internalization compared to the reference [$^{nat/177}$Lu]**PSMA-49**. Since every compound in this work displaying a HSA binding value > 99% suffered from low affinity and drastically decreased internalization, the compound [^{177}Lu]**PSMA-57** was evaluated without the presence of BSA in the internalization assay to exemplify the impact of high protein binding (Figure 36).

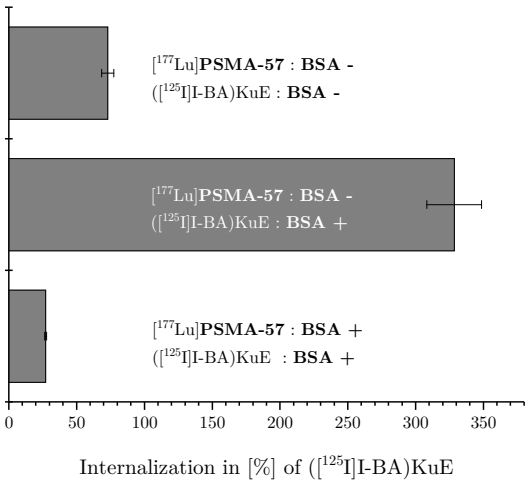

Figure 36. Illustration of BSA-dependent (conc.) cellular uptake of radiolabeled PSMA inhibitors. Cell internalization assays were conducted using LNCaP cells (1.25 * 10^5 cells/well, 1 h, 37 °C, c = 1.0 nM for [^{177}Lu]**PSMA-57** and 0.2 nM for ([^{125}I]I-BA)KuE) either with DMEM/F-12 medium (+ 5% BSA) or DMEM/F-12 solution without BSA. All other parameter were kept constant as described in chapter **II 3.4.2**. Internalization is shown as relative uptake to ([^{125}I]I-BA)KuE.

The withdrawal of BSA from the wells containing [^{177}Lu]**PSMA-57** in the *in vitro* assays, increased the relative cell uptake more than twelvefold from 27.1 ± 0.7 to 328.5 ± 20.1%.

Simultaneous withdrawal of BSA from the wells containing the radioligand ([^{125}I]I-BA)KuE and [^{177}Lu]**PSMA-57** also increased the relative uptake to 72.9 ± 4.5%. These results show, that BSA has enormous influence on the *in vitro* parameter and that albumin binding is a key parameter of new compounds that has to be considered [226].

1.2.4 Combinatorial design of EuE-based PSMA inhibitors

The last step of PSMA tracer development dealt with the linker and peptide spacer modifications from the previous chapters in combination with the EuE binding scaffold.

Table 16. Summary of all parameter *in vitro* investigated for the EuE-based PSMA inhibitors **PSMA-64** to **PSMA-66** and the references **PSMA I&T** and **PSMA-62**. The half maximal inhibitory concentration (IC_{50}) of the PSMA inhibitors was determined in a competitive binding assay using LNCaP cell (1.5 * 10^5 cells/well, 1 h, 4°C, HBSS + 1% BSA) and ([^{125}I]I-BA)KuE as radioligand. Internalized activity expressed in [%] as relative cellular uptake to ([^{125}I]I-BA)KuE (1.25 * 10^5 cells/well, PLL-coated plates, c = 0.2 nM for ([^{125}I]I-BA)KuE and c = 1.0 nM for ^{177}Lu-labeled PSMA inhibitors, DMEM/F-12 + 5% BSA, 37°C, 60 min). Data are corrected for non-specific binding (10 µM 2-PMPA). IC_{50} and internalization data are expressed as mean ± SD (n=3). Lipophilicity expressed as log*P* (distribution coefficient in n-octanol/PBS) of radiolabeled PSMA inhibitors. Data for log*P* expressed as mean ± SD (n=6). Albumin binding (HSA) expressed in [%] after logarithmic plotting and calibration (n=1). Strucure describes the *N*- to *C*-terminal structural composition of the complete inhibitor. n.d. = not determined. * = data obtained from Wirtz et al. [204].

PSMA inhibitor	Structure	IC_{50} [nM]	Internalization [%]	log*P*	HSA [%]
[$^{nat/177}$Lu]**PSMA I&T**	DOTAGA-y(3-I)fk(Sub-KuE)	7.9 ± 2.4*	75.5 ± 1.6*	-4.12 ± 0.11*	78.6
[$^{nat/177}$Lu]**PSMA-62**	DOTAGA-**F(4-NH$_2$)**y-2-nal-k(**d**[N^5-orn-C^4-**EuE**]-**TMA**)	4.0 ± 0.2	343.9 ± 6.0	-4.12 ± 0.05	98.1
[$^{nat/177}$Lu]**PSMA-64**	DOTAGA-**F(4-NO$_2$)**y-2-nal-k(Suc-N^5-orn-2-nal-C^4-**EuE**)	18.8 ± 3.0	32.8 ± 0.8	-3.72 ± 0.19	> 99
[$^{nat/177}$Lu]**PSMA-65**	**2,4-DNBA-Dap**(DOTAGA)y-2-nal-**e**(**Abz**-N^5-orn-C^4-**EuE**)	3.5 ± 0.3	340.2 ± 18.9	-4.15 ± 0.08	98.7
[$^{nat/177}$Lu]**PSMA-66**	DOTAGA-**Dap(TMA)**y-2-nal-k(**d**[N^5-orn-C^4-**EuE**]-**TMA**)	3.8 ± 0.3	297.8 ± 2.0	-4.25 ± 0.14	64.4

The combination of 2-D-nal in the linker and 4-NO_2-L-phenylalanine in the peptide spacer in [^{nat}]**PSMA-64** resulted in enhanced HSA binding as shown in Table 16. The enhanced albumin binding was again associated with low affinity and low internalization as observed for other derivatives with high HSA binding (chapter **III 1.2.3**).

Internalization and affinity towards PSMA is for [^{nat}]**PSMA-65** among the highest of all investigated ligands in this work. The pronounced effect from the Abz group in the linker

(**PSMA-60**) on HSA binding was transferable together with the beneficial effect of the 2,4-dinitrobenzoic acid group in the peptide spacer (**PSMA-53**) on cellular uptake.

PSMA-66 was modified with trimesic acid in the linker and peptide spacer as substitution for 2,4-dinitrobenzoic acid, since the comparison of [^{177}Lu]**PSMA-61** and [^{177}Lu]**PSMA-62** (Table 15, chapter **III 1.2.2**) showed that the exchange is possible without significant loss of internalization capacity. However, introduction of TMA into the peptide spacer slightly lowered the cell uptake of [^{177}Lu]**PSMA-66** in comparison to the reference [^{177}Lu]**PSMA-62**, whereas affinity was almost not affected (4.0 nM vs. 3.8 nM; respectively). Possible explanations are that TMA is conjugated through the side chain of L-Dap in **PSMA-66**, whereas in **PSMA-53** and **PSMA-65** the conjugation was performed with the *N*-terminal amino group of L-Dap. Another explanation are the positions of the functionalities in the arene. While the nitro groups are in ortho- and para position, the carboxyl groups are arranged in meta-position.

The influence of internalization on the cellular retention *in vitro* was evaluated for the compounds [^{177}Lu]**PSMA-62** and [^{177}Lu]**PSMA-66** in comparison to [^{177}Lu]**PSMA I&T** and [^{177}Lu]**PSMA-617** and shown in Figure 37.

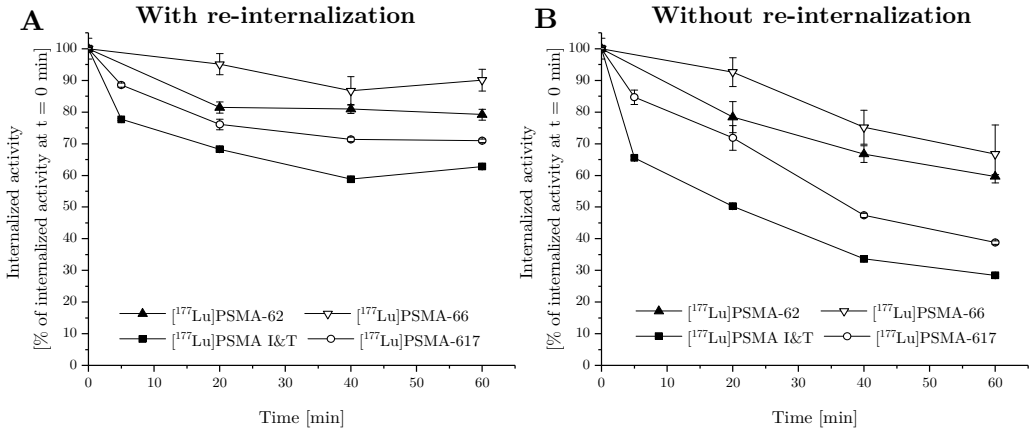

Figure 37. Externalization kinetics of selected ^{177}Lu-labeled PSMA inhibitors from LNCaP cells. 1.25 * 10^5 cells/well were incubated 1 h with the respective radioligand (c = 1.0 nM) at 37 °C in DMEM-solution (5% BSA). Then, the supernatant was removed and once washed with DMEM-solution (5% BSA, 37 °C). Afterwards, either **A**) only DMEM-solution (5% BSA) or **B**) blockade DMEM-solution (5% BSA, 10 µM 2-PMPA) were added for replacement. The total cellular internalized activity at t = 0 min was corrected for non-specific binding (10 µM 2-PMPA) and normalized to 100 %. All data are expressed as mean ± SD (n=3).

[^{177}Lu]**PSMA-66** demonstrated the highest intracellular activity in the tumor cells after 1 h (Figure 37 A) followed by [^{177}Lu]**PSMA-62**, although the internalization of [^{177}Lu]**PSMA-62** was found to be higher than for [^{177}Lu]**PSMA-66** (343.9% vs. 297.8%; respectively). Interestingly, even when re-internalization was blocked with 100 µM 2-PMPA-solution, the intracellular clearance [^{177}Lu]**PSMA-66** was lower than for all other investigated compounds. The difference compared to reference [^{177}Lu]**PSMA I&T** was more than twofold, if re-internalization was blocked (Figure 37 B).

[^{177}Lu]**PSMA-66** inherits nine free carboxylic groups, which equal nine negative charges *in vivo* (pH = 7.4). The extensively charged character of this compound could be a possible explanation for the protracted intracellular retention due to electrostatic repulsive effects from the negatively charged cell membranes.

2. *In vivo* evaluation

2.1 *In vivo* metabolism

A significant problem of small molecules *in vivo* is related to metabolic stability. Natural ligands for receptors or enzymes are acting as signal transduction units, thus a rapid regulation has to occur in order to maintain a steady signal flow. Concerning peptides, enzymatic metabolism by endopeptidase and exopeptidases highly impedes the development of new agents and has therefore to be addressed carefully [292]. Earlier investigations of our and other groups demonstrated the effect of high metabolic stability on the *in vivo* pharmacokinetics and tumor uptake, e.g. for PSMA inhibitors, $\alpha_v\beta_3$ integrin peptides or somatostatin analogs [188,193,204,293-295]. The current preclinical gold standard to determine *in vivo* stability is the injection of a radiolabeled compound into an experimental animal, with subsequent extraction of body fluids and tissue samples for quantification of metabolites via radio-RP-HPLC [193,194].

[^{177}Lu]**PSMA-16** and [^{177}Lu]**PSMA-20** were evaluated in healthy mice in order to investigate the metabolic stability of 4-amino-D-phenylalanine in the peptide spacer (**PSMA-16**) and the galactose residue (**PSMA-20**).

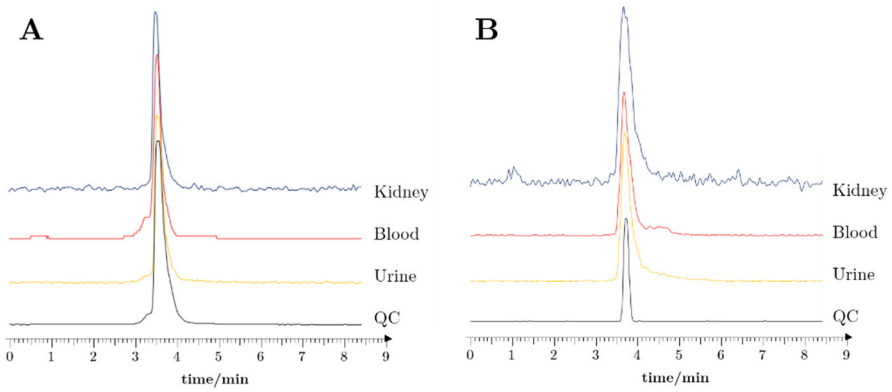

Figure 38. Metabolic stability of [^{177}Lu]**PSMA-20** (**A**) and [^{177}Lu]**PSMA-16** (**B**). Radio-RP-HPLC analyses of quality control (QC) and extracts from homogenized organs and body fluids from male CB-17 SCID mice (60 min p.i., 25 MBq [^{177}Lu]**PSMA-20 and** 25 MBq [^{177}Lu]**PSMA-16**). Chromolith column, binary gradient, flow rate 3 mL/min, 3% MeCN to 95% MeCN in 6 min, 95% MeCN for 3 min.

The representative RP-HPLC chromatograms of the extracted tissue-samples in Figure 38 show that the investigated ligands inherited high metabolic stability > 99% after 60 p.i. *in vivo*. Wirtz et al. showed that the introduction of D-amino acids highly increased the metabolic resistance of the radiolabeled compounds [193]. This is in agreement with the findings for [^{177}Lu]**PSMA-16**, which is only composed of D-configured amino acids in the peptide spacer. The high metabolic resistance of [^{177}Lu]**PSMA-20** is supported through the galactose residue. This modification increases the hydrophilicity, which induces water molecule binding and concomitantly reduces the access of proteolitic enzymes towards the peptide [262,296,297].

Powell et al. investigated the effect of D-amino acid substitution and other modifications, for instance *N*-acetylation, on the stability of peptides in human blood serum [298]. *C*- or *N*-terminal substitution with D-amino acids resulted in up to tenfold higher stability against degradation by exopeptidases. Combination of terminal D-amino acids and further *N*-acetylation or *C*-terminal carbamylation enabled even greater metabolic resistance, rendering this strategy highly effective.

2.2 *Ex vivo* metabolism

The procedure from chapter **III 2.1** necessitates to sacrifice at least one animal per study, although the reduction of laboratory animals is currently an intensively discussed topic [299]. A less valid, but commonly used method is the incubation of the radiolabeled tracer in human blood plasma with concomitant analysis [210]. However, metabolism occurs not only inside the bloodstream, but plenty of other important enzymes are located elsewhere like in the liver, lung, kidney or in the intestines. Therefore, these protocols inherit disadvantages concerning animal use or validity.

A compromise of valid animal-based data and reduction of animal sacrifice is the utilization of subcellular fractions (S9-fraction; 9 indicates centrifugation at 9,000 g) from extracted organs, which increase the number of possible applications per animal [300]. These S9 fractions contain cytosolic and microsomal enzymes and cover a wide range of possible metabolic phase 1 and phase 2 reactions [247]. For that reason, an *in vitro* S9 fraction-based assay was developed and established to evaluate the stability of radiolabeled PSMA inhibitors.

2.2.1 Preparation of S9 fractions

Two batches containing four or five CB-17 SCID mice were used to produce the S9 liver and kidney fractions. The additional direct perfusion after extraction with a syringe facilitated the almost complete removal of the residual blood in the extracted organs. Whole body perfusion with isotonic NaCl-solution and with *buffer-A* (chapter **II 4.1.2.1**) was not sufficient, which was visible through a still reddish color of the organs at the end of the procedure. The homogenization step was performed in a chilled mortar for 10 min to avoid denaturation of the proteins as indicated in the literature [247]. Finally, the liver and kidney homogenates were centrifuged at 10,000 g for 20 min at 4°C and subsequently stored in cryo-vials under liquid nitrogen.

2.2.2 Determination of the S9- protein concentration

The Bradford assay is a common procedure to determine the protein concentration in solution and was used to assess the S9-fractions [301,302]. All reagents were allowed to temper at RT for 2 h before start of the measurements. The determination of the protein concentration required the creation of a regression curve with samples containing 0.2 to 0.8 mg/mL BSA

dissolved in *buffer-B* (chapter **II 4.1.2.1**) and a blank sample. The concentration range was chosen due to the restricted linearity of the Bradford assay in this range.

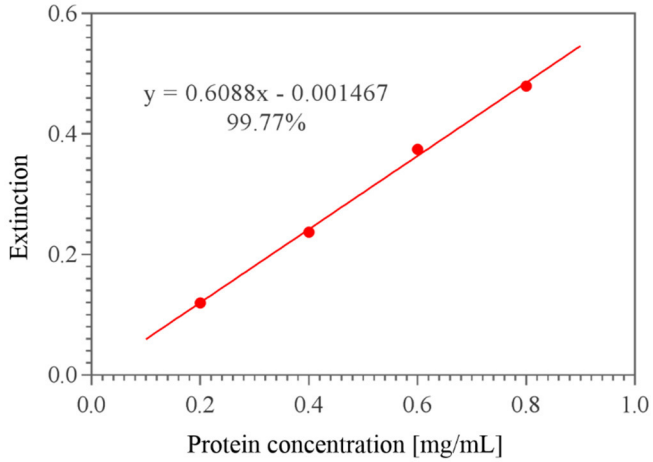

Figure 39. Exemplary illustration of the Bradford-assay regression curve. Samples containing 0.2 to 0.8 mg/mL BSA were prepared, mixed with *buffer-B* and *Bradford-reagent* and their extinction measured.

The reproducibility is highly depended on strict adherence to the chosen procedure. Exact incubation for 4 min at RT after mixing 30 µL of the BSA-samples and *Bradford-reagent* and subsequent measurement enabled the establishment of the regression curve as depicted in Figure 39. Two samples of each S9-fraction were evaluated to determine the protein-concentration of the liver and kidney homogenates. The results in Table 17 show, that the differences in the protein concentration between the two batches varied considerably.

Table 17. S9-fraction yield after extraction. Either 4 (batch 1) or 5 (batch 2) healthy CB-17 SCID mice were sacrificed. The caval vein was cannulated and the internal organs perfused with isotonic NaCl-solution (30 mL), a second perfusion step was conducted with *buffer-A* (30 mL). Then, liver and kidneys were removed and manually punctuated and perfused with a syringe containing *buffer-A* until the organs appeared pale pink. Finally, organs were homogenized in a mortar and the homogenous solution transferred into a chilled tube and centrifuged (10,000 g, 20 min, 4°C). Two samples of each fraction were used to determine the protein concentration with the Bradford-assay. 30 µL of each samples were mixed with 1.5 mL *Bradford-reagent* and measured at $\lambda = 595$ nm [247,301].

	Batch 1 (n = 4)		Batch 2 (n=5)	
	Volume [mL]	Conc. [mg/mL]	Volume [mL]	Conc. [mg/mL]
Liver	20.4	17.7 ± 0.1	14.7	15.8 ± 0.1
Kidney	6.6	15.6 ± 0.6	4.5	12.0 ± 0.8

Although batch 1 contained only four and not five animals as in batch 2, it was possible to extract more S9-fraction volume with higher protein concentration. The examination of the tissue homogenate of batch 2 after centrifugation revealed a markedly higher content of less homogenized tissue, which probably caused reduced S9-volume and simultaneously a lower

protein concentration. In this respect, the homogenization step is crucial and has to be conducted thoroughly. The manual homogenization with a pestle seems therefore unfavorable and a transition to an automatic tissue homogenizer should be pursued in order to warrant a higher grade of homogeneity.

2.2.3 Influence of incubation time and S9-protein concentration on metabolite formation

The available *in vivo* metabolism data of **PSMA-68** (Figure 40) from Wirtz et al. enabled the utilization of this ligand for the evaluation of the S9-assay and to assess the influence of varying factors like protein concentration and incubation time [193].

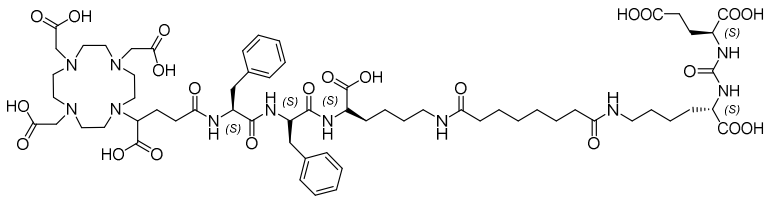

Figure 40. Molecular structure of **PSMA-68**. Metabolic instability was reported by Wirtz et al. for this ligand [204].

Due to the known degradation of **PSMA-68**, the necessary incubation time for the S9-kidney assay was determined. The assay protein concentration was set to 10 mg/mL and the ^{177}Lu-labeled peptide (**PSMA-68**) was incubated up to 6 h at 37°C.

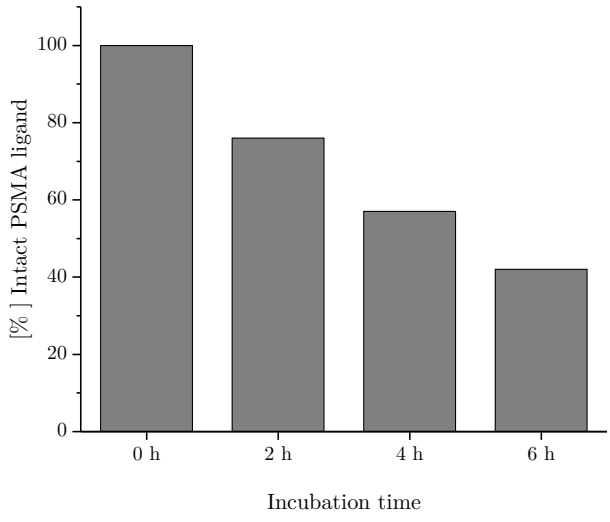

Figure 41. Radio-HPLC analysis of [^{177}Lu]**PSMA-68** after incubation in S9-kidney fraction (protein conc. = 10 mg/mL, 37 °C, c = 2.0 nM for [^{177}Lu]**PSMA-68**.

The results in Figure 41 show that metabolite formation occurred in the kidney-fraction with 42% intact tracer after 6 h. The initial metabolite formation proceeded almost linearly while the 6 h value showed a decrease of enzymatic activity. These findings are in agreement with

the literature, in which a loss of 10% to 15% of enzymatic activity per hour was observed. The utilization of additives like the cofactor Nicotinamide adenine dinucleotide 2'-phosphate (NADPH) could extend the applicable time frame but has yet to be evaluated. Since the value at 4 h (57%) enabled reasonable metabolite detection, all further experiments were evaluated only up to four hours.

Each experiment was initially stopped either through the addition of ice-cold MeCN or transition of the mixture into an oil-bath for 10 min at 95°C for enzyme denaturation. The addition of MeCN influenced occasionally the retention on the RP-HPLC-column and was found to be problematic regarding the assessment of metabolite formation. On account of that, the incubation was stopped through denaturation of the sample with subsequent ultra-centrifugation. Since all PSMA tracer were initially radiolabeled at 95°C for 30 min, it was assumed that the additional denaturation-step would not affect metabolite formation. The extraction of total activity after the last step was in average 73% but necessitated time-consuming centrifugation of 20 min at 5000 rpm.

In the next step, the optimal ratio between necessary protein concentration and minimal S9-fraction requirement was determined. Samples containing 33.3 vol.% DMEM-solution, radiolabeled peptide (2.0 nM) and varying S9-volume of the kidney fraction were incubated for 0, 2 and 4 h at 37°C and analyzed via radio-RP-HPLC. To address the question if the metabolite formation is due to enzymatic activity or caused through other components in the assay, separate incubations were performed in heat-denatured S9-fractions, which eliminates enzymatic activity as possible factor. As expected, none of the tested radiolabeled peptides showed any degradation using heat-denatured proteins.

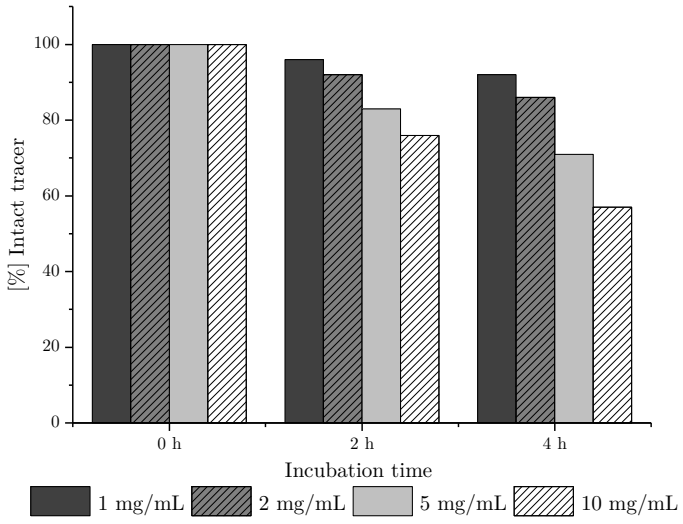

Figure 42. Radio-HPLC analysis of [^{177}Lu]**PSMA-68** after incubation in S9-kidney fraction with varying protein concentration (37 °C, c = 2.0 nM for [^{177}Lu]**PSMA-68**).

Metabolite formation over time with native enzymes was directly correlating with the applied protein concentration, displaying only 57% intact tracer after 4 h with 10 mg/mL protein concentration as shown in Figure 42. Using 1.0 or 2.0 mg/mL for protein concentration resulted in 92% and 86% intact tracer after 4 h, respectively. Although degradation occurred, these low concentrations were avoided for future investigations since it was difficult to predict if they would be sufficient to detect metabolism of potentially more stable peptides.

The same investigations were conducted for [^{177}Lu]**PSMA-68** using the S9-liver fractions. However, applying even a 9.0 mg/mL protein concentration with 4 h incubation resulted in only 2.5% metabolite formation.

A possible explanation is the absence of necessary co-factors or other additives to support the metabolic pathways of phase 1 and phase 2 reactions. Necessary exogenous additives like NADPH, Uridine 5'-diphosphoglucuronic acid (UDPGA) or 3'-Phosphoadenosine 5'-phosphosulfate (PAPS) were absent during the conducted S9-assays and further investigations have to be carried out to determine their influence [303].

Other possible obstacles are the conditions and time of storage of the S9-fractions. Storage under liquid nitrogen is able to preserve most of the enzymatic activity more than a year, however, the process of freezing and thawing reduces the enzymatic activity of especially CYP-enzymes as shown by Förlin et al. [304]. The utilization of fresh S9-samples should demonstrate a higher grade of enzymatic activity but it would also ultimately destroy the aspect of convenient handling.

Since [^{177}Lu]**PSMA-68** showed almost no metabolic degradation in the S9-liver fraction, another positive control peptide was chosen to evaluate enzymatic activity in the liver. Compound **S9-PCP-1** (Figure 43) is a derivative of Obestatin, an endogenous hormone which is known for its rapid *in vivo* metabolic transformation [305].

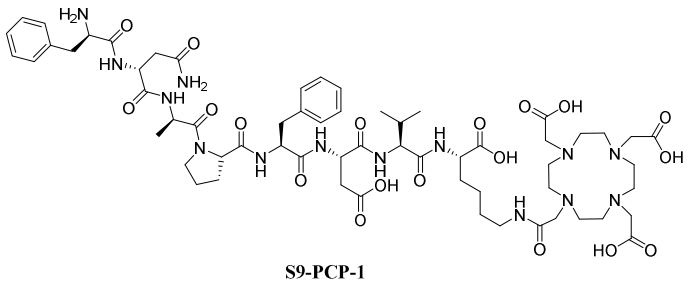

Figure 43. Molecular structure of the Obestatine-derivative **S9-PCP-1**.

[^{177}Lu]**S9-PCP-1** was incubated in the S9-liver fractions up to 4 h, applying a protein concentration of 10 mg/mL. After 1 h already 100% of the tracer was metabolized, which was confirmed through the investigation of the samples after 2 and 4 h respectively. To reduce the metabolic degradation and to prove that the reason for metabolite formation is based on enzymatic activity, the protein concentration was set to 1, 2 and 5 mg/mL. However, as in the experiments using 10 mg/mL, after 1 h complete decomposition of the radiolabeled peptide was visible for each protein concentration as shown in Figure 44.

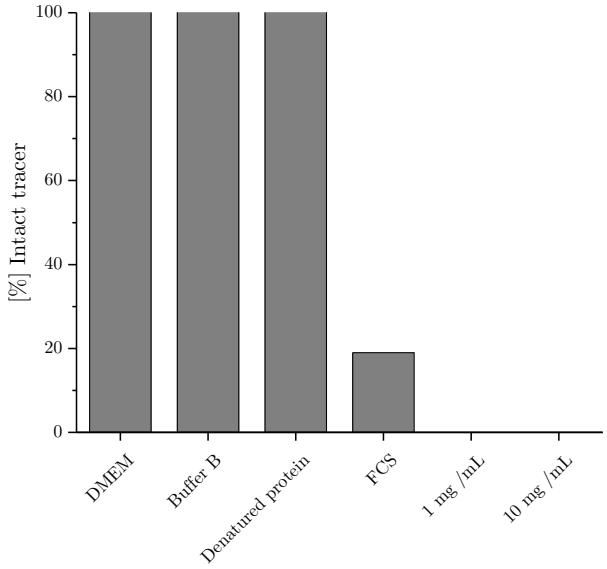

Figure 44. Radio-HPLC analysis of [^{177}Lu]**S9-PCP-1** after incubation in various media and S9-liver fraction with varying protein concentration (1 h, 37 °C, c = 2.0 nM for [^{177}Lu] **S9-PCP-1**).

To confirm that metabolite formation emanated from enzymatic activity and not through any other component in the incubation mixture, [^{177}Lu]**S9-PCP-1** was incubated in pure DMEM-solution, *buffer-B*, denatured S9-liver proteins and additionally in FCS for 1 h at 37°C and subsequently analyzed via radio-RP-HPLC. As expected, no degradation was visible in the DMEM solution and *buffer-B* as shown in Figure 44. The same findings were observed for the investigation with denatured proteins, which confirmed that the observed metabolite formation using native proteins was due to enzymatic activity. Incubation in FCS showed that even the low enzymatic activity of FCS, is sufficient to metabolize [^{177}Lu]**S9-PCP-1**. These observations led to the conclusion that [^{177}Lu]**PSMA-68** is metabolically too stable while the metabolic instability of [^{177}Lu]**S9-PCP-1** is too high to qualify as positive control for the S9-liver fractions and a suitable compound has to be found for future investigations.

The last experiment addressed the question if the incubation in sole blood plasma is able to determine metabolite formation of [^{177}Lu]**PSMA-68**, since several groups applied this method in order to prove the metabolic stability of their compounds *in vivo* [210,306,307]. The ligand

[^{177}Lu]**PSMA-68** was incubated up to 4 h in human blood plasma from a volunteer and compared to the incubation in S9-kidney fractions (5.0 mg/mL). As shown in Figure 45, the sole incubation in blood plasma was not sufficient to identify possible metabolite formation while the incubation in S9-kidney fractions showed ongoing metabolite formation over 4 h.

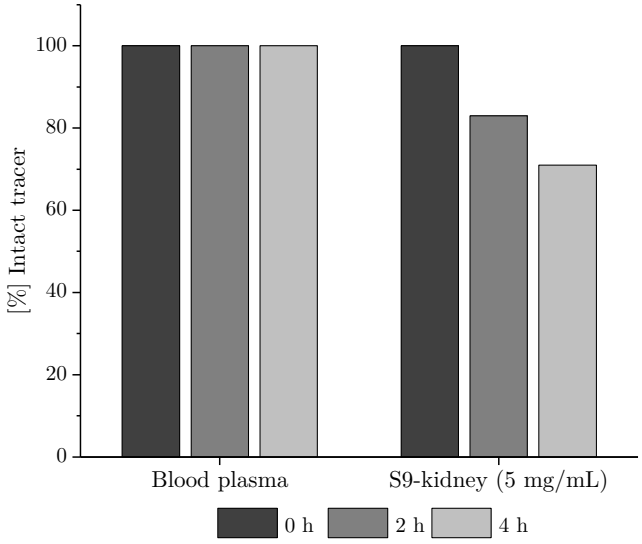

Figure 45. Radio-HPLC analysis of [^{177}Lu]**PSMA-68** after incubation in either blood plasma or S9-kidney fraction (protein conc. S9 = 5.0 mg/mL, 1 h, 37 °C, c = 2.0 nM for [^{177}Lu]**S9-PCP-1**).

These results render the S9-approach superior compared to sole incubation in blood plasma for the evaluation of new tracer. Further, sole blood plasma incubation should be avoided to prevent the translation of potentially unstable tracer into preclinical settings.

2.2.4 Influence of stereochemistry on metabolic stability

To investigate the influence of L- and D-amino acids on the metabolic stability of compounds based on **PSMA I&T**, several isomers were synthesized and evaluated in the S9-liver and kidney-fractions. The protein concentration was set 5.0 mg/mL and the S9-samples incubated at 37°C up to 4 h.

Table 18. Summary of all investigated **PSMA I&T**-stereoisomers (**PSMA-2** to **PSMA-7**) and **PSMA I&T** as reference. Radio-RP-HPLC analysis was performed to assess metabolite formation after incubation of the respective ^{177}Lu-labeled radioligand in S9-liver and S9-kidney fractions (protein conc. = 5.0 mg/mL, 1 h, 37°C, c = 2.0 nM for the ^{177}Lu-labeled tracer). + indicates stable (100%), number indicates intact tracer in [%].

PSMA inhibitor	L/D configuration	S9-Liver			S9-kidney		
		0 h	2 h	4 h	0 h	2 h	4 h
[^{177}Lu]**PSMA I&T**	-y(3-I)fk-	+	+	+	+	+	+
[^{177}Lu]**PSMA-2**	-y(3-I)f**K**-	+	+	+	+	+	+
[^{177}Lu]**PSMA-3**	-**Y(3-I)**fk-	+	+	+	+	+	+
[^{177}Lu]**PSMA-4**	-y(3-I)**FK**-	+	+	+	+	+	+
[^{177}Lu]**PSMA-5**	-y(3-I)**F**k-	+	+	+	+	+	+
[^{177}Lu]**PSMA-6**	-**Y(3-I)**f**K**-	+	+	+	+	+	+
[^{177}Lu]**PSMA-7**	-**Y(3-I)FK**-	+	88%	83%	+	45%	32%

The results in Table 18 show that the substitution of one L-amino acid to its D-isomer was enough to inhibit metabolic degradation completely, independent of the position within the peptide spacer. The only unstable derivative was found to be [^{177}Lu]**PSMA-7**, which inherits a complete L-configured peptide spacer. Interestingly, compared to the compound [^{177}Lu]**PSMA-68** (chapter **III 4.2.3**), a moderate but higher degradation was observed using the S9-liver fractions and the same observation was done using the S9-kidney fractions. This implies, that 3-iodo-L-tyrosine inherits destabilizing character, since the only difference between **PSMA-68** and **PSMA-7** is the existence of a second L-phenylalanine in **PSMA-68** (-Y(3-I)FK- vs. -FFK-; respectively). It further enables the utilization of **PSMA-7** as potential positive control regarding the evaluation of the enzymatic activity of the S9-liver proteins. The confirmation of enzymatic activity as source for metabolite formation was conducted through the incubation of [^{177}Lu]**PSMA-7** in denatured S9-samples (5.0 mg/mL). None of the samples showed any trace of metabolism after 4 h incubation at 37°C.

The *in vivo* comparison of [^{68}Ga]**PSMA I&T** and its unstable isomer [^{68}Ga]**PSMA-7** was reported by Wirtz et al. [204]. The direct comparison of both tracer in a biodistribution- and PET-study is shown in Figure 46 and depicts the influence of metabolic degradation *in vivo*.

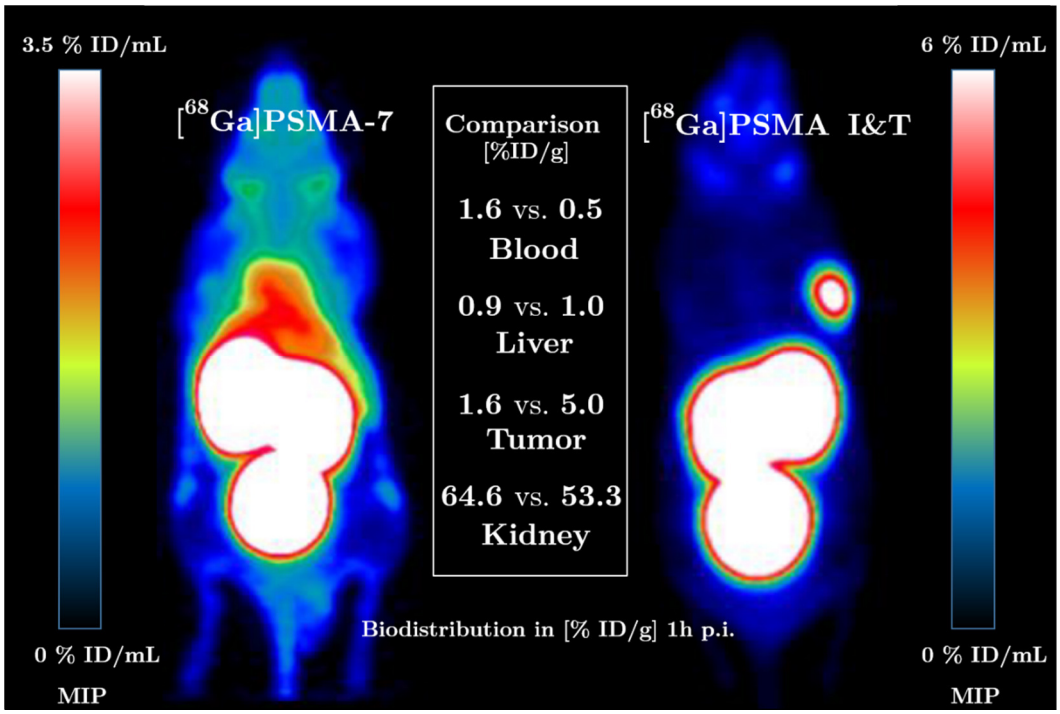

Figure 46. Maximum intensity projections (MIP) of static µPET (1 h p.i. for 15 min) scans in LNCaP xenograft bearing mice of [^{68}Ga]**PSMA-7** and [^{68}Ga]**PSMA I&T** (0.15 to 0.25 nmol peptide, respectively) and biodistribution data (in %ID/g) of selected organs for [^{68}Ga]**PSMA-7** and [^{68}Ga]**PSMA I&T** at 1 h p.i.. (n=4; respectively). Data taken from Wirtz et al. [204].

The metabolic unstable tracer [^{68}Ga]**PSMA-7** showed high background activity and low tumor accumulation, most probably due to the pronounced degradation *in vivo*. In contrast, tumor uptake of [^{68}Ga]**PSMA I&T** was more than threefold higher with fast background clearance and overall superior pharmacokinetics.

To evaluate if the extension with 4-amino-phenylalanine influences the metabolic stability, the S9-assay was applied for the compounds [^{177}Lu]**PSMA-15** to [^{177}Lu]**PSMA-19**.

Table 19. Summary of the investigated stereoisomers **PSMA-15** to **PSMA-19**. Radio-RP-HPLC analysis was performed to assess metabolite formation after incubation of the respective ^{177}Lu-labeled radioligand in S9-liver and S9-kidney fractions (protein conc. = 5 mg/mL, 1 h, 37°C, c = 2.0 nM for the ^{177}Lu-labeled tracer). + indicates stable (100%), number indicates intact tracer in [%].

PSMA inhibitor	L/D configuration	S9-Liver		S9-kidney	
		0 h	4 h	0 h	4 h
[$^{nat/177}$Lu]**PSMA-15**	-f(4-NH$_2$)y(3-I)fk-	+	+	+	+
[$^{nat/177}$Lu]**PSMA-16**	-**F(4-NH$_2$)**y(3-I)fk-	+	+	+	+
[$^{nat/177}$Lu]**PSMA-17**	-f(4-NH$_2$)y(3-I)f**K**-	+	+	+	+
[$^{nat/177}$Lu]**PSMA-18**	-f(4-NH$_2$)y(3-I)**FK**-	+	+	+	+
[$^{nat/177}$Lu]**PSMA-19**	-**F(4-NH$_2$)**y(3-I)f**K**-	+	+	+	+

The results in Table 19 show that no degradation of the investigated compounds occurred. The findings are in agreement with the results from the **PSMA I&T** isomers, in which one single L- to D-amino acid substitution enabled complete inhibition of metabolite formation (Table 18). The results regarding metabolic stability of [^{177}Lu]**PSMA-15** was also in agreement with the *in vivo* metabolite analysis, in which no metabolite formation was observed (chapter **III 2.1**) and thus proving partially the validity of the S9-assay.

2.2.5 Influence of nitro and ester groups on the metabolic stability

The established S9-assay was used to investigate the metabolic stability of [^{177}Lu]**PSMA-53** and [^{177}Lu]**PSMA-67**. Both tracer inherit metabolically unstable groups like 2,4-dinitrobenzoic acid in **PSMA-53** or the ester conjugation in **PSMA-67**. The radiolabeled compounds were incubated in S9-liver and kidney fractions with a protein concentration of 5 mg/mL up to 4 h at 37°C and were subsequently analyzed via radio-RP-HPLC.

Table 20. Summary of the investigated inhibitors [^{177}Lu]**PSMA-53** and [^{177}Lu]**PSMA-67**. Radio-RP-HPLC analysis was performed to assess metabolite formation after incubation of the respective ^{177}Lu-labeled radioligand in S9-liver and S9-kidney fractions (protein conc. = 5.0 mg/mL, 1 h, 37°C, c = 2.0 nM for the ^{177}Lu-labeled tracer). + indicates stable (100%), number indicates intact tracer in [%].

PSMA Inhibitor	Labile group	S9-Liver		S9-kidney	
		0 h	4 h	0 h	4 h
[$^{nat/177}$Lu]**PSMA-53**	2,4-dinitrobenzoic acid	+	82%	+	92%
[$^{nat/177}$Lu]**PSMA-67**	Ester-conjugation	+	+	+	+

The results in Table 20 show that metabolite formation of [^{177}Lu]**PSMA-53** occurred in both S9-fractions, however, degradation was more pronounced using the S9-liver fraction. The metabolic instability of dinitro-substituted aromatic systems is well characterized in the literature [291,308]. A common metabolite formation is the nitroreductive bioactivation that results in hepatocellular toxic nitroanion radicals, nitroso intermediates and *N*-hydroxy functionalities [309]. Reduction of one of the nitro groups to the corresponding amino group in dinitrobenzoic acid was also reported to occur in the liver [310].

In contrast to [^{177}Lu]**PSMA-53**, no metabolite formation was observed for [^{177}Lu]**PSMA-67**. (Table 20). Although intentionally developed to increase the metabolic degradation, it was unexpected that [^{177}Lu]**PSMA-67** remained stable, since ester groups are prone for *in vivo* cleavage and are therefore used in prod-drug approaches [311]. Further, carboxylesterases are reported to be in the liver and kidney of mammals [311-313]. Thus, they should be present in the extracted S9-fractions.

[^{68}Ga]**PSMA-67** was further evaluated in a PET study to partially confirm the observed results from the S9-assay (chapter **III 4.3**). Although PET is not able to discriminate between the intact compound and a potential metabolite, the work of Wirtz et al. showed that metabolic degradation *in vivo* impedes PSMA-imaging, visible through diffuse whole body uptake and slower background clearance (Figure 46) [204].

The pharmacokinetic distribution of [^{68}Ga]**PSMA-67**, however, resembled the *in vivo* behavior of [^{68}Ga]**PSMA I&T**, which is known for its high metabolic stability (Figure 62) [194]. The PET-study confirmed that intense metabolic degradation did not occur and was therefore in agreement with the findings of the S9-assay. This feature was visible through a linear decline of blood-pool and muscle activity in the logarithmic plots of the time-activity-curves. Non-linear decrease would indicate that further mechanisms, e.g. metabolism, are involved in the elimination process besides renal excretion. Yet, further experiments are necessary since a single S9- and PET-study are not sufficient to fully elucidate the metabolic degradation. Previous reports showed that strong interindividual differences in humans regarding tumor uptake and *in vivo* disposition can occur applying the same tracer [314,315].

Richardson et al. recently reported about the robustness of S9-metabolite assays in comparison to hepatocyte assays, which are regarded as the current gold standard *in vitro*. The direct comparison showed that S9-liver assays provide the same quality of data as the assays using hepatocytes and that both deliver similar results in 70% to 84% of all investigated cases. However, the cost-benefit of S9-assays was found to be 15-fold compared to the corresponding hepatocyte assays [303].

2.3 Biodistribution

The biodistribution of the radiolabeled PSMA inhibitors was investigated at several time points in male LNCaP-tumor xenograft bearing CB-17 SCID mice. To warrant comparability, each study was conducted according to a constant experimental setup using 0.15 to 0.25 nmol of the respective radiolabeled tracer per animal. In contrast to the experiments of Wirtz et al., the animal model used in this work were CB-17 SCID mice since tumor-growth upon inoculation was found to be faster and more reliable compared to the CD-1 nu/nu mice [204]. The reference ligands **PSMA I&T** and **PSMA-617** were included to enable comparability with the literature [194,206].

2.3.1 Influence of the animal model

The possibility to compare the results of the biodistribution studies with the earlier work of Wirtz et al. necessitated the evaluation of [^{177}Lu]**PSMA I&T** and [^{68}Ga]**PSMA I&T** in healthy and tumor-bearing CB-17 SCID mice in order to eliminate possible influence from the used animal-model. Data for the CD-1 nu/nu experiments were taken from the literature [194].

Table 21. Biodistribution of **PSMA I&T** (in % ID/g) at 1 h p.i. in LNCaP-tumor bearing CD-1 nu/nu mice and LNCaP-tumor bearing CB-17 SCID mice. Approx. 2.0 to 3.0 MBq of the ^{177}Lu-labeled inhibitor or 8.0 to 12 MBq of the ^{68}Ga-labeled inhibitor (0.15 to 0.25 nmol peptide) were injected (n = 4 , respectively). n.d. = not determined. Data for CD-1 nu/nu mice are taken from Wirtz et al. [204].

	[^{177}Lu]**PSMA I&T** 1 h p.i.		[^{68}Ga]**PSMA I&T** 1 h p.i.	
	CB-17 SCID	CD-1 nu/nu	CB-17 SCID	CD-1 nu/nu
blood	0.37 ± 0.10	0.44 ± 0.19	0.96 ± 0.12	0.45 ± 0.23
heart	0.58 ± 0.15	0.29 ± 0.08	0.63 ± 0.11	0.26 ± 0.08
lung	1.32 ± 0.45	1.65 ± 0.56	2.24 ± 0.39	1.49 ± 0.38
liver	0.37 ± 0.10	1.10 ± 0.41	0.78 ± 0.32	1.00 ± 0.39
spleen	13.8 ± 4.59	5.85 ± 2.26	15.03 ± 3.10	3.88 ± 1.46
pancreas	1.30 ± 1.39	0.57 ± 0.24	0.65 ± 0.17	0.54 ± 0.15
stomach	0.29 ± 0.06	0.42 ± 0.14	0.46 ± 0.14	0.42 ± 0.10
intestine	0.59 ± 0.50	0.69 ± 0.14	0.41 ± 0.17	0.27 ± 0.07
kidney	128.90 ± 10.74	107.24 ± 15.61	71.81 ± 9.34	53.26 ± 9.02
adrenal gland	6.25 ± 2.59	n.d.	3.01 ± 2.57	n.d.
muscle	0.18 ± 0.07	0.56 ± 0.36	0.21 ± 0.03	0.35 ± 0.08
bone	0.14 ± 0.04	0.22 ± 0.05	0.23 ± 0.05	0.27 ± 0.08
brain	0.03 ± 0.01	0.04 ± 0.03	0.03 ± 0.01	0.03 ± 0.02
tumor	4.69 ± 0.95	7.96 ± 1.76	n.d.	4.95 ± 1.57
tumor/blood	12.7	18.1	-	11.0
tumor/kidney	0.04	0.07	-	0.09
tumor/muscle	26.1	14.2	-	14.1

The comparison in Table 21 between the two animal models demonstrated that a moderate influence is present. The difference between the ^{68}Ga- and ^{177}Lu-labeled ligands in the respective models was clearly visible. Compared to its ^{177}Lu-labeled analog exhibited [^{68}Ga]**PSMA I&T**

a lower kidney and spleen uptake but a higher accumulation in the muscle, independent of the model. Regarding [^{177}Lu]**PSMA I&T**, the tumor to blood and tumor to kidney ratios were more favorable using the CD-1 nu/nu model. The tumor to muscle ratio was almost twofold higher in the CB-17 model for [^{177}Lu]**PSMA I&T**. It is also interesting, that the tumor uptake was almost twofold higher for [^{177}Lu]**PSMA I&T** in the CD-1 nu/nu tribe compared to the CB-17 SCID mice. Blood-pool uptake of [^{68}Ga]**PSMA I&T** in CB-17 SCID mice seemed somewhat higher compared to all other blood-values. A possible explanation is ^{68}Ga-colloid formation during radiosynthesis, which would lead to increased radioactivity in the liver as previously reported for an ^{68}Ga-labeled exendin derivative [316]. However, radio-TLC showed only minimal amounts of ^{68}Ga-colloid formation during radiosynthesis (< 5%).

2.3.2 Influence of the peptide spacer extension with 4-amino-D-phenylalanine

The extension of the peptide spacer with 4-amino-D-phenylalanine in [$^{nat/177}$Lu]**PSMA-16** (-f(4-NH_2)y(3-I)fk-) increased the affinity (2.3 nM vs. 7.9 nM, respectively) and internalization (122.2% vs. 75.7%, respectively) compared to [$^{nat/177}$Lu]**PSMA I&T** (-y(3-I)fk) (chapter **III 1.1.1**). In order to investigate these effects on the biodistribution, [^{177}Lu]**PSMA-16** was evaluated and compared to [^{177}Lu]**PSMA I&T** in CB-17 SCID mice 1 h p.i..

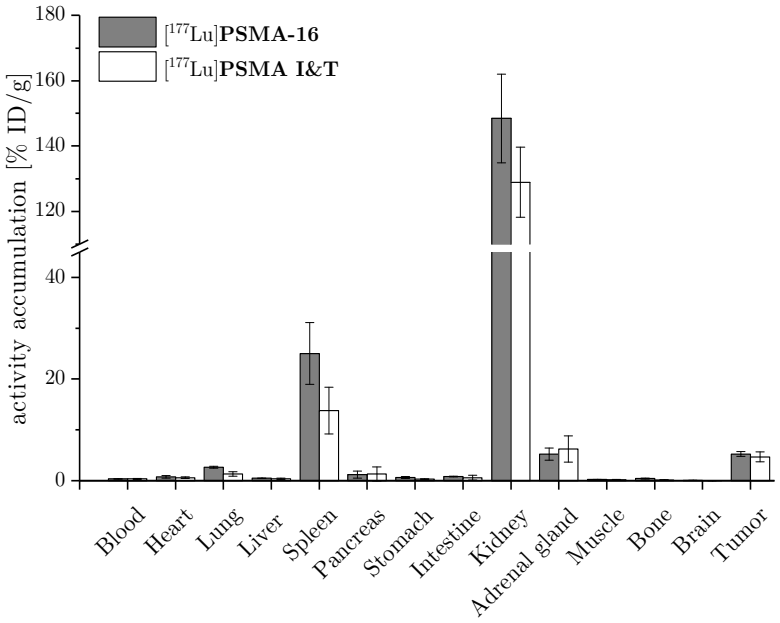

	[^{177}Lu]**PSMA-16**
blood	0.36 ± 0.04
heart	0.74 ± 0.26
lung	2.64 ± 0.18
liver	0.48 ± 0.04
spleen	25.03 ± 6.08
pancreas	1.20 ± 0.69
stomach	0.63 ± 0.19
intestine	0.82 ± 0.08
kidney	148.44 ± 13.60
adrenal g.	5.23 ± 1.19
muscle	0.22 ± 0.02
bone	0.43 ± 0.11
brain	0.04 ± 0.01
tumor	5.24 ± 0.48

Figure 47. Biodistribution (in %ID/g) of 5.0 to 7.0 MBq (0.15 to 0.25 nmol) of [^{177}Lu]**PSMA-16** in LNCaP-tumor bearing CB-17 SCID mice (n = 4, right) and direct comparison with [^{177}Lu]**PSMA I&T** (left).

The direct comparison in Figure 47 shows that the uptake of [^{177}Lu]**PSMA-16** in PSMA expressing tissues (kidney and tumor) was somewhat higher than for [^{177}Lu]**PSMA I&T**. This could be due to the higher internalization rate and affinity of [$^{nat/177}$Lu]**PSMA-16**. The uptake in the lung, spleen and the kidneys were higher for [^{177}Lu]**PSMA-16**, whereas all other tissues

showed similar accumulation of the radiolabeled peptides. The tumor to tissue ratios of [^{177}Lu]**PSMA-16** compared to [^{177}Lu]**PSMA I&T** was regarding blood 14.6 vs. 12.7 and equally 0.04 for the kidneys. However, the tumor to muscle ratio was found to be more favorable for [^{177}Lu]**PSMA I&T** than for [^{177}Lu]**PSMA-16** (26.1 vs. 23.8, respectively). Overall, both tracer demonstrated similar *in vivo* pharmacokinetics. The improved *in vitro* characteristics through the extension of the peptide spacer (4-amino-D-phenylalanine) increased the tumor uptake only minimal, yet, the concomitant higher kidney accumulation is concerning, since the kidneys represent currently the dose-limiting organ for [^{177}Lu]**PSMA I&T** in humans [215,257].

2.3.3 Effect of carbohydration on PSMA I&T

In order to investigate the effect of carbohydration on the biodistribution of [^{68}Ga]**PSMA I&T**, [^{68}Ga]**PSMA-20** was investigated 1 h p.i. and 3 h p.i. in LNCaP tumor-xenograft bearing CB-17 SCID mice applying approx. 12 MBq of [^{68}Ga]**PSMA-20** (0.15 to 0.2 nmol peptide).

Table 22. Biodistribution data of [^{68}Ga]**PSMA-20** (in % ID/g) in LNCaP-tumor xenograft bearing CB-17 SCID mice at 1 h p.i. and 3 h p.i. (n = 4, respectively).

	[^{68}Ga]**PSMA-20** 1 h p.i.	[^{68}Ga]**PSMA-20** 3 h p.i.
blood	1.53 ± 0.19	1.16 ± 0.13
heart	0.51 ± 0.23	0.40 ± 0.10
lung	1.12 ± 0.50	0.83 ± 0.12
liver	0.57 ± 0.12	0.42 ± 0.04
spleen	6.67 ± 3.11	3.16 ± 1.31
pancreas	0.24 ± 0.10	0.28 ± 0.02
stomach	0.42 ± 0.25	0.33 ± 0.18
intestine	0.25 ± 0.11	0.40 ± 0.18
kidney	58.92 ± 13.95	38.80 ± 11.03
adrenal gland	2.39 ± 1.30	2.31 ± 0.44
muscle	0.16 ± 0.06	0.12 ± 0.03
bone	0.24 ± 0.02	0.26 ± 0.03
brain	0.05 ± 0.02	0.05 ± 0.01
tumor	3.87 ± 1.32	3.85 ± 0.54
tumor/blood	2.5	3.3
tumor/kidney	0.07	0.1
tumor/muscle	24.2	32.1

The data in Table 22 show that especially the kidneys, tumor and spleen were organs with high tracer accumulation. The ongoing clearance of [^{68}Ga]**PSMA-20** from the kidneys and other regions was visible over a course of 3 h p.i., while tumor accumulation of [^{68}Ga]**PSMA-20** remained stable. The difference of tracer retention in the kidneys and tumor is probably a consequence of the diversity in blood perfusion and the concomitant degree of clearance, which is in the case of the kidneys also partially influenced by the renal excretion.

The introduction of the carbohydrate moiety not only decreased the internalization rate (18.7% vs. 59.2%, respectively), but also drastically reduced binding to human albumin, which is more than six times lower for [^{nat}Ga]**PSMA-20** compared to [^{nat}Ga]**PSMA I&T** (7.7% vs. 52.0%, respectively). Although sole albumin binding does not account for the total plasma protein binding *in vivo*, this observation would lead to the expectation of reduced blood uptake in the biodistribution study of [^{nat}Ga]**PSMA-20**.

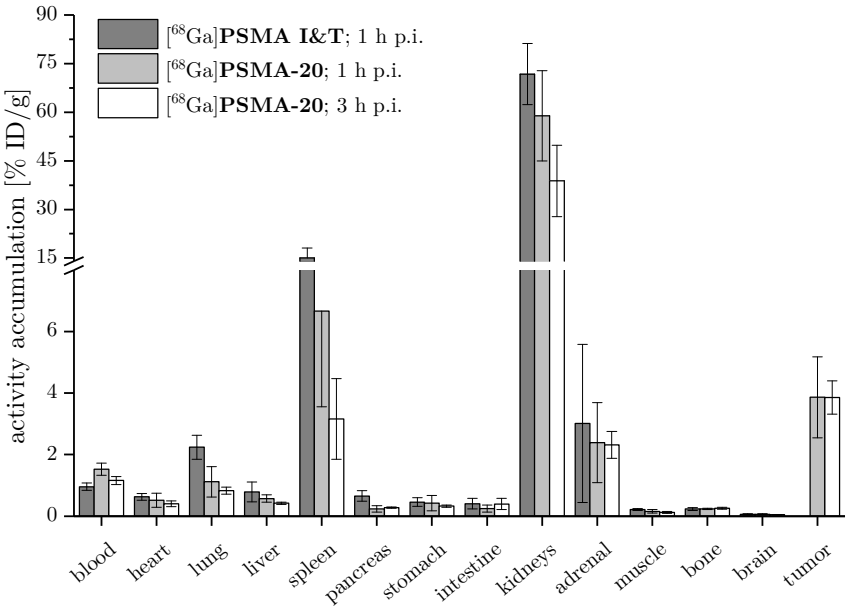

Figure 48. Biodistribution data (in % ID/g) for [^{68}Ga]**PSMA-20** and [^{68}Ga]**PSMA I&T** at 1 h p.i. and at 3 h p.i. [^{68}Ga]**PSMA-20** in healthy CB-17 SCID mice (**[**^{68}Ga]**PSMA I&T**) and LNCaP-tumor bearing mice ([^{68}Ga]**PSMA-20)** (n = 4; respectively).

The higher blood uptake 1 h p.i. of [^{68}Ga]**PSMA-20** compared to [^{68}Ga]**PSMA I&T** (1.53% ID/g vs. 0.96% ID/g, respectively) as shown in Figure 48 was therefore unexpected. However, such observation was also reported to some extent by Albert et al. [317]. His results showed that the conjugation of somatostatin with a sugar moiety (D-maltose) results in delayed blood clearance compared to the parent compound and that the elimination pattern was redirected from hepatobiliary towards renal excretion. Similar observation were reported by Haubner et al. for a RGP containing glycosylated peptide [318]. Pronounced delayed blood clearance and reduced liver uptake were visible in two different animal models.

Except for the blood value 1 h p.i., all other investigated organs were either similar or lower for the carbohydrated compound and demonstrated the reduced unspecific tissue binding of [^{68}Ga]**PSMA-20** compared to [^{68}Ga]**PSMA I&T.** The feature of reduced tissue uptake might be useful for therapeutic application in order to reduce the unwanted radiation-toxicity.

2.3.4 Influence of strong albumin binding on the biodistribution

As indicated in chapter **III 1.1.6**, plasma protein binding affects the *in vivo* biodistribution and is a key parameter during the design of novel compounds that has to be taken into account [226-228].

To investigate if the strong albumin binding of [^{177}Lu]**PSMA-40** (-f(4-NH_2)y(3-I)fk-) and [^{177}Lu]**PSMA-41** (-f(4-NH_2)y-2-nal-k-) is able to increase the tumor uptake, both ^{177}Lu-labeled tracer were injected into male LNCaP tumor xenograft bearing CB-17 SCID mice and evaluated 1 h p.i. (**PSMA-41**) and 24 h p.i. (**PSMA-40** and **PSMA-41**). The references [^{177}Lu]**PSMA I&T** and [^{177}Lu]**PSMA-617** were included for comparison. The data for [^{177}Lu]**PSMA-43** (-y(3-I)fk-) as reference were taken from the literature [204].

Table 23. Biodistribution data of [^{68}Ga]**PSMA-40,** [^{68}Ga]**PSMA-41,** [^{68}Ga]**PSMA-43,** [^{68}Ga]**PSMA I&T and** [^{68}Ga]**PSMA-617** (in % ID/g) in LNCaP-tumor xenograft bearing CB-17 SCID mice at 24 h p.i. (n = 4, respectively). Between 4.5 MBq and 7.9 MBq of the respective ^{177}Lu-labeled radioligand were injected (0.15 to 0.25 nmol tracer). * = Data taken from Wirtz et al. [204].

	[^{177}Lu]**PSMA-40** 24 h p.i.	[^{177}Lu]**PSMA-41** 24 h p.i.	[^{177}Lu]**PSMA-43** 24 h p.i. *	[^{177}Lu]**PSMA I&T** 24 h p.i.	[^{177}Lu]**PSMA-617** 24 h p.i.
blood	0.09 ± 0.03	0.17 ± 0.03	0.05 ± 0.02	0.01 ± 0.01	0.01 ± 0.01
heart	0.33 ± 0.09	0.25 ± 0.10	0.10 ± 0.03	0.05 ± 0.03	0.01 ± 0.01
lung	2.56 ± 0.58	0.51 ± 0.16	0.26 ± 0.10	0.16 ± 0.03	0.04 ± 0.01
liver	0.42 ± 0.09	0.62 ± 0.41	0.16 ± 0.06	0.05 ± 0.01	0.12 ± 0.06
spleen	14.34 ± 4.24	4.71 ± 2.45	6.63 ± 3.25	1.94 ± 1.01	0.08 ± 0.01
pancreas	0.40 ± 0.15	0.16 ± 0.06	0.20 ± 0.11	0.05 ± 0.02	0.01 ± 0.01
stomach	0.66 ± 0.17	0.12 ± 0.03	0.13 ± 0.04	0.05 ± 0.02	0.02 ± 0.01
intestine	0.89 ± 0.25	0.12 ± 0.03	0.14 ± 0.06	0.12 ± 0.06	0.12 ± 0.08
kidney	206.34 ± 80.52	194.62 ± 39.84	100.92 ± 45.43	34.66 ± 17.20	1.44 ± 0.42
adrenal g.	4.09 ± 2.56	1.27 ± 0.16	2.37 ± 0.41	1.06 ± 0.24	0.13 ± 0.12
muscle	0.07 ± 0.02	0.06 ± 0.02	0.07 ± 0.04	0.01 ± 0.01	0.01 ± 0.01
bone	0.06 ± 0.11	0.06 ± 0.02	0.03 ± 0.01	0.01 ± 0.01	0.03 ± 0.01
brain	0.04 ± 0.01	0.03 ± 0.02	0.11 ± 0.03	0.02 ± 0.01	0.02 ± 0.01
tumor	14.03 ± 2.20	14.01 ± 1.25	16.05 ± 2.51	4.06 ± 1.12	7.46 ± 0.90
t/blood	155.9	82.4	321	406	746
t/kidney	0.07	0.07	0.16	0.1	5.2
t/muscle	200.4	233.5	229.3	406	746

The results in Table 23 show that all three compounds with high albumin binding (> 96%) exhibited an almost two- to fourfold higher tumor uptake after 24 h than the references [^{177}Lu]**PSMA I&T** and [^{177}Lu]**PSMA-617**. The high tumor accumulation confirmed, that increase of albumin binding, through the introduction of 4-iodo-D-phenylalanine into the linker region, enables prolonged tumor targeting *in vivo*.

The direct comparison of [^{177}Lu]**PSMA-40 and** [^{177}Lu]**PSMA-41** revealed that unspecific organ uptake was less for [^{177}Lu]**PSMA-41.** The only exception was the liver uptake, which

was slightly higher after 24 h p.i. for [^{177}Lu]**PSMA-41.** The higher unspecific tissue uptake rendered the peptide spacer configuration of [^{177}Lu]**PSMA-40** (-f(4-NH_2)y(3-I)fk-) less favorable compared to the amino acid sequence in [^{177}Lu]**PSMA-41** (-f(4-NH_2)y-2-nal-k-). Higher unspecific uptake of [^{177}Lu]**PSMA-40** could be a consequence of the amino acid 3-iodo-D-tyrosine, which was reported to undergo metabolic transformation *in vivo* [270-273]. The extended *in vivo* half-life was also visible through the higher blood uptake of the strong albumin-binding compounds after 24 h p.i. compared to the references [^{177}Lu]**PSMA I&T** and [^{177}Lu]**PSMA-617**. The activity concentration in the blood was more than 17-fold higher when comparing [^{177}Lu]**PSMA-41** and [^{177}Lu]**PSMA I&T** (0.17% vs. 0.01%, respectively).

Although [^{177}Lu]**PSMA-40** and [^{177}Lu]**PSMA-43** displayed similar *in vitro* characteristics regarding affinity, internalization and albumin binding, the tumor uptake was higher for [^{177}Lu]**PSMA-43** (16.05% vs. 14.03%, respectively). At the same time, renal uptake was almost twofold higher for [^{177}Lu]**PSMA-40** compared to [^{177}Lu]**PSMA-43**. Since [^{177}Lu]**PSMA-41** displayed a similar high kidney uptake as [^{177}Lu]**PSMA-40** and they both possess 4-amino-D-phenylalanine within the peptide spacer compared to [^{177}Lu]**PSMA-43**, the extension of the peptide spacer must be responsible for this unfavorable renal accumulation.

The high kidney uptake, however, could also account for the unexpected lower tumor uptake of [^{177}Lu]**PSMA-40** and [^{177}Lu]**PSMA-41** compared to [^{177}Lu]**PSMA-43**. Considering the kidney and the tumor as two competing *in vivo* target-expressing regions, the high renal accumulation could reduce the possible amount of ^{177}Lu-labeled tracer, which is able to reach the tumor. Further investigations have to be carried out in order to determine the reason of the high renal uptake of compounds possessing 4-amino-D-phenylalanine in the peptide spacer. Although the kidneys physiologically express PSMA in the proximal tubules, this does not necessarily account for the total uptake in this region. Other factors like charge, hydrophilicity and the influence of peptide scavenger receptors like megalin and cubilin may be involved [319-321].

The slightly higher albumin binding of [^{177}Lu]**PSMA-41** compared to [^{177}Lu]**PSMA-43** (97.6% vs. 96.6%, respectively) was displayed through the increased residual blood uptake after 24 h p.i. (0.17% vs. 0.05%, respectively). Compared to the reference [^{177}Lu]**PSMA-43**, this suggests that the *in vivo* distribution is not completed after 24 h and that evaluation at later time points is necessary for strong albumin binding compounds. An uncomplete distribution phase impedes the comparability between the ligands, since the tumor to tissue ratios significantly depend on the respective stage of tracer distribution. While the ligand [^{177}Lu]**PSMA-43** showed the most favorable tumor to tissue ratios (Figure 49), [^{177}Lu]**PSMA-40** displayed the most inferior 24 h p.i.. [^{177}Lu]**PSMA-41** showed better ratios for all strong blood perfused organs like the

heart, lung and liver compared to [^{177}Lu]**PSMA-43**, which could be caused through the higher plasma protein binding of [^{177}Lu]**PSMA-43** and the apparent unfinished distribution phase.

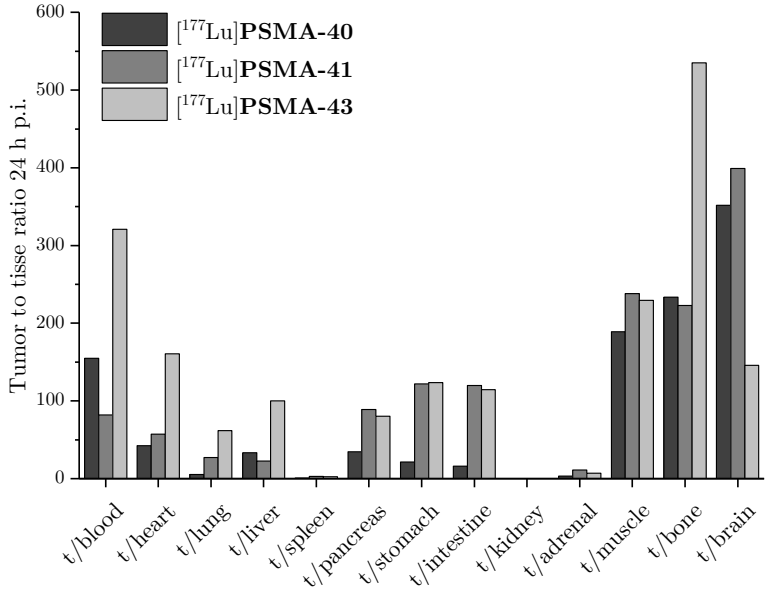

Figure 49. Tumor to tissue ratios for [^{177}Lu]**PSMA-40**, [^{177}Lu]**PSMA-41** and [^{177}Lu]**PSMA-43** at 24 h p.i. in LNCaP-tumor bearing CB-17 SCID mice (n = 4; respectively).

It is not clear, if the tumor uptake of the strong albumin binding compounds would increase or decrease after 24 h and has yet to be determined. However, tracer accumulation over time in the tumor tissue between 1 h p.i. and 24 h p.i. for [^{177}Lu]**PSMA-41**, [^{177}Lu]**PSMA I&T** and [^{177}Lu]**PSMA-617** indicates that tumor wash-out occurs faster for weak albumin binding compounds than for strong binding tracer as shown in Figure 50. Although [^{177}Lu]**PSMA-617** demonstrated a slightly higher initial tumor uptake compared to [^{177}Lu]**PSMA-41**, the total area under the curve (AUC) of accumulated radioactivity in the tumor tissue was lower.

	[^{177}Lu]**PSMA-41** 1 h p.i.	[^{177}Lu]**PSMA-617** 1 h p.i.
blood	1.34 ± 0.12	0.36 ± 0.09
heart	1.30 ± 0.04	0.19 ± 0.04
lung	2.46 ± 0.41	0.48 ± 0.12
liver	0.97 ± 0.19	0.50 ± 0.12
spleen	24.66 ± 4.74	3.67 ± 0.99
pancreas	0.75 ± 0.06	0.15 ± 0.03
stomach	0.51 ± 0.11	0.43 ± 0.24
intestine	0.40± 0.06	0.27 ± 0.06
kidney	165.86 ± 45.49	64.84 ± 30.03
adrenal g.	4.54 ± 0.70	2.65 ± 0.72
muscle	0.26 ± 0.07	0.10 ± 0.03
bone	0.34 ± 0.17	0.19 ± 0.09
brain	0.03± 0.01	0.04 ± 0.02
tumor	8.51 ± 1.10	8.98 ± 1.86

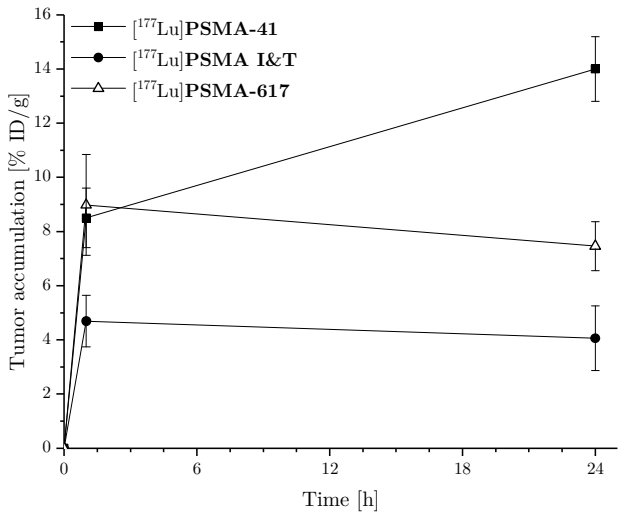

Figure 50. Biodistribution data (in % ID/g) for [^{177}Lu]**PSMA-41** (n = 3) and [^{177}Lu]**PSMA-617** (n = 4) at 1 h p.i. in LNCaP-tumor bearing CB-17 SCID mice (left). Approx. 8 to 10 MBq (0.15 to 0.2 nmol) were injected. Dynamic tumor uptake over 24 h at 1 h p.i. and 24 h p.i. for [^{177}Lu]**PSMA-41**, [^{177}Lu]**PSMA I&T** and [^{177}Lu]**PSMA-617** (right).

Although attention should be paid regarding high tracer accumulation in the kidneys, a recent investigation of Kulkarni et al. found no occurring renal toxicity in humans after treatment with [^{177}Lu]**PSMA I&T**. Further, no evidence for a significant change in serum creatinine, creatinine clearance and tubular extraction rate were detected after the well tolerated treatment [215]. These findings would justify a first in human application of [^{177}Lu]**PSMA-41** for therapy, despite the higher renal uptake in the preclinical studies compared to [^{177}Lu]**PSMA I&T** (165.86% ID/g vs. 128.90% ID/g, respectively).

The effect of strong plasma protein binding for PSMA ligands was recently published by Choi et al. and Kelly et al. [230,322]. A striking increase of tumor uptake was observed for the respective compounds inheriting strong albumin binding over 24 to 72 h compared to the references without enhanced plasma protein binding. However, kidney uptake of these PSMA tracer was also drastically increased, which is in agreement with the finding for [^{177}Lu]**PSMA-40** and [^{177}Lu]**PSMA-41** in this work.

2.3.5 Influence of the binding motif EuE on the biodistribution

The strong internalizing compounds [^{177}Lu]**PSMA-49** (245.0%), [^{177}Lu]**PSMA-62** (343.9%) and [^{177}Lu]**PSMA-66** (297.8%) were used to evaluate the influence of strong internalization on tumor uptake in tumor bearing CB-17 SCID mice 1 h p.i..

Table 24. Biodistribution data of [^{177}Lu]**PSMA-49,** [^{177}Lu]**PSMA-62 and** [^{177}Lu]**PSMA-66** (in % ID/g) in LNCaP-tumor xenograft bearing CB-17 SCID mice at 1 h p.i. (n = 4, respectively). Between 3.5 MBq and 5.5 MBq of the respective ^{177}Lu-labeled radioligand were injected (0.15 to 0.25 nmol tracer).

	[^{177}Lu]**PSMA-49** 1 h p.i.	[^{177}Lu]**PSMA-62** 1 h p.i.	[^{177}Lu]**PSMA-66** 1 h p.i.
blood	0.46 ± 0.06	0.52 ± 0.03	0.50 ± 0.03
heart	0.57 ± 0.11	0.58 ± 0.06	0.49 ± 0.06
lung	1.47 ± 0.25	0.87 ± 0.11	0.62 ± 0.12
liver	0.99 ± 0.19	0.37 ± 0.04	0.32 ± 0.02
spleen	20.53 ± 6.79	4.62 ± 1.81	1.93 ± 0.04
pancreas	0.56 ± 0.07	0.18 ± 0.05	0.15 ± 0.04
stomach	0.35 ± 0.10	0.51 ± 0.2	0.28 ± 0.04
intestine	0.30 ± 0.08	0.49 ± 0.25	0.21 ± 0.03
kidney	162.96 ± 23.20	106.45 ± 17.18	117.47 ± 6.86
adrenal gland	5.66 ± 1.66	1.92 ± 0.80	0.78 ± 0.07
muscle	0.17 ± 0.02	0.12 ± 0.03	0.19 ± 0.07
bone	0.29 ± 0.14	0.30 ± 0.08	0.37 ± 0.13
brain	0.03 ± 0.01	0.03 ± 0.01	0.02 ± 0.01
tumor	8.21 ± 0.23	8.00 ± 0.78	10.00 ± 0.44
tumor/blood	17.8	15.4	20.0
tumor/kidney	0.05	0.08	0.09
tumor/muscle	48.3	66.7	52.6

Compared to the tumor uptake of [^{177}Lu]**PSMA I&T** after 1h p.i. (4.69 ± 0.95%, chapter **III 2.3.1**, Table 21), a significant increase in tumor activity was achieved through the improvement of internalization and affinity as shown in Table 24. As already observed for [^{177}Lu]**PSMA-16** (chapter **III 2.3.2**), [^{177}Lu]**PSMA-40** and [^{177}Lu]**PSMA-41** (chapter **III 2.3.4**), the extension of the peptide spacer with 4-amino-D-phenylalanine led to high kidney uptake and confirmed that this modification increases renal accumulation.

The introduction of trimesic acid into the linker of [^{177}Lu]**PSMA-62** (Figure 51) led to a reduction of renal uptake (106.45 ± 17.18% vs. 162.96 ± 23.20%, respectively) and slightly lower tumor uptake compared to the reference. Since the internalization for [^{177}Lu]**PSMA-62** was higher in direct comparison to [^{177}Lu]**PSMA-49**, the lower tumor uptake was unexpected. As discussed in chapter **III 1.1.8**, it is unclear to what extent internalization contributes to tumor uptake and if it is less important than affinity. The direct comparison of [^{177}Lu]**PSMA-49** and [^{177}Lu]**PSMA-62** indicates that affinity is more crucial since [^{177}Lu]**PSMA-49** was more affine towards PSMA (2.5 ± 0.6 nM vs. 4.0 ± 0.2 nM, respectively).

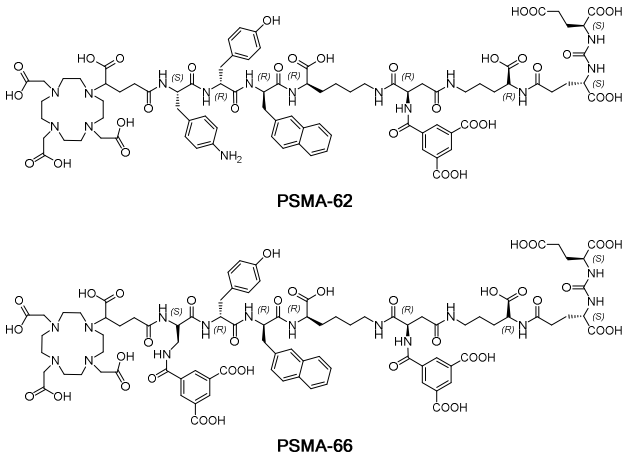

Figure 51. Illustration of the trimesic acid-modified PSMA inhibitors **PSMA-62** and **PSMA-66.**

The exchange of 4-amino-D-phenylalanine to L-Dap(TMA) in the peptide spacer and incorporation of TMA into the linker of [^{177}Lu]**PSMA-66** (Figure 51) resulted in the highest tumor accumulation after 1 h p.i. in this work (10.00 ± 0.44% ID/g) and at the same time it was possible to reduce the kidney uptake compared to [^{177}Lu]**PSMA-49** (117.47 ± 6.86% ID/g vs. 162.96 ± 23.20% ID/g, respectively). Direct comparison with [^{177}Lu]**PSMA-62** showed that unspecific binding to PSMA-negative tissue, except for the muscle, was even lower. A possible explanation is the extreme negatively charged character of this compound, which exhibits nine negative charges at pH 7.4. Huang et al. reported about similar findings after incorporation of negative charges into the molecular structure of PSMA inhibitors [252]. It was also shown that the incorporation of negative charges is able to reduce the liver uptake of affibodies [323]. This is in agreement with the findings for the liver accumulation of [^{177}Lu]**PSMA-66**, since it displayed the lowest liver uptake among the investigated compounds.

[^{177}Lu]**PSMA-66** demonstrated in direct comparison with [^{177}Lu]**PSMA-49** and [^{177}Lu]**PSMA-62** neither the highest internalization nor the highest affinity towards PSMA to explain the higher tumor accumulation. However, [^{177}Lu]**PSMA-66** showed the lowest cellular efflux upon internalization (chapter **III 1.2.4**, Figure 37). If the total tracer accumulation in the target tissue is considered as a steady process of binding, internalization and externalization (clearance), a higher cell retention could increase the effective uptake in the PSMA-expressing tissues over time.

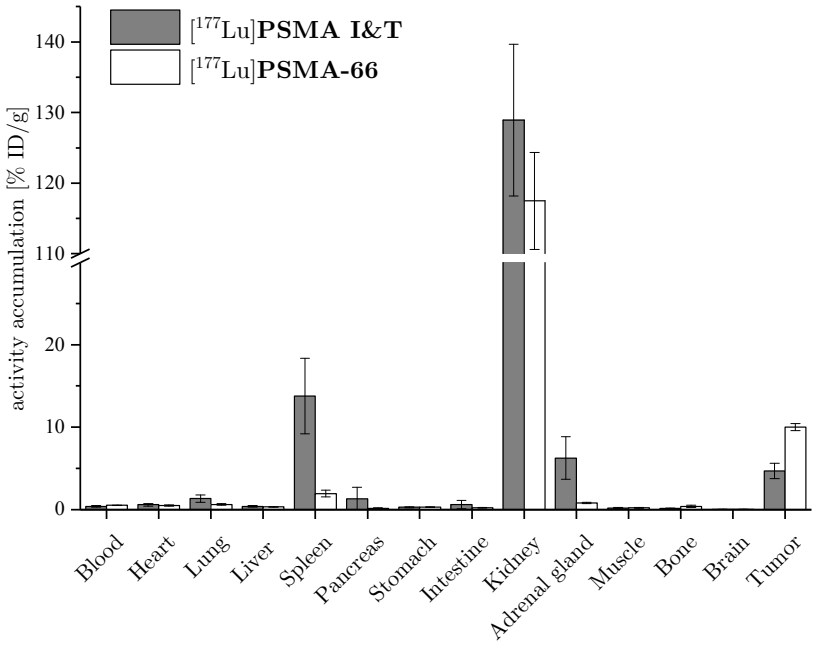

Figure 52. Biodistribution (in %ID/g) of 2.5 to 3.0 MBq (0.15 to 0.25 nmol) of [^{177}Lu]**PSMA-66** and [^{177}Lu]**PSMA I&T** in LNCaP-tumor bearing CB-17 SCID mice (n = 4, respectively).

The comparison of [^{177}Lu]**PSMA I&T** and [^{177}Lu]**PSMA-66** in Figure 52 demonstrates that the stepwise improvement of **PSMA I&T** from its basic molecular structure to **PSMA-66** was able to increase the tumor uptake more than twofold, to reduce binding to PSMA-unspecific tissue and to reduce simultaneously the renal accumulation of the radiolabeled tracer. The *in vivo* disposition of [^{177}Lu]**PSMA-66** together with its optimized *in vitro* characteristics render it especially attractive for endoradiotherapy, since fast body clearance and long retention in the tumor tissue are crucial determinants for efficacy and safety.

2.4 Small-animal PET imaging

The distribution of the developed ^{68}Ga-labeled PSMA inhibitors *in vivo* was visualized using a small animal PET scanner (Siemens Inveon PET Scanner). Between approx. 4.0 and 17.0 MBq (0.15 nmol to 0.25 nmol) of the ^{68}Ga-labeled tracer were injected into healthy and LNCaP xenograft tumor bearing CB-17 SCID mice and the images recorded immediately after injection over 1.5 h in dynamic scans or for 15 min after 1 h p.i.. All experiments were conducted using an identical protocol to assure comparability. Three-dimensional regions of interest (ROI) were drawn in OSEM 3D reconstructed images and quantified. The results were illustrated as time-activity curves (TACs) in logarithmic plots.

2.4.1 Influence of the animal model

The utilization of a different animal model compared to Wirtz et al. [204], required the investigation of [^{68}Ga]**PSMA I&T** in CB-17 SCID mice to examine if the animal model affects the distribution pattern.

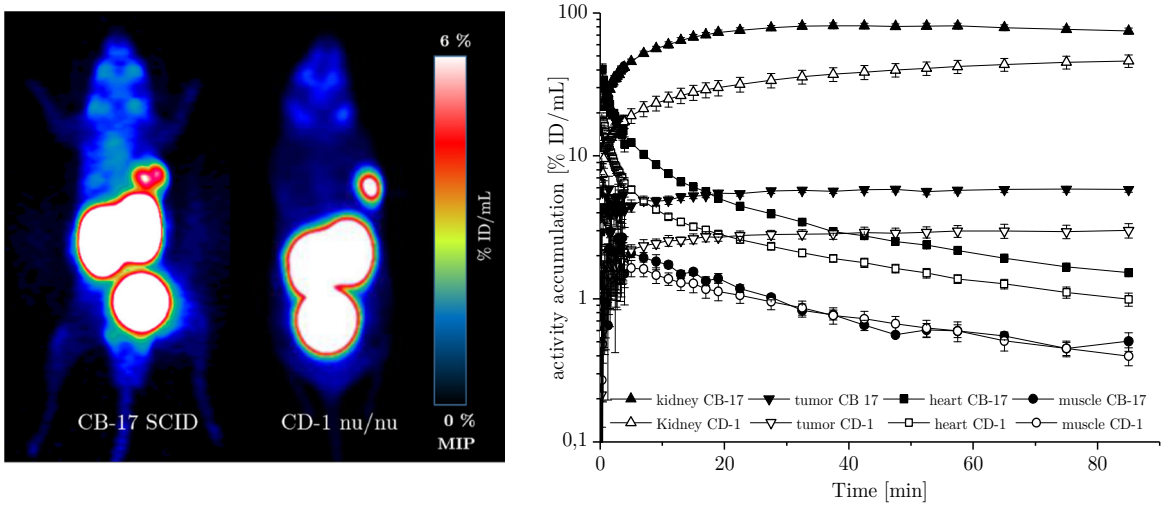

Figure 53. Maximum intensity projection (MIP) of a µPET scan in a LNCaP-tumor bearing CB-17 SCID mouse after injection of approx. 7.0 MBq [^{68}Ga]**PSMA I&T** (dynamic scan, summed up frames 1 to 1.5 h p.i.) and PET image of 15.8 MBq [^{68}Ga]**PSMA I&T** in a LNCaP-tumor bearing CD-1 nu/nu mouse (static, MIP at 1 h p.i.) (left). TACs (logarithmic plot) in %ID/mL derived from dynamic PET data (90 min acquisition time, OSEM 3D reconstruction) in a LNCaP-tumor bearing CB-17 SCID or CD-1 nu/nu mouse (right). Data for the CD-1 nu/nu scan are taken from Wirtz et al. [204].

The *in vivo* disposition of [^{68}Ga]**PSMA I&T** revealed distinct differences in the two models as shown in Figure 53 and confirmed the found differences in the biodistribution studies (chapter **III 4.3.1**). Dissimilarities were observed in the total tracer uptake in the kidneys, which was higher in CB-17 SCID compared to CD-1 nu/nu (74.6% ID/mL vs. 46.1% ID/mL after 85 min, respectively). Whereas a steady increase of kidney activity was observed in the CD-1 nu/nu model over the investigated time, the highest tracer accumulation in the CB-17 SCID animal was already reached after 37 min with subsequent decrease. The accumulation in the blood and the muscle was also slightly higher for the CB-17 model, indicating a distinct difference in

unspecific binding, which is also visible through the overall higher background activity (Figure 53). Confirmation of this unspecific perfusion-dependent uptake in both models was shown through linear decrease in the logarithmic plot in Figure 53.

The results in Figure 53 are well correlating with the observed values from the biodistribution study. The obtained kidney uptake values after 57.5 min in PET (80.9% ID/mL vs. 42.1% ID/mL, CB-17 vs. CD-1, respectively) differed only marginal from the biodistribution study (71.8% ID/g vs. 53.2% ID/g, respectively). Blood and muscle uptake in the PET scan were, however, approx. twofold higher compared to the biodistribution study of both models. Regarding the tumor, tracer accumulation in the CB-17 SCID mouse was higher (5.8% ID/mL vs. 3.0% ID/mL, respectively) and remained, similar to the CD-1 nu/nu animal, steady over 85 min.

It is noteworthy that single experiments exhibit only limited informative value and that the investigations should be done at least in triplicate to minimize interindividual physiological differences. Especially the tracer uptake in the tumor has to be assessed carefully, since several publications reported about the correlation between tumor size and uptake in PET studies probably caused through the partial volume effect [184,324,325].

2.4.2 Influence of spacer extension and stereochemistry on EuK-based inhibitors

The PSMA derivatives **PSMA-15** to **PSMA-19** were investigated in ^{68}Ga-PET scans to evaluate the influence of the peptide spacer extension with 4-amino-phenylalanine on the *in vivo* behavior. Further, the influence of the stereochemistry (chapter **III 1.1.4**) was examined and compared among the tracer.

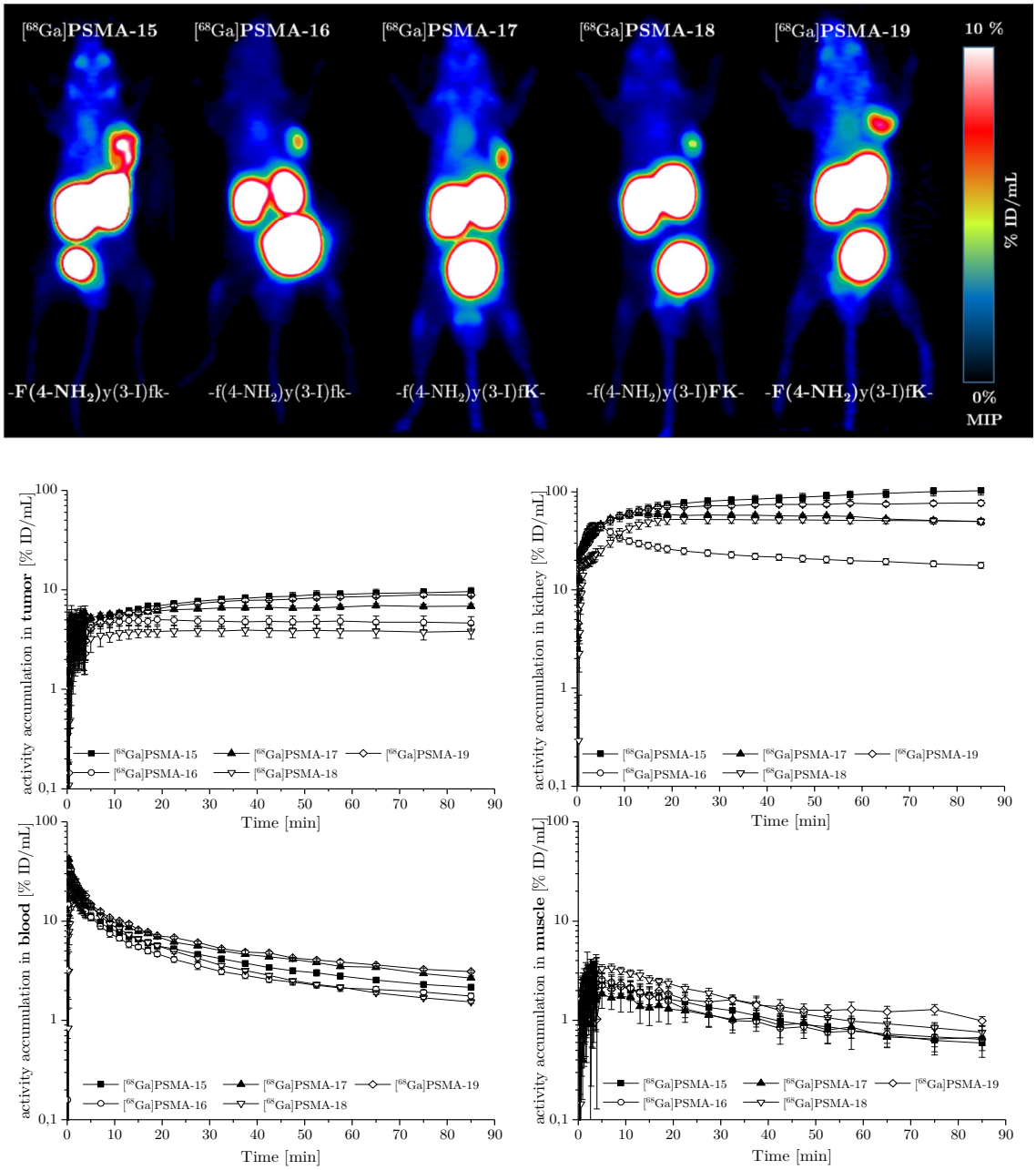

Figure 54. Maximum intensity projection (MIP) of µPET scans in LNCaP-tumor bearing CB-17 SCID mice after injection of approx. 3.8 to 9.4 MBq (0.15 to 0.25 nmol tracer) of the respective ^{68}Ga-labeled PSMA inhibitor (**PSMA-15** to **PSMA-19**) (dynamic scan, summed up frames 1 to 1.5 h p.i.) (top). TACs (logarithmic plot) in %ID/mL of the respective ^{68}Ga-labeled PSMA inhibitor derived from dynamic PET data (90 min acquisition time, OSEM 3D reconstruction) in LNCaP-tumor bearing CB-17 SCID mice (bottom) for tumor, kidney, blood pool (heart) and muscle.

The influence of the stereochemistry was distinctive as shown in Figure 54. Highest background activity was seen for [^{68}Ga]**PSMA-19**, which also exhibited an albumin binding of almost 90% as ^{nat}Lu-labeled analog. All ligands showed a non-logarithmic decrease in blood pool activity, indicating a more complex distribution process. Pronounced differences were seen in the kidney uptake. [^{68}Ga]**PSMA-16** showed the lowest renal accumulation with a rapid onset of clearance after 27 mins, whereas [^{68}Ga]**PSMA-15** displayed the highest value with 103.1% ID/mL after 85 min with ongoing tracer accumulation. Utilization of 4-amino-D-phenylalanine in [^{68}Ga]**PSMA-17** and [^{68}Ga]**PSMA-18** was not able to reduce the kidney uptake in the same extent as for [^{68}Ga]**PSMA-16**. This implies that the whole configuration of the PSMA inhibitor itself and not the stereochemistry of a single amino acid is determining regarding kidney uptake.

A clear correlation between internalization capacity of the respective ^{68}Ga-radiolabeled ligand and tumor uptake was visible as shown in Figure 55 (left panel), rendering the internalization rate as determining *in vitro* parameter for enhanced tumor accumulation. Yet, this observation was only done for this set of compounds. A relationship between internalization and renal uptake was, however, not observed (Figure 55, right panel). Although the kidneys express PSMA physiologically, it is not clear why both target-expressing tissues behave differently regarding tracer accumulation. The difference in organ perfusion could account for this phenomenon but has, yet, to be evaluated.

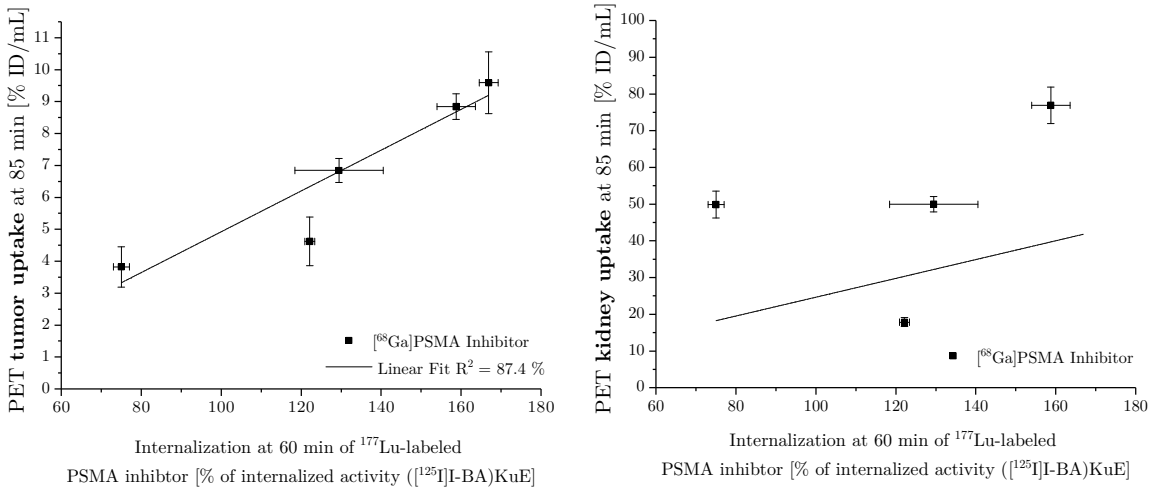

Figure 55. Linear correlation plot between PET tumor uptake (left) or kidney uptake (right) in %ID/mL of the respective ^{68}Ga-labeled PSMA inhibitor (**PSMA-15** to **PSMA-19**) and internalization of the respective ^{177}Lu-labeled PSMA inhibitor (**PSMA-15** to **PSMA-19**).

2.4.3 Effect of carbohydration on EuK-based inhibitors

The influence of carbohydration alone and in combination with 4-amino-D-phenylalnine as peptide spacer extension was investigated in small animal PET scans. Additionally, the influence of a second carbohydrate group in [^{68}Ga]**PSMA-29** was evaluated and compared regarding kidney uptake with [^{68}Ga]**PSMA I&T**.

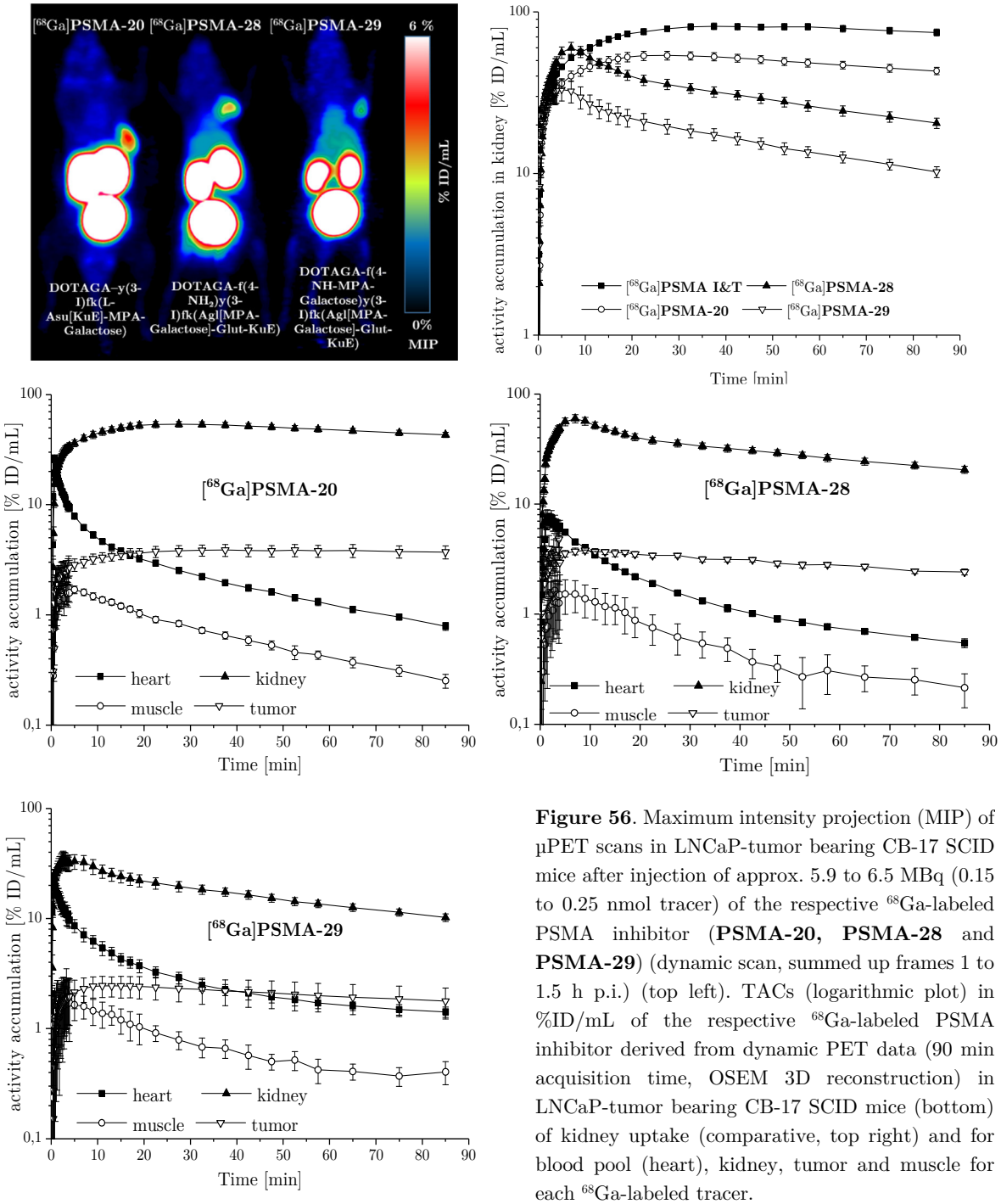

Figure 56. Maximum intensity projection (MIP) of µPET scans in LNCaP-tumor bearing CB-17 SCID mice after injection of approx. 5.9 to 6.5 MBq (0.15 to 0.25 nmol tracer) of the respective ^{68}Ga-labeled PSMA inhibitor (**PSMA-20, PSMA-28** and **PSMA-29**) (dynamic scan, summed up frames 1 to 1.5 h p.i.) (top left). TACs (logarithmic plot) in %ID/mL of the respective ^{68}Ga-labeled PSMA inhibitor derived from dynamic PET data (90 min acquisition time, OSEM 3D reconstruction) in LNCaP-tumor bearing CB-17 SCID mice (bottom) of kidney uptake (comparative, top right) and for blood pool (heart), kidney, tumor and muscle for each ^{68}Ga-labeled tracer.

The comparative logarithmic TAC plot for kidney uptake in Figure 56 demonstrates the favorable benefit of the carbohydrate moiety in [^{68}Ga]**PSMA-20** compared to [^{68}Ga]**PSMA I&T**, displaying a difference of more than 30% ID/mL after 85 min p.i. and confirmed the observed results in the comparative biodistribution study (chapter **III 2.3.3**). Unspecific accumulation of [^{68}Ga]**PSMA-20** was lower and resulted in less background activity compared to [^{68}Ga]**PSMA I&T**. The combination of the extended peptide spacer and carbohydration was able to even accelerate the kidney clearance for [^{68}Ga]**PSMA-28** compared to [^{68}Ga]**PSMA-20**. This observation seems reasonable since the sole carbohydration in [^{68}Ga]**PSMA-20** and sole peptide spacer extension in [^{68}Ga]**PSMA-16** showed already less renal tracer uptake compared to [^{68}Ga]**PSMA I&T**.

The introduction of second carbohydrate moiety in [^{68}Ga]**PMSA-29** resulted in the lowest kidney uptake of all investigated ligands in this work. Upon injection, kidney clearance was already visible after 22 min and declined to 10.2% ID/mL after 85 min, being sevenfold lower compared to [^{68}Ga]**PSMA I&T**.

Tracer accumulation in the tumor xenograft was highest for [^{68}Ga]**PMSA-20** followed by [^{68}Ga]**PSMA-28** and [^{68}Ga]**PSMA-29**. Only [^{68}Ga]**PSMA-20** displayed constant tumor retention in the xenograft, whereas the other two ligands showed tendencies of clearance with slight decrease over time. In contrast to the findings from chapter **III 2.4.2**, no direct correlation between affinity or internalization and tumor uptake was observed.

[^{68}Ga]**PSMA-28** and [^{68}Ga]**PSMA-29** showed a slightly higher background activity in the liver and intestine region during the small animal PET scans. [^{68}Ga]**PSMA-16** (extended peptide spacer) and [^{68}Ga]**PSMA-20** (galactose moiety) were evaluated regarding their metabolic stability and found to be stable, which excludes metabolite formation as possible reason. Further µPET studies are necessary to determine if this higher abdominal background activity is caused through the inhibitors or the experimental setup. In conclusion, carbohydration proved to be useful for less background uptake and might therefore be especially attractive for therapeutic agents.

2.4.4 Effect of strong albumin-binding on EuK-based inhibitors

The strong albumin-binding tracer **PSMA-40** and **PSMA-41** were investigated in LNCaP xenograft tumor bearing CB-17 SCID mice to determine their pharmacokinetic traits in ^{68}Ga-PET imaging.

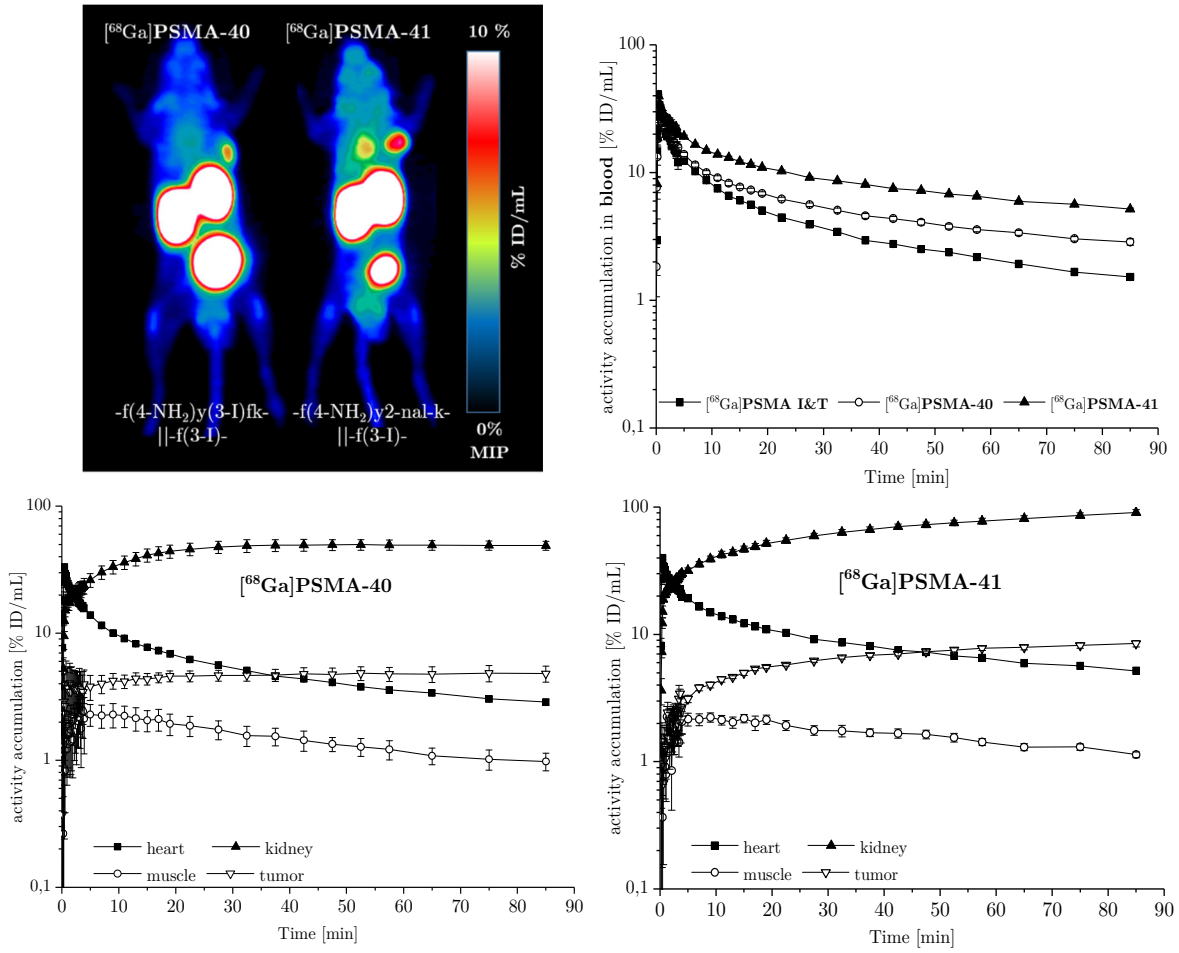

Figure 57. Maximum intensity projection (MIP) of µPET scans in LNCaP-tumor bearing CB-17 SCID mice after injection of approx. 9.2 and 10.6 MBq (0.15 to 0.25 nmol tracer) of the ^{68}Ga-labeled PSMA inhibitor **PSMA-40 and PSMA-41,** respectively (dynamic scan, summed up frames 1 to 1.5 h p.i.) (top left). TACs (logarithmic plot) in %ID/mL of the respective ^{68}Ga-labeled PSMA inhibitor derived from dynamic PET data (90 min acquisition time, OSEM 3D reconstruction) in LNCaP-tumor bearing CB-17 SCID mice of blood pool (heart) uptake (comparative, top right) and for blood pool (heart), kidney, tumor and muscle for each ^{68}Ga-labeled tracer.

The strong plasma protein binding of [^{68}Ga]**PSMA-40** and [^{68}Ga]**PSMA-41** resulted in high blood pool activity during the acquisition of the PET images as shown in Figure 57. Blood pool activity was found to be two- to threefold higher compared to [^{68}Ga]**PSMA I&T** 85 min p.i. and to be in accordance with the biodistribution studies (chapter **III 2.3.4**). Both tracer were primarily taken up in the PSMA-expressing tumor and kidneys and excreted into the bladder. Direct comparison of [^{68}Ga]**PSMA-40** and [^{68}Ga]**PSMA-41** regarding tumor uptake indicated stronger tumor accumulation in the case of [^{68}Ga]**PSMA-41**.

High contrast imaging is necessary for optimal diagnostic approaches, which therefore renders high plasma-protein binding PSMA inhibitors inferior to fast clearing compounds within the first few hours after tracer injection. Tumor to tissues rations should, however, increase over time and finally result in more favorable image properties. The short half-life of ^{68}Ga limits its applications regarding long circulating PSMA inhibitors and necessitates the utilization to radionuclides with longer half-lives as for instance ^{64}Cu, which is employable for PET-imaging and endoradiotherapy.

2.4.5 Effect of 2,4-dinitrobenzoic linker substitution on EuK-based inhibitors

The EuK-based inhibitor **PSMA-36** was evaluated in a small animal PET scan to examine the influence of the 2,4-dinitrobenzoic acid in the linker on the *in vivo* distribution.

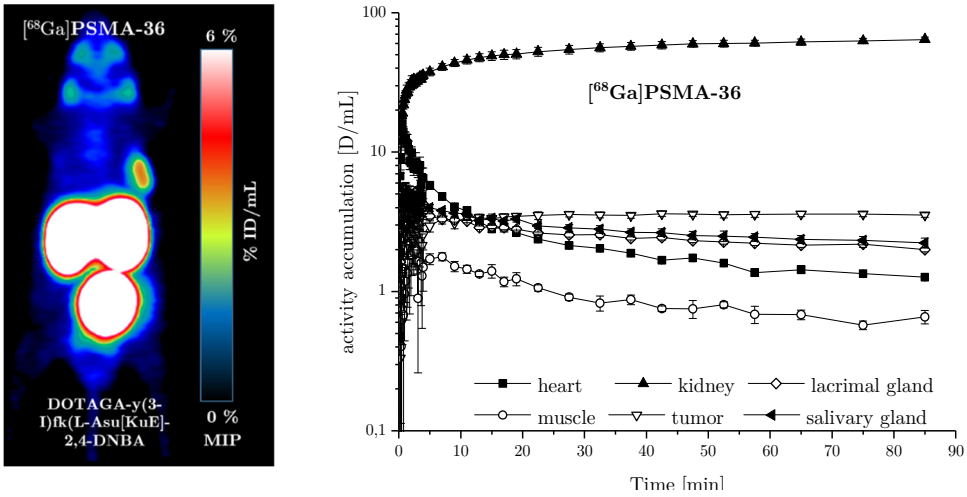

Figure 58. Maximum intensity projection (MIP) of a µPET scan in LNCaP-tumor bearing CB-17 SCID mice after injection of approx. 10.3 MBq (0.19 nmol tracer) of [^{68}Ga]**PSMA-36** (dynamic scan, summed up frames 1 to 1.5 h p.i.) (top left). TACs (logarithmic plot) in %ID/mL of [^{68}Ga]**PSMA-36** derived from dynamic PET data (90 min acquisition time, OSEM 3D reconstruction) in a LNCaP-tumor bearing CB-17 SCID mouse of blood pool (heart), kidney, tumor, muscle, lacrimal- and salivary gland.

The logarithmic TACs plot in Figure 58 shows specific kidney and tumor uptake of [^{68}Ga]**PSMA-36**. Linear decrease of the blood pool activity and in the muscle region imply low unspecific binding and fast excretion. Accumulation in the tumor remained steady over the observed period. Although [^{177}Lu]**PSMA-36** exhibited a more than threefold higher internalization rate than [^{177}Lu]**PSMA I&T**, tumor uptake was only moderate with 3.5% ID/mL after 85 min p.i.. The most significant difference compared to [^{68}Ga]**PSMA I&T** was the high and steady uptake in the lacrimal and salivary gland, displaying approx. 2% ID/mL in both regions (Figure 57). Since the only structural difference to the reference [^{68}Ga]**PSMA I&T** is the introduction of 2,4-dinitrobenzoic acid, the linker modification must be the reason for this enhanced uptake. However, further studies are necessary to confirm this effect.

It is also interesting, that the clearance in these regions was slower compared to the blood pool and muscle, which implies that a distinct retaining mechanism is involved. It was reported that PSMA participates in angiogenesis during ocular neovascularization in mice and might therefore explain the uptake of [^{68}Ga]**PSMA-36** [116]. Tracer accumulation in the salivary glands is a common problem during clinical therapeutic approaches with ^{177}Lu-labeled PSMA inhibitors [215]. Drug uptake into the salivary glands depends on intra- or extracellular pathways and most commonly on simple diffusion among the phospholipid bilayer of the acinar cells. Saliva drug concentrations are reflected predominantly by the free, non-ionized fraction in the blood plasma regarding passive diffusion [326-328]. In this respect, it seems highly unlikely that passive diffusion is responsible for the salivary gland uptake. Other mechanisms have to be involved since EuK-based PSMA inhibitors are highly charged *in vivo* and thus exhibit high polarity. Further, passive diffusion would be visualized during PET scans in every region as high background activity, which does not occur for most PSMA ligands since the rapid clearance removes the tracer from the blood pool.

2.4.6 Effect of the EuE binding motif

Since the change from EuK to EuE as binding motif resulted in a favorable increase of internalization for [^{177}Lu]**PSMA-46** compared to [^{177}Lu]**PSMA-30** (216.2 ± 9.2% vs. 77.3 ± 0.7%, respectively), the tracer kinetics of [^{68}Ga]**PSMA-46** were investigated in a PET scan and compared to its EuK-based analog [^{68}Ga]**PSMA-30**. TAC-Data for [^{68}Ga]**PSMA-30** were taken from Wirtz et al. [204].

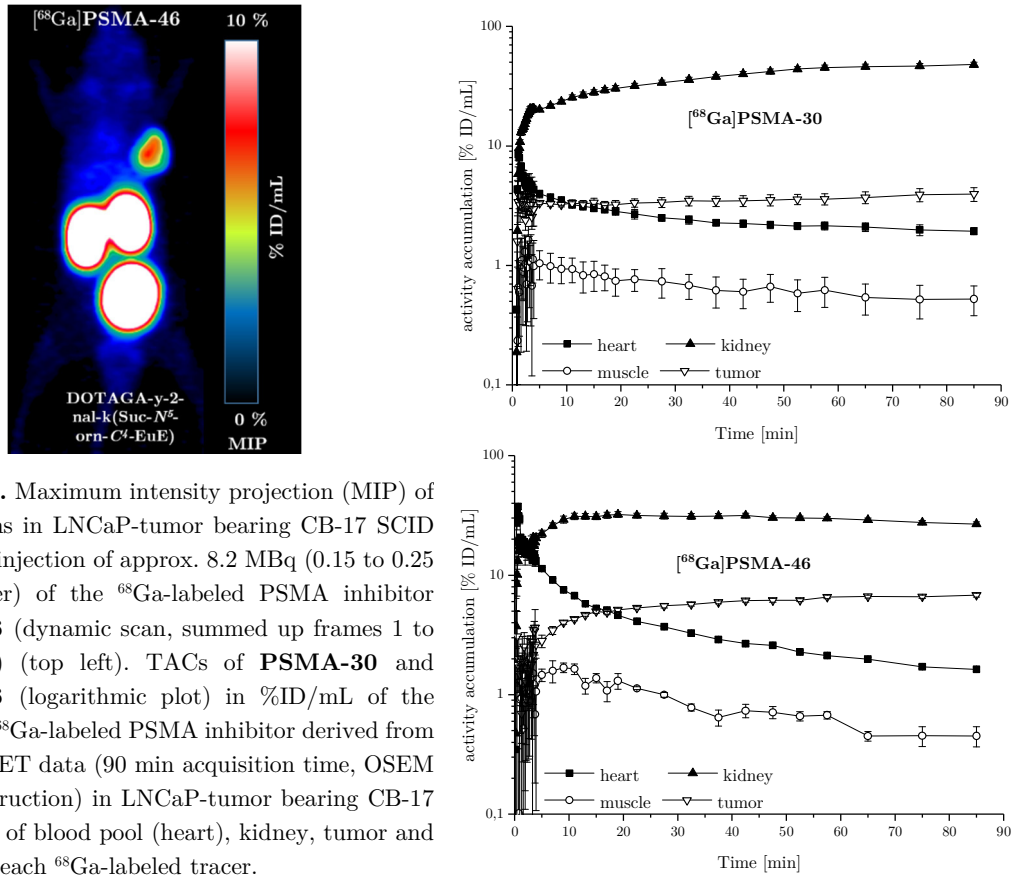

Figure 59. Maximum intensity projection (MIP) of µPET scans in LNCaP-tumor bearing CB-17 SCID mice after injection of approx. 8.2 MBq (0.15 to 0.25 nmol tracer) of the ^{68}Ga-labeled PSMA inhibitor **PSMA-46** (dynamic scan, summed up frames 1 to 1.5 h p.i.) (top left). TACs of **PSMA-30** and **PSMA-46** (logarithmic plot) in %ID/mL of the respective ^{68}Ga-labeled PSMA inhibitor derived from dynamic PET data (90 min acquisition time, OSEM 3D reconstruction) in LNCaP-tumor bearing CB-17 SCID mice of blood pool (heart), kidney, tumor and muscle for each ^{68}Ga-labeled tracer.

Both ligands showed fast body clearance and elevated tumor uptake with low unspecific background activity after 85 min p.i. as shown in Figure 59. The direct comparison regarding kidney uptake showed that the switch to the EuE-binding motif, drastically reduced renal tracer accumulation of [^{68}Ga]**PSMA-46** compared to [^{68}Ga] **PSMA-30** (26.7% ID/mL vs. 47.9% ID/mL after 85 min p.i., respectively). Distinct lower activities in the blood pool and the muscle region were also detected at the end of the dynamic PET scan for [^{68}Ga]**PSMA-46,** which indicated faster elimination of this tracer and less unspecific binding. In agreement with the elevated internalization capacity of [^{177}Lu]**PSMA-46** compared to [^{177}Lu]**PSMA-30**, an increase in tumor uptake was observable (6.8% ID/mL vs. 4.0% ID/mL, respectively). Utilization of the EuE binding motif proved to be superior to the EuK scaffold and considerably improved the tracer kinetics *in vivo*. These *in vivo* findings together with the significantly ameliorated *in vitro* internalization, led to the conclusion to employ the EuE-scaffold for further PSMA tracer development.

2.4.7 Effect of the stereochemistry and peptide spacer extension on EuE-based inhibitors

The diverse *in vitro* characteristics of **PSMA-49** to **PSMA-51** were evaluated in small animal PET scans to determine the impact of peptide spacer extension and stereochemistry on tracer kinetics.

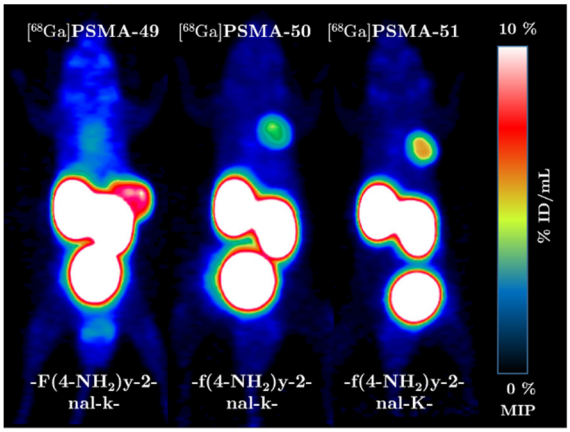

Figure 60. Maximum intensity projection (MIP) of µPET scans in LNCaP-tumor bearing CB-17 SCID mice after injection of approx. 5.0 to 8.3 MBq (0.15 to 0.25 nmol tracer) of the respective ^{68}Ga-labeled PSMA inhibitor (**PSMA-49, PSMA-50** and **PSMA-51**) (dynamic scan, summed up frames 1 to 1.5 h p.i.) (top left). Comparative TACs (logarithmic plot) in %ID/mL of the ^{68}Ga-labeled PSMA inhibitors derived from dynamic PET data (90 min acquisition time, OSEM 3D reconstruction) in LNCaP-tumor bearing CB-17 SCID mice (bottom) of blood pool (heart), kidney, tumor and muscle accumulation.

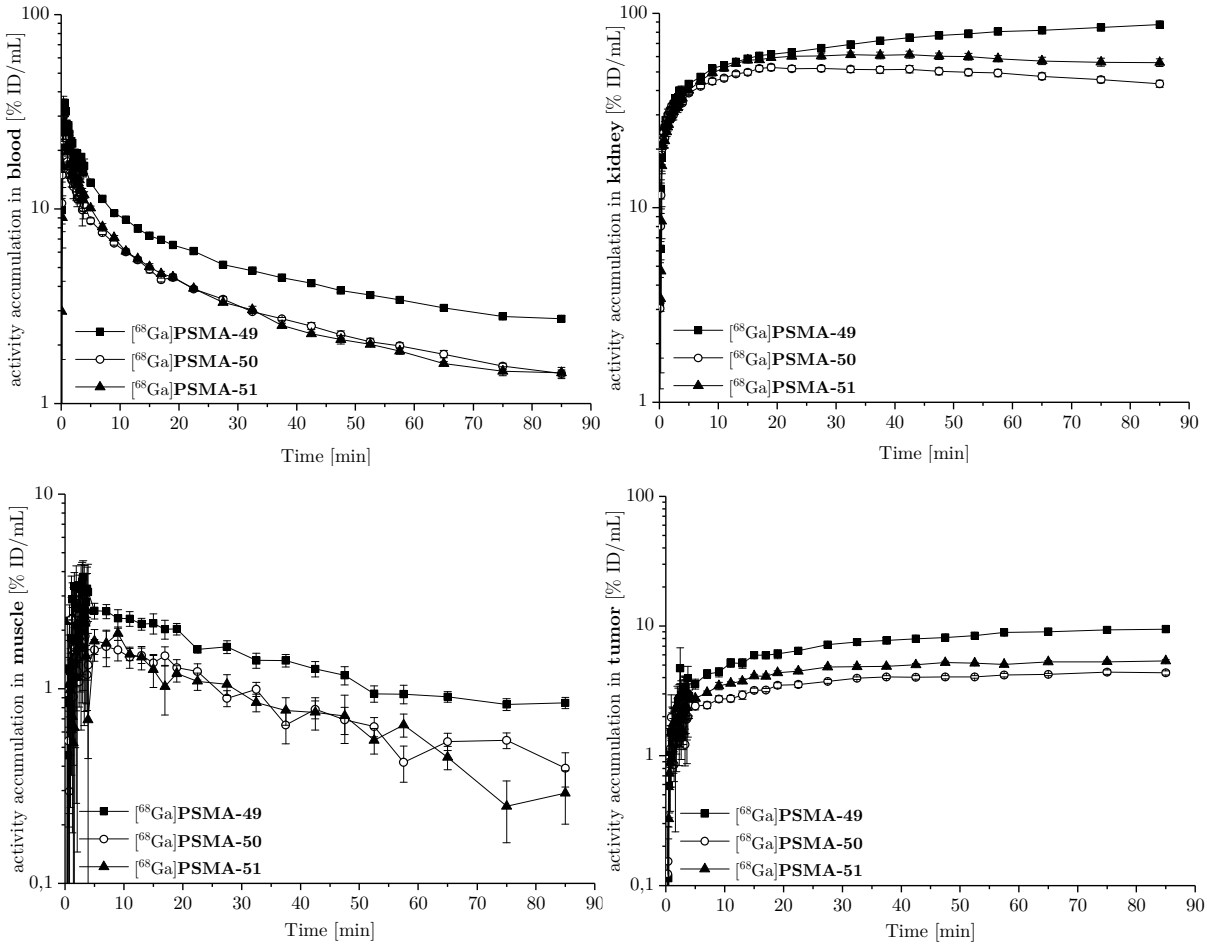

Blood pool uptake was the highest for [^{68}Ga]**PSMA-49** and visible through higher background activity compared to its isomers [^{68}Ga]**PSMA-50** and [^{68}Ga]**PSMA-51** as shown in Figure 60.

Although [^{nat}Ga]**PSMA-49** and [^{nat}Ga]**PSMA-50** exhibited similar HSA binding values (85.1% vs. 84.4%, respectively), the difference in blood pool activity at the end of the PET scan was approx. twofold. This emphasizes that albumin binding does not account for total plasma protein binding as reported by Gillette et al. [329]. Other components of the blood system may also influence the total binding and thus further experiments with blood samples are necessary.

Marked differences were also observed in the logarithmic TACs plot regarding kidney and muscle uptake, in which [^{68}Ga]**PSMA-49** demonstrated the highest accumulation. Linear decrease in the muscle tissue was found for all three derivatives, indicating unspecific binding and ongoing clearance. Since [$^{nat/68}$Ga]**PSMA-49** and [$^{nat/68}$Ga]**PSMA-50** displayed similar affinities (3.3 ± 0.6 nM vs. 3.1 ± 0.2 nM, respectively) and a slightly difference regarding internalization (245.0% vs. 207.3%, respectively), the considerable difference regarding kidney and tumor uptake must emanate from the divergent amino acid configuration. Already after approx. 28 min, the activity in the kidneys started to decline for [^{68}Ga]**PSMA-50** and resembled to some extent the tracer kinetics of [^{68}Ga]**PSMA-16**, the EuK-based analog of [^{68}Ga]**PSMA-50**. This indicates that complete D-configuration of the peptide spacer beneficially influences elimination of the radiolabeled tracer from the kidneys.

In contrast to [^{68}Ga]**PSMA-50**, ongoing renal accumulation was seen for [^{68}Ga]**PSMA-49**. Likewise to the relationship between [^{68}Ga]**PSMA-50** and [^{68}Ga]**PSMA-16**, L-configuration of 4-amino-phenylalanine in the peptide spacer resulted in [^{68}Ga]**PSMA-15** (EuK-based) and [^{68}Ga]**PSMA-49** (EuE-based) in similar persistent renal accumulation.

Tumor uptake showed good correlation with the *in vitro* parameter of all three ligands, in which [^{68}Ga]**PSMA-49** displayed the highest internalization and tumor accumulation, followed by [^{68}Ga]**PSMA-51** and [^{68}Ga]**PSMA-50**. Compared to [^{68}Ga]**PSMA-46**, the extension of the peptide spacer with 4-amino-L-phenylalanine in [^{68}Ga]**PSMA-50** resulted in improved tumor targeting but concomitantly elevated kidney uptake (6.8% ID/mL vs. 9.5% ID/mL and 26.7% ID/mL vs. 87.5% ID/mL, respectively).

2.4.8 Effect of trimesic acid on EuE-based inhibitors

Substitution of the PSMA ligands with electron deficient aromatic systems resulted in enhanced internalization rates of [^{177}Lu]**PSMA-62** and [^{177}Lu]**PSMA-66** (343.9% and 297.8%, respectively). Both ligands were therefore evaluated and compared among each other in PET studies.

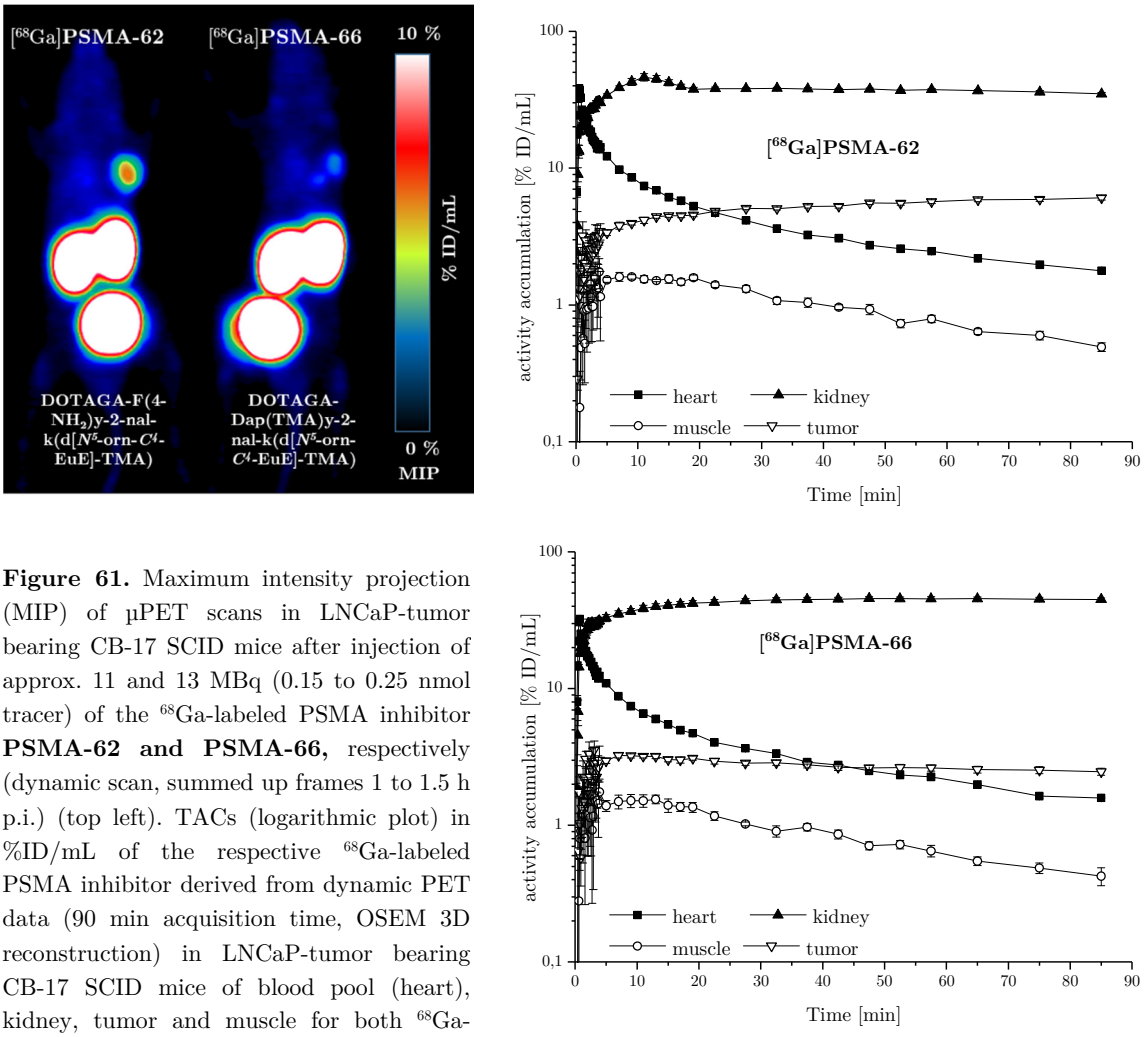

Figure 61. Maximum intensity projection (MIP) of µPET scans in LNCaP-tumor bearing CB-17 SCID mice after injection of approx. 11 and 13 MBq (0.15 to 0.25 nmol tracer) of the ^{68}Ga-labeled PSMA inhibitor **PSMA-62 and PSMA-66,** respectively (dynamic scan, summed up frames 1 to 1.5 h p.i.) (top left). TACs (logarithmic plot) in %ID/mL of the respective ^{68}Ga-labeled PSMA inhibitor derived from dynamic PET data (90 min acquisition time, OSEM 3D reconstruction) in LNCaP-tumor bearing CB-17 SCID mice of blood pool (heart), kidney, tumor and muscle for both ^{68}Ga-labeled tracer.

Both tracer exhibited excellent tracer kinetics regarding kidney, muscle and blood pool uptake as shown in Figure 61. Specific uptake in the kidneys was slightly higher for [^{68}Ga]**PSMA-66** compared to [^{68}Ga]**PSMA-62** (45.3% ID/mL vs. 34.8% ID/mL, respectively). The higher renal accumulation in the PET scan of [^{68}Ga]**PSMA-66** compared to [^{68}Ga]**PSMA-62** nicely correlated with the biodistribution experiments (chapter **III 2.3.5**). TACs for muscle and blood pool activity showed linear uptake and ongoing clearance from these compartments.

Striking differences were observed regarding tumor uptake. Although both ligands demonstrated high tumor accumulation in the biodistribution studies (≥ 8.0% ID/g), only 6.0% ID/mL were observed for [^{68}Ga]**PSMA-62** and even less with 2.5% ID/mL for

[^{68}Ga]**PSMA-66**. Similar differences between tumor uptake in PET and biodistribution studies was recently reported from several groups [156,287,325]. Wüstemann et al. investigated the influence of the chelating moiety on the *in vivo* behavior of PSMA ligands based on **PSMA-617**. Whereas the CHX-A''-DTPA derivative showed an almost twofold higher tumor uptake during the PET studies compared to its DOTA analog, the biodistribution resulted in reversed findings in which the tumor accumulation for the DOTA analog was more than twofold higher. Similar high discrepancy between PET tumor uptake and biodistribution study was reported by Young et al., in which an almost fourfold higher tracer accumulation during the biodistribution study was detected [287].

In this respect, it appears reasonable to confirm unfavorable PET scans regarding tumor uptake through biodistribution studies, if the *in vitro* characteristics of the new compounds seem promising enough to expect better tracer performance *in vivo*. The partial volume effect (PVE) and unsteady biological properties of LNCaP cells may contribute to such deviant results [156,184]. The findings of Bao et al. showed that the recovery coefficient for a rod with 5 mm diameter was in average 0.93 using an Inveon preclinical PET system, whereas for a rod with 2 mm diameter the recovery was only 0.48 [330]. Thus, only animals harboring a tumor $>$ 5 mm in diameter should be used for preclinical PET-studies.

A possible further complication results through the utilization of Matrigel for tumor cell inoculation. Assuming that resected tumor tissue incorporates remnants of Matrigel, the biased tumor-tissue weight would ultimately lead to lower tumor uptake values in the biodistribution studies.

2.4.9 Effect of ester conjugation on EuE-based inhibitors

With the intention to develop a metabolically unstable tracer to reduce kidney uptake, [^{68}Ga]**PSMA-67** was investigated in a PET study to evaluate the influence of the ester conjugation between peptide spacer and the chelator.

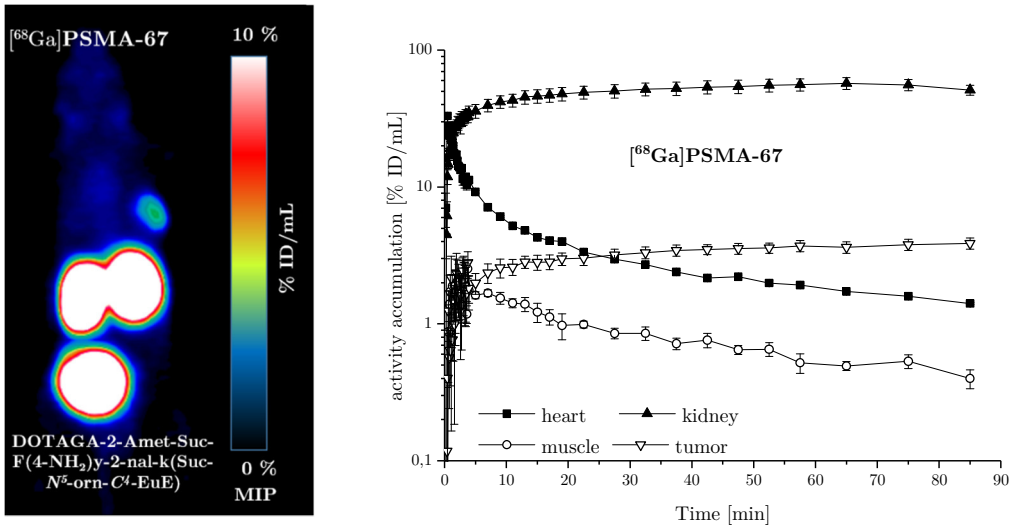

Figure 62. Maximum intensity projection (MIP) of a µPET scan in LNCaP-tumor bearing CB-17 SCID mice after injection of approx. 9,0 MBq (0.18 nmol tracer) of [^{68}Ga]**PSMA-67** (dynamic scan, summed up frames 1 to 1.5 h p.i.) (top left). TACs (logarithmic plot) in % ID/mL of [^{68}Ga]**PSMA-67** derived from dynamic PET data (90 min acquisition time, OSEM 3D reconstruction) in a LNCaP-tumor bearing CB-17 SCID mouse of blood pool (heart), kidney, tumor and muscle.

Similar to the results for [^{68}Ga]**PSMA-62** and [^{68}Ga]**PSMA-66,** only low tumor uptake was observed for [^{68}Ga]**PSMA-67** at the end of the PET scan (3.9% ID/mL, Figure 62.), although the ligand displayed similar affinity and even higher internalization than the reference **PSMA-49** (no ester conjugation).

Marked differences were detected regarding accumulation and retention in the kidneys. While [^{68}Ga]**PSMA-49** displayed high and steady renal uptake, [^{68}Ga]**PSMA-67** accumulated less in the kidneys at the end of the PET scans (51.1% ID/mL vs. 87.5% ID/mL, respectively). Muscle and blood pool clearance were found to decline linearly in the semi-logarithmic plots and to be almost twofold lower for [^{68}Ga]**PSMA-67** compared to [^{68}Ga]**PSMA-49**.

The introduction of the ester conjugation resulted in lower background activity and favorable *in vivo* kinetics. As the results from biodistribution studies of [^{177}Lu]**PSMA-62** and [^{177}Lu]**PSMA-66** implied, additional experiments have to be conducted to evaluate the full potential of **PSMA-67**. The development of a metabolically unstable tracer with rapid renal clearance and high tumor uptake at the same time is elaborate. The ester-conjugation has to be optimized in order to display favorable metabolic resistance while at the same time the structural modifications should retain high affinity and high internalization. A further

complication is the different metabolism in mice and humans, which impedes such tracer development.

2.5 *Ex vivo* autoradiography

Due to the significant differences in kidney uptake between **PSMA I&T** and **PSMA-617** (chapter **III 2.3.1** and **2.3.4**), both tracer were used to evaluate their affinity towards murine PSMA on 20 µm thick frozen murine kidney slices via autoradiography.

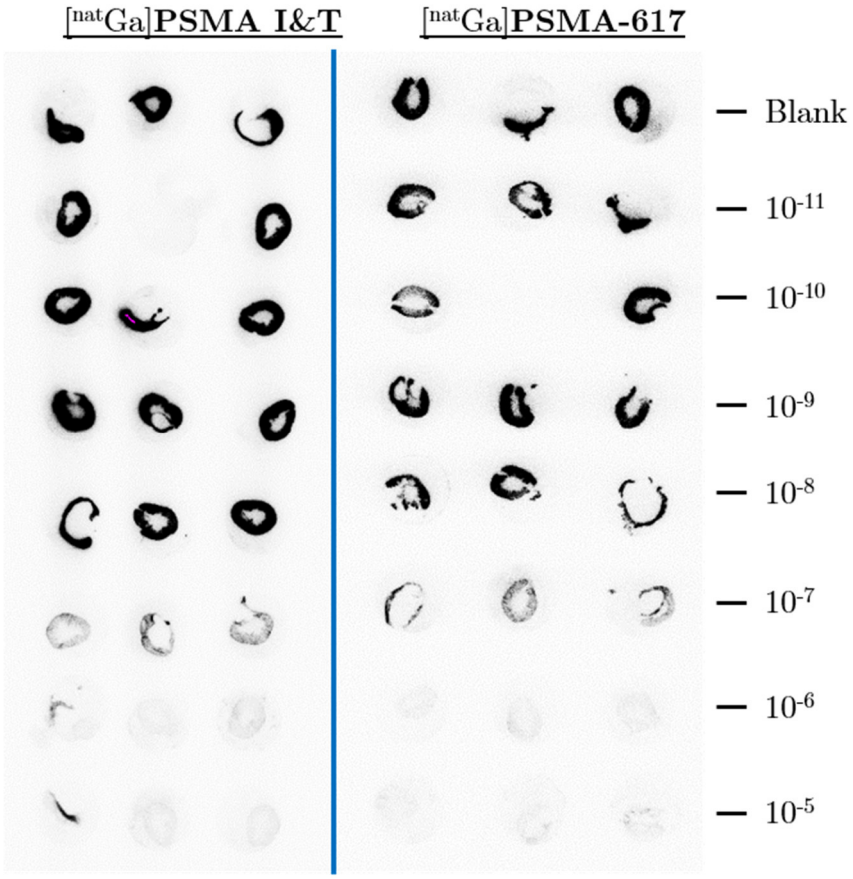

Figure 63. Autoradiographic images of the competitive binding-assay using [natGa]**PSMA I&T**, [natGa]**PSMA-617** and ([125I]I-BA)KuE as radioligand (c = 10^{-10} to 10^{-4} M in HBSS (1% BSA) for [natGa]**PSMA I&T** and [natGa]**PSMA-617**, c = 0.2 nM for ([125I]I-BA)KuE in HBSS (1% BSA), murine kidney slices (CB-17 SCID), 4°C, 1 h). Frozen kidney-slices were washed once with 500 µL ice-cold HBSS (1% BSA) and left for 15 min on ice to equilibrate in 200 µL HBSS (1% BSA). Next, 25 µL per well of solutions were added, containing either HBSS (1% BSA, control) or the respective ligand in increasing concentration with subsequent addition of 25 µL of ([125I]I-BA)KuE (2.0 nM) in HBSS (1% BSA). After 60 min incubation on ice, the experiments were terminated by removal of the medium and consecutive rinsing with 200 µL of HBSS. The circular glass inlays with the tissue sections on it were afterwards removed from the 24-well plates and placed in apposition to phosphor screens for 14 d. Images were evaluated using AIDA software.

The autoradiographic images shown in Figure 63 demonstrate the concentration dependent inhibition of the radioligand ([125I]I-BA)KuE through increasing amounts of [natGa]**PSMA I&T** (left panel) and [natGa]**PSMA-617** (right panel). Quantitative assessment for both tracer

revealed IC_{50} values of 24.2 nM ($R^2 = 93.2\%$) for [^{nat}Ga]**PSMA I&T** and 23.2 nM ($R^2 = 85.3\%$) for [^{nat}Ga]**PSMA-617**. Although the correlation coefficient for [^{nat}Ga]**PSMA-617** was suboptimal, it was visible that decline of intensity occurred for both tracer using 10^{-7} M PSMA inhibitor solution. This indicates, that both tracer exhibit affinities towards murine PSMA in the same order of magnitude. The found IC_{50} value for [^{nat}Ga]**PSMA I&T** is approx. twofold higher than the measured affinity in the LNCaP cell-based IC_{50} assay (24.2 nM vs. 9.4 nM, respectively). Variation in target expression, altered protein interaction and individual size differences of the kidney sections could account for the low correlation coefficients. However, as the affinities for both tracer were found to be similar, this parameter can not be responsible for the difference in murine kidney uptake and further experiments have to be carried out in order to understand the mechanism being responsible for the low kidney accumulation of **PSMA-617** in mice.

It is noteworthy that the marked difference of renal uptake between [^{177}Lu]**PSMA I&T** and [^{177}Lu]**PSMA-617** in mice was not observed in human applications [215]. The mean absorbed doses in the human kidneys were 0.9 mGy/MBq and 0.8 mGy/MBq for [^{177}Lu]**PSMA I&T** and [^{177}Lu]**PSMA-617**, respectively. It remains therefore questionable how important the obtained values for kidney uptake in preclinical biodistribution studies are and if they are transferable to humans. Similar differences were observed between the animal model and the human application for [^{68}Ga]Pentixafor. Particularly low kidney accumulation was reported in mice, however, in humans were the kidneys among the tissues with the highest absorbed doses [331,332].

3. Synthesis

The current literature concerning PSMA inhibitor development describes primarily small molecules and their SAR within the binding cavity of PSMA [158,160,164,263]. The possibility to extend the molecular structure of the inhibitor and thus to improve the interaction with PSMA is less thoroughly characterized [156,193,206,333].

In order to investigate the influence of various modifications, fragment based coupling of several building blocks in solution phase was performed to accelerate tracer development, especially if modifications within specific regions of the molecules were of interest. The synthesis was further supported through utilization of a modified Fmoc-peptide solid phase strategy, which afforded rapid and feasible preparation of the peptidic scaffolds. The procedure used for the development of the PSMA inhibitors was also applied for the S9-positive-control peptide **S9-PCP-1**.

The final synthesis yield for the developed PSMA inhibitors after RP-HPLC purification ranged between 0.5% and 20%. Especially the introduction of carbohydrates diminished the final yield due to elaborate purification steps.

The reference ligand **PSMA-45** was synthesized according to previously published protocols and used after radio-iodination with [^{125}I]NaI as radioligand in *in vitro* assays [193,194,239,240].

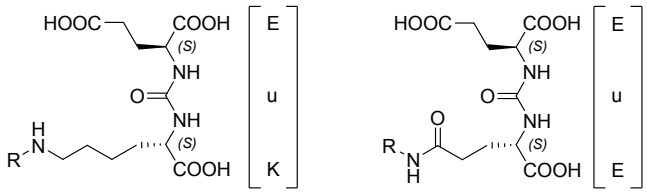

Figure 64. Structural formulas of the binding motives for PSMA based on the urea-bridged amino acids L-glutamic acid and L-lysine (EuK; left) or two L-glutamic acid components (EuE; right). R indicates variable residues.

The following chapters are at first instance divided between the binding motives EuK and EuE (see Figure 64) and separately discussed due to the divergent synthesis procedures.

3.1 Synthesis of EuK-based PSMA inhibitors

3.1.1 Synthesis of EuK fragments

The synthesis of the binding motif EuK (**1**) was achieved in solution phase utilizing orthogonally protected L-glutamic acid and L-lysine and the application of CDI to form a urea bridge between the free *N*-terminal amino groups in a simplified method from the literature [239]. After Cbz-deprotection, the overall yield was approx. 70%. The EuK binding motif (**1**) was further used for the synthesis of the building blocks **4**, **12** and **15** (Figure 65). Preparation of **4** was accomplished through the reaction of **1** and Sub(OPfp)$_2$ (**3**) under basic condition utilizing DMAP in DMF. Purification via flash-chromatography applying a stepwise gradient of EtOAc and PE resulted in 58% yield of **4**.

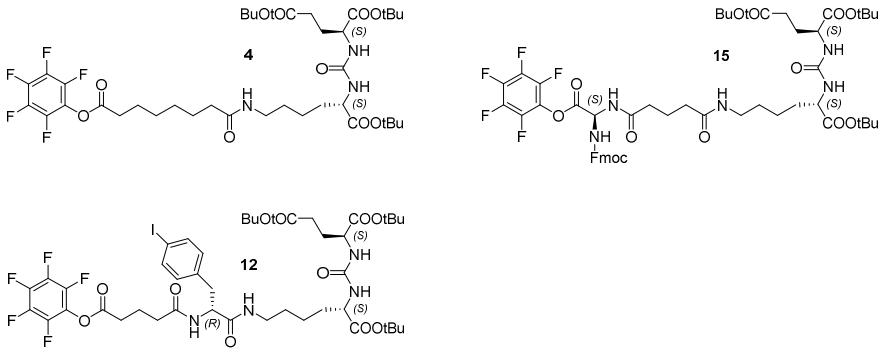

Figure 65. Structural formulas of the EuK-based, *t*Bu-protected and Pfp-activated building blocks **4**, **12** and **15** for the synthesis of the PSMA inhibitors.

The synthesis of **12** necessitated a stepwise reaction with subsequent flash-chromatography and RP-HPLC purification steps, starting from the reaction of **1** with Fmoc-D-4-iodo-phenylalanine using HOBT, TBTU and DMAP. In the final reaction step, Glut(OPfp)$_2$ (**10**) was added to **11** in DMF in the presence of DMAP. The laborious synthesis and purification resulted in a moderate reaction yield of only 39%.

The activation of **14** to the pentafluorophenyl ester **15** required the application of pyridine as catalyst and thus caused side-reactions, which diminished the overall yield. The separation of **15** from the reaction mixture via RP-HPLC resulted in a final yield of approx. 20%.

3.1.2 General synthesis procedure for the EuK-based PSMA inhibitors

The general procedure to develop the final PSMA inhibitors based on EuK (**1**) involved the synthesis of the peptidic fragments on solid phase applying the Fmoc-peptide strategy and a subsequent condensation with one of the EuK-derivatives **4**, **12** or **15**. After initial loading of the 2-CTC resin with orthogonally protected lysine, conjugation with the next amino acid (Fmoc-AA$_X$-OH) was consecutively performed via orthogonal Fmoc-deprotection of the *N*-

terminal amino groups or the amino group of the side chains. Coupling was always conducted using HOBt and TBTU in combination with DIPEA as depicted in the exemplary synthesis of the derivatives **PSMA-15**, **PSMA-40** and precursor-synthesis of **PSMA-28** (Figure 66). Approximately 2 to 3 h were necessary to complete amino acid coupling with the resin-loaded fragments and the procedure was subsequently repeated. Notably, after the conjugation of the third amino acid, reaction times for completion of coupling increased slightly to 3 to 4 h. An increase in steric hindrance may explain this finding.

DOTAGA-anhydride was preferably coupled to the peptide on solid phase as previously described if the previous reactions proceeded without significant side-product formation [193,194]. Otherwise, the peptide was cleaved from the resin with preservation of the side chain protecting groups (**SP-7.1**) and coupled to DOTAGA-anhydride after purification via RP-HPLC in solution phase with DIPEA. Especially the utilization of Fmoc-3-iodo-tyrosine caused side-product formation if the reaction was allowed to stir overnight. The nucleophilic property of the phenolic OH-group under basic reaction conditions was high enough to induce ester conjugation with the free carboxyl group of unbound Fmoc-3-iodo-tyrosine in the reaction solution, which rendered the monitoring of the reaction progress necessary. The conjugation of the chelator DOTA was performed according to a published method through preactivation of DOTA·6 H_2O with NHS, EDCL and DIPEA in water and the consecutive addition to the peptide [193,334].

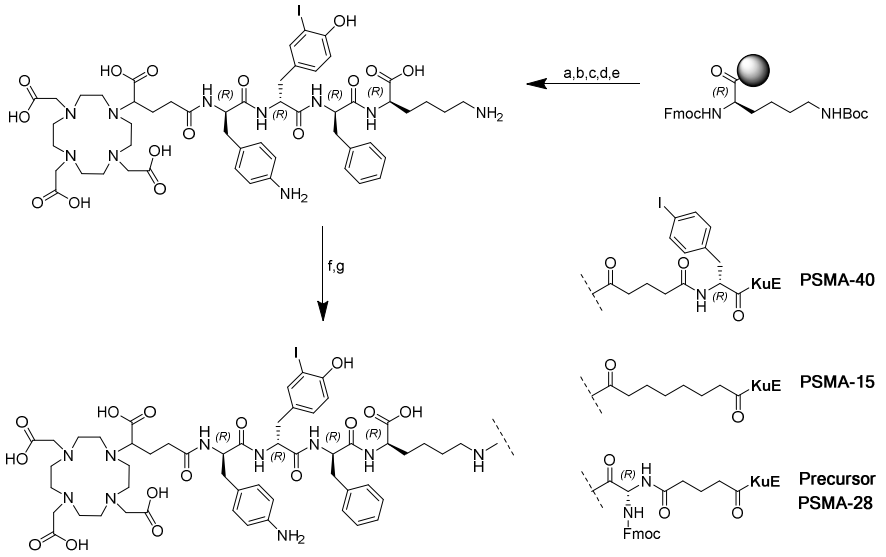

Figure 66. Schematic illustration of resin-bound peptide spacer synthesis and conjugation to the EuK-building blocks for the synthesis of **PSMA-15**, **PSMA-40** and the precursor for **PSMA-28**. (a) 20 % piperidine in DMF, Fmoc-D-Phe-OH, HOBt, TBTU, DIPEA [DMF]; (b) 20 % piperidine in DMF, Fmoc-3-I-D-Tyr-OH, HOBt, TBTU, DIPEA [DMF]; (c) 20 % piperidine in DMF, Fmoc-D-Phe(4NHBoc)-OH, HOBt, TBTU, DIPEA [DMF]; (d) 20 % piperidine in DMF, DOTAGA-anhydride, DIPEA [DMF]; (e) TFA; (f) **4** or **12** or **15**, DIPEA [DMF]; (g) TFA;

The chelator-conjugated peptides were cleaved from the resin according to **SP-7** and purified via RP-HPLC, resulting as white powder after lyophilization. The yield ranged in average between 20% and 80%. Final conjugation of the peptidic moieties with **4**, **12** or **15** was performed in solution phase under basic conditions over 24 to 72 h. The reaction progress highly depended on the utilization of 4.0 to 10 eq. DIPEA to increase the nucleophilicity of the amine group and side-product formation was frequently detectable. The overall yield for this reaction step ranged between 20 and 60%.

If further reactions were necessary as for **PSMA-24** to **PSMA-26**, **PSMA-28**, **PSMA-29**, **PSMA-38** and **PSMA-39**, the Fmoc-protected amino group of the glycine residue was orthogonally deprotected and reacted with the pentafluorophenyl-activated compounds **19**, **20** or **22** under basic conditions in solution phase (Figure 67). Acetyl-deprotection with KCN in MeOH of the carbohydrate derivatives again induced side-product formation and reduced the yield of the final carbohydrated compounds.

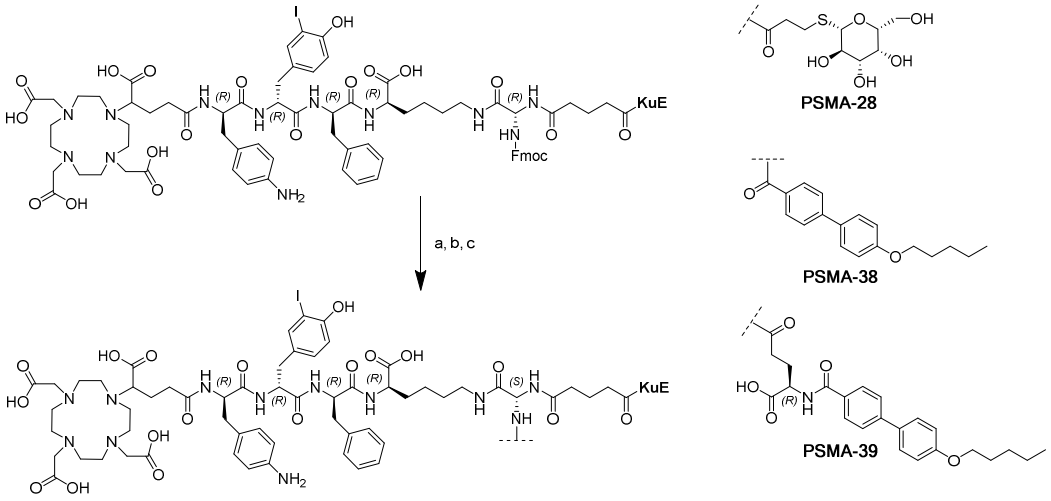

Figure 67. Schematic synthesis of the linker-modified PSMA inhibitors **PSMA-28**, **PSMA-38** and **PSMA-39**. (a) 20 % piperdine in DMF [DMF]; (b) **19** or **20** or **22**, DIPEA [DMF]; (c) TFA or KCN in MeOH, TFA;

3.1.3 Synthesis of linker-modified L-aminosuberic acid-based compounds

Synthesis of the EuK-derivative **9** was achieved using L-Fmoc-Asu(O*t*Bu)-OH as starting point (Figure 68). In a first step, the carboxylic group was Cbz-protected via benzyl alcohol, HATU, HOAt and DIPEA and concomitant removal of the *t*Bu protecting group with TFA, yielding 90% of **6** after RP-HPLC purification. After coupling of **6** with the binding motif **1**, Cbz-deprotection was achieved with palladium on activated charcoal (10%) in EtOH under H_2 atmosphere in 92% yield. The synthesis of **7** necessitated 2 to 3 purification steps via RP-HPLC and thus caused a loss of product yield. A solid-phase supported synthesis

route would be helpful in order to avoid the utilization of the RP-HPLC, however L-Fmoc-Asu(O*t*Bu)-OH was only available in this configuration. After RP-HPLC purification, **8** was activated with DIC, PfpOH and pyridine to **9**, which enabled direct condensation with the chelator-conjugated peptidic fragments. However, the activation with PfpOH remained laborious and not optimized since the necessary reaction time ranged between several hours and several days (approx. 3 d). It was noticed that a high purification grade of **8** was mandatory in order to reduce the necessary reaction time. Deprotection of the *t*Bu and Fmoc-protecting groups with subsequent RP-HPLC purification yielded in 41% of **PSMA-8**.

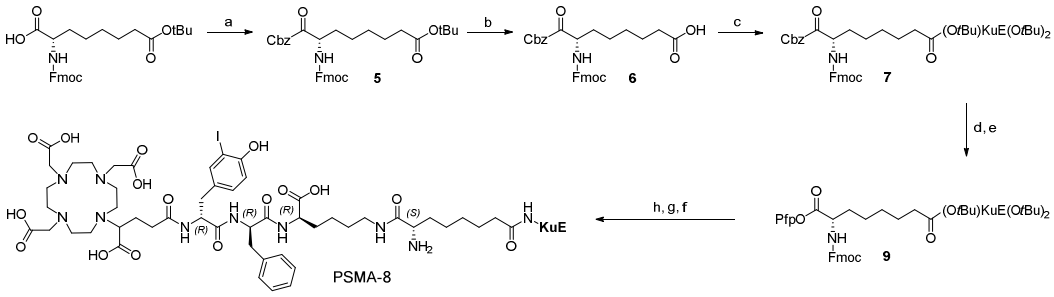

Figure 68. Schematic illustration of the synthesis of **PSMA-8**. (a) HOAt, HATU, DIPEA, benzyl-alcohol, [DMF]; (b) 95% TFA, 5% DCM; **(c) 1**, HOBt, TBTU, DIPEA, [DMF]; (d) Pd/C (10%), H_2, [EtOH]; **(e)** DIC, PFP, pyridine, [DMF]; (f) **30**, DIPEA, [DMF]; (g) 20% piperidine in DMF, [DMF]; (h) TFA

N-acetylation of the amino group of **PSMA-8** offered the possibility to introduce several structures into the linker region of the PSMA inhibitor. The acetylation with the activated esters of the compounds **22** to **27** and **29** was performed in DMF using DIPEA to increase the nucleophilicity of the free amino group of **PSMA-8** (Figure 69). Utilization of KCN in MeOH resulted in deacetylation of the carbohydrated PSMA inhibitors [235]. As already mentioned in the previous section, utilization of KCN for deprotection induced side-product formation and reduced the overall yield.

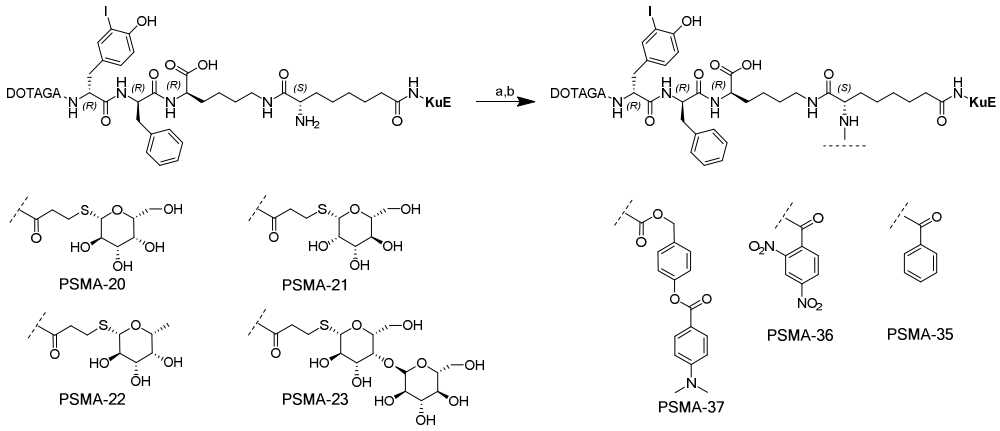

Figure 69. Schematic illustration of the synthesis of the linker modified PSMA inhibitors **PSMA-20** to **PSMA-23** and **PSMA-35** to **PSMA-37**. (a) **22** to **27** or **29**, DIPEA [DMF]; (b) TFA or KCN in MeOH, TFA;

3.1.4 Synthesis of small carbohydrated EuK-based PSMA inhibitors

The general synthesis procedure was further modified in order to generate the PSMA inhibitors **PSMA-24** to **PSMA-26**. Starting from Fmoc-D-Lys(NHBoc), the peptidic scaffold was conjugated either with the consecutive amino acids or directly with Boc-AOAc-OH applying the same reaction conditions as described in **SP-2**. Conjugation with 4-fluorobenzaldehyde (4-FBA) was achieved via direct addition of an aqueous MeCN (H_2O/MeCN, 3/7, *v*/*v*) mixture containing 4-FBA to the freshly TFA treated peptidic fragments without prior purification. Since the progress of oximligation can be accelerated through the utilization of higher molar amounts, 10 eq. 4-FBA were used and resulted in completion of reaction after 5 to 10 min at RT. Further, the residual TFA decreased the pH and supported fast oxime ligation of 4-FBA and the *t*Boc-deprotected amino-oxy function as shown in Figure 70.

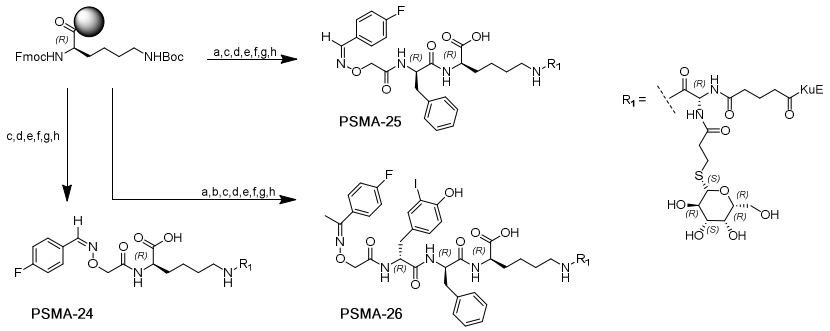

Figure 70. Schematic illustration of the synthesis of **PSMA-24** to **PSMA-26**. (a) 20% piperidine in DMF, Fmoc-D-Phe-OH, HOBt, TBTU, DIPEA [DMF]; (b) 20% piperidine in DMF, Fmoc-D-Tyr(3-I)-OH, HOBt, TBTU, DIPEA [DMF]; (c) 20% piperidine in DMF, Boc-AOAc-OH, HOBt, TBTU, DIPEA [DMF]; (d) TFA; (e) 4-FBA, H_2O [MeCN]; (f) **15**, DIPEA [DMF]; (g) 20% piperidine in DMF, **22**, DIPEA [DMF]; (h) KCN in MeOH, TFA;

After purification via RP-HPLC, conjugation with **15** was achieved using DIPEA in DMF. The reaction was always performed overnight and excess of **15** (1.5 eq.) was used for quantitative reaction yield. Fmoc-deprotection facilitated direct conjugation with **22** under basic conditions. In the last step, KCN in MeOH was used to deacetylate the galactose-derivatives and TFA to remove the remaining *t*Bu-groups.

3.2 Synthesis of EuE-based PSMA inhibitors

3.2.1 General synthesis procedure for EuE-based PSMA inhibitors

The protected binding motif **2** was similarly synthesized as described for **1** with the only exception of using H-L-Glu(OBzl)-O*t*Bu · HCl instead of H-L-Lys(Cbz)-O*t*Bu · HCl. All further reaction steps were performed on solid phase starting from the resin bound Fmoc-D-Orn(NHDde)-OH (Figure 71). Selective Fmoc-deprotection as depicted in Figure 71 enabled the conjugation of **2** applying the same conditions as described in **SP-2**.

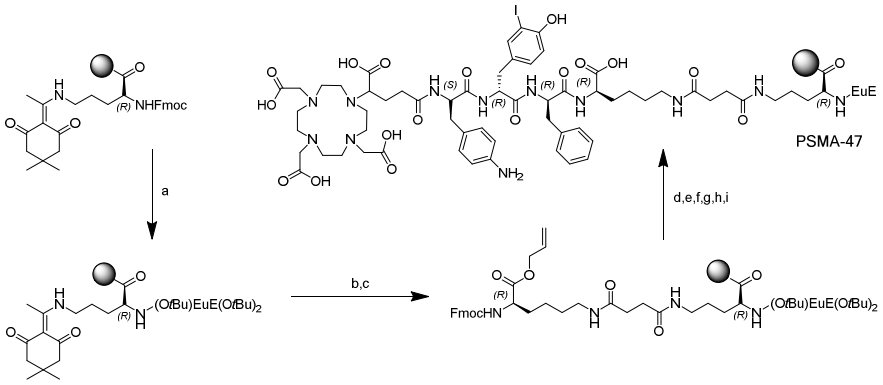

Figure 71. Schematic illustration of the general synthesis procedure of EuE-based PSMA inhibitors exemplified by **PSMA-47**. (a) 20% piperidine in DMF, **2**, HOBt, TBTU, DIPEA [DMF]; (b) succinic anhydride, DIPEA [DMF]; (c) Fmoc-D/L-Lys-OAll · HCl, HOBt, TBTU, DIPEA [DMF]; (d) 20% piperidine in DMF, Fmoc-D-Phe-OH, HOBt, TBTU, DIPEA [DMF]; (e) 20% piperidine in DMF, Fmoc-3-I-D-Tyr-OH, HOBt, TBTU, DIPEA [DMF]; (f) 20% piperidine in DMF, Fmoc-D-Phe(4-NHBoc)-OH, HOBt, TBTU, DIPEA [DMF]; (g) DOTAGA-anhydride, DIPEA [DMF]; (h) $Pd(PPh_3)_4$, TIPS [DCM]; (i) TFA;

To ensure similar linker length compared to the EuK-based compounds, the Dde-deprotected amino group of D-Orn was coupled to succinic anhydride with DIPEA in DMF. Fmoc-D- or L-Lys-OAll · HCl was conjugated in the next step via the amino acid side-chain, utilizing HOBT and TBTU with DIPEA in DMF. The next reaction steps were performed as described for the EuK-based derivatives applying always the same conditions as mentioned in **SP-2** and depicted exemplary for **PSMA-47** in Figure 71. The chelator DOTAGA-anhydride was either coupled in solution phase after resin-cleavage of the peptidic fragments and subsequently purified via RP-HPLC or directly conjugated to DOTAGA-anhydride on resin if the previous reaction steps were achieved without significant side-product formation. If the conjugation with DOTAGA-anhydride was performed in solution phase, the Alloc-protecting group was removed beforehand via **SP-5** and the peptidic fragments cleaved from the resin according to **SP-7.1**. Deprotection of the Alloc-protecting group was tedious and remained often uncomplete, even when the procedure was repeated three times and the molar amount of $Pd(PPh_3)_4$ increased from 0.3 to 0.5 eq.. Besides the reduced product yield, the unfinished Alloc-deprotection led to a more cumbersome RP-HPLC purification since the Alloc-protected and Alloc-deprotected derivatives showed almost identical retention behavior on the RP-HPLC-column. The final PSMA inhibitors were obtained in yields ranging from 10 to 30% as white solid powder.

3.2.2 Linker modified EuE-based PSMA inhibitors

To investigate modifications within the linker region, the synthesis route was slightly adjusted. After *N*-terminal conjugation of **2** to the resin bound D-Orn(NHDde)-OH and subsequent Dde-deprotection via **SP-4**, the resin bound fragment was extended in three separate synthesis-routes as shown in Figure 72. Conjugation of Fmoc-D-Asp-OAll (**21**) offered the possibility to introduce further modifications (Route A). In order to introduce the protected amino acids D-Glu or D-Arg, while simultaneously ensure similar linker length as for the other inhibitors, glycine was beforehand coupled (Route B). The conjugation of Fmoc-4-Abz-OH required the combination of HOAt and HATU with DIPEA in DMF, since the utilization of HOBt and TBTU resulted in only moderate reaction yield after several hours probably due to the reduced nucleophilicity of aromatic amine groups compared to aliphatic amine groups (Route C).

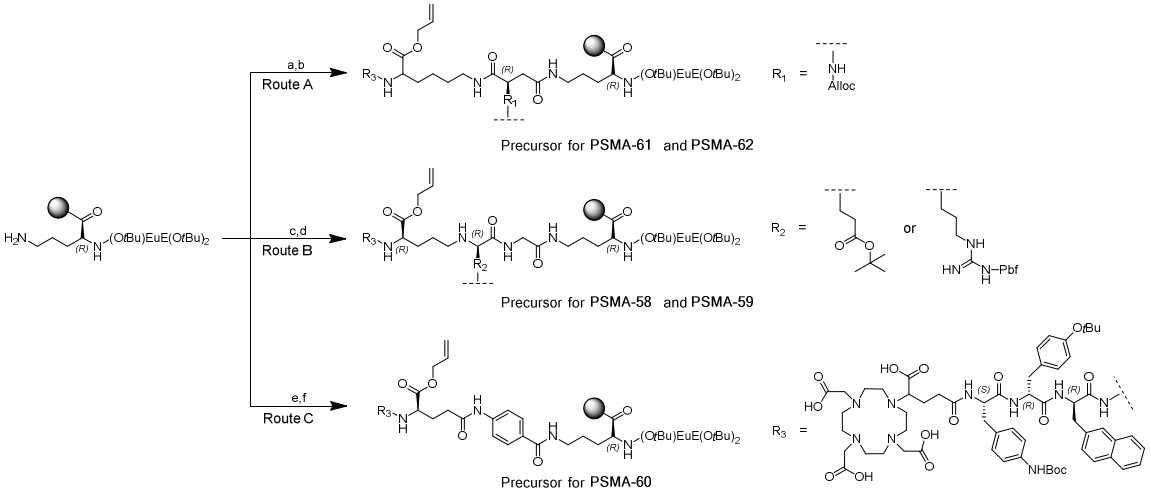

Figure 72. Schematic illustration of the precursor synthesis for the linker-modified EuE-based PSMA inhibitors **PSMA-58** to **PSMA-62**. **Route A:** (a) Fmoc-D-Asp-OAll, HOBt, TBTU, DIPEA [DMF]; (b) 20% piperidine in DMF, Fmoc-D-Lys-OAll, HOBt, TBTU, DIPEA [DMF]; **Route B:** (c) Fmoc-Gly-OH, HOBt, TBTU, DIPEA [DMF]; (d) 20% piperidine in DMF, Fmoc-D-Orn-OAll, HOBt, TBTU, DIPEA [DMF]; **Route C:** (e) Fmoc-4-Abz-OH, HOAt, HATU, DIPEA [DMF]; (f) Fmoc-D-Glu-OAll, HOBt, TBTU, DIPEA [DMF];

After conjugation with Fmoc-D-Lys-OAll (Route A), Fmoc-D-Orn-OAll (Route B) or Fmoc-D-Glu-OAll (Route C), the extension of the peptidic fragments was performed as already described using HOBt, TBTU and DIPEA in DMF. For the derivatives **PSMA-61** and **PSMA-65**, 2, 4-dinitrobenzoic acid was directly coupled to the free amine group of the aspartic acid in the linker after Alloc-deprotection. Also during this synthesis, Alloc-deprotection remained unfinished (approx. 90 ± 5%) and reduced the overall yield. Trimesic acid was coupled through preactivation of it with DIC, PfpOH and DIPEA in order to synthesize the derivatives **PSMA-62** and **PSMA-66**. The chelator DOTAGA-anhydride was always coupled in the last step. Finally, the resin bound PSMA inhibitors were deprotected and cleaved from

the resin. The crude products were subsequently purified via RP-HPLC. The final yields ranged between 10 and 30%.

3.2.3 2-Naphtylalanine linker-modified EuE-based PSMA inhibitors

PSMA-63 and **PSMA-64** were synthesized according to the general procedure described in chapter **III 3.2.1.** After loading of the resin with Fmoc-D-Orn(NHDde)-OH, Fmoc-deprotection enabled the conjugation with Fmoc-D-2-Nal-OH and the subsequent conjugation with **2.** The following steps were performed as described in chapter **III 3.2.1** and are shown in Figure 73.

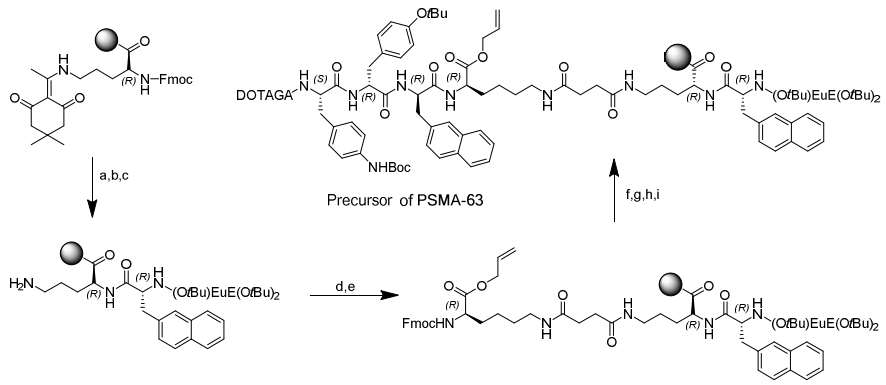

Figure 73. Schematic illustration of the precursors synthesis of the D-2-Nal linker-modified PSMA inhibitor **PSMA-63**. (a) 20% piperidine in DMF, Fmoc-D-2-Nal-OH, HOBt, TBTU, DIPEA [DMF]; (b) 20% piperidine in DMF, **2**, HOBt, TBTU, DIPEA [DMF]; (c) Hydrazine in DMF; (d) succinic anhydride, DIPEA [DMF]; (e) Fmoc-D-Lys-OAll, HOBt, TBTU, DIPEA [DMF]; (f) 20% piperidine in DMF, Fmoc-D-2-Nal-OH, HOBt, TBTU, DIPEA [DMF]; (g) 20% piperidine in DMF, Fmoc-D-Tyr(*t*Bu)-OH, HOBt, TBTU, DIPEA [DMF]; (h) 20% piperidine in DMF, Fmoc-L-Phe(4-NHBoc)-OH, HOBt, TBTU, DIPEA [DMF]; (i) 20% piperidine in DMF, DOTAGA-

3.2.4 Synthesis of a EuE-based PSMA inhibitor with an ester-group

The synthesis of **PSMA-67** was achieved as described in chapter **III 3.2.1** with some modifications. After conjugation of Fmoc-L-Phe(4-NHBoc)-OH and subsequent Fmoc-deprotection, the peptidic fragment was conjugated with Fmoc-AE-suc (**31**) in order to expand the distance between chelator and peptide spacer and to introduce the ester group. Notably, the ester conjugation remained stable during the synthesis and no hydrolysation products were detected. The conjugation with **31** was achieved using DIC and ethyl isonitrosocyanoacetate in DMF. The final steps included Fmoc- and Allyl-deprotection, which was followed by cleavage from the resin of the peptidic compound. The chelator DOTAGA-anhydride was coupled in solution phase with DIPEA in DMF. Although initial product formation was seen after several hours, the completion of the reaction was not achieved even after 3 d. The further addition of either DOTAGA-anhydride or DIPEA did not result in faster product formation. Instead, the reaction solution became unclear. Therefore, the reaction was stopped and the product extracted from the reaction mixture via RP-HPLC, since 60% product-formation were sufficient for further *in vitro* investigations.

4. Radiolabeling

^{68}Ga-labeling: Readily production of the ^{68}Ga-labeled compounds was accomplished within 15 min after start of the radiosynthesis in a fully automated GMP-compliant system. Utilization of 5.0 nmol of the respective PSMA inhibitor yielded in specific activities ranging from 36 to 53 GBq/µmol after cartridge purification. The determined radiochemical purity for all compounds was ≥ 95% and was determined by radio-RP-HPLC and radio-TLC. Prior to *in vitro* and *in vivo* applications, the EtOH was evaporated and the ^{68}Ga-labeled compounds were diluted with PBS (pH 7.4).

^{177}Lu-labeling: ^{177}Lu-labeling was accomplished according to a previously published protocol [243]. Radiochemical purities at the end of the labeling procedure were ≥ 97% and A_S ranged from 10 to 200 GBq/µmol. The ^{177}Lu-labeled compounds were diluted with PBS (pH 7.4) for further applications.

^{125}I-labeling: For *in vitro* studies, ([^{125}I]I-BA)KuE was used as reference ligand and synthesized in solution according to described literature [234,239-241]. The respective stannylated precursor **PSMA-45** was treated with [^{125}I]NaI and peracetic acid for 10 min at RT. Consecutive cartridge purification, *t*Bu deprotection with TFA and purification via RP-HPLC resulted in the final product ([^{125}I]I-BA)KuE in a radiochemical purity ≥ 99% and a radiochemical yield of 40 ± 10%. The non-radioactive analog for chromatographic analysis was synthesized by conjugating 4-iodo-benzoic acid to **1** with following *t*Bu deprotection and RP-HPLC purification.

5. HSA binding

The mobile phase was freshly prepared for each experiment and only used for one day. The column was kept at room temperature and each run was stopped after detection of the signal to reduce the acquisition time. Strong influence of column temperature on retention time was noticed. The chosen reference substances displayed a range of HSA binding from 13% to 99%, since a broad variety of albumin binding was assumed during the evaluation of the novel inhibitors. Table 25 shows the utilized references and the influence of albumin interaction on the obtained chromatographic retention.

Table 25. Exemplary illustration of measured retention time (t_R) for the selected HSA reference substances. Log t_R: logarithmic value of t_R; Lit. HSA: literature value of human serum albumin binding in [%]; Log*K* HSA logarithmic value of Lit. HSA [%] [244,245].

Reference	t_R	Log t_R	Lit. HSA %	Log*K* HSA
p-benzyl alcohol	2.40	0.38	13.15	-0.82
Aniline	2.72	0.43	14.06	-0.79
Phenol	3.28	0.52	20.69	-0.59
Benzoic acid	4.08	0.61	34.27	-0.29
Carbamazepine	4.15	0.62	75.00	0.46
p-nitrophenol	5.62	0.75	77.65	0.52
Estradiol	8.15	0.91	94.81	1.19
Probenecid	8.84	0.95	95.00	1.20
Glibenclamide	29.18	1.47	99.00	1.69

Figure 74 shows an exemplary sigmoidal plot of the good correlation between Log*K* HSA and log retention time (t_R), which was found for each experiment to be ≥ 92%. Extreme strong binding compounds (> 99.0%) necessitated protracted column elution steps and impeded efficiency of this method.

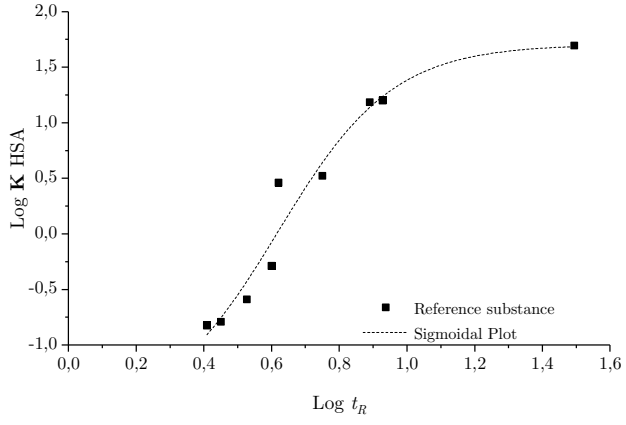

Figure 74. Exemplary daily determined sigmoidal plot of the correlation between Log*K* HSA and Log t_R. The Plot was obtained using OriginPro 2016G.

IV. SUMMARY AND CONCLUSION

"How much it is easier to be critical than to be correct."

- Benjamin Disraeli -

Sensitive and specific targeting of PCa as well as local and distant metastasis is necessary for individual patient-specific staging, surveillance and treatment. In this respect, several biochemical properties render PSMA as valuable target for the development of small molecules intended for imaging (diagnostics) and endoradiotherapy. This work focused on the synthesis of structurally modified PSMA ligands based on **PSMA I&T** and their predominantly *in vitro*-based evaluation [225]. On the basis of PSMA binding affinity, tracer internalization, lipophilicity and HSA binding, four structural regions of the PSMA inhibitors were subsequently investigated.

The first attempt focused on the introduction of a free amino group (positive charge) into the peptide spacer scaffold. While most PSMA ligands exhibited reasonably high affinities in the low nanomolar range, some configuration decreased drastically the affinity towards PSMA. The observed negative effect on internalization and HSA binding led to the conclusion that positive charges should be avoided to warrant high tumor uptake. The possibility to introduce positive charges into the tracer scaffold extends the repertoire of structural modifications for PSMA tracer development and may be useful for PSMA imaging agents suffering from high plasma protein binding.

Encouraged by the positive findings regarding carbohydration of RGD peptides, several carbohydrated PSMA derivatives were developed. The preservation of high affinity after carbohydration indicated the cooperativity of PSMA to encompass bulky hydrophilic moieties in the linker region. While internalization was negatively affected, albumin binding was drastically reduced. Carbohydration resulted in lower unspecific organ binding and less kidney retention. These features together with constant tumor retention rendered carbohydration as valuable tool for the design of theranostic agents.

Selective D- or L-configured amino acids in the peptide spacer displayed considerable influence on the *in vitro* and *in vivo* properties of stereoisomeric PSMA ligands and were able to enhance affinity and internalization. Emanating from the improved *in vitro* properties, tumor uptake of a new developed compounds was almost doubled in PET studies compared to the reference. Yet, the still high renal accumulation limited the overall improvement and remained considerably problematic. Evaluation of the tracer revealed that HSA binding of the PSMA inhibitors was rather influenced by the structure of the whole ligand, than the stereochemistry

of single residues within the peptide scaffold. Improvement of affinity did not always correlate with concomitant increase of internalization. Since no transferability or correlations were detected, the optimization of affinity and internalization resembled two separate mechanisms.

In a further attempt, linker-modified PSMA inhibitors were developed in order to increase albumin binding for *in vivo* half-life extension. High affinity and enhanced internalization were achieved upon modification of the linker. High plasma protein binding facilitated extended target delivery over 24 h and resulted in an almost threefold higher tumor uptake compared to the parent compound. The findings from the biodistribution studies indicated that enhanced plasma protein binding is feasible in order to increase the tumor uptake.

In the context of extremely strong HSA binding compounds, limitations regarding the evaluation of internalization were noticed. The results demonstrated the influence of BSA in the assay medium and highlighted the complexity of *in vitro* ligand assessment. The findings emphasized the importance of HSA binding as crucial parameter during tracer development. Hence, reduction of BSA concentration in the *in vitro* assays may allow evaluation that is more precise. However, preclinical evaluation in animal models remains the most valid method in order to assess the potency of novel tracer.

The modification of the binding motif EuK towards EuE allowed the design of highly affine PSMA ligands with highly increased internalization capacities. Direct PET comparison highlighted the superiority of the EuE binding motif compared to its EuK-analog. The most convincing outcome was reduced kidney accumulation, less unspecific binding and increased tumor uptake.

The final optimization included the EuE binding motif and electron deficient aromatic residues within the linker and peptide spacer and resulted in PSMA ligands exhibiting extreme high intracellular uptake *in vitro*. The improved *in vitro* properties were well reflected by the pharmacokinetic profile and enabled high tumor uptake. Further, a moderate benefit regarding kidney uptake was detected in comparison to the parent compound, rendering the electron deficient aromatic residues as highly valuable for the future design of PSMA ligands.

Since stereochemistry fundamentally influences metabolic stability *in vivo*, the establishment of an efficient and fast metabolite assay was performed. Utilization of extracted subcellular S9-liver and kidney fractions from mice allowed demonstrating that single L- to D-amino acid transfer was sufficient to inhibit metabolite formation. A remaining drawback of the S9-assay is the laborious centrifugation step at the end of the experiments, which significantly increased the necessary time per investigation. However, the efficient S9-metabolism assay will allow to

reduce the number of necessary animal experiments and to exclude tracer, which suffer from high metabolic instability.

On the basis of the obtained *in vivo* data from human xenograft models, it was surprising, that dosimetry studies revealed similar renal uptake of [^{177}Lu]**PSMA I&T** and [^{177}Lu]**PSMA-617** in PCa patients. Therefore, the question of interspecies differences regarding affinity was addressed through quantitative autoradiographic experiments using murine kidney slices. However, no significant differences were detected. Affinity towards murine PSMA was found to not account for the obscure high renal retention of most ligands in mice. Elucidation of the mechanisms involved in this mechanism could support the identification of strategies to reduce the renal uptake in humans and thereby ameliorate endoradiotherapeutic outcome in PCa patients.

V. SUPPLEMENTARY INFORMATION

1. Figure, table and formula index

2. Chemical structure index of PSMA inhibitors

DOTAGA-y(3-I)fk(Sub-KuE) (PSMA I&T) (PSMA-1):

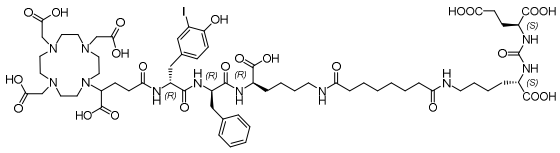

DOTAGA-y(3-I)fK(Sub-KuE) (PSMA-2):

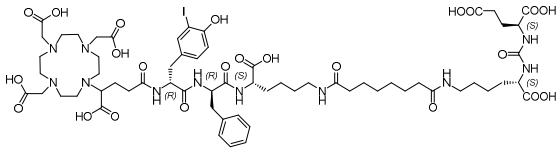

DOTAGA-Y(3-I)fk(Sub-KuE) (PSMA-3):

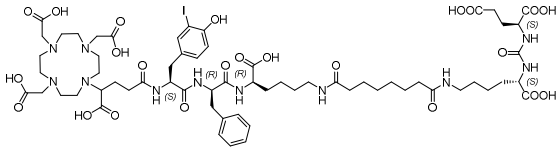

DOTAGA-y(3-I)FK(Sub-KuE) (PSMA-4):

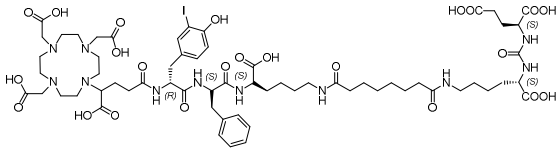

DOTAGA-y(3-I)Fk(Sub-KuE) (PSMA-5):

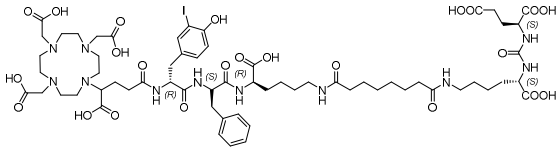

DOTAGA-Y(3-I)fK(Sub-KuE) (PSMA-6):

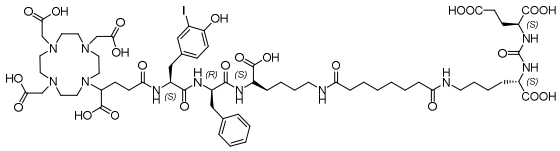

DOTAGA-Y(3-I)FK(Sub-KuE) (PSMA-7):

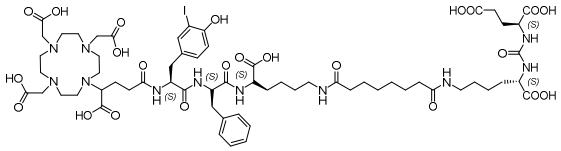

DOTAGA–y(3-I)fk(L-Asu[KuE]) (PSMA-8):

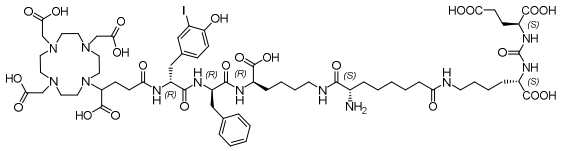

DOTAGA-y(3-I)fkk(Sub-KuE) (PSMA-9):

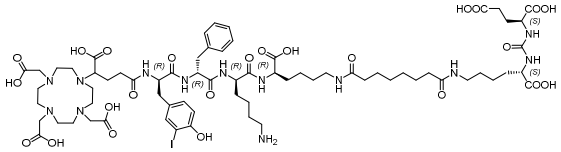

DOTAGA-y(3-I)f-N^6-kk(Sub-KuE)) (PSMA-10):

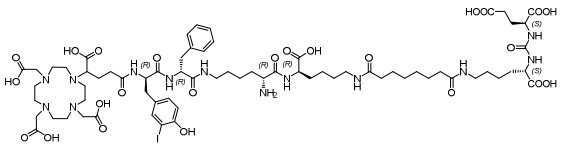

DOTAGA-y(3-I)kfk(Sub-KuE) (PSMA-11):

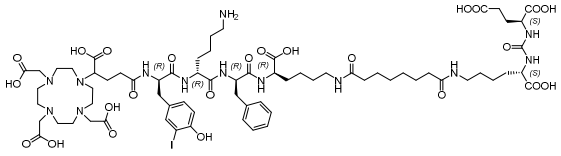

DOTAGA-y(3-I)-N^6-kfk(Sub-KuE) (PSMA-12):

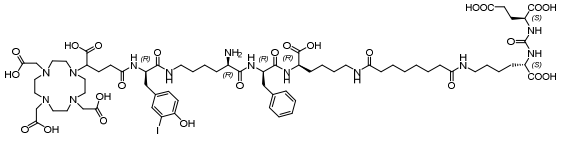

DOTAGA-ky(3-I)fk(Sub-KuE) (PSMA-13):

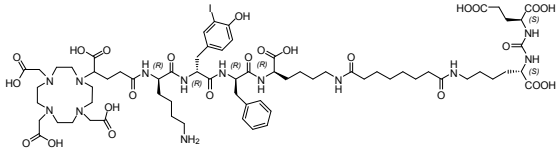

DOTAGA-N^6-ky(3-I)fk(Sub-KuE) (PSMA-14):

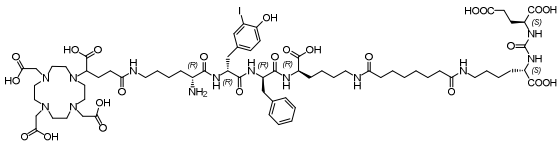

DOTAGA-F(4-NH₂)y(3-I)fk(Sub-KuE) (PSMA-15):

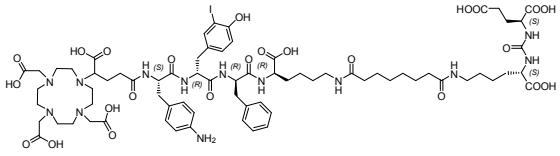

DOTAGA-f(4-NH₂)y(3-I)fk(Sub-KuE) (PSMA-16):

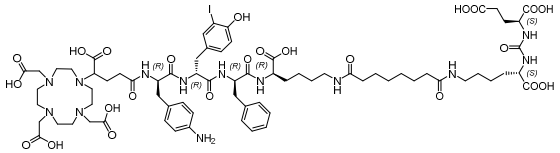

DOTAGA-f(4-NH₂)y(3-I)fK(Sub-KuE) (PSMA-17):

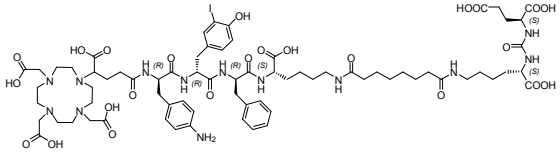

DOTAGA-f(4-NH₂)y(3-I)FK(Sub-KuE) (PSMA-18):

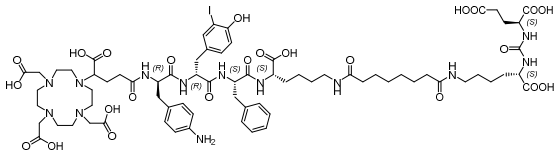

DOTAGA-F(4-NH₂)y(3-I)fK(Sub-KuE) (PSMA-19):

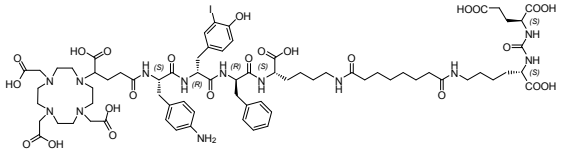

DOTAGA–y(3-I)fk(L-Asu[KuE]-MPA-Galactose) (PSMA-20):

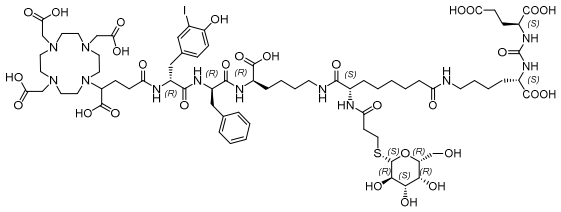

DOTAGA–y(3-I)fk(L-Asu[KuE]-MPA-Mannose) (PSMA-21):

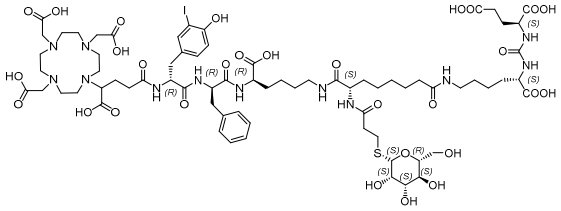

DOTAGA-y(3-I)fk(L-Asu[KuE]-MPA-Fucose) (PSMA-22):

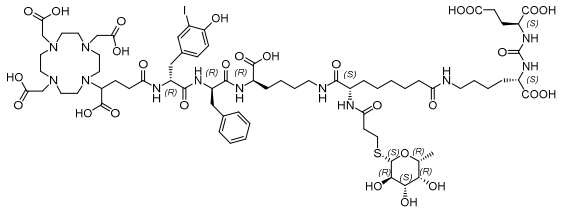

DOTAGA–y(3-I)fk(L-Asu[KuE]-MPA-Cellobiose) (PSMA-23):

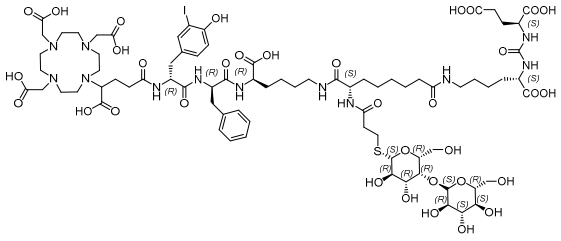

F-BA-AOAc-k(Agl[MPA-Galactose]-Glut-KuE) (PSMA-24):

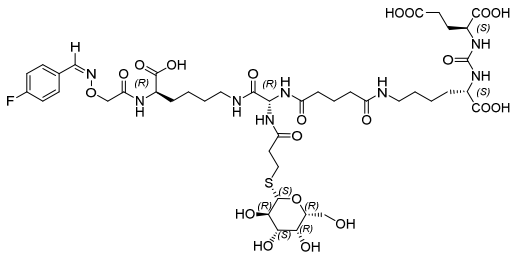

F-BA-AOAc-fk(Agl[MPA-Galactose]-Glut-KuE) (PSMA-25):

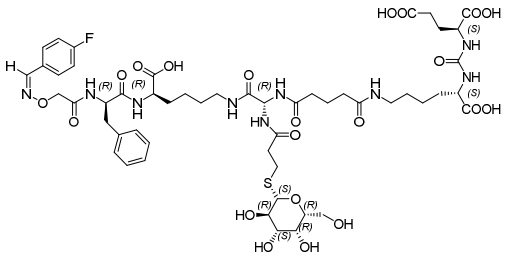

F-BA–AOAc–y(3-I)fk(Agl[MPA-Galactose]-Glut-KuE) (PSMA-26):

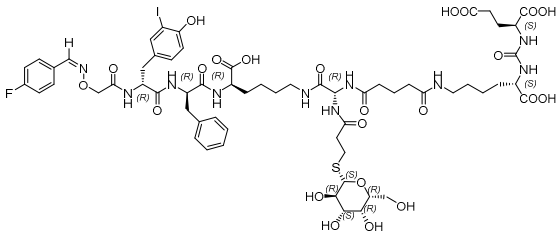

DOTAGA-f(4-NH$_2$)y(3-I)fk(L-Asu[KuE]-MPA-Galactose) (PSMA-27):

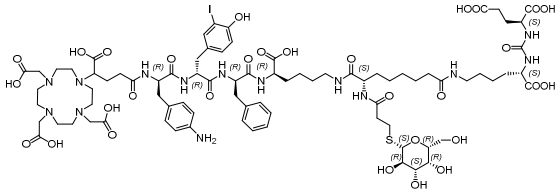

DOTAGA-f(4-NH$_2$)y(3-I)fk(Agl[MPA-Galactose]-Glut-KuE) (PSMA-28):

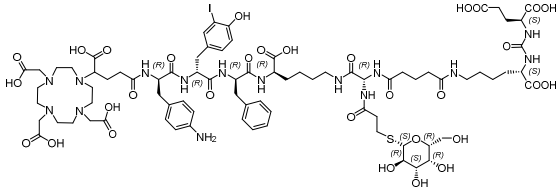

DOTAGA-f(4-NH-MPA-Galactose)y(3-I)fk(Agl[MPA-Galactose]-Glut-KuE) (PSMA-29):

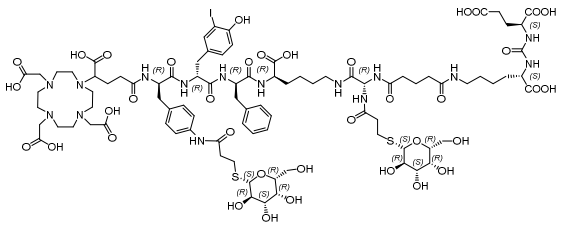

DOTAGA-y-2-nal-k(Sub-KuE) (PSMA-30):

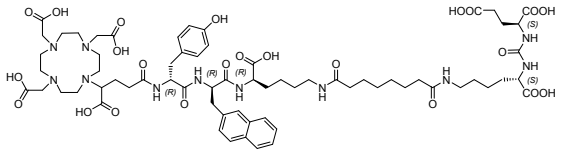

DOTAGA-F(4-NH$_2$)y-2-nal-k(Sub-KuE) (PSMA-31):

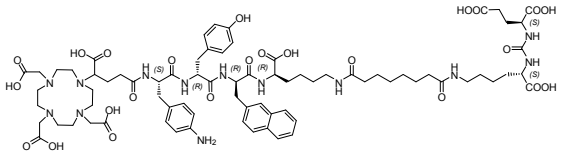

DOTAGA-f(4-NH$_2$)y-2-nal-k(Sub-KuE) (PSMA-32):

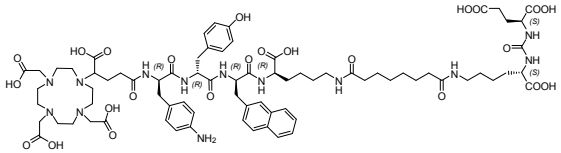

DOTAGA-f(4-NH$_2$)y-2-nal-K(Sub-KuE) (PSMA-33):

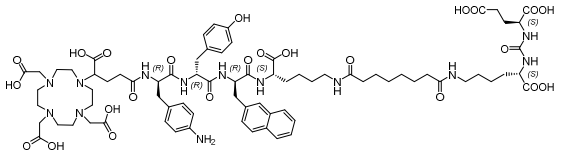

DOTAGA-F(4-NH$_2$)y-2-nal-K(Sub-KuE) (PSMA-34):

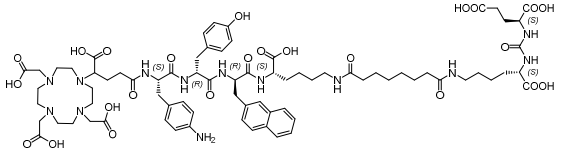

DOTAGA–y(3-I)fk(L-Asu[KuE]-BA) (PSMA-35):

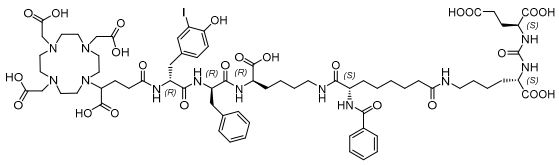

DOTAGA–y(3-I)fk(L-Asu[KuE]-2,4-DNBA) (PSMA-36):

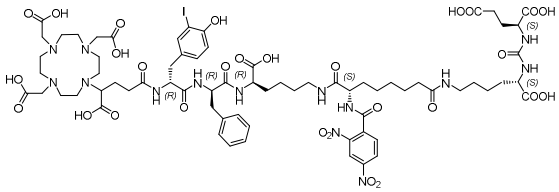

DOTAGA-y(3-I)fk(L-Asu[KuE]-DMBA) (PSMA-37):

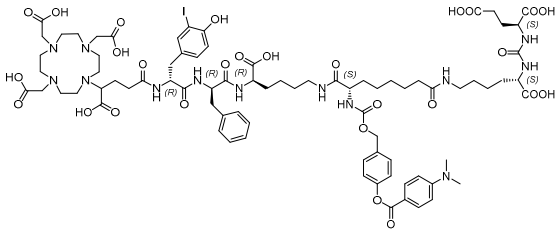

DOTAGA-f(4-NH₂)y(3-I)fk(Agl[PBP]-Glut-KuE) (PSMA-38):

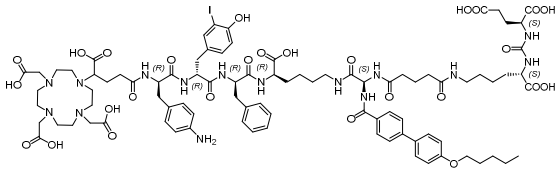

DOTAGA-f(4-NH₂)y(3-I)fk(Agl[C^4-e-PBP]-Glut-KuE) (PSMA-39):

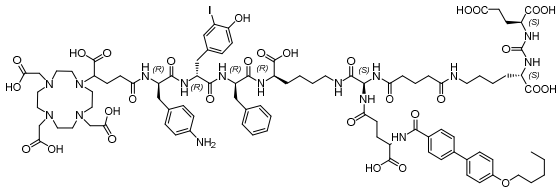

DOTAGA-f(4-NH₂)y(3-I)fk(Glut-f[4-I]-KuE) (PSMA-40):

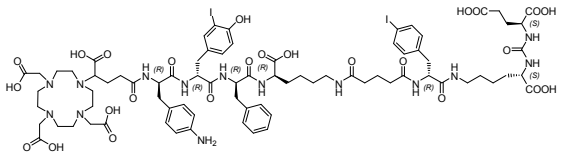

DOTAGA-f(4-NH₂)y-2-nal-k(Glut-f[4-I]-KuE) (PSMA-41):

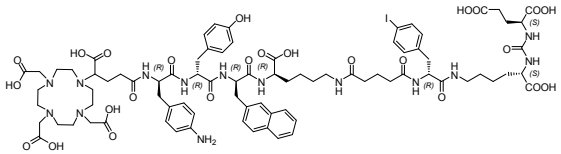

DOTAGA-f(4-NH₂)y-2-nal-K(Glut-f[4-I]-KuE) (PSMA-42):

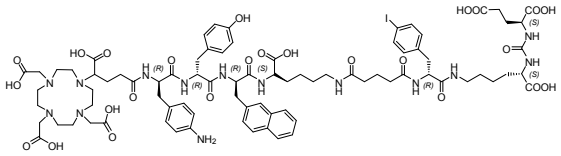

DOTAGA-y-2-nal-K(Glut-f[4-I]-KuE) (PSMA-43):

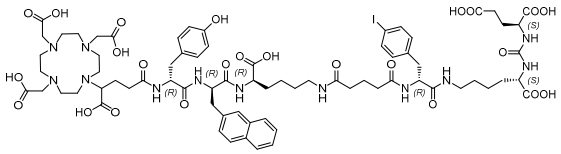

DOTA-f(4-NH₂)-y-2-nal-k(Sub-KuE) (PSMA-44):

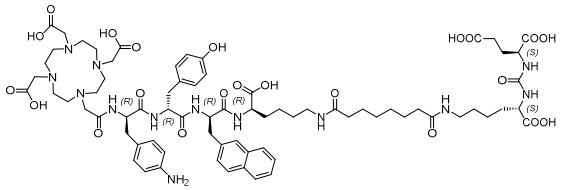

(SnBu₃-BA)(O*t*Bu)KuE(O*t*Bu)₂ (PSMA-45):

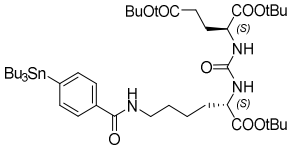

DOTAGA-y-2-nal-k(Suc-N^5-orn-C^4-EuE) (PSMA-46):

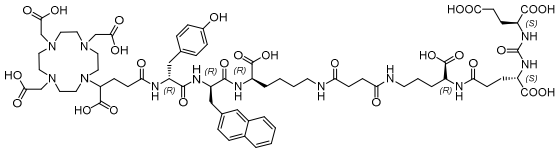

DOTAGA-F(4-NO_2)-y-2-nal-k(Suc-N^5-orn-C^4-EuE) (PSMA-52):

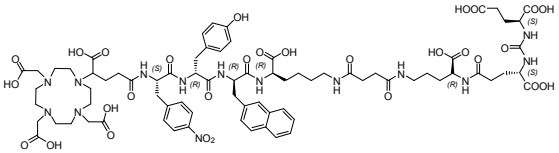

DOTAGA-F(4-NH_2)y(3-I)fk(Suc-N^5-orn-C^4-EuE) (PSMA-47):

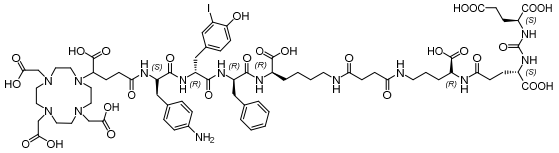

2,4-DNBA-Dap(DOTAGA)-y-2-nal-k(Suc-N^5-orn-C^4-EuE) (PSMA-53):

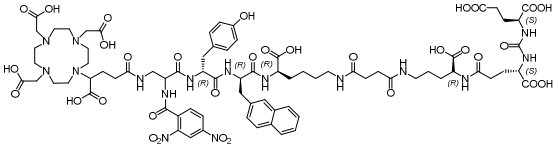

DOTAGA-f(4-NH_2)y(3-I)fk(Suc-N^5-orn-C^4-EuE) (PSMA-48):

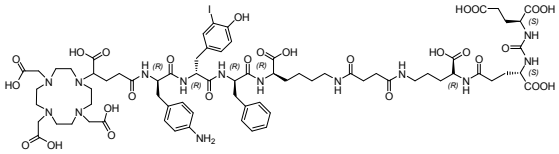

DOTAGA-Yy-2-nal-k(Suc-N^5-orn-C^4-EuE (PSMA-54):

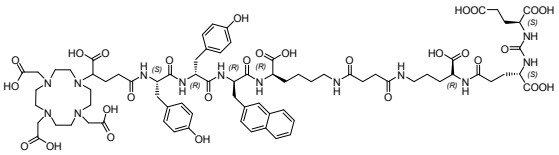

DOTAGA-F(4-NH_2)y-2-nal-k(Suc-N^5-orn-C^4-EuE) (PSMA-49):

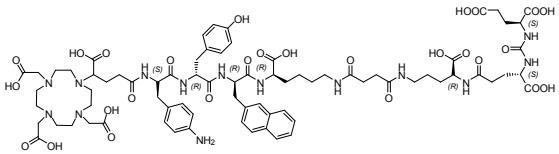

DOTAGA-2-Nal-y-2-nal-k(Suc-N^5-orn-C^4-EuE) (PSMA-55):

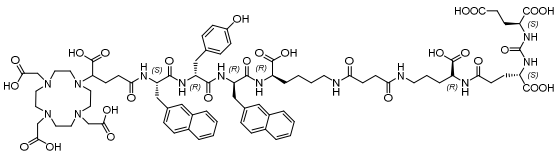

DOTAGA-f(4-NH_2)-y-2-nal-k(Suc-N^5-orn-C^4-EuE) (PSMA-50):

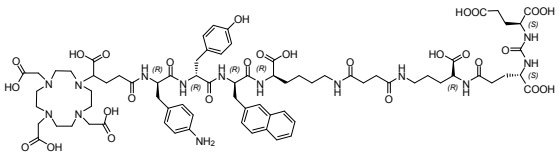

DOTAGA-K(PBP)y-2-nal-k(Suc-N^5-orn-C^4-EuE) (PSMA-56):

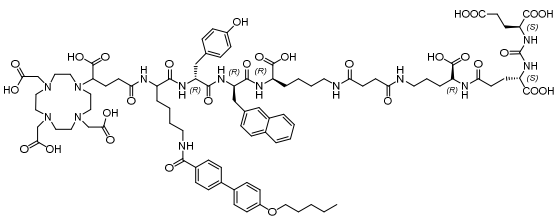

DOTAGA-f(4-NH_2)-y-2-nal-K(Suc-N^5-orn-C^4-EuE) (PSMA-51):

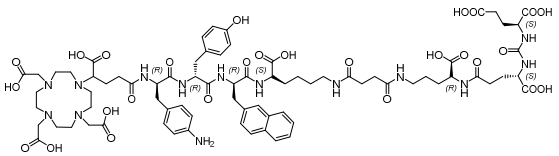

DOTAGA-K(C^4-e-PBP)y-2-nal-k(Suc-N^5-orn-C^4-EuE) (PSMA-57):

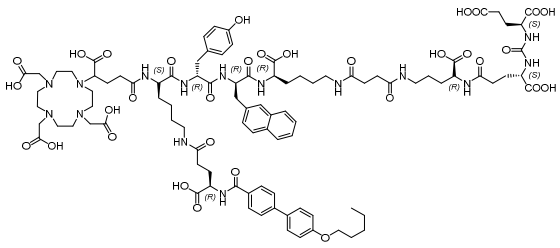

DOTAGA-F(4-NH_2)y-2-nal-e(r-G-N^5-orn-C^4-EuE) (PSMA-58):

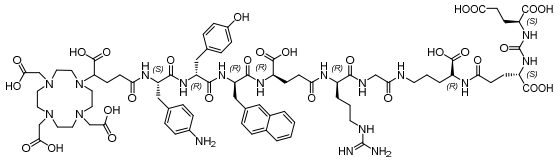

DOTAGA-F(4-NH_2)y-2-nal-e(e-G-N^5-orn-C^4-EuE) (PSMA-59):

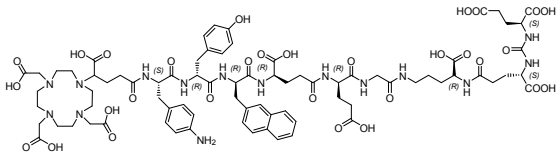

DOTAGA-F(4-NH_2)y-2-nal-e(Abz-N^5-orn-C^4-EuE) (PSMA-60):

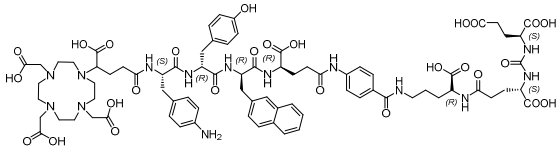

DOTAGA-F(4-NH_2)y-2-nal-k(d[N^5-orn-C^4-EuE]-2,4-DNBA) (PSMA-61):

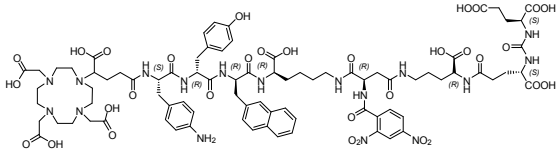

DOTAGA-F(4-NH_2)y-2-nal-k(d[N^5-orn-C^4-EuE]-TMA) (PSMA-62):

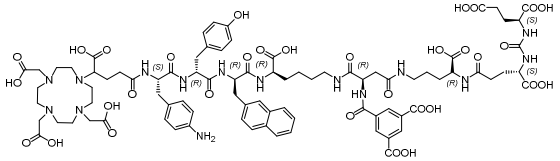

DOTAGA-F(4-NH_2)y-2-nal-k(Suc-N^5-orn-2-nal-C^4-EuE) (PSMA-63):

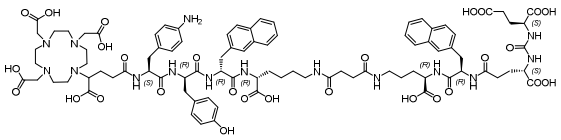

DOTAGA-F(4-NO_2)y-2-nal-k(Suc-N^5-orn-2-nal-C^4-EuE) (PSMA-64):

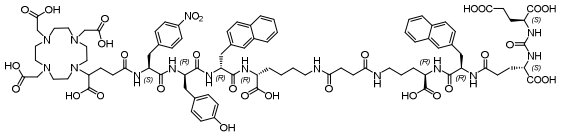

2,4-DNBA-Dap(DOTAGA)y-2-nal-e(Abz-N^5-orn-C^4-EuE) (PSMA-65):

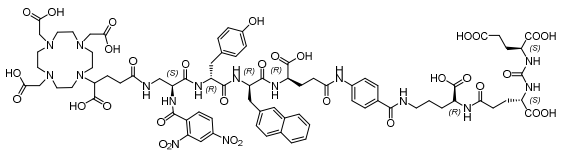

DOTAGA-Dap(TMA)y-2-nal-k(d[N^5-orn-C^4-EuE]-TMA) (PSMA-66):

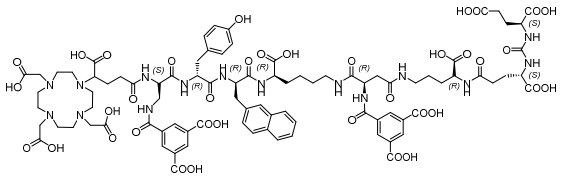

DOTAGA-2-Amet-Suc-F(4-NH_2)y-2-nal-k(Suc-N^5-orn-C^4-EuE) (PSMA-67):

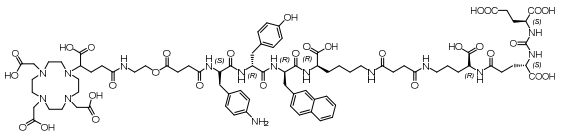

DOTAGA-FFK(Sub-KuE) (PSMA-68):

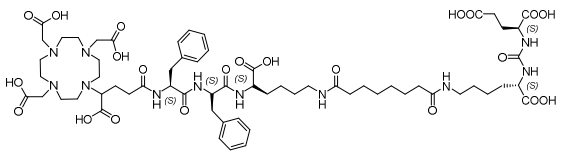

3. Abbreviations

% ID/mL	percentage injected dose per mL
2-CTC	2-chlorotrityl chloride
2-MPPA	2-(3-mercaptopropyl)pentanedioic acid
2-PMPA	2-(phosphonomethyl)pentanedioic acid
3-MPA	3-mercaptopropionic acid
4-FBA	4-fluorobenzaldehyde
AA	amino acids
ACD	annihilation coincidence detection
AcOH	acetic acid
ADT	androgen deprivation therapy
2-Amet	2-ethanolamine
AP-2	adaptor protein-2
aq.	aqueous
AR	androgen receptor
A_S	specific activity
Boc	*tert*-butyloxycarbonyl
BPH	benign prostatic hyperplasia
BSA	bovine serum albumin
BW	body weight
Bzl	benzyl alcohol
CDI	1,1'-carbonyldiimidazole
CT	computer tomography
DCC	*N*, *N*'-dicyclohexylcarbodiimide
DCE	1,2-dichloroethane
DCM	dichloromethane
Dde	*N*-1-(4,4-dimethyl-2,6-dioxocyclohexylidene)ethyl
DHT	5-α-dihydrotestosterone
DIC	*N,N'*-Diisopropylcarbodiimide

DIPEA	*N*,*N*-Diisopropylethylamine
DMAP	4-(dimethylamino)pyridine
DMBA	4-(dimethylamino)benzoic acid
DMEM-F12	Dulbecco modified Eagle medium/Nutrition Mixture F-12 (1/1)
DMF	dimethylformamide
DNA	deoxyribonucleic acid
DNBA	2,4-dinitrobenzoic acid
DOTA	1,4,7,10-tetraazacyclododecane-1,4,7,10-tetraacetic acid
DOTAGA	2-(4,7,10-tris(carboxymethyl)-1,4,7,10-tetraazacyclododecan-1-yl)pentanedioic acid
DRE	digital-rectal examination
EC	electron capture
EDC	1-ethyl-3-(3-dimethylaminopropyl)carbodiimide
EDTA	ethylenediaminetetraacetic acid
ESI-MS	electrospray ionization mass spectrometry
Et_2O	diethyl ether
EtOAc	ethyl acetate
EtOH	ethanol
FAK	focal adhesion kinase
FCS	fetal calf serum
FLNa	Filamin a
Fmoc	9-fluorenylmethoxycarbonyl (protecting group)
FOLH1	folate hydrolase
GCPII	glutamate carboxypeptidase II
GS	Gleason score
HATU	1-[Bis(dimethylamino)methylene]-1*H*-1,2,3-triazolo[4,5-b]pyridinium 3-oxid hexafluorophosphate
HBSS	Hank's buffered salt solution
HEPES	2-(4-(2-hydroxyethyl)-1-piperazinyl)-ethanesulfonic acid
HOBt	*N*-Hydroxybenzotriazole

HSA	human serum albumin
I&T	Imaging & Therapy
IC_{50}	half maximal inhibitory concentration
IL-1	interleukin 1
IT	isomeric transition
K'	capacity factors
Lit. HSA %	literature value of HSA binding
Log t_R	logarithmic retention time
Log$K$ HSA	logarithmic Log t_R using the calibration plot
mAb	murine antibody
mCRPC	metastatic castration resistant prostate cancer
MeCN	acetonitrile
MeOH	methanol
MET	mesenchymal-epithelial transition
ML-EM	maximum-likelihood expectation-maximization
MMP-2	matrix metalloproteinase-2
mPSMA	murine PSMA
MRI	magnetic resonance imaging
NAAG	*N*-acetyl-aspartyl glutamate
NET	neuroendocrine tumors
NHS	*N*-hydroxysuccinimide
NK	natural killer
NMP	*N*-methyl-2-pyrrolidone
NSAIDs	non-steroidal anti-inflammatory drugs
OSEM	ordered-subset expectation-maximization
PBP	4'-(pentyloxy)-[1,1'-biphenyl]-4-carboxylic acid
PBS	phosphate buffered saline
PCa	prostate cancer
PE	petroleum ether
PET	positron emission tomography

PfpOH	pentafluorophenol
PIN	prostatic intraepithelial neoplasia
PM	photo multiplier
PRLT	peptide radioligand therapy
PSMA	prostate specific membrane antigen
PSME	PSMA enhancer
PVE	Partial volume effect
QC	quality control
RP-HPLC	reversed phase high performance liquid chromatography
RT	room temperature
SAR	structure activity relationship
SDF1	stromal-cell-derived factor 1
SP	synthesis protocols
SPECT	single photon emission computed tomography
SUV	standardized uptake value
TBTU	*N,N,N′,N′*-Tetramethyl-O-(benzotriazol-1-yl)uronium tetrafluoroborate
TEA	trimethylamine
TFA	trifluoroacetic acid
TFE	trifluoroethanol
TGFβ	transforming growth factor-β
THF	tetrahydrofurane
TIPS	triisopropylsilane
TLC	thin-layer chromatography
TMA	trimesic acid
TNF-α	tumor necrosis factor-α
t_R	retention time
TSG	tumor suppressor gene

4. References

(1) Evan, G. I. Can't kick that oncogene habit. *Cancer Cell* **2006**, *10*, 345-347.

(2) Garcia, M.; Jemal, A.; Ward, E.; Center, M.; Hao, Y.; Siegel, R.; Thun, M. Global cancer facts & figures 2007. 2007. *Atlanta, GA: American Cancer Society* **2009**.

(3) Jemal, A.; Bray, F.; Center, M. M.; Ferlay, J.; Ward, E.; Forman, D. Global cancer statistics. *CA: a cancer journal for clinicians* **2011**, *61*, 69-90.

(4) Statistics, S. a. t. C. f. D. C. a. P. s. N. C. f. H. SEER Cancer Stat Facts: Cancer of Any Site. National Cancer Institute. Bethesda, MD, http://seer.cancer.gov/statfacts/html/all.html. **2017**.

(5) Siegel, R. L.; Miller, K. D.; Jemal, A. Cancer statistics, 2016. *CA: a cancer journal for clinicians* **2016**, *66*, 7-30.

(6) Luengo-Fernandez, R.; Leal, J.; Gray, A.; Sullivan, R. Economic burden of cancer across the European Union: a population-based cost analysis. *The lancet oncology* **2013**, *14*, 1165-1174.

(7) Greaves, M. Darwinian medicine: a case for cancer. *Nature Reviews Cancer* **2007**, *7*, 213-221.

(8) Cahill, D. P.; Kinzler, K. W.; Vogelstein, B.; Lengauer, C. Genetic instability and darwinian selection in tumours. *Trends in cell biology* **1999**, *9*, M57-M60.

(9) Nowell, P. C. Mechanisms of tumor progression. *Cancer Research* **1986**, *46*, 2203-2207.

(10) Nowell, P. C. The clonal evolution of tumor cell populations. *Science* **1976**, *194*, 23-28.

(11) Tomlins, S. A.; Rhodes, D. R.; Perner, S.; Dhanasekaran, S. M.; Mehra, R.; Sun, X.-W.; Varambally, S.; Cao, X.; Tchinda, J.; Kuefer, R. Recurrent fusion of TMPRSS2 and ETS transcription factor genes in prostate cancer. *Science* **2005**, *310*, 644-648.

(12) Stratton, M. R.; Campbell, P. J.; Futreal, P. A. The cancer genome. *Nature* **2009**, *458*, 719-724.

(13) Attard, G.; Reid, A. H.; Olmos, D.; de Bono, J. S. Antitumor activity with CYP17 blockade indicates that castration-resistant prostate cancer frequently remains hormone driven. *Cancer research* **2009**, *69*, 4937-4940.

(14) Coussens, L. M.; Werb, Z. Inflammation and cancer. *Nature* **2002**, *420*, 860-867.

(15) Pathmanathan, R.; Prasad, U.; Sadler, R.; Flynn, K.; Raab-Traub, N. Clonal proliferations of cells infected with Epstein–Barr virus in preinvasive lesions related to nasopharyngeal carcinoma. *New England Journal of Medicine* **1995**, *333*, 693-698.

(16) Ahuja, N.; Li, Q.; Mohan, A. L.; Baylin, S. B.; Issa, J.-P. J. Aging and DNA methylation in colorectal mucosa and cancer. *Cancer research* **1998**, *58*, 5489-5494.

(17) Valko, M.; Rhodes, C.; Moncol, J.; Izakovic, M.; Mazur, M. Free radicals, metals and antioxidants in oxidative stress-induced cancer. *Chemico-biological interactions* **2006**, *160*, 1-40.

(18) Calle, E. E.; Rodriguez, C.; Walker-Thurmond, K.; Thun, M. J. Overweight, obesity, and mortality from cancer in a prospectively studied cohort of US adults. *New England Journal of Medicine* **2003**, *348*, 1625-1638.

(19) Muirhead, C.; O'hagan, J.; Haylock, R.; Phillipson, M.; Willcock, T.; Berridge, G.; Zhang, W. Mortality and cancer incidence following occupational radiation exposure: third analysis of the National Registry for Radiation Workers. *British journal of cancer* **2009**, *100*, 206-212.

(20) Poirier, M. C. Chemical-induced DNA damage and human cancer risk. *Nature reviews. Cancer* **2004**, *4*, 630.

(21) Armstrong, B. K.; Kricker, A. The epidemiology of UV induced skin cancer. *Journal of Photochemistry and Photobiology B: Biology* **2001**, *63*, 8-18.

(22) Pope III, C. A.; Burnett, R. T.; Thun, M. J.; Calle, E. E.; Krewski, D.; Ito, K.; Thurston, G. D. Lung cancer, cardiopulmonary mortality, and long-term exposure to fine particulate air pollution. *Jama* **2002**, *287*, 1132-1141.

(23) Doll, R.; Hill, A. B. Lung cancer and other causes of death in relation to smoking. *British medical journal* **1956**, *2*, 1071.

(24) Miller, D. G. On the nature of susceptibility to cancer. The presidential address. *Cancer* **1980**, *46*, 1307-1318.

(25) Schinzel, A. C.; Hahn, W. C. Oncogenic transformation and experimental models of human cancer. *Frontiers in bioscience: a journal and virtual library* **2007**, *13*, 71-84.

(26) Beerenwinkel, N.; Antal, T.; Dingli, D.; Traulsen, A.; Kinzler, K. W.; Velculescu, V. E.; Vogelstein, B.; Nowak, M. A. Genetic progression and the waiting time to cancer. *PLoS Comput Biol* **2007**, *3*, e225.

(27) Robinson, D.; Van Allen, E. M.; Wu, Y.-M.; Schultz, N.; Lonigro, R. J.; Mosquera, J.-M.; Montgomery, B.; Taplin, M.-E.; Pritchard, C. C.; Attard, G. Integrative clinical genomics of advanced prostate cancer. *Cell* **2015**, *161*, 1215-1228.

(28) Rausch, T.; Jones, D. T.; Zapatka, M.; Stütz, A. M.; Zichner, T.; Weischenfeldt, J.; Jäger, N.; Remke, M.; Shih, D.; Northcott, P. A. Genome sequencing of pediatric medulloblastoma links catastrophic DNA rearrangements with TP53 mutations. *Cell* **2012**, *148*, 59-71.

(29) Kloosterman, W. P.; Koster, J.; Molenaar, J. J. Prevalence and clinical implications of chromothripsis in cancer genomes. *Current opinion in oncology* **2014**, *26*, 64-72.

(30) Stephens, P. J.; Greenman, C. D.; Fu, B.; Yang, F.; Bignell, G. R.; Mudie, L. J.; Pleasance, E. D.; Lau, K. W.; Beare, D.; Stebbings, L. A. Massive genomic rearrangement acquired in a single catastrophic event during cancer development. *cell* **2011**, *144*, 27-40.

(31) Baca, S. C.; Prandi, D.; Lawrence, M. S.; Mosquera, J. M.; Romanel, A.; Drier, Y.; Park, K.; Kitabayashi, N.; MacDonald, T. Y.; Ghandi, M. Punctuated evolution of prostate cancer genomes. *Cell* **2013**, *153*, 666-677.

(32) Greaves, M.; Maley, C. C. Clonal evolution in cancer. *Nature* **2012**, *481*, 306-313.

(33) Bozic, I.; Antal, T.; Ohtsuki, H.; Carter, H.; Kim, D.; Chen, S.; Karchin, R.; Kinzler, K. W.; Vogelstein, B.; Nowak, M. A. Accumulation of driver and passenger mutations during tumor progression. *Proceedings of the National Academy of Sciences* **2010**, *107*, 18545-18550.

(34) Zhou, S.; Abdouh, M.; Arena, V.; Arena, M.; Arena, G. O. Reprogramming Malignant Cancer Cells toward a Benign Phenotype following Exposure to Human Embryonic Stem Cell Microenvironment. *PloS one* **2017**, *12*, e0169899.

(35) Hendrix, M. J.; Seftor, E. A.; Seftor, R. E.; Kasemeier-Kulesa, J.; Kulesa, P. M.; Postovit, L.-M. Reprogramming metastatic tumour cells with embryonic microenvironments. *Nature Reviews Cancer* **2007**, *7*, 246-255.

(36) DeCosse, J. J.; Gossens, C. L.; Kuzma, J. F.; Unsworth, B. R. Breast cancer: induction of differentiation by embryonic tissue. *Science* **1973**, *181*, 1057-1058.

(37) Bissell, M. J.; Hines, W. C. Why don't we get more cancer? A proposed role of the microenvironment in restraining cancer progression. *Nat Med* **2011**, *17*, 320-329.

(38) Morgan, J. E.; Gross, J. G.; Pagel, C. N.; Beauchamp, J. R.; Fassati, A.; Thrasher, A. J.; Di Santo, J. P.; Fisher, I. B.; Shiwen, X.; Abraham, D. J. Myogenic cell proliferation and generation of a reversible tumorigenic phenotype are triggered by preirradiation of the recipient site. *J Cell Biol* **2002**, *157*, 693-702.

(39) Barcellos-Hoff, M. H.; Lyden, D.; Wang, T. C. The evolution of the cancer niche during multistage carcinogenesis. *Nature Reviews Cancer* **2013**, *13*, 511-518.

(40) Lu, P.; Weaver, V. M.; Werb, Z. The extracellular matrix: A dynamic niche in cancer progression. *The Journal of Cell Biology* **2012**, *196*, 395-406.

(41) Ayala, G.; Tuxhorn, J. A.; Wheeler, T. M.; Frolov, A.; Scardino, P. T.; Ohori, M.; Wheeler, M.; Spitler, J.; Rowley, D. R. Reactive stroma as a predictor of biochemical-free recurrence in prostate cancer. *Clinical Cancer Research* **2003**, *9*, 4792-4801.

(42) Tuxhorn, J. A.; Ayala, G. E.; Rowley, D. R. Reactive stroma in prostate cancer progression. *The Journal of urology* **2001**, *166*, 2472-2483.

(43) Finak, G.; Bertos, N.; Pepin, F.; Sadekova, S.; Souleimanova, M.; Zhao, H.; Chen, H.; Omeroglu, G.; Meterissian, S.; Omeroglu, A. Stromal gene expression predicts clinical outcome in breast cancer. *Nature medicine* **2008**, *14*, 518-527.

(44) Webb, B. A.; Chimenti, M.; Jacobson, M. P.; Barber, D. L. Dysregulated pH: a perfect storm for cancer progression. *Nature Reviews Cancer* **2011**, *11*, 671-677.

(45) Coca, S.; Perez-Piqueras, J.; Martinez, D.; Colmenarejo, A.; Saez, M. A.; Vallejo, C.; Martos, J. A.; Moreno, M. The prognostic significance of intratumoral natural killer cells in patients with colorectal carcinoma. *Cancer* **1997**, *79*, 2320-2328.

(46) Ishigami, S.; Natsugoe, S.; Tokuda, K.; Nakajo, A.; Che, X.; Iwashige, H.; Aridome, K.; Hokita, S.; Aikou, T. Prognostic value of intratumoral natural killer cells in gastric carcinoma. *Cancer* **2000**, *88*, 577-583.

(47) McArdle, P.; Canna, K.; McMillan, D.; McNicol, A.; Campbell, R.; Underwood, M. The relationship between T-lymphocyte subset infiltration and survival in patients with prostate cancer. *British journal of cancer* **2004**, *91*, 541-543.

(48) Nonomura, N.; Takayama, H.; Nakayama, M.; Nakai, Y.; Kawashima, A.; Mukai, M.; Nagahara, A.; Aozasa, K.; Tsujimura, A. Infiltration of tumour-associated macrophages in prostate biopsy specimens is predictive of disease progression after hormonal therapy for prostate cancer. *BJU international* **2011**, *107*, 1918-1922.

(49) Ness, N.; Andersen, S.; Valkov, A.; Nordby, Y.; Donnem, T.; Al-Saad, S.; Busund, L. T.; Bremnes, R. M.; Richardsen, E. Infiltration of CD8+ lymphocytes is an independent prognostic factor of biochemical failure-free survival in prostate cancer. *The Prostate* **2014**, *74*, 1452-1461.

(50) Liu, Y.; Sæter, T.; Vlatkovic, L.; Servoll, E.; Waaler, G.; Axcrona, U.; Giercksky, K.-E.; Nesland, J. M.; Suo, Z.-H.; Axcrona, K. Dendritic and lymphocytic cell infiltration in prostate carcinoma. *Histology and histopathology* **2013**, *28*, 1621-1628.

(51) Balkwill, F.; Charles, K. A.; Mantovani, A. Smoldering and polarized inflammation in the initiation and promotion of malignant disease. *Cancer cell* **2005**, *7*, 211-217.

(52) Jacobs, E. J.; Rodriguez, C.; Mondul, A. M.; Connell, C. J.; Henley, S. J.; Calle, E. E.; Thun, M. J. A Large Cohort Study of Aspirin and Other Nonsteroidal Anti-inflammatory Drugs and Prostate Cancer Incidence. *JNCI: Journal of the National Cancer Institute* **2005**, *97*, 975-980.

(53) Ulrich, C. M.; Bigler, J.; Potter, J. D. Non-steroidal anti-inflammatory drugs for cancer prevention: promise, perils and pharmacogenetics. *Nature Reviews Cancer* **2006**, *6*, 130-140.

(54) Logothetis, C. J.; Gallick, G. E.; Maity, S. N.; Kim, J.; Aparicio, A.; Efstathiou, E.; Lin, S.-H. Molecular classification of prostate cancer progression: foundation for marker-driven treatment of prostate cancer. *Cancer discovery* **2013**, *3*, 849-861.

(55) Tomlins, S. A.; Mehra, R.; Rhodes, D. R.; Cao, X.; Wang, L.; Dhanasekaran, S. M.; Kalyana-Sundaram, S.; Wei, J. T.; Rubin, M. A.; Pienta, K. J. Integrative molecular concept modeling of prostate cancer progression. *Nature genetics* **2007**, *39*, 41-51.

(56) Wang, X.; Kruithof-de Julio, M.; Economides, K. D.; Walker, D.; Yu, H.; Halili, M. V.; Hu, Y.-P.; Price, S. M.; Abate-Shen, C.; Shen, M. M. A luminal epithelial stem cell that is a cell of origin for prostate cancer. *Nature* **2009**, *461*, 495-500.

(57) Harries, L. W.; Stubbins, M. J.; Forman, D.; Howard, G.; Wolf, C. R. Identification of genetic polymorphisms at the glutathione S-transferase Pi locus and association with susceptibility to bladder, testicular and prostate cancer. *Carcinogenesis* **1997**, *18*, 641-644.

(58) Perner, S.; Demichelis, F.; Beroukhim, R.; Schmidt, F. H.; Mosquera, J.-M.; Setlur, S.; Tchinda, J.; Tomlins, S. A.; Hofer, M. D.; Pienta, K. G. TMPRSS2: ERG fusion-associated deletions provide insight into the heterogeneity of prostate cancer. *Cancer research* **2006**, *66*, 8337-8341.

(59) Gundem, G.; Van Loo, P.; Kremeyer, B.; Alexandrov, L. B.; Tubio, J. M. C.; Papaemmanuil, E.; Brewer, D. S.; Kallio, H. M. L.; Hognas, G.; Annala, M.; Kivinummi, K.; Goody, V.; Latimer, C.; O'Meara, S.; Dawson, K. J.; Isaacs, W.; Emmert-Buck, M. R.; Nykter, M.; Foster, C.; Kote-Jarai, Z.; Easton, D.; Whitaker, H. C.; Group, I. P. U.; Neal, D. E.; Cooper, C. S.; Eeles, R. A.; Visakorpi, T.; Campbell, P. J.; McDermott, U.; Wedge, D. C.; Bova, G. S. The evolutionary history of lethal metastatic prostate cancer. *Nature* **2015**, *520*, 353-357.

(60) King, J. C.; Xu, J.; Wongvipat, J.; Hieronymus, H.; Carver, B. S.; Leung, D. H.; Taylor, B. S.; Sander, C.; Cardiff, R. D.; Couto, S. S. Cooperativity of TMPRSS2-ERG with PI3-kinase pathway activation in prostate oncogenesis. *Nature genetics* **2009**, *41*, 524-526.

(61) Singareddy, R.; Semaan, L.; Conley-LaComb, M. K.; John, J. S.; Powell, K.; Iyer, M.; Smith, D.; Heilbrun, L. K.; Shi, D.; Sakr, W. Transcriptional regulation of CXCR4 in prostate cancer: significance of TMPRSS2-ERG fusions. *Molecular Cancer Research* **2013**, *11*, 1349-1361.

(62) Perner, S.; Mosquera, J.-M.; Demichelis, F.; Hofer, M. D.; Paris, P. L.; Simko, J.; Collins, C.; Bismar, T. A.; Chinnaiyan, A. M.; De Marzo, A. M. TMPRSS2-ERG fusion prostate cancer: an early molecular event associated with invasion. *The American journal of surgical pathology* **2007**, *31*, 882-888.

(63) Fischer, A. H.; Bardarov, S.; Jiang, Z. Molecular aspects of diagnostic nucleolar and nuclear envelope changes in prostate cancer. *Journal of cellular biochemistry* **2004**, *91*, 170-184.

(64) Network, C. G. A. R. The molecular taxonomy of primary prostate cancer. *Cell* **2015**, *163*, 1011-1025.

(65) Denis, L.; Murphy, G. Overview of phase III trials on combined androgen treatment in patients with metastatic prostate cancer. *Cancer* **1993**, *72*, 3888-3895.

(66) Sharifi, N.; Gulley, J. L.; Dahut, W. L. Androgen deprivation therapy for prostate cancer. *Jama* **2005**, *294*, 238-244.

(67) Visakorpi, T.; Hyytinen, E.; Koivisto, P.; Tanner, M.; Keinänen, R.; Palmberg, C.; Palotie, A.; Tammela, T.; Isola, J.; Kallioniemi, O.-P. In vivo amplification of the androgen receptor gene and progression of human prostate cancer. *Nature genetics* **1995**, *9*, 401-406.

(68) Feldman, B. J.; Feldman, D. The development of androgen-independent prostate cancer. *Nature Reviews Cancer* **2001**, *1*, 34-45.

(69) Gregory, C. W.; Johnson, R. T.; Mohler, J. L.; French, F. S.; Wilson, E. M. Androgen receptor stabilization in recurrent prostate cancer is associated with hypersensitivity to low androgen. *Cancer research* **2001**, *61*, 2892-2898.

(70) Makridakis, N.; Ross, R. K.; Pike, M. C.; Chang, L.; Stanczyk, F. Z.; Kolonel, L. N.; Shi, C.-Y.; Mimi, C. Y.; Henderson, B. E.; Reichardt, J. K. A prevalent missense substitution that modulates activity of prostatic steroid 5 α -reductase. *Cancer research* **1997**, *57*, 1020-1022.

(71) Taplin, M.-E.; Bubley, G. J.; Ko, Y.-J.; Small, E. J.; Upton, M.; Rajeshkumar, B.; Balk, S. P. Selection for androgen receptor mutations in prostate cancers treated with androgen antagonist. *Cancer research* **1999**, *59*, 2511-2515.

(72) Zhao, X.-Y.; Malloy, P. J.; Krishnan, A. V.; Swami, S.; Navone, N. M.; Peehl, D. M.; Feldman, D. Glucocorticoids can promote androgen-independent growth of prostate cancer cells through a mutated androgen receptor. *Nature medicine* **2000**, *6*, 703-706.

(73) Miyamoto, H.; Yeh, S.; Wilding, G.; Chang, C. Promotion of agonist activity of antiandrogens by the androgen receptor coactivator, ARA70, in human prostate cancer DU145 cells. *Proceedings of the National Academy of Sciences* **1998**, *95*, 7379-7384.

(74) Jennbacken, K.; Tešan, T.; Wang, W.; Gustavsson, H.; Damber, J.-E.; Welén, K. N-cadherin increases after androgen deprivation and is associated with metastasis in prostate cancer. *Endocrine-related cancer* **2010**, *17*, 469-479.

(75) Lee, Y. C.; Cheng, C. J.; Huang, M.; Bilen, M. A.; Ye, X.; Navone, N. M.; Chu, K.; Kao, H. H.; Yu-Lee, L. Y.; Wang, Z. Androgen depletion up-regulates cadherin-11 expression in prostate cancer. *The Journal of pathology* **2010**, *221*, 68-76.

(76) Yin, L.; Rao, P.; Elson, P.; Wang, J.; Ittmann, M.; Heston, W. D. Role of TMPRSS2-ERG gene fusion in negative regulation of PSMA expression. *PLoS One* **2011**, *6*, e21319.

(77) Singh, D.; Febbo, P. G.; Ross, K.; Jackson, D. G.; Manola, J.; Ladd, C.; Tamayo, P.; Renshaw, A. A.; D'Amico, A. V.; Richie, J. P. Gene expression correlates of clinical prostate cancer behavior. *Cancer cell* **2002**, *1*, 203-209.

(78) Alshalalfa, M.; Crisan, A.; Vergara, I. A.; Ghadessi, M.; Buerki, C.; Erho, N.; Yousefi, K.; Sierocinski, T.; Haddad, Z.; Black, P. C. Clinical and genomic analysis of metastatic prostate cancer progression with a background of postoperative biochemical recurrence. *BJU international* **2015**, *116*, 556-567.

(79) Seligson, D. B.; Horvath, S.; Shi, T.; Yu, H.; Tze, S.; Grunstein, M.; Kurdistani, S. K. Global histone modification patterns predict risk of prostate cancer recurrence. *Nature* **2005**, *435*, 1262-1266.

(80) Markert, E. K.; Mizuno, H.; Vazquez, A.; Levine, A. J. Molecular classification of prostate cancer using curated expression signatures. *Proceedings of the National Academy of Sciences* **2011**, *108*, 21276-21281.

(81) Lotan, T. L.; Gurel, B.; Sutcliffe, S.; Esopi, D.; Liu, W.; Xu, J.; Hicks, J. L.; Park, B. H.; Humphreys, E.; Partin, A. W. PTEN protein loss by immunostaining: analytic validation and prognostic indicator for a high risk surgical cohort of prostate cancer patients. *Clinical cancer research* **2011**, *17*, 6563-6573.

(82) Chen, Z.; Trotman, L. C.; Shaffer, D.; Lin, H.-K.; Dotan, Z. A.; Niki, M.; Koutcher, J. A.; Scher, H. I.; Ludwig, T.; Gerald, W. Crucial role of p53-dependent cellular senescence in suppression of Pten-deficient tumorigenesis. *Nature* **2005**, *436*, 725-730.

(83) Haffner, M. C.; Mosbruger, T.; Esopi, D. M.; Fedor, H.; Heaphy, C. M.; Walker, D. A.; Adejola, N.; Gürel, M.; Hicks, J.; Meeker, A. K. Tracking the clonal origin of lethal prostate cancer. *The Journal of clinical investigation* **2013**, *123*, 4918-4922.

(84) Iglesias-Gato, D.; Wikström, P.; Tyanova, S.; Lavallee, C.; Thysell, E.; Carlsson, J.; Hägglöf, C.; Cox, J.; Andrén, O.; Stattin, P. The proteome of primary prostate cancer. *European urology* **2016**, *69*, 942-952.

(85) Varambally, S.; Yu, J.; Laxman, B.; Rhodes, D. R.; Mehra, R.; Tomlins, S. A.; Shah, R. B.; Chandran, U.; Monzon, F. A.; Becich, M. J.; Wei, J. T.; Pienta, K. J.; Ghosh, D.; Rubin, M. A.; Chinnaiyan, A. M. Integrative genomic and proteomic analysis of prostate cancer reveals signatures of metastatic progression. *Cancer Cell* **2005**, *8*, 393-406.

(86) Rajasekaran, A. K.; Anilkumar, G.; Christiansen, J. J. Is prostate-specific membrane antigen a multifunctional protein? *American Journal of Physiology-Cell Physiology* **2005**, *288*, C975-C981.

(87) O'Keefe, D. S.; Su, S. L.; Bacich, D. J.; Horiguchi, Y.; Luo, Y.; Powell, C. T.; Zandvliet, D.; Russell, P. J.; Molloy, P. L.; Nowak, N. J. Mapping, genomic organization and promoter analysis of the human prostate-specific membrane antigen gene. *Biochimica et Biophysica Acta (BBA)-Gene Structure and Expression* **1998**, *1443*, 113-127.

(88) Holmes, E. H.; Greene, T. G.; Tino, W. T.; Boynton, A. L.; Aldape, H. C.; Misrock, S. L.; Murphy, G. P. Analysis of glycosylation of prostate-specific membrane antigen derived from LNCaP cells, prostatic carcinoma tumors, and serum from prostate cancer patients. *The Prostate* **1996**, *29*, 25-29.

(89) Barinka, C.; Šácha, P.; Sklenář, J.; Man, P.; Bezouška, K.; Slusher, B. S.; Konvalinka, J. Identification of the N-glycosylation sites on glutamate carboxypeptidase II necessary for proteolytic activity. *Protein Science* **2004**, *13*, 1627-1635.

(90) Ghosh, A.; Heston, W. D. Effect of carbohydrate moieties on the folate hydrolysis activity of the prostate specific membrane antigen. *The Prostate* **2003**, *57*, 140-151.

(91) Davis, M. I.; Bennett, M. J.; Thomas, L. M.; Bjorkman, P. J. Crystal structure of prostate-specific membrane antigen, a tumor marker and peptidase. *Proceedings of the National Academy of Sciences* **2005**, *102*, 5981-5986.

(92) Mesters, J. R.; Barinka, C.; Li, W.; Tsukamoto, T.; Majer, P.; Slusher, B. S.; Konvalinka, J.; Hilgenfeld, R. Structure of glutamate carboxypeptidase II, a drug target in neuronal damage and prostate cancer. *The EMBO journal* **2006**, *25*, 1375-1384.

(93) Mlčochová, P.; Plechanovova, A.; Bařinka, C.; Mahadevan, D.; Saldanha, J. W.; Rulíšek, L.; Konvalinka, J. Mapping of the active site of glutamate carboxypeptidase II by site-directed mutagenesis. *FEBS journal* **2007**, *274*, 4731-4741.

(94) Mesters, J. R.; Henning, K.; Hilgenfeld, R. Human glutamate carboxypeptidase II inhibition: structures of GCPII in complex with two potent inhibitors, quisqualate and 2-PMPA. *Acta Crystallographica Section D: Biological Crystallography* **2007**, *63*, 508-513.

(95) Anilkumar, G.; Rajasekaran, S. A.; Wang, S.; Hankinson, O.; Bander, N. H.; Rajasekaran, A. K. Prostate-specific membrane antigen association with filamin A modulates its internalization and NAALADase activity. *Cancer research* **2003**, *63*, 2645-2648.

(96) Robinson, M. B.; Blakely, R.; Couto, R.; Coyle, J. Hydrolysis of the brain dipeptide N-acetyl-L-aspartyl-L-glutamate. Identification and characterization of a novel N-acetylated alpha-linked acidic dipeptidase activity from rat brain. *Journal of Biological Chemistry* **1987**, *262*, 14498-14506.

(97) Whitaker, H.; Shiong, L.; Kay, J.; Grönberg, H.; Warren, A.; Seipel, A.; Wiklund, F.; Thomas, B.; Wiklund, P.; Miller, J. N-acetyl-L-aspartyl-L-glutamate peptidase-like 2 is overexpressed in cancer and promotes a pro-migratory and pro-metastatic phenotype. *Oncogene* **2014**, *33*, 5274-5287.

(98) Tiffany, C. W.; Lapidus, R. G.; Merion, A.; Calvin, D. C.; Slusher, B. S. Characterization of the enzymatic activity of PSM: comparison with brain NAALADase. *The Prostate* **1999**, *39*, 28-35.

(99) Yao, V.; Berkman, C. E.; Choi, J. K. Expression of prostate-specific membrane antigen (PSMA), increases cell folate uptake and proliferation and suggests a novel role for PSMA in the uptake of the non-polyglutamated folate, folic acidDenise S. O'Keefe and Dean J. Bacich contributed equally to this work. *Prostate* **2010**, *70*, 305.

(100) Tasch, J.; Gong, M.; Sadelain, M.; Heston, W. D. A unique folate hydrolase, prostate-specific membrane antigen (PSMA): a target for immunotherapy? *Critical Reviews™ in Immunology* **2001**, *21*.

(101) Bacich, D. J.; Pinto, J. T.; Tong, W. P.; Heston, W. D. Cloning, expression, genomic localization, and enzymatic activities of the mouse homolog of prostate-specific membrane antigen/NAALADase/folate hydrolase. *Mammalian Genome* **2001**, *12*, 117-123.

(102) Pinto, J. T.; Suffoletto, B. P.; Berzin, T. M.; Qiao, C. H.; Lin, S.; Tong, W. P.; May, F.; Mukherjee, B.; Heston, W. Prostate-specific membrane antigen: a novel folate hydrolase in human prostatic carcinoma cells. *Clinical Cancer Research* **1996**, *2*, 1445-1451.

(103) Schülke, N.; Varlamova, O. A.; Donovan, G. P.; Ma, D.; Gardner, J. P.; Morrissey, D. M.; Arrigale, R. R.; Zhan, C.; Chodera, A. J.; Surowitz, K. G. The homodimer of prostate-specific membrane antigen is a functional target for cancer therapy. *Proceedings of the National Academy of Sciences* **2003**, *100*, 12590-12595.

(104) Barinka, C.; Rinnová, M.; Šácha, P.; Rojas, C.; Majer, P.; Slusher, B. S.; Konvalinka, J. Substrate specificity, inhibition and enzymological analysis of recombinant human glutamate carboxypeptidase II. *Journal of neurochemistry* **2002**, *80*, 477-487.

(105) Liu, H.; Rajasekaran, A. K.; Moy, P.; Xia, Y.; Kim, S.; Navarro, V.; Rahmati, R.; Bander, N. H. Constitutive and antibody-induced internalization of prostate-specific membrane antigen. *Cancer research* **1998**, *58*, 4055-4060.

(106) Rajasekaran, S. A.; Anilkumar, G.; Oshima, E.; Bowie, J. U.; Liu, H.; Heston, W.; Bander, N. H.; Rajasekaran, A. K. A novel cytoplasmic tail MXXXL motif mediates the internalization of prostate-specific membrane antigen. *Molecular biology of the cell* **2003**, *14*, 4835-4845.

(107) Schmittgen, T. D.; Teske, S.; Vessella, R. L.; True, L. D.; Zakrajsek, B. A. Expression of prostate specific membrane antigen and three alternatively spliced variants of PSMA in prostate cancer patients. *International journal of cancer* **2003**, *107*, 323-329.

(108) Yao, V.; Bacich, D. J. Prostate specific membrane antigen (PSMA) expression gives prostate cancer cells a growth advantage in a physiologically relevant folate environment in vitro. *The Prostate* **2006**, *66*, 867-875.

(109) Chang, S. S.; Reuter, V. E.; Heston, W.; Bander, N. H.; Grauer, L. S.; Gaudin, P. B. Five different anti-prostate-specific membrane antigen (PSMA) antibodies confirm PSMA expression in tumor-associated neovasculature. *Cancer research* **1999**, *59*, 3192-3198.

(110) Heitkötter, B.; Trautmann, M.; Grünewald, I.; Bögemann, M.; Rahbar, K.; Gevensleben, H.; Wardelmann, E.; Hartmann, W.; Steinestel, K.; Huss, S. Expression of PSMA in tumor neovasculature of high grade sarcomas including synovial sarcoma, rhabdomyosarcoma, undifferentiated sarcoma and MPNST. *prostate* **2016**, *2*, 6-12.

(111) Haffner, M. C.; Kronberger, I. E.; Ross, J. S.; Sheehan, C. E.; Zitt, M.; Mühlmann, G.; Öfner, D.; Zelger, B.; Ensinger, C.; Yang, X. J. Prostate-specific membrane antigen expression in the neovasculature of gastric and colorectal cancers. *Human pathology* **2009**, *40*, 1754-1761.

(112) Baccala, A.; Sercia, L.; Li, J.; Heston, W.; Zhou, M. Expression of prostate-specific membrane antigen in tumor-associated neovasculature of renal neoplasms. *Urology* **2007**, *70*, 385-390.

(113) Chang, S. S.; O'Keefe, D. S.; Bacich, D. J.; Reuter, V. E.; Heston, W. D.; Gaudin, P. B. Prostate-specific membrane antigen is produced in tumor-associated neovasculature. *Clinical Cancer Research* **1999**, *5*, 2674-2681.

(114) Conway, R. E.; Petrovic, N.; Li, Z.; Heston, W.; Wu, D.; Shapiro, L. H. Prostate-specific membrane antigen regulates angiogenesis by modulating integrin signal transduction. *Molecular and cellular biology* **2006**, *26*, 5310-5324.

(115) Bacich, D. J.; Ramadan, E.; O'keefe, D. S.; Bukhari, N.; Wegorzewska, I.; Ojeifo, O.; Olszewski, R.; Wrenn, C. C.; Bzdega, T.; Wroblewska, B. Deletion of the glutamate carboxypeptidase II gene in mice reveals a second enzyme activity that hydrolyzes N-acetylaspartylglutamate. *Journal of neurochemistry* **2002**, *83*, 20-29.

(116) Grant, C. L.; Caromile, L. A.; Durrani, K.; Rahman, M. M.; Claffey, K. P.; Fong, G.-H.; Shapiro, L. H. Prostate specific membrane antigen (PSMA) regulates angiogenesis independently of VEGF during ocular neovascularization. *PloS one* **2012**, *7*, e41285.

(117) Conway, R. E.; Joiner, K.; Patterson, A.; Bourgeois, D.; Rampp, R.; Hannah, B. C.; McReynolds, S.; Elder, J. M.; Gilfilen, H.; Shapiro, L. H. Prostate specific membrane antigen produces pro-angiogenic laminin peptides downstream of matrix metalloprotease-2. *Angiogenesis* **2013**, *16*, 847-860.

(118) Conway, R. E.; Rojas, C.; Alt, J.; Nováková, Z.; Richardson, S. M.; Rodrick, T. C.; Fuentes, J. L.; Richardson, N. H.; Attalla, J.; Stewart, S. Prostate-specific membrane antigen (PSMA)-mediated laminin proteolysis generates a pro-angiogenic peptide. *Angiogenesis* **2016**, *19*, 487-500.

(119) Colombatti, M.; Grasso, S.; Porzia, A.; Fracasso, G.; Scupoli, M. T.; Cingarlini, S.; Poffe, O.; Naim, H. Y.; Heine, M.; Tridente, G. The Prostate Specific Membrane Antigen Regulates the Expression of IL-6 and CCL5 in Prostate Tumour Cells by Activating the MAPK Pathways 1. *PloS one* **2009**, *4*, e4608.

(120) Perico, M. E.; Grasso, S.; Brunelli, M.; Martignoni, G.; Munari, E.; Moiso, E.; Fracasso, G.; Cestari, T.; Naim, H. Y.; Bronte, V. Prostate-specific membrane antigen (PSMA) assembles a macromolecular complex regulating growth and survival of prostate cancer cells "in vitro" and correlating with progression "in vivo". *Oncotarget* **2016**, *7*, 74189-74202.

(121) Höti, N.; Shah, P.; Hu, Y.; Yang, S.; Zhang, H. Proteomics analyses of prostate cancer cells reveals cellular pathways associated with androgen resistance. *Proteomics* **2017**.

(122) Chow, H.; Ghosh, P. M.; deVere White, R.; Evans, C. P.; Dall'Era, M. A.; Yap, S. A.; Li, Y.; Beckett, L. A.; Lara, P. N.; Pan, C. X. A phase 2 clinical trial of everolimus plus bicalutamide for castration-resistant prostate cancer. *Cancer* **2016**, *122*, 1897-1904.

(123) Israeli, R. S.; Powell, C. T.; Corr, J. G.; Fair, W. R.; Heston, W. D. Expression of the prostate-specific membrane antigen. *Cancer research* **1994**, *54*, 1807-1811.

(124) Wright, G. L.; Grob, B. M.; Haley, C.; Grossman, K.; Newhall, K.; Petrylak, D.; Troyer, J.; Konchuba, A.; Schellhammer, P. F.; Moriarty, R. Upregulation of prostate-specific membrane antigen after androgen-deprivation therapy. *Urology* **1996**, *48*, 326-334.

(125) Silver, D. A.; Pellicer, I.; Fair, W. R.; Heston, W.; Cordon-Cardo, C. Prostate-specific membrane antigen expression in normal and malignant human tissues. *Clinical Cancer Research* **1997**, *3*, 81-85.

(126) Wright, G. L.; Haley, C.; Beckett, M. L.; Schellhammer, P. F. In *Tilte*1995; Elsevier.

(127) Murphy, G. P.; Barren, R. J.; Erickson, S. J.; Bowes, V. A.; Wolfert, R. L.; Bartsch, G.; Klocker, H.; Pointner, J.; Reissigl, A.; McLeod, D. G. Evaluation and comparison of two new prostate carcinoma markers: Free-prostate specific antigen and prostate specific membrane antigen. *Cancer* **1996**, *78*, 809-818.

(128) Gordon, I. O.; Tretiakova, M. S.; Noffsinger, A. E.; Hart, J.; Reuter, V. E.; Al-Ahmadie, H. A. Prostate-specific membrane antigen expression in regeneration and repair. *Modern Pathology* **2008**, *21*, 1421-1427.

(129) Evans, J. C.; Malhotra, M.; Cryan, J. F.; O'driscoll, C. M. The therapeutic and diagnostic potential of the prostate specific membrane antigen/glutamate carboxypeptidase II (PSMA/GCPII) in cancer and neurological disease. *British journal of pharmacology* **2016**.

(130) Rahn, K. A.; Watkins, C. C.; Alt, J.; Rais, R.; Stathis, M.; Grishkan, I.; Crainiceau, C. M.; Pomper, M. G.; Rojas, C.; Pletnikov, M. V. Inhibition of glutamate carboxypeptidase II (GCPII) activity as a treatment for cognitive impairment in multiple sclerosis. *Proceedings of the National Academy of Sciences* **2012**, *109*, 20101-20106.

(131) Ghadge, G. D.; Slusher, B. S.; Bodner, A.; Dal Canto, M.; Wozniak, K.; Thomas, A. G.; Rojas, C.; Tsukamoto, T.; Majer, P.; Miller, R. J. Glutamate carboxypeptidase II inhibition protects motor neurons from death in familial amyotrophic lateral sclerosis models. *Proceedings of the National Academy of Sciences* **2003**, *100*, 9554-9559.

(132) Bostwick, D. G.; Pacelli, A.; Blute, M.; Roche, P.; Murphy, G. P. Prostate specific membrane antigen expression in prostatic intraepithelial neoplasia and adenocarcinoma. *Cancer* **1998**, *82*, 2256-2261.

(133) Jemaa, A. B.; Bouraoui, Y.; Sallami, S.; Banasr, A.; Rais, N. B.; Ouertani, L.; Nouira, Y.; Horchani, A.; Oueslati, R. Co-expression and impact of prostate specific membrane antigen and prostate specific antigen in prostatic pathologies. *Journal of Experimental & Clinical Cancer Research* **2010**, *29*, 1.

(134) Sweat, S. D.; Pacelli, A.; Murphy, G. P.; Bostwick, D. G. Prostate-specific membrane antigen expression is greatest in prostate adenocarcinoma and lymph node metastases. *Urology* **1998**, *52*, 637-640.

(135) Perner, S.; Hofer, M. D.; Kim, R.; Shah, R. B.; Li, H.; Möller, P.; Hautmann, R. E.; Gschwend, J. E.; Kuefer, R.; Rubin, M. A. Prostate-specific membrane antigen expression as a predictor of prostate cancer progression. *Human pathology* **2007**, *38*, 696-701.

(136) Tsourlakis, M. C.; Klein, F.; Kluth, M.; Quaas, A.; Graefen, M.; Haese, A.; Simon, R.; Sauter, G.; Schlomm, T.; Minner, S. PSMA expression is highly homogenous in primary prostate cancer. *Applied Immunohistochemistry & Molecular Morphology* **2015**, *23*, 449-455.

(137) Ross, J. S.; Sheehan, C. E.; Fisher, H. A.; Kaufman, R. P.; Kaur, P.; Gray, K.; Webb, I.; Gray, G. S.; Mosher, R.; Kallakury, B. V. Correlation of primary tumor prostate-specific membrane antigen expression with disease recurrence in prostate cancer. *Clinical cancer research* **2003**, *9*, 6357-6362.

(138) Watt, F.; Martorana, A.; Brookes, D. E.; Ho, T.; Kingsley, E.; O'Keefe, D. S.; Russell, P. J.; Heston, W. D.; Molloy, P. L. A tissue-specific enhancer of the prostate-specific membrane antigen gene, FOLH1. *Genomics* **2001**, *73*, 243-254.

(139) Wissenbach, U.; Niemeyer, B. A.; Fixemer, T.; Schneidewind, A.; Trost, C.; Cavalié, A.; Reus, K.; Meese, E.; Bonkhoff, H.; Flockerzi, V. Expression of CaT-like, a novel calcium-selective channel, correlates with the malignancy of prostate cancer. *Journal of Biological Chemistry* **2001**, *276*, 19461-19468.

(140) Kozikowski, A. P.; Nan, F.; Conti, P.; Zhang, J.; Ramadan, E.; Bzdega, T.; Wroblewska, B.; Neale, J. H.; Pshenichkin, S.; Wroblewski, J. T. Design of remarkably simple, yet potent urea-based inhibitors of glutamate carboxypeptidase II (NAALADase)[1]. *Journal of medicinal chemistry* **2001**, *44*, 298-301.

(141) Zhou, J.; Neale, J. H.; Pomper, M. G.; Kozikowski, A. P. NAAG peptidase inhibitors and their potential for diagnosis and therapy. *Nature Reviews Drug Discovery* **2005**, *4*, 1015-1026.

(142) Kozikowski, A. P.; Zhang, J.; Nan, F.; Petukhov, P. A.; Grajkowska, E.; Wroblewski, J. T.; Yamamoto, T.; Bzdega, T.; Wroblewska, B.; Neale, J. H. Synthesis of urea-based inhibitors as active site probes of glutamate carboxypeptidase II: efficacy as analgesic agents. *Journal of medicinal chemistry* **2004**, *47*, 1729-1738.

(143) Tsukamoto, T.; Majer, P.; Vitharana, D.; Ni, C.; Hin, B.; Lu, X.-C. M.; Thomas, A. G.; Wozniak, K. M.; Calvin, D. C.; Wu, Y. Enantiospecificity of glutamate carboxypeptidase II inhibition. *Journal of medicinal chemistry* **2005**, *48*, 2319-2324.

(144) Majer, P.; Jackson, P. F.; Delahanty, G.; Grella, B. S.; Ko, Y.-S.; Li, W.; Liu, Q.; Maclin, K. M.; Poláková, J.; Shaffer, K. A. Synthesis and biological evaluation of thiol-based inhibitors of glutamate carboxypeptidase II: discovery of an orally active GCP II inhibitor. *Journal of medicinal chemistry* **2003**, *46*, 1989-1996.

(145) Majer, P.; Hin, B.; Stoermer, D.; Adams, J.; Xu, W.; Duvall, B. R.; Delahanty, G.; Liu, Q.; Stathis, M. J.; Wozniak, K. M. Structural optimization of thiol-based inhibitors of glutamate carboxypeptidase II by modification of the P1 'side chain. *Journal of medicinal chemistry* **2006**, *49*, 2876-2885.

(146) Stoermer, D.; Vitharana, D.; Hin, N.; Delahanty, G.; Duvall, B.; Ferraris, D. V.; Grella, B. S.; Hoover, R.; Rojas, C.; Shanholtz, M. K. Design, synthesis, and pharmacological evaluation of glutamate carboxypeptidase II (GCPII) inhibitors based on thioalkylbenzoic acid scaffolds. *Journal of medicinal chemistry* **2012**, *55*, 5922-5932.

(147) Stoermer, D.; Liu, Q.; Hall, M. R.; Flanary, J. M.; Thomas, A. G.; Rojas, C.; Slusher, B. S.; Tsukamoto, T. Synthesis and biological evaluation of hydroxamate-based inhibitors of glutamate carboxypeptidase II. *Bioorganic & medicinal chemistry letters* **2003**, *13*, 2097-2100.

(148) Blank, B. R.; Alayoglu, P.; Engen, W.; Choi, J. K.; Berkman, C. E.; Anderson, M. O. N-Substituted Glutamyl Sulfonamides as Inhibitors of Glutamate Carboxypeptidase II (GCP2). *Chemical biology & drug design* **2011**, *77*, 241-247.

(149) Jackson, P. F.; Tays, K. L.; Maclin, K. M.; Ko, Y.-S.; Li, W.; Vitharana, D.; Tsukamoto, T.; Stoermer, D.; Lu, X.-C. M.; Wozniak, K. Design and pharmacological activity of phosphinic acid based NAALADase inhibitors. *Journal of medicinal chemistry* **2001**, *44*, 4170-4175.

(150) Graham, K.; Lesche, R.; Gromov, A. V.; Böhnke, N.; Schäfer, M.; Hassfeld, J.; Dinkelborg, L.; Kettschau, G. Radiofluorinated derivatives of 2-(phosphonomethyl) pentanedioic acid as inhibitors of prostate specific membrane antigen (PSMA) for the imaging of prostate cancer. *Journal of medicinal chemistry* **2012**, *55*, 9510-9520.

(151) Lesche, R.; Kettschau, G.; Gromov, A. V.; Böhnke, N.; Borkowski, S.; Mönning, U.; Hegele-Hartung, C.; Döhr, O.; Dinkelborg, L. M.; Graham, K. Preclinical evaluation of BAY 1075553, a novel 18F-labelled inhibitor of prostate-specific membrane antigen for PET imaging of prostate cancer. *European journal of nuclear medicine and molecular imaging* **2014**, *41*, 89-101.

(152) Liu, T.; Toriyabe, Y.; Kazak, M.; Berkman, C. E. Pseudoirreversible inhibition of prostate-specific membrane antigen by phosphoramidate peptidomimetics. *Biochemistry* **2008**, *47*, 12658-12660.

(153) Nedrow-Byers, J. R.; Moore, A. L.; Ganguly, T.; Hopkins, M. R.; Fulton, M. D.; Benny, P. D.; Berkman, C. E. PSMA-targeted SPECT agents: Mode of binding effect on in vitro performance. *The Prostate* **2013**, *73*, 355-362.

(154) Novakova, Z.; Cerny, J.; Choy, C. J.; Nedrow, J. R.; Choi, J. K.; Lubkowski, J.; Berkman, C. E.; Barinka, C. Design of composite inhibitors targeting glutamate carboxypeptidase II: the importance of effector functionalities. *FEBS journal* **2016**, *283*, 130-143.

(155) Zhang, A. X.; Murelli, R. P.; Barinka, C.; Michel, J.; Cocleaza, A.; Jorgensen, W. L.; Lubkowski, J.; Spiegel, D. A. A remote arene-binding site on prostate specific membrane antigen revealed by antibody-recruiting small molecules. *Journal of the American Chemical Society* **2010**, *132*, 12711-12716.

(156) Wüstemann, T.; Bauder-Wüst, U.; Schäfer, M.; Eder, M.; Benesova, M.; Leotta, K.; Kratochwil, C.; Haberkorn, U.; Kopka, K.; Mier, W. Design of Internalizing PSMA-specific Glu-ureido-based Radiotherapeuticals. *Theranostics* **2016**, *6*, 1085.

(157) Rong, S.-B.; Zhang, J.; Neale, J. H.; Wroblewski, J. T.; Wang, S.; Kozikowski, A. P. Molecular modeling of the interactions of glutamate carboxypeptidase II with its potent NAAG-based inhibitors. *Journal of medicinal chemistry* **2002**, *45*, 4140-4152.

(158) Barinka, C.; Byun, Y.; Dusich, C. L.; Banerjee, S. R.; Chen, Y.; Castanares, M.; Kozikowski, A. P.; Mease, R. C.; Pomper, M. G.; Lubkowski, J. Interactions between Human Glutamate Carboxypeptidase II and Urea-Based Inhibitors: Structural Characterization†. *Journal of medicinal chemistry* **2008**, *51*, 7737-7743.

(159) Wang, H.; Byun, Y.; Barinka, C.; Pullambhatla, M.; Hyo-eun, C. B.; Fox, J. J.; Lubkowski, J.; Mease, R. C.; Pomper, M. G. Bioisosterism of urea-based GCPII inhibitors: synthesis and structure–activity relationship studies. *Bioorganic & medicinal chemistry letters* **2010**, *20*, 392-397.

(160) Pavlicek, J.; Ptacek, J.; Cerny, J.; Byun, Y.; Skultetyova, L.; Pomper, M. G.; Lubkowski, J.; Barinka, C. Structural characterization of P1'-diversified urea-based inhibitors of glutamate carboxypeptidase II. *Bioorganic & medicinal chemistry letters* **2014**, *24*, 2340-2345.

(161) Barinka, C.; Starkova, J.; Konvalinka, J.; Lubkowski, J. A high-resolution structure of ligand-free human glutamate carboxypeptidase II. *Acta Crystallographica Section F: Structural Biology and Crystallization Communications* **2007**, *63*, 150-153.

(162) Liu, T.; Nedrow-Byers, J. R.; Hopkins, M. R.; Berkman, C. E. Spacer length effects on in vitro imaging and surface accessibility of fluorescent inhibitors of prostate specific membrane antigen. *Bioorganic & medicinal chemistry letters* **2011**, *21*, 7013-7016.

(163) Benešová, M.; Bauder-Wüst, U.; Schäfer, M.; Klika, K. D.; Mier, W.; Haberkorn, U.; Kopka, K.; Eder, M. Linker modification strategies to control the prostate-specific membrane antigen (PSMA)-targeting and pharmacokinetic properties of DOTA-conjugated PSMA inhibitors. *Journal of medicinal chemistry* **2016**, *59*, 1761-1775.

(164) Oliver, A. J.; Wiest, O.; Helquist, P.; Miller, M. J.; Tenniswood, M. Conformational and SAR analysis of NAALADase and PSMA inhibitors. *Bioorganic & medicinal chemistry* **2003**, *11*, 4455-4461.

(165) Ding, P.; Miller, M. J.; Chen, Y.; Helquist, P.; Oliver, A. J.; Wiest, O. Syntheses of conformationally constricted molecules as potential NAALADase/PSMA inhibitors. *Organic letters* **2004**, *6*, 1805-1808.

(166) Tykvart, J.; Schimer, J. í.; Jančařík, A.; Bařinková, J.; Navrátil, V. c.; Starková, J.; Sramkova, K.; Konvalinka, J.; Majer, P.; Šácha, P. Design of highly potent urea-based, exosite-binding inhibitors selective for glutamate carboxypeptidase ii. *Journal of medicinal chemistry* **2015**, *58*, 4357-4363.

(167) Mottet, N.; Bellmunt, J.; Bolla, M.; Briers, E.; Cumberbatch, M. G.; De Santis, M.; Fossati, N.; Gross, T.; Henry, A. M.; Joniau, S. EAU–ESTRO–SIOG Guidelines on Prostate Cancer. Part 1: Screening, Diagnosis, and Local Treatment with Curative Intent. *European Urology* **2016**.

(168) George, A. K.; Turkbey, B.; Valayil, S. G.; Muthigi, A.; Mertan, F.; Kongnyuy, M.; Pinto, P. A. A urologist's perspective on prostate cancer imaging: past, present, and future. *Abdominal Radiology* **2016**, *41*, 805-816.

(169) Maurer, T.; Eiber, M.; Schwaiger, M.; Gschwend, J. E. Current use of PSMA-PET in prostate cancer management. *Nature Reviews Urology* **2016**.

(170) Hövels, A.; Heesakkers, R.; Adang, E.; Jager, G.; Strum, S.; Hoogeveen, Y.; Severens, J.; Barentsz, J. The diagnostic accuracy of CT and MRI in the staging of pelvic lymph nodes in patients with prostate cancer: a meta-analysis. *Clinical radiology* **2008**, *63*, 387-395.

(171) Jadvar, H. Prostate cancer: PET with 18F-FDG, 18F-or 11C-acetate, and 18F-or 11C-choline. *Journal of Nuclear Medicine* **2011**, *52*, 81-89.

(172) Evangelista, L.; Zattoni, F.; Guttilla, A.; Saladini, G.; Zattoni, F.; Colletti, P. M.; Rubello, D. Choline PET or PET/CT and biochemical relapse of prostate cancer: a systematic review and meta-analysis. *Clinical nuclear medicine* **2013**, *38*, 305-314.

(173) Jadvar, H. Imaging evaluation of prostate cancer with 18F-fluorodeoxyglucose PET/CT: utility and limitations. *European journal of nuclear medicine and molecular imaging* **2013**, *40*, 5-10.

(174) Lindenberg, L.; Choyke, P.; Dahut, W. Prostate cancer imaging with novel PET tracers. *Current urology reports* **2016**, *17*, 1-8.

(175) Magill, J.; Pfennig, G.; Dreher, R.; Sóti, Z.: *Karlsruher Nuklidkarte*; Nucleonica, 2015.

(176) Peterson, T. E.; Furenlid, L. R. SPECT detectors: the Anger Camera and beyond. *Physics in medicine and biology* **2011**, *56*, R145.

(177) Holly, T. A.; Abbott, B. G.; Al-Mallah, M.; Calnon, D. A.; Cohen, M. C.; DiFilippo, F. P.; Ficaro, E. P.; Freeman, M. R.; Hendel, R. C.; Jain, D. Single photon-emission computed tomography. *Journal of nuclear cardiology* **2010**, *17*, 941-973.

(178) Cherry, S. R.; Sorenson, J. A.; Phelps, M. E.: *Physics in nuclear medicine*; Elsevier Health Sciences, 2012.

(179) van der Have, F.; Vastenhouw, B.; Ramakers, R. M.; Branderhorst, W.; Krah, J. O.; Ji, C.; Staelens, S. G.; Beekman, F. J. U-SPECT-II: an ultra-high-resolution device for molecular small-animal imaging. *Journal of Nuclear Medicine* **2009**, *50*, 599-605.

(180) Genna, S.; Smith, A. The development of ASPECT, an annular single crystal brain camera for high efficiency SPECT. *IEEE Transactions on Nuclear Science* **1988**, *35*, 654-658.

(181) Phelps, M. E. PET: the merging of biology and imaging into molecular imaging. *The Journal of Nuclear Medicine* **2000**, *41*, 661.

(182) Watabe, H.; Ikoma, Y.; Kimura, Y.; Naganawa, M.; Shidahara, M. PET kinetic analysis—compartmental model. *Annals of nuclear medicine* **2006**, *20*, 583-588.

(183) Turkington, T. G. Introduction to PET instrumentation. *Journal of nuclear medicine technology* **2001**, *29*, 4-11.

(184) Soret, M.; Bacharach, S. L.; Buvat, I. Partial-volume effect in PET tumor imaging. *Journal of Nuclear Medicine* **2007**, *48*, 932-945.

(185) Pomper, M. G.; Musachio, J. L.; Zhang, J.; Scheffel, U.; Zhou, Y.; Hilton, J.; Maini, A.; Dannals, R. F.; Wong, D. F.; Kozikowski, A. P. 11C-MCG: synthesis, uptake selectivity, and primate PET of a probe for glutamate carboxypeptidase II (NAALADase). *Molecular imaging* **2002**, *1*, 15353500200202109.

(186) Foss, C. A.; Mease, R. C.; Fan, H.; Wang, Y.; Ravert, H. T.; Dannals, R. F.; Olszewski, R. T.; Heston, W. D.; Kozikowski, A. P.; Pomper, M. G. Radiolabeled small-molecule ligands for prostate-specific membrane antigen: in vivo imaging in experimental models of prostate cancer. *Clinical cancer research* **2005**, *11*, 4022-4028.

(187) Banerjee, S. R.; Foss, C. A.; Castanares, M.; Mease, R. C.; Byun, Y.; Fox, J. J.; Hilton, J.; Lupold, S. E.; Kozikowski, A. P.; Pomper, M. G. Synthesis and evaluation of technetium-99m-and rhenium-labeled inhibitors of the prostate-specific membrane antigen (PSMA). *Journal of medicinal chemistry* **2008**, *51*, 4504-4517.

(188) Robu, S.; Schottelius, M.; Eiber, M.; Maurer, T.; Gschwend, J.; Schwaiger, M.; Wester, H.-J. Preclinical evaluation and first patient application of 99mTc-PSMA-I&S for SPECT imaging and radioguided surgery in prostate cancer. *Journal of Nuclear Medicine* **2016**, jnumed. 116.178939.

(189) Chen, Y.; Foss, C. A.; Byun, Y.; Nimmagadda, S.; Pullambhatla, M.; Fox, J. J.; Castanares, M.; Lupold, S. E.; Babich, J. W.; Mease, R. C. Radiohalogenated prostate-specific membrane antigen (PSMA)-based ureas as imaging agents for prostate cancer. *Journal of medicinal chemistry* **2008**, *51*, 7933-7943.

(190) Mease, R. C.; Dusich, C. L.; Foss, C. A.; Ravert, H. T.; Dannals, R. F.; Seidel, J.; Prideaux, A.; Fox, J. J.; Sgouros, G.; Kozikowski, A. P. N-[N-[(S)-1, 3-Dicarboxypropyl] carbamoyl]-4-[18F] fluorobenzyl-L-cysteine,[18F] DCFBC: a new imaging probe for prostate cancer. *Clinical Cancer Research* **2008**, *14*, 3036-3043.

(191) Hillier, S. M.; Maresca, K. P.; Femia, F. J.; Marquis, J. C.; Foss, C. A.; Nguyen, N.; Zimmerman, C. N.; Barrett, J. A.; Eckelman, W. C.; Pomper, M. G. Preclinical evaluation of novel glutamate-urea-lysine analogues that target prostate-specific membrane antigen as molecular imaging pharmaceuticals for prostate cancer. *Cancer research* **2009**, *69*, 6932-6940.

(192) Banerjee, S. R.; Pullambhatla, M.; Byun, Y.; Nimmagadda, S.; Green, G.; Fox, J. J.; Horti, A.; Mease, R. C.; Pomper, M. G. 68Ga-labeled inhibitors of prostate-specific membrane antigen (PSMA) for imaging prostate cancer. *Journal of medicinal chemistry* **2010**, *53*, 5333-5341.

(193) Weineisen, M.; Simecek, J.; Schottelius, M.; Schwaiger, M.; Wester, H.-J. Synthesis and preclinical evaluation of DOTAGA-conjugated PSMA ligands for functional imaging and endoradiotherapy of prostate cancer. *EJNMMI research* **2014**, *4*, 63.

(194) Weineisen, M.; Schottelius, M.; Simecek, J.; Baum, R. P.; Yildiz, A.; Beykan, S.; Kulkarni, H. R.; Lassmann, M.; Klette, I.; Eiber, M. 68Ga-and 177Lu-labeled PSMA I&T: optimization of a PSMA-targeted theranostic concept and first proof-of-concept human studies. *Journal of Nuclear Medicine* **2015**, *56*, 1169-1176.

(195) Chen, Y.; Pullambhatla, M.; Foss, C. A.; Byun, Y.; Nimmagadda, S.; Senthamizhchelvan, S.; Sgouros, G.; Mease, R. C.; Pomper, M. G. 2-(3-{1-Carboxy-5-[(6-[18F] fluoro-pyridine-3-carbonyl)-amino]-pentyl}-ureido)-pentanedioic acid,[18F] DCFPyL, a PSMA-based PET imaging agent for prostate cancer. *Clinical Cancer Research* **2011**, *17*, 7645-7653.

(196) Schottelius, M.; Wirtz, M.; Eiber, M.; Maurer, T.; Wester, H.-J. [111 In] PSMA-I&T: expanding the spectrum of PSMA-I&T applications towards SPECT and radioguided surgery. *EJNMMI research* **2015**, *5*, 68.

(197) Kiess, A.; Banerjee, S.; Mease, R.; Rowe, S.; Rao, A.; Foss, C.; Chen, Y.; Yang, X.; Cho, S.; Nimmagadda, S. Prostate-specific membrane antigen as a target for cancer imaging and therapy. *The quarterly journal of nuclear medicine and molecular imaging: official publication of the Italian Association of Nuclear Medicine (AIMN)[and] the International Association of Radiopharmacology (IAR),[and] Section of the Society of...* **2015**, *59*, 241.

(198) Sanford, E.; Grzonka, R.; Heal, A.; Helal, M.; Persky, L.; Tyson, I. Prostate cancer imaging with a new monoclonal antibody: a preliminary report. *Annals of surgical oncology* **1994**, *1*, 400-404.

(199) Eder, M.; Schäfer, M.; Bauder-Wüst, U.; Hull, W.-E.; Wängler, C.; Mier, W.; Haberkorn, U.; Eisenhut, M. 68Ga-complex lipophilicity and the targeting property of a urea-based PSMA inhibitor for PET imaging. *Bioconjugate chemistry* **2012**, *23*, 688-697.

(200) Afshar-Oromieh, A.; Avtzi, E.; Giesel, F. L.; Holland-Letz, T.; Linhart, H. G.; Eder, M.; Eisenhut, M.; Boxler, S.; Hadaschik, B. A.; Kratochwil, C. The diagnostic value of PET/CT imaging with the 68Ga-labelled PSMA ligand HBED-CC in the diagnosis of recurrent prostate cancer. *European journal of nuclear medicine and molecular imaging* **2015**, *42*, 197-209.

(201) Perera, M.; Papa, N.; Christidis, D.; Wetherell, D.; Hofman, M. S.; Murphy, D. G.; Bolton, D.; Lawrentschuk, N. Sensitivity, specificity, and predictors of positive 68 Ga–prostate-specific membrane antigen positron emission tomography in advanced prostate cancer: a systematic review and meta-analysis. *European urology* **2016**, *70*, 926-937.

(202) Maurer, T.; Gschwend, J. E.; Rauscher, I.; Souvatzoglou, M.; Haller, B.; Weirich, G.; Wester, H.-J.; Heck, M.; Kübler, H.; Beer, A. J.; Schwaiger, M.; Eiber, M. Diagnostic Efficacy of 68Gallium-PSMA Positron Emission Tomography Compared to Conventional Imaging for Lymph Node Staging of 130 Consecutive Patients with Intermediate to High Risk Prostate Cancer. *The Journal of Urology* **2016**, *195*, 1436-1443.

(203) Afshar-Oromieh, A.; Zechmann, C. M.; Malcher, A.; Eder, M.; Eisenhut, M.; Linhart, H. G.; Holland-Letz, T.; Hadaschik, B. A.; Giesel, F. L.; Debus, J. Comparison of PET imaging with a 68Ga-labelled PSMA ligand and 18F-choline-based PET/CT for the diagnosis of recurrent prostate cancer. *European journal of nuclear medicine and molecular imaging* **2014**, *41*, 11-20.

(204) Wirtz, M. Development of biomarkers for molecular imaging and endoradiotherapy of prostate cancer. Dissertation, München, Technische Universität München, 2015, 2015.

(205) Kabasakal, L.; AbuQbeitah, M.; Aygün, A.; Yeyin, N.; Ocak, M.; Demirci, E.; Toklu, T. Pre-therapeutic dosimetry of normal organs and tissues of 177Lu-PSMA-617 prostate-specific membrane antigen (PSMA) inhibitor in patients with castration-resistant prostate cancer. *European journal of nuclear medicine and molecular imaging* **2015**, *42*, 1976-1983.

(206) Benešová, M.; Schäfer, M.; Bauder-Wüst, U.; Afshar-Oromieh, A.; Kratochwil, C.; Mier, W.; Haberkorn, U.; Kopka, K.; Eder, M. Preclinical evaluation of a tailor-made DOTA-conjugated PSMA inhibitor with optimized linker moiety for imaging and endoradiotherapy of prostate cancer. *Journal of Nuclear Medicine* **2015**, *56*, 914-920.

(207) Afshar-Oromieh, A.; Hetzheim, H.; Kratochwil, C.; Benesova, M.; Eder, M.; Neels, O. C.; Eisenhut, M.; Kübler, W.; Holland-Letz, T.; Giesel, F. L. The theranostic PSMA ligand PSMA-617 in the diagnosis of prostate cancer by PET/CT: biodistribution in humans, radiation dosimetry, and first evaluation of tumor lesions. *Journal of Nuclear Medicine* **2015**, *56*, 1697-1705.

(208) Szabo, Z.; Mena, E.; Rowe, S. P.; Plyku, D.; Nidal, R.; Eisenberger, M. A.; Antonarakis, E. S.; Fan, H.; Dannals, R. F.; Chen, Y. Initial evaluation of [18F] DCFPyL for prostate-specific membrane antigen (PSMA)-targeted PET imaging of prostate cancer. *Molecular Imaging and Biology* **2015**, *17*, 565-574.

(209) Dietlein, M.; Kobe, C.; Kuhnert, G.; Stockter, S.; Fischer, T.; Schomäcker, K.; Schmidt, M.; Dietlein, F.; Zlatopolskiy, B. D.; Krapf, P. Comparison of [18F] DCFPyL and [68Ga] Ga-PSMA-HBED-CC for PSMA-PET imaging in patients with relapsed prostate cancer. *Molecular Imaging and Biology* **2015**, *17*, 575-584.

(210) Cardinale, J.; Schäfer, M.; Benešová, M.; Bauder-Wüst, U.; Leotta, K.; Eder, M.; Neels, O. C.; Haberkorn, U.; Giesel, F. L.; Kopka, K. Preclinical Evaluation of 18F-PSMA-1007, a New Prostate-Specific Membrane Antigen Ligand for Prostate Cancer Imaging. *Journal of Nuclear Medicine* **2017**, *58*, 425-431.

(211) Giesel, F. L.; Hadaschik, B.; Cardinale, J.; Radtke, J.; Vinsensia, M.; Lehnert, W.; Kesch, C.; Tolstov, Y.; Singer, S.; Grabe, N. F-18 labelled PSMA-1007: biodistribution, radiation dosimetry and histopathological validation of tumor lesions in prostate cancer patients. *European Journal of Nuclear Medicine and Molecular Imaging* **2016**, 1-11.

(212) Kirby, M.; Hirst, C.; Crawford, E. Characterising the castration-resistant prostate cancer population: a systematic review. *International journal of clinical practice* **2011**, *65*, 1180-1192.

(213) Basch, E.; Loblaw, D. A.; Oliver, T. K.; Carducci, M.; Chen, R. C.; Frame, J. N.; Garrels, K.; Hotte, S.; Kattan, M. W.; Raghavan, D. Systemic therapy in men with metastatic castration-resistant prostate cancer: American Society of Clinical Oncology and Cancer Care Ontario clinical practice guideline. *Journal of Clinical Oncology* **2014**, *32*, 3436-3448.

(214) Krebsgesellschaft, D.; Deutsche Krebshilfe, A.: Leitlinienprogramm Onkologie. Interdisziplinäre Leitlinie der Qualität S3 zur Früherkennung, Diagnose und Therapie der verschiedenen Stadien des Prostatakarzinoms, Langversion 3.1, 2014 AWMF Registernummer: 034/022OL. 2016.

(215) Kulkarni, H. R.; Singh, A.; Schuchardt, C.; Niepsch, K.; Sayeg, M.; Leshch, Y.; Wester, H.-J.; Baum, R. P. PSMA-Based Radioligand Therapy for Metastatic Castration-Resistant Prostate Cancer: The Bad Berka Experience Since 2013. *Journal of Nuclear Medicine* **2016**, *57*, 97S-104S.

(216) Kratochwil, C.; Giesel, F. L.; Stefanova, M.; Benešová, M.; Bronzel, M.; Afshar-Oromieh, A.; Mier, W.; Eder, M.; Kopka, K.; Haberkorn, U. PSMA-targeted radionuclide therapy of metastatic castration-resistant prostate cancer with 177Lu-labeled PSMA-617. *Journal of Nuclear Medicine* **2016**, *57*, 1170-1176.

(217) Cremonesi, M.; Ferrari, M.; Bodei, L.; Tosi, G.; Paganelli, G. Dosimetry in peptide radionuclide receptor therapy: a review. *Journal of nuclear medicine* **2006**, *47*, 1467-1475.

(218) Imam, S. K. Advancements in cancer therapy with alpha-emitters: a review. *International Journal of Radiation Oncology* Biology* Physics* **2001**, *51*, 271-278.

(219) Ahmadzadehfar, H.; Eppard, E.; Kürpig, S.; Fimmers, R.; Yordanova, A.; Schlenkhoff, C. D.; Gärtner, F.; Rogenhofer, S.; Essler, M. Therapeutic response and side effects of repeated radioligand therapy with 177Lu-PSMA-DKFZ-617 of castrate-resistant metastatic prostate cancer. *Oncotarget* **2016**, *7*, 12477.

(220) Baum, R. P.; Kulkarni, H. R.; Schuchardt, C.; Singh, A.; Wirtz, M.; Wiessalla, S.; Schottelius, M.; Mueller, D.; Klette, I.; Wester, H.-J. 177Lu-labeled prostate-specific membrane antigen radioligand therapy of metastatic castration-resistant prostate cancer: safety and efficacy. *Journal of Nuclear Medicine* **2016**, *57*, 1006-1013.

(221) Kratochwil, C.; Bruchertseifer, F.; Giesel, F. L.; Weis, M.; Verburg, F. A.; Mottaghy, F.; Kopka, K.; Apostolidis, C.; Haberkorn, U.; Morgenstern, A. 225Ac-PSMA-617 for PSMA targeting alpha-radiation therapy of patients with metastatic castration-resistant prostate cancer. *Journal of Nuclear Medicine* **2016**.

(222) Kratochwil, C.; Bruchertseifer, F.; Giesel, F. L.; Weis, M.; Verburg, F. A.; Mottaghy, F.; Kopka, K.; Apostolidis, C.; Haberkorn, U.; Morgenstern, A. 225Ac-PSMA-617 for PSMA-targeted α-radiation therapy of metastatic castration-resistant prostate cancer. *Journal of Nuclear Medicine* **2016**, *57*, 1941-1944.

(223) Okamoto, S.; Thieme, A.; Allmann, J.; D'Alessandria, C.; Maurer, T.; Retz, M.; Tauber, R.; Heck, M. M.; Wester, H.-J.; Tamaki, N.; Fendler, W. P.; Herrmann, K.; Pfob, C. H.; Scheidhauer, K.; Schwaiger, M.; Ziegler, S.; Eiber, M. Radiation Dosimetry for 177Lu-PSMA I&T in Metastatic Castration-

Resistant Prostate Cancer: Absorbed Dose in Normal Organs and Tumor Lesions. *Journal of Nuclear Medicine* **2017**, *58*, 445-450.

(224) Weineisen, M.; Schottelius, M.; Simecek, J.; Eiber, M.; Schwaiger, M.; Wester, H. Development and first in human evaluation of PSMA I&T-A ligand for diagnostic imaging and endoradiotherapy of prostate cancer. *Journal of Nuclear Medicine* **2014**, *55*, 1083-1083.

(225) Weineisen, M.; Schottelius, M.; Simecek, J.; Baum, R. P.; Yildiz, A.; Beykan, S.; Kulkarni, H. R.; Lassmann, M.; Klette, I.; Eiber, M.; Schwaiger, M.; Wester, H.-J. 68Ga- and 177Lu-Labeled PSMA I&T: Optimization of a PSMA-Targeted Theranostic Concept and First Proof-of-Concept Human Studies. *Journal of Nuclear Medicine* **2015**, *56*, 1169-1176.

(226) Smith, D. A.; Di, L.; Kerns, E. H. The effect of plasma protein binding on in vivo efficacy: misconceptions in drug discovery. *Nature Reviews Drug Discovery* **2010**, *9*, 929-939.

(227) Trainor, G. L. The importance of plasma protein binding in drug discovery. *Expert opinion on drug discovery* **2007**, *2*, 51-64.

(228) Trainor, G. L. Plasma protein binding and the free drug principle: recent developments and applications. *Annual reports in medicinal chemistry* **2007**, *42*, 489-502.

(229) Müller, C.; Struthers, H.; Winiger, C.; Zhernosekov, K.; Schibli, R. DOTA Conjugate with an Albumin-Binding Entity Enables the First Folic Acid–Targeted 177Lu-Radionuclide Tumor Therapy in Mice. *Journal of Nuclear Medicine* **2013**, *54*, 124-131.

(230) Kelly, J. M.; Amor-Coarasa, A.; Nikolopoulou, A.; Wüstemann, T.; Barelli, P.; Kim, D.; Williams, C.; Zheng, X.; Bi, C.; Hu, B. Double Targeting Ligands with Modulated Pharmacokinetics for Endoradiotherapy of Prostate Cancer. *Journal of Nuclear Medicine* **2017**, jnumed. 116.188722.

(231) Osl, T. M. Development of cyclic pentapeptide ligands for chemokine receptor targeting. Dissertation, München, Technische Universität München, 2017, 2017, unpublished.

(232) Schottelius, M.; Osl, T.; Poschenrieder, A.; Hoffmann, F.; Beykan, S.; Hänscheid, H.; Schirbel, A.; Buck, A. K.; Kropf, S.; Schwaiger, M. [177Lu] pentixather: Comprehensive Preclinical Characterization of a First CXCR4-directed Endoradiotherapeutic Agent. *Theranostics* **2017**, *7*, 2350.

(233) Šimeček, J.; Zemek, O.; Hermann, P.; Wester, H. J.; Notni, J. A Monoreactive Bifunctional Triazacyclononane Phosphinate Chelator with High Selectivity for Gallium-68. *ChemMedChem* **2012**, *7*, 1375-1378.

(234) Weineisen, M.; Simecek, J.; Schottelius, M.; Schwaiger, M.; Wester, H.-J. Synthesis and preclinical evaluation of DOTAGA-conjugated PSMA ligands for functional imaging and endoradiotherapy of prostate cancer. *EJNMMI research* **2014**, *4*, 1.

(235) Herzig, J.; Nudelman, A.; Gottlieb, H. E.; Fischer, B. Studies in sugar chemistry. 2. A simple method for O-deacylation of polyacylated sugars. *The Journal of Organic Chemistry* **1986**, *51*, 727-730.

(236) Elofsson, M.; Walse, B.; Kihlberg, J. Building blocks for glycopeptide synthesis: glycosylation of 3-mercaptopropionic acid and Fmoc amino acids with unprotected carboxyl groups. *Tetrahedron letters* **1991**, *32*, 7613-7616.

(237) Kihlberg, J.; Elofsson, M.; Salvador, L. A.: [11] Direct synthesis of glycosylated amino acids from carbohydrate peracetates and Fmoc amino acids: Solid-phase synthesis of biomedicinally interesting glycopeptides. In *Methods in Enzymology*; Academic Press, 1997; Vol. Volume 289; pp 221-245.

(238) Schottelius, M.; Reubi, J. C.; Eltschinger, V.; Schwaiger, M.; Wester, H.-J. N-Terminal Sugar Conjugation and C-Terminal Thr-for-Thr(ol) Exchange in Radioiodinated Tyr3-octreotide: Effect on Cellular Ligand Trafficking in Vitro and Tumor Accumulation in Vivo. *Journal of Medicinal Chemistry* **2005**, *48*, 2778-2789.

(239) Maresca, K.; Hillier, S.; Femia, F.; Keith, D.; Barone, C.; Joyal, J.; Zimmerman, C.; Kozikowski, A. P.; Barrett, J.; Eckelman, W. A series of halogenated heterodimeric inhibitors of prostate specific membrane antigen (PSMA) as radiolabeled probes for targeting prostate cancer. *Journal of medicinal chemistry* **2008**, *52*, 347-357.

(240) Vaidyanathan, G.; Zalutsky, M. R. Preparation of N-succinimidyl 3-[* I] iodobenzoate: an agent for the indirect radioiodination of proteins. *Nature protocols* **2006**, *1*, 707-713.

(241) Dekker, B.; Keen, H.; Shaw, D.; Disley, L.; Hastings, D.; Hadfield, J.; Reader, A.; Allan, D.; Julyan, P.; Watson, A. Functional comparison of annexin V analogues labeled indirectly and directly with iodine-124. *Nuclear medicine and biology* **2005**, *32*, 403-413.

(242) Porcheddu, A.; Giacomelli, G.; Piredda, I.; Carta, M.; Nieddu, G. A Practical and Efficient Approach to PNA Monomers Compatible with Fmoc-Mediated Solid-Phase Synthesis Protocols. *European Journal of Organic Chemistry* **2008**, *2008*, 5786-5797.

(243) Sosabowski, J. K.; Mather, S. J. Conjugation of DOTA-like chelating agents to peptides and radiolabeling with trivalent metallic isotopes. *Nat. Protocols* **2006**, *1*, 972-976.

(244) Valko, K.; Nunhuck, S.; Bevan, C.; Abraham, M. H.; Reynolds, D. P. Fast gradient HPLC method to determine compounds binding to human serum albumin. Relationships with octanol/water and immobilized artificial membrane lipophilicity. *Journal of pharmaceutical sciences* **2003**, *92*, 2236-2248.

(245) Yamazaki, K.; Kanaoka, M. Computational prediction of the plasma protein-binding percent of diverse pharmaceutical compounds. *Journal of pharmaceutical sciences* **2004**, *93*, 1480-1494.

(246) Kruger, N. J. The Bradford method for protein quantitation. *Basic protein and peptide protocols* **1994**, 9-15.

(247) Johanning, K.; Hancock, G.; Escher, B.; Adekola, A.; Bernhard, M. J.; Cowan-Ellsberry, C.; Domoradzki, J.; Dyer, S.; Eickhoff, C.; Embry, M. Assessment of metabolic stability using the rainbow trout (Oncorhynchus mykiss) liver S9 fraction. *Current Protocols in Toxicology* **2012**, 14.10. 11-14.10. 28.

(248) Chatalic, K. L.; Heskamp, S.; Konijnenberg, M.; Molkenboer-Kuenen, J. D.; Franssen, G. M.; Clahsen-van Groningen, M. C.; Schottelius, M.; Wester, H.-J.; van Weerden, W. M.; Boerman, O. C. Towards personalized treatment of prostate cancer: PSMA I&T, a promising prostate-specific membrane antigen-targeted theranostic agent. *Theranostics* **2016**, *6*, 849.

(249) Hlouchová, K.; Bařinka, C.; Klusák, V.; Šácha, P.; Mlčochová, P.; Majer, P.; Rulíšek, L.; Konvalinka, J. Biochemical characterization of human glutamate carboxypeptidase III. *Journal of neurochemistry* **2007**, *101*, 682-696.

(250) Barinka, C.; Byun, Y.; Dusich, C. L.; Banerjee, S. R.; Chen, Y.; Castanares, M.; Kozikowski, A. P.; Mease, R. C.; Pomper, M. G.; Lubkowski, J. Interactions between human glutamate carboxypeptidase II and urea-based inhibitors: structural characterization. *Journal of medicinal chemistry* **2008**, *51*, 7737-7743.

(251) Barinka, C.; Rovenská, M.; Mlčochová, P.; Hlouchová, K.; Plechanovová, A.; Majer, P.; Tsukamoto, T.; Slusher, B. S.; Konvalinka, J.; Lubkowski, J. Structural Insight into the Pharmacophore Pocket of Human Glutamate Carboxypeptidase II⊥. *Journal of medicinal chemistry* **2007**, *50*, 3267-3273.

(252) Huang, S. S.; Wang, X.; Zhang, Y.; Doke, A.; DiFilippo, F. P.; Heston, W. D. Improving the biodistribution of PSMA-targeting tracers with a highly negatively charged linker. *The Prostate* **2014**, *74*, 702-713.

(253) London, N.; Movshovitz-Attias, D.; Schueler-Furman, O. The structural basis of peptide-protein binding strategies. *Structure* **2010**, *18*, 188-199.

(254) Ermondi, G.; Lorenti, M.; Caron, G. Contribution of Ionization and Lipophilicity to Drug Binding to Albumin: A Preliminary Step toward Biodistribution Prediction. *Journal of Medicinal Chemistry* **2004**, *47*, 3949-3961.

(255) Zhang, Z.; Zhu, Z.; Yang, D.; Fan, W.; Wang, J.; Li, X.; Chen, X.; Wang, Q.; Song, X. Preparation and affinity identification of glutamic acid-urea small molecule analogs in prostate cancer. *Oncology Letters* **2016**, *12*, 1001-1006.

(256) García Garayoa, E.; Schweinsberg, C.; Maes, V.; Brans, L.; Bläuenstein, P.; Tourwé, D. A.; Schibli, R.; Schubiger, P. A. Influence of the molecular charge on the biodistribution of bombesin analogues labeled with the [99mTc (CO) 3]-core. *Bioconjugate chemistry* **2008**, *19*, 2409-2416.

(257) Baum, R. P.; Kulkarni, H. R.; Schuchardt, C.; Singh, A.; Wirtz, M.; Wiessalla, S.; Schottelius, M.; Mueller, D.; Klette, I.; Wester, H.-J. Lutetium-177 PSMA radioligand therapy of

metastatic castration-resistant prostate cancer: safety and efficacy. *Journal of Nuclear Medicine* **2016**, jnumed. 115.168443.

(258) Prasad, V.; Bodei, L.; Kidd, M.; Modlin, I. M. Whither peptide receptor radionuclide therapy for neuroendocrine tumors: an Einsteinian view of the facts and myths. *European Journal of Nuclear Medicine and Molecular Imaging* **2014**, *41*, 1825-1830.

(259) Richter, S.; Wuest, M.; Bergman, C. N.; Way, J. D.; Krieger, S.; Rogers, B. E.; Wuest, F. Rerouting the metabolic pathway of 18F-labeled peptides: the influence of prosthetic groups. *Bioconjugate chemistry* **2015**, *26*, 201-212.

(260) Schottelius, M.; Rau, F.; Reubi, J. C.; Schwaiger, M.; Wester, H.-J. Modulation of pharmacokinetics of radioiodinated sugar-conjugated somatostatin analogues by variation of peptide net charge and carbohydration chemistry. *Bioconjugate chemistry* **2005**, *16*, 429-437.

(261) Schottelius, M.; Wester, H.-J.; Reubi, J. C.; Senekowitsch-Schmidtke, R.; Schwaiger, M. Improvement of pharmacokinetics of radioiodinated Tyr3-octreotide by conjugation with carbohydrates. *Bioconjugate chemistry* **2002**, *13*, 1021-1030.

(262) Suzuki, K.; Susaki, H.; Okuno, S.; Yamada, H.; Watanabe, H. K.; Sugiyama, Y. Specific renal delivery of sugar-modified low-molecular-weight peptides. *Journal of Pharmacology and Experimental Therapeutics* **1999**, *288*, 888-897.

(263) Barinka, C.; Hlouchova, K.; Rovenska, M.; Majer, P.; Dauter, M.; Hin, N.; Ko, Y.-S.; Tsukamoto, T.; Slusher, B. S.; Konvalinka, J. Structural basis of interactions between human glutamate carboxypeptidase II and its substrate analogs. *Journal of molecular biology* **2008**, *376*, 1438-1450.

(264) Tucker, G. Measurement of the renal clearance of drugs. *British journal of clinical pharmacology* **1981**, *12*, 761-770.

(265) Wang, X.; Tian, H.; Lee, Z.; Heston, W. D. Structure-activity relationships of 2', 5'-oligoadenylate analogue modifications of prostate-specific membrane antigen (PSMA) antagonists. *Nucleosides, Nucleotides and Nucleic Acids* **2012**, *31*, 432-444.

(266) Baranyai, Z.; Reich, D.; Vágner, A.; Weineisen, M.; Tóth, I.; Wester, H.-J.; Notni, J. A shortcut to high-affinity Ga-68 and Cu-64 radiopharmaceuticals: one-pot click chemistry trimerisation on the TRAP platform. *Dalton Transactions* **2015**, *44*, 11137-11146.

(267) Kassis, A. I.; Adelstein, S. J. Radiobiologic principles in radionuclide therapy. *Journal of Nuclear Medicine* **2005**, *46*, 4S-12S.

(268) Shuryak, I. Mechanistic Modeling of Dose and Dose Rate Dependences of Radiation-Induced DNA Double Strand Break Rejoining Kinetics in Saccharomyces cerevisiae. *PLOS ONE* **2016**, *11*, e0146407.

(269) Lomax, M. E.; Folkes, L. K.; O'Neill, P. Biological Consequences of Radiation-induced DNA Damage: Relevance to Radiotherapy. *Clinical Oncology* **2013**, *25*, 578-585.

(270) Kuhnast, B.; Bodenstein, C.; Haubner, R.; Wester, H.; Senekowitsch-Schmidtke, R.; Schwaiger, M.; Weber, W. Targeting of gelatinase activity with a radiolabeled cyclic HWGF peptide. *Nuclear medicine and biology* **2004**, *31*, 337-344.

(271) Koenig, J.; Edwardson, J.; Humphrey, P. Somatostatin receptors in Neuro2A neuroblastoma cells: ligand internalization. *British journal of pharmacology* **1997**, *120*, 52-59.

(272) Bunnett, N. W.; Reeve Jr, J. R.; Walsh, J. H. Catabolism of bombesin in the interstitial fluid of the rat stomach. *Neuropeptides* **1983**, *4*, 55-64.

(273) KOENIG, J. A.; Rejbinder, K.; DODGEON, I.; EDWARDSON, J. M.; HUMPHREY, P. P. Fates of endocytosed somatostatin sst2 receptors and associated agonists. *Biochemical Journal* **1998**, *336*, 291-298.

(274) Rusnak, D. W.; Lai, Z.; Lansing, T. J.; Rhodes, N.; Gilmer, T. M.; Copeland, R. A. A simple method for predicting serum protein binding of compounds from IC 50 shift analysis for in vitro assays. *Bioorganic & medicinal chemistry letters* **2004**, *14*, 2309-2312.

(275) Olsson, T. S.; Williams, M. A.; Pitt, W. R.; Ladbury, J. E. The thermodynamics of protein–ligand interaction and solvation: insights for ligand design. *Journal of molecular biology* **2008**, *384*, 1002-1017.

(276) Robinson, J. M.; Philp, D.; Harris, K. D.; Kariuki, B. M. Weak interactions in crystal engineering—understanding the recognition properties of the nitro group. *New Journal of Chemistry* **2000**, *24*, 799-806.

(277) Cockroft, S. L.; Hunter, C. A.; Lawson, K. R.; Perkins, J.; Urch, C. J. Electrostatic Control of Aromatic Stacking Interactions. *Journal of the American Chemical Society* **2005**, *127*, 8594-8595.

(278) Cockroft, S. L.; Perkins, J.; Zonta, C.; Adams, H.; Spey, S. E.; Low, C. M.; Vinter, J. G.; Lawson, K. R.; Urch, C. J.; Hunter, C. A. Substituent effects on aromatic stacking interactions. *Organic & biomolecular chemistry* **2007**, *5*, 1062-1080.

(279) Varma, M. V.; Feng, B.; Obach, R. S.; Troutman, M. D.; Chupka, J.; Miller, H. R.; El-Kattan, A. Physicochemical determinants of human renal clearance. *Journal of medicinal chemistry* **2009**, *52*, 4844-4852.

(280) Poschenrieder, A.; Schottelius, M.; Schwaiger, M.; Kessler, H.; Wester, H.-J. The influence of different metal-chelate conjugates of pentixafor on the CXCR4 affinity. *EJNMMI research* **2016**, *6*, 36.

(281) Poschenrieder, A.; Osl, T.; Schottelius, M.; Hoffmann, F.; Wirtz, M.; Schwaiger, M.; Wester, H.-J. First 18F-labeled pentixafor-based imaging agent for PET imaging of CXCR4 expression in vivo. *Tomography* **2016**, *2*, 85-93.

(282) Poschenrieder, A.; Schottelius, M.; Schwaiger, M.; Wester, H.-J. Preclinical evaluation of [68 Ga] NOTA-pentixafor for PET imaging of CXCR4 expression in vivo—a comparison to [68 Ga] pentixafor. *EJNMMI research* **2016**, *6*, 70.

(283) Poschenrieder, A.; Schottelius, M.; Osl, T.; Schwaiger, M.; Wester, H.-J. [64Cu] NOTA-pentixather enables high resolution PET imaging of CXCR4 expression in a preclinical lymphoma model. *EJNMMI Radiopharmacy and Chemistry* **2017**, *2*, 2.

(284) Reubi, J. C.; Erchegyi, J.; Cescato, R.; Waser, B.; Rivier, J. E. Switch from antagonist to agonist after addition of a DOTA chelator to a somatostatin analog. *European journal of nuclear medicine and molecular imaging* **2010**, *37*, 1551-1558.

(285) Yang, X.; Mease, R. C.; Pullambhatla, M.; Lisok, A.; Chen, Y.; Foss, C. A.; Wang, Y.; Shallal, H.; Edelman, H.; Hoye, A. T. [18F] fluorobenzoyllysinepentanedioic acid carbamates: new scaffolds for positron emission tomography (PET) imaging of prostate-specific membrane antigen (PSMA). *Journal of medicinal chemistry* **2016**, *59*, 206.

(286) Benešová, M.; Bauder-Wüst, U.; Schäfer, M.; Klika, K. D.; Mier, W.; Haberkorn, U.; Kopka, K.; Eder, M. Linker Modification Strategies To Control the Prostate-Specific Membrane Antigen (PSMA)-Targeting and Pharmacokinetic Properties of DOTA-Conjugated PSMA Inhibitors. *Journal of Medicinal Chemistry* **2016**, *59*, 1761-1775.

(287) Young, J. D.; Abbate, V.; Imberti, C.; Meszaros, L. K.; Ma, M. T.; Terry, S. Y.; Hider, R. C.; Mullen, G. E.; Blower, P. J. 68Ga-THP-PSMA: a PET imaging agent for prostate cancer offering rapid, room temperature, one-step kit-based radiolabeling. *Journal of Nuclear Medicine* **2017**, jnumed. 117.191882.

(288) Simon, E. Mechanisms of dinitrophenol toxicity. *Biological Reviews* **1953**, *28*, 453-478.

(289) Grundlingh, J.; Dargan, P. I.; El-Zanfaly, M.; Wood, D. M. 2, 4-dinitrophenol (DNP): a weight loss agent with significant acute toxicity and risk of death. *Journal of Medical Toxicology* **2011**, *7*, 205-212.

(290) She, Z.; Gao, M.; Jin, C.; Chen, Y.; Yu, J. Toxicity and biodegradation of 2, 4-dinitrophenol and 3-nitrophenol in anaerobic systems. *Process Biochemistry* **2005**, *40*, 3017-3024.

(291) Rickert, D. E. Metabolism of nitroaromatic compounds. *Drug metabolism reviews* **1987**, *18*, 23-53.

(292) Akizawa, H.; Uehara, T.; Arano, Y. Renal uptake and metabolism of radiopharmaceuticals derived from peptides and proteins. *Advanced drug delivery reviews* **2008**, *60*, 1319-1328.

(293) Haubner, R.; Kuhnast, B.; Mang, C.; Weber, W. A.; Kessler, H.; Wester, H.-J.; Schwaiger, M. [18F] Galacto-RGD: synthesis, radiolabeling, metabolic stability, and radiation dose estimates. *Bioconjugate chemistry* **2004**, *15*, 61-69.

(294) Tatsi, A.; Maina, T.; Cescato, R.; Waser, B.; Krenning, E. P.; de Jong, M.; Cordopatis, P.; Reubi, J. C.; Nock, B. A. [111 In-DOTA] Somatostatin-14 analogs as potential pansomatostatin-like radiotracers-first results of a preclinical study. *EJNMMI research* **2012**, *2*, 25.

(295) Maina, T.; Cescato, R.; Waser, B.; Tatsi, A.; Kaloudi, A.; Krenning, E. P.; de Jong, M.; Nock, B. A.; Reubi, J. C. [111In-DOTA] LTT-SS28, a first pansomatostatin radioligand for in vivo targeting of somatostatin receptor-positive tumors. *Journal of medicinal chemistry* **2014**, *57*, 6564-6571.

(296) Powell, M. F.; Stewart, T.; Urge, L.; Gaeta, F. C.; Sette, A.; Arrhenius, T.; Thomson, D.; Soda, K.; Colon, S. M. Peptide stability in drug development. II. Effect of single amino acid substitution and glycosylation on peptide reactivity in human serum. *Pharmaceutical research* **1993**, *10*, 1268-1273.

(297) Suzuki, K.; Susaki, H.; Okuno, S.; Sugiyama, Y. Renal drug targeting using a vector "alkylglycoside". *Journal of Pharmacology and Experimental Therapeutics* **1999**, *288*, 57-64.

(298) Hong, S. Y.; Oh, J. E.; Lee, K.-H. Effect of D-amino acid substitution on the stability, the secondary structure, and the activity of membrane-active peptide. *Biochemical pharmacology* **1999**, *58*, 1775-1780.

(299) Workman, P.; Aboagye, E.; Balkwill, F.; Balmain, A.; Bruder, G.; Chaplin, D.; Double, J.; Everitt, J.; Farningham, D.; Glennie, M. Guidelines for the welfare and use of animals in cancer research. *British journal of cancer* **2010**, *102*, 1555-1577.

(300) Plant, N. Strategies for using in vitro screens in drug metabolism. *Drug discovery today* **2004**, *9*, 328-336.

(301) Kruger, N. J. The Bradford method for protein quantitation. *The protein protocols handbook* **2009**, 17-24.

(302) Olson, B. J.; Markwell, J. Assays for determination of protein concentration. *Current protocols in protein science* **2007**, 3.4. 1-3.4. 29.

(303) J Richardson, S.; Bai, A.; A Kulkarni, A.; F Moghaddam, M. Efficiency in drug discovery: liver S9 fraction assay as a screen for metabolic stability. *Drug metabolism letters* **2016**, *10*, 83-90.

(304) Förlin, L.; Andersson, T. Storage conditions of rainbow trout liver cytochrome P-450 and conjugating enzymes. *Comparative Biochemistry and Physiology Part B: Comparative Biochemistry* **1985**, *80*, 569-572.

(305) Vergote, V.; Van Dorpe, S.; Peremans, K.; Burvenich, C.; De Spiegeleer, B. In vitro metabolic stability of obestatin: kinetics and identification of cleavage products. *Peptides* **2008**, *29*, 1740-1748.

(306) Garayoa, E. G. a.; Allemann-Tannahill, L.; Bläuenstein, P.; Willmann, M.; Carrel-Rémy, N.; Tourwé, D.; Iterbeke, K.; Conrath, P.; Schubiger, P. A. In vitro and in vivo evaluation of new radiolabeled neurotensin(8–13) analogues with high affinity for NT1 receptors. *Nuclear Medicine and Biology* **2001**, *28*, 75-84.

(307) Zwanziger, D.; Khan, I. U.; Neundorf, I.; Sieger, S.; Lehmann, L.; Friebe, M.; Dinkelborg, L.; Beck-Sickinger, A. G. Novel Chemically Modified Analogues of Neuropeptide Y for Tumor Targeting §. *Bioconjugate chemistry* **2008**, *19*, 1430-1438.

(308) Boelsterli, U. A.; Ho, H. K.; Zhou, S.; Yeow Leow, K. Bioactivation and hepatotoxicity of nitroaromatic drugs. *Current drug metabolism* **2006**, *7*, 715-727.

(309) Kalgutkar, A. S.; Gardner, I.; Obach, R. S.; Shaffer, C. L.; Callegari, E.; Henne, K. R.; Mutlib, A. E.; Dalvie, D. K.; Lee, J. S.; Nakai, Y. A comprehensive listing of bioactivation pathways of organic functional groups. *Current drug metabolism* **2005**, *6*, 161-225.

(310) Rickert, D. E.; Butterworth, B. E.; Popp, J. A.; Krahn, D. F. Dinitrotoluene: acute toxicity, oncogenicity, genotoxicity, and metabolism. *CRC critical reviews in toxicology* **1984**, *13*, 217-234.

(311) Liederer, B. M.; Borchardt, R. T. Enzymes involved in the bioconversion of ester-based prodrugs. *Journal of pharmaceutical sciences* **2006**, *95*, 1177-1195.

(312) Taketani, M.; Shii, M.; Ohura, K.; Ninomiya, S.; Imai, T. Carboxylesterase in the liver and small intestine of experimental animals and human. *Life sciences* **2007**, *81*, 924-932.

(313) Hatfield, M. J.; Tsurkan, L.; Garrett, M.; Shaver, T. M.; Hyatt, J. L.; Edwards, C. C.; Hicks, L. D.; Potter, P. M. Organ-specific carboxylesterase profiling identifies the small intestine and kidney

as major contributors of activation of the anticancer prodrug CPT-11. *Biochemical pharmacology* **2011**, *81*, 24-31.

(314) Reske, S. N.; Winter, G.; Baur, B.; Machulla, H.-J.; Kull, T. Comment on Afshar-Oromieh et al.: PET imaging with a [68Ga] gallium-labelled PSMA ligand for the diagnosis of prostate cancer: biodistribution in humans and first evaluation of tumour lesions. *European journal of nuclear medicine and molecular imaging* **2013**, *40*, 969-970.

(315) Baur, B.; Solbach, C.; Andreolli, E.; Winter, G.; Machulla, H.-J.; Reske, S. N. Synthesis, radiolabelling and in vitro characterization of the gallium-68-, yttrium-90-and lutetium-177-labelled PSMA ligand, CHX-A''-DTPA-DUPA-Pep. *Pharmaceuticals* **2014**, *7*, 517-529.

(316) Brom, M.; Franssen, G. M.; Joosten, L.; Gotthardt, M.; Boerman, O. C. The effect of purification of Ga-68-labeled exendin on in vivo distribution. *EJNMMI research* **2016**, *6*, 65.

(317) Albert, R.; Marbach, P.; Bauer, W.; Briner, U.; Fricker, G.; Brums, C.; Pless, J. SDZ CO 611: a highly potent glycated analog of somatostatin with improved oral activity. *Life sciences* **1993**, *53*, 517-525.

(318) Haubner, R.; Wester, H.-J.; Burkhart, F.; Senekowitsch-Schmidtke, R.; Weber, W.; Goodman, S. L.; Kessler, H.; Schwaiger, M. Glycosylated RGD-containing peptides: tracer for tumor targeting and angiogenesis imaging with improved biokinetics. *Journal of Nuclear Medicine* **2001**, *42*, 326-336.

(319) Gotthardt, M.; van Eerd-Vismale, J.; Oyen, W. J.; de Jong, M.; Zhang, H.; Rolleman, E.; Maecke, H. R.; Béhé, M.; Boerman, O. Indication for different mechanisms of kidney uptake of radiolabeled peptides. *Journal of Nuclear Medicine* **2007**, *48*, 596-601.

(320) Vegt, E.; De Jong, M.; Wetzels, J. F.; Masereeuw, R.; Melis, M.; Oyen, W. J.; Gotthardt, M.; Boerman, O. C. Renal toxicity of radiolabeled peptides and antibody fragments: mechanisms, impact on radionuclide therapy, and strategies for prevention. *Journal of nuclear medicine* **2010**, *51*, 1049-1058.

(321) Vegt, E.; Melis, M.; Eek, A.; de Visser, M.; Brom, M.; Oyen, W. J.; Gotthardt, M.; de Jong, M.; Boerman, O. C. Renal uptake of different radiolabelled peptides is mediated by megalin: SPECT and biodistribution studies in megalin-deficient mice. *European journal of nuclear medicine and molecular imaging* **2011**, *38*, 623-632.

(322) Choy, C. J.; Ling, X.; Geruntho, J. J.; Beyer, S. K.; Latoche, J. D.; Langton-Webster, B.; Anderson, C. J.; Berkman, C. E. 177Lu-Labeled Phosphoramidate-Based PSMA Inhibitors: The Effect of an Albumin Binder on Biodistribution and Therapeutic Efficacy in Prostate Tumor-Bearing Mice. *molecules* **2017**, *7*, 1929.

(323) Hofström, C.; Orlova, A.; Altai, M.; Wångsell, F.; Gräslund, T. r.; Tolmachev, V. Use of a HEHEHE purification Tag instead of a hexahistidine tag improves biodistribution of affibody molecules site-specifically labeled with 99mTc, 111In, and 125I. *Journal of medicinal chemistry* **2011**, *54*, 3817-3826.

(324) Hillier, S. M.; Kern, A. M.; Maresca, K. P.; Marquis, J. C.; Eckelman, W. C.; Joyal, J. L.; Babich, J. W. 123I-MIP-1072, a small-molecule inhibitor of prostate-specific membrane antigen, is effective at monitoring tumor response to taxane therapy. *Journal of Nuclear Medicine* **2011**, *52*, 1087-1093.

(325) Hao, G.; Kumar, A.; Dobin, T.; Öz, O. K.; Hsieh, J.-T.; Sun, X. A multivalent approach of imaging probe design to overcome an endogenous anion binding competition for noninvasive assessment of prostate specific membrane antigen. *Molecular pharmaceutics* **2013**, *10*, 2975-2985.

(326) Haeckel, R. Factors influencing the saliva/plasma ratio of drugs. *Annals of the New York Academy of Sciences* **1993**, *694*, 128-142.

(327) Jusko, W. J.; Milsap, R. L. Pharmacokinetic Principles of Drug Distribution in Salivaa. *Annals of the New York Academy of Sciences* **1993**, *694*, 36-47.

(328) Aps, J. K.; Martens, L. C. Review: the physiology of saliva and transfer of drugs into saliva. *Forensic science international* **2005**, *150*, 119-131.

(329) Gillette, J. R. Overview of drug-protein binding. *Annals of the New York Academy of Sciences* **1973**, *226*, 6-17.

(330) Bao, Q.; Newport, D.; Chen, M.; Stout, D. B.; Chatziioannou, A. F. Performance evaluation of the inveon dedicated PET preclinical tomograph based on the NEMA NU-4 standards. *Journal of Nuclear Medicine* **2009**, *50*, 401-408.

(331) Gourni, E.; Demmer, O.; Schottelius, M.; D'Alessandria, C.; Schulz, S.; Dijkgraaf, I.; Schumacher, U.; Schwaiger, M.; Kessler, H.; Wester, H.-J. PET of CXCR4 expression by a 68Ga-labeled highly specific targeted contrast agent. *Journal of Nuclear Medicine* **2011**, *52*, 1803-1810.

(332) Herrmann, K.; Lapa, C.; Wester, H.-J.; Schottelius, M.; Schiepers, C.; Eberlein, U.; Bluemel, C.; Keller, U.; Knop, S.; Kropf, S. Biodistribution and radiation dosimetry for the chemokine receptor CXCR4-targeting probe 68Ga-pentixafor. *Journal of nuclear medicine* **2015**, *56*, 410-416.

(333) Gourni, E.; Canovas, C.; Goncalves, V.; Denat, F.; Meyer, P. T.; Maecke, H. R. (R)-NODAGA-PSMA: A versatile precursor for radiometal labeling and nuclear imaging of PSMA-positive tumors. *PloS one* **2015**, *10*, e0145755.

(334) Schottelius, M.; Schwaiger, M.; Wester, H.-J. Rapid and high-yield solution-phase synthesis of DOTA-Tyr 3-octreotide and DOTA-Tyr 3-octreotate using unprotected DOTA. *Tetrahedron letters* **2003**, *44*, 2393-2396.

5. Publications

Peer-reviewed journal articles

- Production of clinical radiopharmaceuticals: general pharmaceutical and radioanalytical aspects; Schmidt, A., Schottelius, M., Herz, M. et al. J Radioanal Nucl Chem (2016). doi:10.1007/s10967-016-5125-6

Articles in preparation

- Effect of glycosylation on the theranostic tracer PSMA I&T; Schmidt A., Wirtz M., Osl T., Färber S., Beck R., Schottelius M., Schwaiger M., Wester HJ.; European journal of nuclear medicine and molecular imaging.

- Development of albumin binding PMSA inhibitors based on PSMA I&T; Schmidt A., Wirtz M., DiCarlo D., Osl T., Schwaiger M., Wester HJ.; Journal of nuclear medicine.

- Current concepts for improving the pharmacokinetics of radiopharmaceuticals; Schmidt A., Wester HJ.; Theranostics

Conference abstract

- Alexander Schmidt, Mara K. Parzinger, Daniel Di Carlo, Roswitha Beck, Martina Wirtz, Hans-Jürgen Wester. Reducing *in vivo* animal studies: Development of a highly efficient S9 metabolic stability assay for radiolabeled peptides using PSMA inhibitors as model compounds. 12. Jahrestagung der österreichischen Gesellschaft für Nuklearmedizin und Molekulare Bildgebung. Zell am See, 2017.

Patents

- 4-amino phenylalanine substituted PSMA I&T based Inhibitors for imaging and endoradiotherapy of prostate cancer; Schmidt A., Wester HJ.;BayPat Zeichen B77011 EP; TUM Zeichen 2017-01E08.

- Glycosylated PSMA inhibitors for imaging and endoradiotherapy; Schmidt A., Schottelius M., Wester HJ.; BayPat Zeichen B76155 EP; TUM Zeichen 2016-10E15

Patent in preparation

- Utilization of electron deficient aromatic residues to increase the internalization of PSMA inhibitors; Schmidt A., Wester HJ.

6. Acknowledgements

Within this last section, I would like to express my gratitude for the people, which were involved regarding this PhD-thesis.

First of all, I would like to thank Prof. Dr. Wester for giving me the opportunity to conduct my work at his department, for allowing me to research on a highly motivating topic, for constant scientific advice and the freedom to pursue my own ideas.

Further, I would like to thank PD Dr. Schottelius for her scientific advice and the approx. 1000 times of ordering Lutetium for me.

Thanks to PD Dr. Notni for explaining me the proper utilization of the ^{68}Ga-module, the free beer and especially the amazing evening with Theresa in Brunnen at the AGRR 2016.

The scientific advice of PD. Dr. Behrooz was always highly appreciated. However, I also thank you for all the non-scientific funny conversations.

Dear Ms. Kaul, thank you for managing everything in the background regarding the graduate school and other paper work.

Special thanks to the former PhD-students Dr. Theresa Osl, Dr. Martina Wirtz, Steffi Robu and Andi Poschenrieder. Tina, thank you so much for helping me out during my first months and showing me all the necessary methods and helping me with the first biodistribution- and PET-studies. Your constant scientific advice was always appreciated. Thanks to Steffi for all the funny moments in the lab and outside of work. I was always very grateful for having you as colleague.

Dear Theresa, thank you for your constant support during the countless experiments, which we did together. Thank you for being always critical when discussing scientific issues. Thank you for showing me that there is more than work in life and the most important thing, thank you for allowing me to ride your horse with this ridiculous plastic sword in order to look cool.

Dr. Hoffmann and Dr. Beck, thank you for the support regarding cell experiments and animal studies. Dear Roswitha, special thanks to you for your immense motivation and your always-bright mood.

I would further like to thank Daniel di Carlo for his excellent work during his master thesis and his contribution to my PhD-thesis. Your dedication was marvelous and I highly appreciate your work ethics.

Dear Mara Parzinger, thank you for the amazing work during your master thesis. Because of you a lot more was possible than I would have imagined. The book from you and Patrick Zanon was a great surprise and was already used countless times to look up idiosyncratic words.

Besides my two excellent master students, I would also like to express my gratitude for my other students Steffi Färber, Elisabeth Bauer, Tobias Milzarek, Maximilian Muhr, Melina Vollmer, Sebastian Pios, Katherina Wißmiller, Julia Evers and Gesa Hertrampf.

Dear Moni and Sven thank you for your help in the lab and support during synthesis and animal experiments. Go SouthPark Thomas!

Prof. Dr. Schwaiger, thank you for providing the excellent facilities of the Klinikum rechts der Isaar. Dear Sybille Reder and Markus Mittelhäuser, thank you so much for your constant and highly appreciated support regarding animal experiments. Thank you for always having time for me, even if you do not have it. Many experiments have been made possible due to you two.

Finally and most importantly, I would like to thank my family. Without your constant support, this PhD-thesis would not have been possible. Your encouragement and belief in me helped to overcome many hindrances. Mum and Dad, thank you for the tons of exquisite food and the always-relaxing atmosphere at home that you provided to me. Dear Sergej, thank you for always taking care of me.